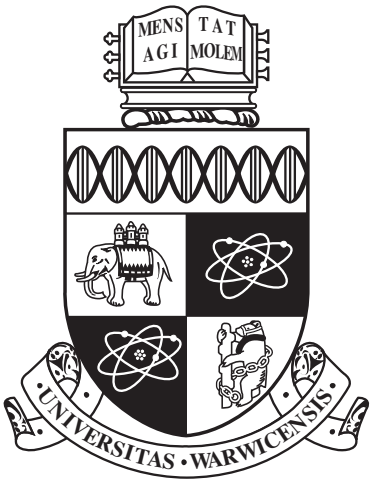

Long-Period Exoplanets from Photometric Transit Surveys

by

Hugh P. Osborn

Thesis

Submitted to the University of Warwick

for the degree of

Doctor of Philosophy

Astronomy and Astrophysics Group

Sept 2017

Contents

Acknowledgments

I would like to thank my supervisor, Don Pollacco, for his guidance, his candour, and his belligerence in trying to make me "get my ass in gear". I would also like to thank the members of the exoplanet group for their support, especially when asking the "stupid questions", and when providing helpful comments on everything along the way, including on this thesis. The people of the astronomy department physics, especially fellow PhD students, also deserve lots of credit for making the office a fun place to come to every morning.

Much of my keen interest in science and space dates back to being a kid, for which I have my parents to thank. The influence of them, and my sister Catherine, also helped mould me into someone capable of such a long and intellectually challenging task.

For keeping me sane (but far from sober), my friends over these four years deserve credit, including, in no particular order: Izaak, Lieke, Simon, Paula, Jess, Josie, Jamie, Max, Tom, both Marks, both Jameses and all four Daves. For heightening my appreciation of fresh air & fine whiskey, I also thank Warwick's Mountains society, and for providing far more pleasant scrapes with astro than at my desk, I thank the postgrad football team. And thanks to Rachel, who might understand this thesis the least, but certainly understands me the most.

Finally, thanks to commenters on Daily Mail science articles for their hilarious and misinformed insights into exoplanetary science, which form the thesis quotes prefixing each chapter.

Declarations

This thesis is entirely my own work. The bulk of three academic papers: Osborn et al. (2016), and Osborn et al. (2017a) and Osborn et al. (2017b) have been reworked into this thesis. Some sections of those papers were performed by collaborators under my guidance. The exact contributions from collaborators are stated at the beginning of each science chapter.

Abstract

Photometric transit surveys on the ground & in space have detected thousands of transiting exoplanets, typically by analytically combining the signals from multiple transits. This technique of exoplanet detection was exploited in K2 to detect nearly 200 candidate planets, and extensive follow-up was able to confirm the planet K2-110b as a $2.6 \pm 0.1 R_{\oplus}$, $16.7 \pm 3.2 M_{\oplus}$ planet on a 14d orbit around a K-dwarf.

The ability to push beyond the time limit set by transit surveys to detect long-period transiting objects from a single eclipse was also studied. This was performed by developing a search technique to search for planets around bright stars in WASP and NGTS photometry, finding NGTS to be marginally better than WASP at detecting such planets with 4.14 ± 0.16 per year compared to 1.43 ± 0.15, and detecting many planet candidates for which follow-up is on-going. This search was then adapted to search for deep, long-duration eclipses in all WASP targets. The results of this survey are described in this thesis, as well as detailed results for the candidate PDS-110, a young T-Tauri star which exhibited ~20d-long, 30%-deep eclipses in 2008 and 2011.

Space-based photometers such as Kepler have the precision to identify small exoplanets and eclipsing binary candidates from only a single eclipse. K2, with its 75d campaign duration and high-precision photometry, is not only ideally suited to detect significant numbers of single-eclipsing objects, but also to characterise them from a single event. The Bayesian transit-fitting tool ("*Namaste*: An MCMC Analysis of Single Transit Exoplanets") was developed to extract planetary and orbital information from single transits, and was applied to 71 candidate events detected in K2 photometry. The techniques developed in this thesis are highly applicable to future transit surveys such as TESS & PLATO, which will be able to discover & characterise large numbers of long period planets in this way.

Chapter 1

Introduction

"Look I'm no scientist, right, but space is like cold right, those planets are too far away from our Sun to get any heat from it, its not only Einstein who has great theory's"

albert47, bradford, United Kingdom, Daily Mail comments, 2017

1.1 Outline and History of Exoplanetary Science

1.1.1 Goals of exoplanetary science

While discoveries in exoplanetary science are an interesting development to human knowledge in their own right, the primary goal of the field is to put the Solar system and its planets into context; to compare and contrast the extrasolar systems of our Galaxy with the eight worlds in our cosmic neighbourhood. Exoplanets, studied in precise detail, add temporal, spatial, compositional and numerical perspectives to our own; and explore such diverse topics as how planets form, how they evolve (both internally and within their parent system), what they are made of, and how common they are.

Life, inevitably, also contemplates itself, asking questions such as how life on Earth arose, whether it is common in the Universe, and how frequently it develops into complex life. In some cases, exoplanetary science is already filling in the blanks and moving towards a more complete understanding. In others, the answers only exist buried in the noise of astronomical observations of exoplanets, waiting for some future instrument, or some innovative way, to reveal them.

1.1.2 History of Exoplanet detection

The contemplation of extrasolar systems has occurred throughout the era of the heliocentric universe: both before (Epicurus, 300BC; Hadzsits, 1916) and after (Bruno, 1584) the era of Ptolmeic geocentrism. With the mathematical construct of planetary orbits (Kepler, 1609), followed by that of gravity (Newton, 1687; Leibniz, 1690), the physical processes behind the solar system began to be explored (e.g. Lagrange, 1772; de Laplace, 1777). The established motion of the planets also led to the first observations of planetary transits (Mercury, Gassendi (1632); and Venus, Horrocks (1662)). It was later realised that these transit observations could give accurate measurements of our own solar system - specifically the Earth-sun distance (Halley, 1716).

As telescopes improved, they were trained on other stars, finding the first examples of extrasolar stellar systems through eclipsing binaries (Algol, Goodricke, 1784) and the first double stars with astrometric orbital motion (Michell, 1767; Mayer, 1779; Herschel, 1804). This technique of accurately measuring the positions of stars to detect the orbits of companions improved in accuracy and even led to erroneous claims of sub-stellar, planetary-mass objects around nearby stars (Jacob, 1855; Van de Kamp, 1963). The development, from spectral observations of the sun (Fraunhofer, 1817), of astronomical spectroscopy (Secchi, 1863) also led to the first measurements of radial velocities in double star systems (Pickering, 1880).

Much of the theoretical ideas that led to modern exoplanet detection techniques have origins in the latter half of the twentieth century. This includes the radial velocity, or RV, method, Struve (1952); the transit method, Rosenblatt (1971); and microlensing Mao and Paczynski (1991). Combined with the gradual development of astronomical instruments throughout the twentieth century, the detection of the first exoplanet by the turn of the millennium seemed inevitable.

The radial velocity technique was at the forefront of this push. Helped by the development of radial velocity analysis by cross-correlation (Griffin, 1967) and simultaneous absorption cell measurements (Campbell and Walker, 1979) which led to spectrometers capable of detecting the reflex motion of substellar bodies by the 1980s (see Section 1.3; Baranne et al., 1979; Campbell and Walker, 1984). The first searches for planets (Campbell et al., 1988; Walker et al., 1995) were underway by 1990, bringing the first tentative detections of bodies with minimum masses in the planetary regime (HD114762, Latham et al. (1989); and γ-Cephei, Walker et al. (1992)). The RV community were usurped by the detection of two terrestrial-mass objects around an unexpected object - the pulsar PSR 1257+12, found with pulsar timing (Wolszczan and Frail, 1992). However, these searches did eventually prove fruitful, with the first unambiguous detection of a planet around a sunlike star - the hot Jupiter 51 Pegasi b (Mayor and Queloz, 1995).

Method	$N_{Planets}$	Mean Size	Mean Period
Astrometry	0	-NA-	-NA-
Imaging	44	12.5 M_J	145 yrs
Pulsar Timing	7	1.2 M_J	0.22 yrs
Microlensing	45	0.51 M_J	7.3 yrs
RVs	632	1.5 M_J	1.05 yrs
Transit (ground)	260	1.24 R_J	3.25 days
Transit (space)	2468	0.19 R_J	11.1 days

Table 1.1: Number of planets by detection method, and the average size (Mass or Radius where appropriate) and orbital period (years or days where appropriate). Data taken from (Akeson et al., 2013) in May 2017.

The detection of 51 Peg was followed by a host of other RV "hot Jupiters" in the next five years. The idea of exoplanet transit detection, which had been channelled into proposals of space-based photometers capable of detecting earth-radius planets (Borucki et al., 1985), was re-awakened by the presence of giant planets in short orbits. Their large transit depth and high transit probability (see Section 1.2) not only meant that some of the already-detected exoplanets should be seen to cross their stars (as HD209457 b was observed to do in Charbonneau et al. (1999)), but also that transiting exoplanets could be detected in large numbers with modest ground-based telescopes. This led to the development of numerous ground-based surveys monitoring thousands of stars every night, with their first planets by the mid '00s (TrES-1b: Alonso et al. (2004), XO-1b: McCullough et al. (2006), WASP-1b: Cameron et al. (2007), HAT-P-1b: Bakos et al. (2007)).

By this point, high-precision RV surveys covered more than a decade, detecting Jupiter-mass planets on long (1-10 year) orbital periods. The era of 8-10m telescopes with adaptive optics had also dawned, and the first directly imaged giant planet candidate was found (Chauvin et al., 2004). Increases in the precision of the OGLE & MOA projects, looking for gravitational microlensing events in the galactic bulge, also had their first planets by the end of exoplanet's first decade (Udalski et al., 2005; Beaulieu et al., 2006). With giant planets now being found at a rapidly growing pace, and with many disparate techniques, the new objective was to push the frontier of exoplanetary science downwards to small planets. For RVs, this meant focussing on nearby low-mass stars. For transiting exoplanet science, this meant going to Space.

I will consider the following ten years of exoplanetary science, and their theoretical background, in the following sections, especially on the detection and study of transiting planets, which is the focus of this thesis.

1.2 Exoplanet Transits

1.2.1 Geometry of a Transit

A small percentage of exoplanetary systems have inclinations relative to the line-of-sight observations such that they pass in front of their parent star. This exoplanet transit will cause a dip in light proportional to the ratio of the areas of the stellar and planetary discs Seager and Mallen-Ornelas (2003):

$$\Delta F = \frac{F_{\text{star}} - F_{\text{transit}}}{F_{\text{star}}} = \left(\frac{R_{\text{p}}}{R_{\text{s}}}\right)^2 \tag{1.1}$$

Figure 1.1 describes the geometry of an exoplanetary transit. The equations are adapted from (Seager and Mallen-Ornelas, 2003), Haswell (2010) and the simplified descriptions of Paul Wilson[1]. The impact parameter, defined as the minimum distance of the transit chord to the stellar centre (normalised to the stellar radius), is also derived from the semi-major axis, inclination and stellar radius (Panel 1).

In Panel 2 the length of transit chord ($2l$) is derived from the impact parameter, planet radius R_p and stellar radius R_s. This is shown in both absolute lengthscales (left) or scaled to stellar radius (right). In this figure and the equations shown here, the orbit is assumed to take a straight chord across the stellar surface. In reality, a further factor of $1 - \cos^2(i)$ is required to account for the curvature from the orbit in this plane. However, for all but the shortest and most inclined orbits, this effect is negligible. For example, an 85° 2-day orbit, has a transit duration only 0.4% larger than computed from this model. The lower left of this figure shows the depth (ΔF), derived as a function of the ratio of planet to star areas (e.g. 1.1).

In Panel 3, the transit duration (T_{dur}) is computed. This is achieved by considering the angle (τ) at the planetary orbit between the centre of transit and the furthest extent (eg ingress or egress). This can be derived from the straight transit chord and the semi-major axis ($\tau = \sin^{-1} l/a$, the triangle outlined in red), as well as from the transit duration as a function of planetary period ($T_{\text{dur}} = P \times \tau/a$, the segment outlined in green). The duration is therefore a function of the orbital period (P), the semi-major axis scaled to radius (a/R_s), the transit depth or radius ratio ($\sqrt{\Delta F} = R_p/R_s$), and the impact parameter (b). These are classically the parameters used when fitting a transit, along with eccentricity (e) and longitude of the ascending node (Ω) which are not considered here.

Although seemingly large in figure 1.1, the geometric parallax between apparent planetary position against the star and real position is negligible as the observer is positioned at effectively infinite distance. This effect is needed to be taken into account for solar system

[1] from www.paulanthonywilson.com/exoplanets/

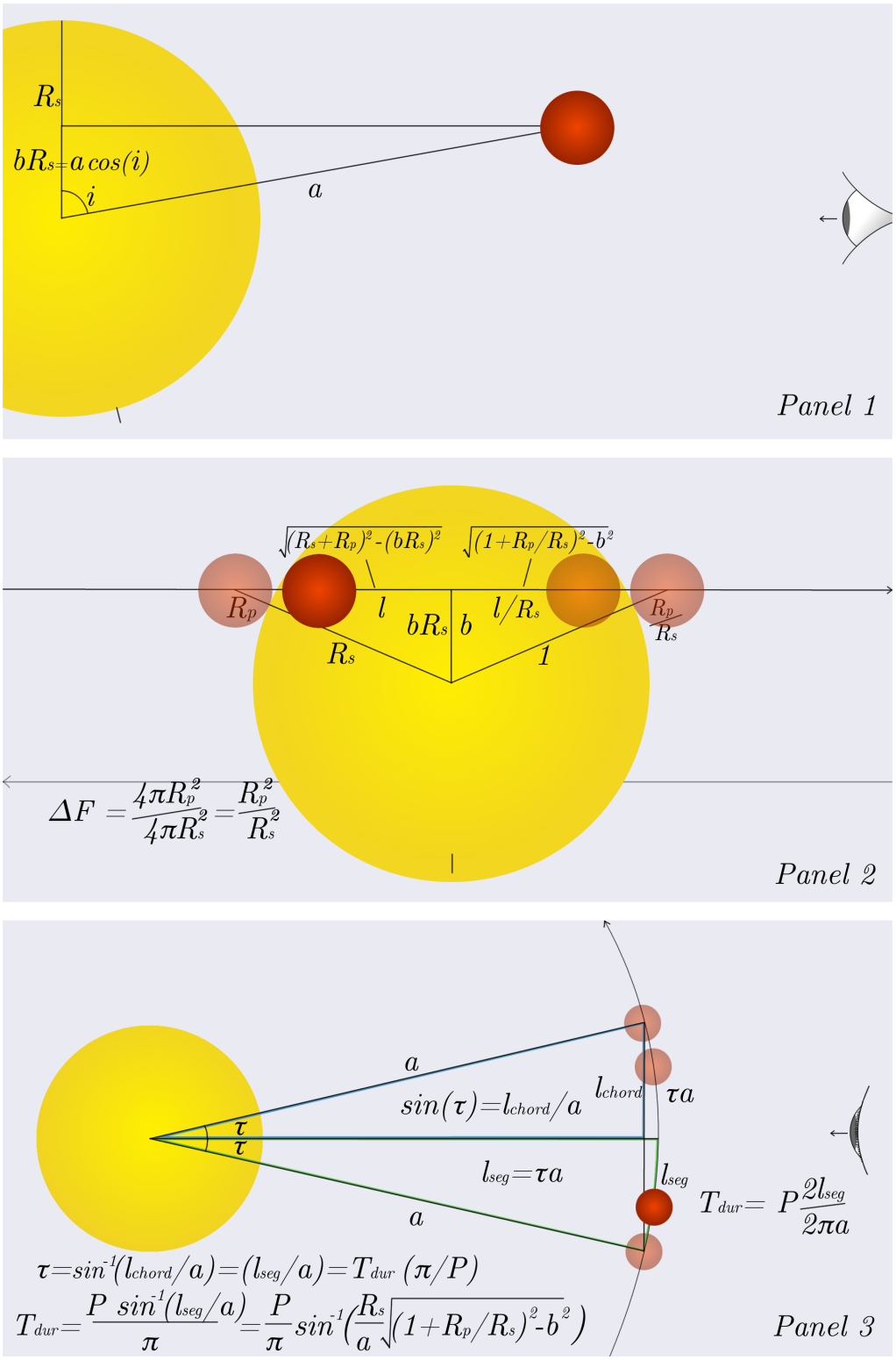

Figure 1.1: The geometry of a transit. Panel 1: As seen from along the plane of planetary orbit, with the observer to the right. Panel 2: The system as seen from the view of the observer. Panel 3: The system as seen from the pole of the planetary orbit, with the observer to the right.

transits, however.

Similarly, Panel 3 suggests that the curved path of the planet during transit ($2l_{\rm seg}$) is significantly different from a straight line ($2l_{\rm chord}$). While this is true for short period objects, for most planets beyond a few days orbit, the transit chord can be approximated as a straight line (e.g. $\sin^{-1}(R_s/a) \sim R_s/a$). In this case:

$$T_{\rm dur} = \frac{PR_s}{\pi a}\sqrt{(1+\frac{R_p}{R_s})^2 - b^2} \tag{1.2}$$

As a and P are related by Kepler's third law ($a^3 \propto P^2 M_s$), we can reduce this formula yet further:

$$a = \left(\frac{P^2 G M_s}{4\pi^2}\right)^{\frac{1}{3}}; T_{\rm dur} = \frac{PR_s}{\pi}\left(\frac{4\pi^2}{P^2 G M_s}\right)^{\frac{1}{3}} l_{\rm ch} \tag{1.3}$$

Where $l_{\rm ch}$ is the transit chord normalised to stellar radius, $\sqrt{(1+R_p/R_s)^2 - b^2}$. Hence, the transit duration scaled to the stellar radius becomes:

$$\frac{T_{\rm dur}}{l_{\rm ch}} = \left(\frac{P^3 R_s^3 4\pi^2}{\pi^3 P^2 G M_s}\right)^{\frac{1}{3}} = \left(\frac{4PR_s^3}{\pi G M_s}\right)^{\frac{1}{3}} = \left(\frac{3P}{\pi^2 G \rho_s}\right)^{\frac{1}{3}} \tag{1.4}$$

Where $\rho_s = (3M_s)/(4\pi R_s^3)$. This shows that the transit duration, when corrected for the size of the planet and its impact parameter, is also directly related to the stellar density and planetary period.

The geometry of transits was first analytically described by Mandel and Agol (2002), which has been adapted by numerous authors to run computational fits to exoplanet transits. The `python` libraries of Ian Crossfield[2], Dan Foreman-Mackey[3] and Laura Kreidberg (Kreidberg, 2015) were all used at points through this thesis.

1.2.2 Limb Darkening

In section 1.2.1, the star was assumed to be of uniform brightness. However this is not the case; stars vary in brightness from the stellar centre to the stellar limb. In optical bandpasses, this manifests itself as limb darkening, and is caused by the variation in the depth of the emitted photons across the stellar atmosphere. This is because of the depth from which observed photons are emitted.Photons emitted at the centre of the disk pass perpendicularly through the stellar atmosphere from an average depth (or path length) l. Photons emitted from increasingly more oblique angles from the centre (large γ in figure 1.2), take similar length optical paths, meaning they must come from shallower depths $l/(\cos\gamma)$. This means

[2]Accessed from http://www.lpl.arizona.edu/ ianc/python/

[3]Accessed from http://dan.iel.fm/transit/current/

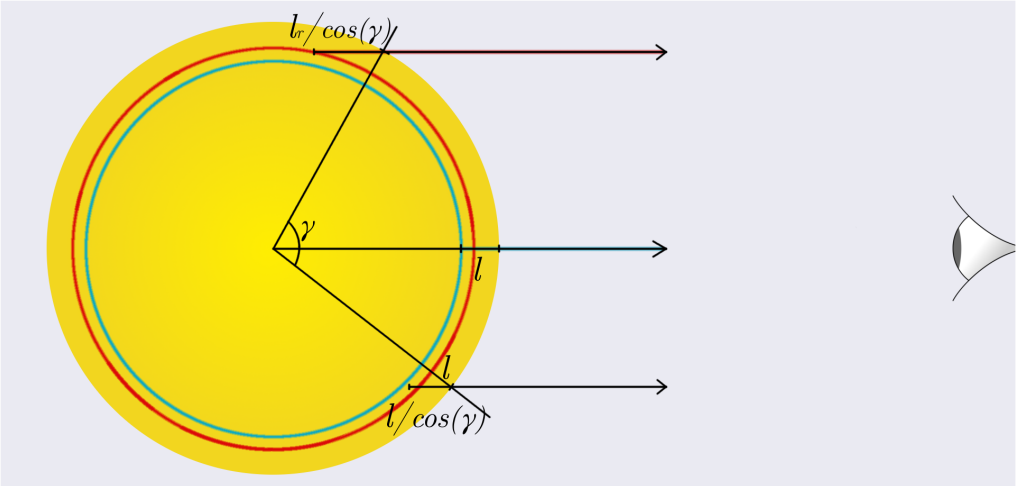

Figure 1.2: The geometry of limb darkening. The upper arrow shows the paths of light from near the limb, originating from the shallow, cooler region shown in red. The middle arrow shows the optical path at the centre of the limb from deeper, hotter regions in blue. The lowest arrow shows the intermediate case.

that photons are more likely to originate from shallower and therefore cooler & lower luminosity regions in the stellar atmosphere. This temperature change also causes the colour to appear redder towards the limb and bluer in the centre.

The strength of limb darkening is wavelength-dependent, with longer wavelengths having shorter optical depths in the stellar atmosphere, and therefore weaker limb darkening. There is no noticeable limb darkening for wavelengths above $\lambda = 1\mu m$ (Seager and Mallen-Ornelas, 2003).

As limb darkening is a function of the depth, structure and temperature of the stellar photosphere, the change in brightness across the disk can be approximated using stellar atmosphere models. These are then convolved with the specific filters used during the transit observation (e.g. Sing, 2010; Claret and Bloemen, 2011). Numerous methods (or "Laws") are used to fit the resulting monochromatic change in brightness from centre to limb. These include a linear (1-parameter) method; quadratic, square-root, logarithmic and exponential 2-parameter laws, and a 3-parameter cubic law. The linear and exponential laws, however, do a poor job of fitting observed transits (Espinoza and Jordán, 2016). Fixing limb darkening parameters to those determined from the stellar parameters should only be performed with caution, as they can be significantly offset from true values due to intrinsic systematics or stellar spots and faculi, potentially change the derived planetary radius by up to 20% (Csizmadia et al., 2013).

1.2.3 Transit Probability

For a body on a circular orbit, the probability that its orbit crosses the line-of-sight of its parent star is simply:

$$P_{\text{transit}} = \frac{(R_s + R_p)}{a_{\text{pl}}} \approx \frac{R_s}{a_{\text{pl}}} \tag{1.5}$$

Where R_s is the stellar radius, R_p is the planet (or other body) radius, and a_{pl} is the semi-major axis.

For an eccentric planet, the distance between star and planet varies over the course of the orbit, increasing the transit probability at perihelion, and decreasing it at aphelion. The net result is that eccentric planets are more likely to transit, with an effect on transit probability of eccentricity, e (from Barnes, 2007) of:

$$P_{\text{transit}} = \frac{R_s}{a_{\text{pl}}\,(1 - e^2)} \tag{1.6}$$

This also means the argument of periastron of a transiting planet is most likely to be near its perihelion, with the distribution in ϕ shifted from flat to $\phi = 1 + e\cos(\phi)$, and the transit velocity (and therefore duration) changing with:

$$\Delta V = \frac{V_\phi}{V_{\text{circ}}} = \frac{1 + e\cos f}{\sqrt{1 - e^2}} \tag{1.7}$$

1.2.4 Ground-based Transit Surveys

After RV surveys showed Hot Jupiters were common, and the microlensing experiment OGLE detected the transits of some strong hot Jupiter candidates (Udalski et al., 2002), many ground-based observers set up simple photometric surveys designed to detect more transiting planets. These tended to consist of several telephoto lenses attached to astronomical-quality imagers or Charged Couple Devices (CCDs) and a telescope mount to track the motion of the stars. In many cases, multiple sites were used to either extend the sky coverage longitudinally and reduce time gaps between observations, or extend latitudinally to cover both northern and southern skies. They include (in order of first planet detection):

- **TrES** (The Transatlantic Exoplanet Survey): 3x100mm cameras in Tenerife, Arizona & California (Alonso et al., 2004). It was the first transit survey to find a transiting planet around a bright star.
- **HAT** (Hungarian Automated Telescope): 6x65mm aperture cameras in Arizona and Hawaii (Bakos et al., 2002). It has detected 67 planets in total.

- **XO**: 2x110mm lenses in a single site in Hawaii (McCullough et al., 2005). It found the second transiting planet (McCullough et al., 2006), and contributed six in total.
- **WASP** (Wide-Angle Search for Planets): 16x72mm aperture cameras in two locations (N - La Palma, ESP; & S - Sutherland, RSA) (Pollacco et al., 2006). It has so far detected over 150 planets (e.g. Lam et al., 2017), making it the most prolific such survey. See Section 2.6.1 for details of the data outputs.
- **HAT-S** (Hungarian Automated Telescope South): 6x64mm aperture cameras across 3 sites in the Southern hemisphere (Chile, Australia & Namibia) allowing near-continuous monitoring and hence is able to target longer-period planets (Bakos et al., 2008). It has detected 35.
- **KELT** (Kilo-degree Extremely Little Telescope): 42mm and 71mm aperture cameras located in Arizona (Pepper et al., 2007). It observes a wider field (and therefore targets brighter stars) than the previouslt listed projects. It has so far found 18 planets.
- **MASCARA** (The Multi-site All-Sky CAmeRA): With 5x24mm cameras, MASCARA is the widest-field of the bunch, and is also unique in not tracking stars by moving the cameras, but allows the stars to move across the CCD (Talens et al., 2017).

Wide sky coverage came at the cost of large pixels, meaning an increased probability of background stars, and therefore background eclipsing binaries (BEBs), within the sizeable (>30") pixel apertures. Such telescopes are also hampered by correlated ("red") noise (see section 1.2.5), significantly reducing the signal-to-noise ratio (SNR) and making the U-shaped transit signals often indistinguishable from V-shaped BEBs. These effects mean ground-based transit surveys have a high false positive (FP) rate of >80%. This even meant some telescopes never detected a planet at all despite monitoring tens of thousands of stars (e.g. RAPTOR, Vestrand et al., 2002). To discard these FPs, extensive follow-up is required for ground-based candidates to be confirmed as planets, often including repeated photometry with more precise telescopes, spectral typing of the primary, and radial velocity measurements of the reflex motion on the star.

More recent ground-based surveys have improved on the original design in an attempt to detect lower-radius planets.

- **MEarth**: 16x400mm telescopes in both Arizona and Chile individually search ~ 3000 nearby M-dwarves in low-cadence observing mode, switching to high-cadence mode when a star appear to be in transit. With a precision of 6mmag, they are able to detect terrestrial-size planets (e.g. GJ1132 Berta-Thompson et al. (2015); LHS1140, Dittmann et al. (2017)).

- **NGTS** (Next Generation Transit Survey): 12x200mm aperture telescopes in Chile with sensitive 2Kx2K detectors in the near-IR. Improvements to tracking and design mean the stars move by less than 0.1 pixel on the CCD, and reduce correlated noise to the level of $\sim$ 1mmag/hr (Wheatley et al., 2013). See Section 2.6.2 for details of the data outputs.

- **TRAPPIST**: A single 60cm robotic telescope in La Silla, Chile (Jehin et al., 2011). It was used to study a handful of ultracool dwarf stars, detecting a seven-planet system of earth-radius planets around the 0.08 $M_{\odot}$ star Trappist-1 (Gillon et al., 2017).

Despite improvements in wide-field ground-based transit surveys, they have so far been limited to detecting planets only after observing multiple transits. The reasons for this will be explored in Section 1.2.5, but the result has been that almost all such planets have orbital period of a few days and no systematic search for longer duration planets has been performed.

1.2.5 Red Noise in Transit Surveys

"Red" noise is the dominant source of uncertainty for ground-based photometry. This is correlated systematic noise varying the mean flux of the star over the timescale of a few hours - the typical timescale of an exoplanet transit. The result of this correlated noise is that the SNR of each transit is lower than expected from white noise, increasing the false-positive rate and meaning the transit detection signal does not strengthen as expected from white noise over time. The effect is so strong that signal detection of a ground-based observatory for a planet on a 2.5d orbit drops from 100% with only white noise, to less than 10% with 3.1ppt of correlated noise present (Figure 1.4). Due to this red noise and the necessity for multiple transits to be observed to high photometric precision, ground based transit surveys have so far been limited to very short-period planets with a median period of only $\sim$4.2 days (see table 1.1).

This correlated noise is often a combination of atmospheric effects (from e.g. trends in airmass and sky background), noise intrinsic to the detector (from e.g. focus changes and pixel-to-pixel variations) and stellar variability itself (Pont et al., 2006). The trends common to many stars across each observed field can, to some extent, be removed by detrending (see Section 2.7). However, correlated noise from variations that are not shared by all stars is not yet easily removed. Differential PSF changes across the field due to temperature changes are often poorly removed by detrending methods. As are colour-depended factors in airmass and sky-background trends. Another important effect is from the drift and movement of the star over the CCD. This means that, every exposure, the pixels that are illuminated vary. As each pixel may have subtly different responses, and the gaps between pixels may vary,

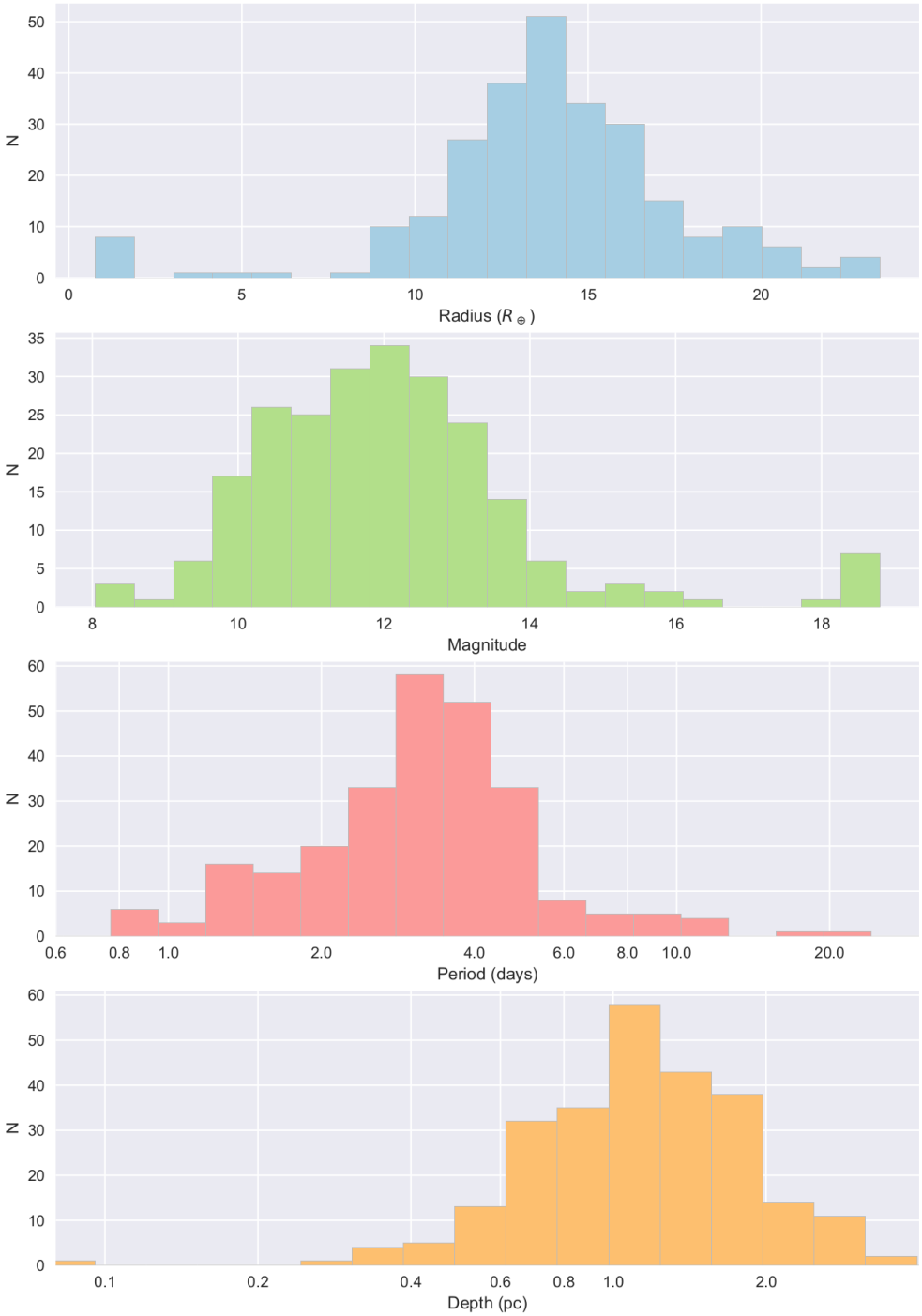

Figure 1.3: The vital statistics of ground-based transiting planets: histograms of planet radii, magnitude, orbital period and transit depth. The majority of planets are jovian, on short periods, and around bright ($V < 14$) stars. The terrestrial planets in the TRAPPIST-1 system and from MEarth are outliers in these histograms.

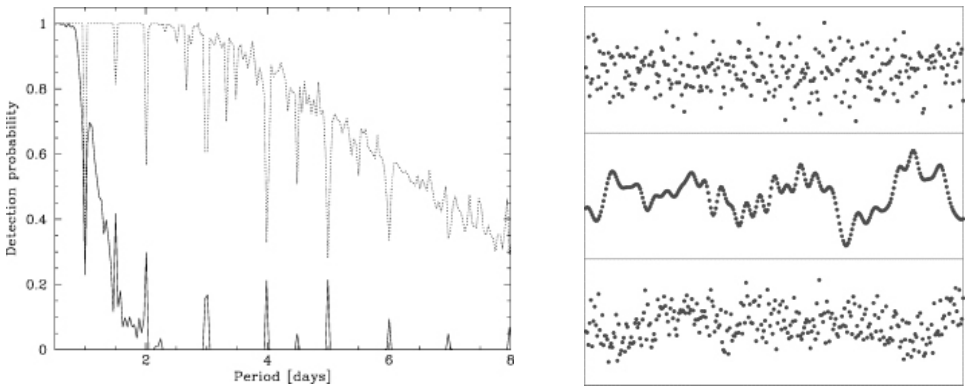

Figure 1.4: **Left:** Detectability of a 1% transit as a function of period in photometry with the BLS technique with only white-noise (0.3ppt, dashed line) and white and red-noise (0.31ppt,solid line). **Right:** An example of the typical white (above), red (central) and combined (lower) noise seen in photometric surveys. Both figures from Pont et al. (2006).

leading to correlated noise on the timescale of pixel drift (Pont et al., 2006). Scintillation of the atmosphere, which varies over rapid timescales (minutes) and over distances shorter than the diameter of the field-of-view, can also be important and is difficult to remove (Fohring, 2014). Intrinsic stellar variability is another example, especially as the poor phase coverage from the ground means variability is often too poorly sampled to be modelled and removed.

For bright and non-variable stars on nights with low levels of correlated noise, planets could be detected from favourably placed single transits, potentially allowing ground-based transit surveys to push far beyond their current period limits and into the warm Jupiter regime.

1.2.6 Space-based transit surveys - Detectable Effects

The limitations of both atmospheric red noise and poor time coverage (Pont et al., 2006) are removed entirely with a space telescope, allowing the detection of smaller and more distantly-orbiting planets than ground-based surveys can reach (Gillon et al., 2005).

The high precision, continuous observations, and rapid time sampling also allows for the potential detection of previously unseen effects.

Host star asteroseismology - By studying the oscillations of stars, which exist in specific modes given the physical parameters of the star, those physical properties can be precisely derived. CoRoT allowed the first such observations of a few dwarf (F/G-type) stars, whereas *Kepler* studied thousands of sun-like stars in this way (Gilliland et al., 2010), including for planet hosts (Aguirre et al., 2015), providing stellar parameters (radius, mass, age, etc.)

with exquisite precision (Huber et al., 2013).

TTVs - Transit Timing Variations are shifts in central transit time of each transit. They are most frequently caused by changes in orbital velocity due to the gravitational pull of outer companions (Holman and Murray, 2005; Lithwick et al., 2012). Their amplitude allows the mass of worlds in multi-planet systems to be measured independently, which was first performed with *Kepler* photometry (Mazeh et al., 2013; Hadden and Lithwick, 2014). Kepler's precise data also allowed the detection of non-transiting planets for the first time using this method (Ballard et al., 2011; Nesvorný et al., 2013).

Centroid shifts - The centroid of a star refers to the position of average brightness of an observed star. This is often found through a weighted mean of the pixels in the aperture, or through a more complex fit of the PSF (point spread function) of the light from the star on the CCD. Blended eclipsing binaries (BEBs) are the result of a fainter background star undergoing a stellar eclipse within the aperture of the target star. They produce planetary-depth eclipses and are a frequent false-positive for transit surveys. The light is therefore dominated by the invariant lightcurve of the primary, with a shallow transit the result of a far deeper eclipse on the background star. For example, a background 15th magnitude star undergoing an eclipse of 50% in the aperture of a 10th magnitude star would appear as a transit with a depth of 50ppt. Such a vast drop in flux from a background star, if it is sufficiently offset from the centre of the target, can produce a noticeable shift in the centroid position, which will move closer to the target star during eclipse. Therefore precise space photometry can measure centroid shifts during transit and indicate a false positive.

Transit shape characterisation - High-precision in-transit photometry allows the shape of the eclipse to be precisely compared to models of exoplanetary transits and eclipsing binaries. This can therefore help determine the probability that such a signal is a transiting planet, or a false-positive. Combined with stellar parameters and a study of potential blended sources, this can help probabilistically confirm an exoplanet without radial velocities (Morton, 2012; Santerne et al., 2015; Armstrong et al., 2017).

Optical phase curves - The combination of reflected light and thermally emitted radiation from a hot planet mean that the total optical flux from star and planet vary over a planetary orbit, and the contribution of the planet is removed completely during secondary eclipse. The precision and long duration of *Kepler* meant phase curves could be studied for dozens of hot planets, including super-Earths (Esteves et al., 2013), and even allowed resolution over the time domain, showing time-varying exoplanetary weather for the first

time (Armstrong et al., 2016c).

Exomoons & exorings - Although not yet detected, the presence of large moons may be detectable from the transit timing and duration variations (TTVs & TDVs) of exoplanet transits (Kipping, 2009), or through the drop in flux due to their transits (Simon et al., 2012). Similarly, the presence of extrasolar Saturn-like rings is theoretically detectable from observations of assymetric or unusual transit shapes (Barnes and Fortney, 2004; Aizawa et al., 2017). In both cases, circumplanetary material is most stable and most detectable around long-period transiting giant planets, which have yet to be found in large numbers (Cassidy et al., 2009).

1.2.7 Past & Current Space-Based Transit Surveys

CoRoT The COnvection ROtation et Transits planétaires mission, or CoRoT, was the first satellite designed to detect transiting planets from orbit (Baglin et al., 2006). With a 27cm-aperture telescope and four CCDs, it launched into a polar orbit 2006 and observed for 1200 days until the telescope failed in 2012, achieving 500ppm photometry precision per hour for a 15th magnitude star. With its ~8 square degree field, CoRoT observed ~160,000 thousand stars in 25 different fields, each for between 20 and 150 days. It detected 530 planet candidates, although subsequent follow-up revealed a high false-positive rate of ~75% (Moutou et al., 2013). Despite this, it observed stars to a level of photometric precision unobtainable from the ground, finding 20 planets including the first ever transiting Super Earth with radius 1.68 ± 0.09 $R_\oplus$ (Léger et al., 2009).

Kepler *Kepler* was first considered in 1997 as a 0.95m aperture telescope that would observe more than 150,000 stars to a photometric precision capable of detecting transiting terrestrial planets (Borucki et al., 1997). It launched in 2009, more or less unchanged, and began observations of 156,000 pre-selected target stars in a 100 square degree field in Cygnus (Borucki et al., 2010). See Section 2.6.3 for observations and data methods.

The failure of a second reaction wheel in 2013 ended the primary mission after 1467 days (4.02 years). Photometric data collected over that time has significantly advanced the field of exoplanets. From more than 16,285 "Threshold crossing events" (Tenenbaum et al., 2014) came 4496 planet candidates of which 2335 have been confirmed (Akeson et al., 2013)[4].

The faint magnitude of many of the *Kepler* targets made follow-up (e.g. RVs) observationally tricky, but validation with stellar characterisation, high-resolution images and the high-precision transit photometry was used to confirm hundreds of planets (Morton et al.,

[4]NASA Exoplanet archive - https://exoplanetarchive.ipac.caltech.edu/

2016). This was especially possible in multi-planet systems, for which the mutual inclinations of planetary systems acts as a powerful argument for a planetary origin over the presence of multiple eclipsing binaries (Rowe et al., 2014). *Kepler* found multi-planet systems in unexpected abundance, with 431 systems with ≥ 2 planets, and 57 with four or more (Fabrycky et al., 2014). These tight multi-planet systems were often found orbiting in resonant chains, with period ratios at (or near) integer fractions, indicative of low-eccentricity migration (Rein, 2012).

The well-characterised sample of stars observed by Kepler, and the number of detections have allowed the occurrence rates of exoplanets from giants down to terrestrial-radius to be studied (see Section 1.5.4), even giving the first ever predictions for the proportion of sunlike stars with Earthlike planets ($\eta_{\oplus}$, see Section 1.5.4).

K2 With only two reaction wheels, *Kepler* previous level of pointing stability (0.003") was impossible, and without a way of maintaining spacecraft pointing along a third axis, precise photometry would be impossible. To maintain stability and make use of the instrument, it was realised that solar radiation pressure could be used to maintain course pointing (Putnam and Wiemer, 2014). This was achieved by orienting the ridged solar panels towards the Sun, meaning fields along the ecliptic could be observed for up to 80 days. This officially became the *K2* mission (Howell et al., 2014), and the method was tested in an initial engineering campaign in late 2013, and the first official *K2* campaign began in March 2014.

Due to the reduced stability, *K2* photometry was dominated by systematics from the motion of the stellar PSF on the detector. Numerous methods were devised to detrend for these systematics, producing photometry of similar quality to the primary mission (see 2.7).

Since the engineering campaign (which observed only ~7 days of useable photometry), fifteen 80-day fields have been observed (C0-C14), with each typically observing 10-20,000 stars, although only photometry from the first eleven fields (C0-C10) are used in this thesis. Numerous groups have searched the photometry for exoplanets, producing more than 500 candidates (Foreman-Mackey et al., 2015; Vanderburg et al., 2015a; Barros et al., 2016; Pope et al., 2016; Adams et al., 2016; Jackson et al., 2017). Many of these were validated or confirmed (Crossfield et al., 2015; Montet et al., 2015; Sinukoff et al., 2016; Crossfield et al., 2016).

The detected planets are similar in size to those from original *Kepler* mission, although the shorter duration means shallower signals (and therefore smaller planets) are less likely to be detected (see Figure 1.5). That 80-day duration also means only short-period planets have been detected, with the longest period only 50d. Reduced bandwidth has meant *K2* observes fewer stars than the original mission, but by covering many more 100 square

Figure 1.5: Comparison of *K2* and *Kepler* planet detections by Radius, magnitude, orbital period and depth.

degree fields, it has also meant that it has been able to increase the number of brighter stars. This has meant the median planet host has a magnitude of 12.9 compared to the *Kepler* median of 14.6, with the number of *K2* planets around stars with *Kepler* magnitude $11 - 12.5$ already exceeding the initial 4-year *Kepler* mission. Despite this increased average brightness, many *K2* planets have been validated using the same technique as *Kepler* rather than directly confirmed and characterised with RVs (e.g. Crossfield et al., 2015).

Some *K2* systems have been observed with RVs, however, including low-mass planets K2-3b, c & d (Almenara et al., 2015; Dai et al., 2016); K2-19b & c (Armstrong et al., 2015b; Barros et al., 2015); K2-27b, K2-32b, K2-39b, & K2-108b (Petigura et al., 2017); K2-38b & c (Sinukoff et al., 2016), etc.

1.2.8 Future space-based transit surveys

TESS The Transit Exoplanet Sky Survey will launch in early 2018 and use four 10.5cm-aperture cameras to observe most of the sky in a series of 26, 27-day long, 24x96 degree fields (Ricker et al., 2015). Over its two year mission, a total of 200,000 pre-selected targets will be observed with short-cadence mode of 2 minutes, whereas as many as 2 million will be observed in the full frame images at 30 minute cadence. The majority of targeted will be observed for a single 27d field, however around 2% of targets at the ecliptic pole will be covered for an entire year. The smaller camera apertures (10.5cm) mean far lower flux precision than *Kepler*, however with such a wide field *TESS* is able to alleviate this by covering far more bright stars. The field duration and high noise mean *TESS* is limited to transit depths of $> 500ppm$, enabling it to probe temperate super-Earths around M-dwarfs and hot Neptunes around FGK stars (Sullivan et al., 2015).

CHEOPS The CHaracterizing ExOPlanet Satellite will be a 30cm space telescope launching in 2018 able to perform photometry on planetary candidates with a similar precision to *TESS* of 2.5ppm/h (Broeg et al., 2013). It will focus on follow-up measurements of *TESS* targets, as well as detecting the transits of small planets found using radial velocities.

PLATO The PLAnetary Transits and Oscillations of Stars will launch in 2026 and perform high-precision photometry capable of finding earth-sized planets around bright stars, including those on long periods. Similar to *TESS*, it will host 12cm-aperture telescopes and cover wide areas of the sky to search for planets around bright stars. Unlike *TESS*, *PLATO* will have 28 of them, and will combine the light from multiple cameras to give far better precision even than Kepler, with a transit precision of 27ppm/h for an 11th magnitude star. Combined with the long field durations (2+ years), this will enabling the detection of long-period terrestrial planets around FGK stars (Rauer et al., 2014).

1.3 Radial Velocities

As a consequence of the Doppler effect (Doppler, 1842), receding stars show a redward shift in their spectrum and vice-versa, $\frac{\Delta\lambda}{\lambda} = \frac{v}{c}$. Hence the wavelength shift directly gives radial velocity[5]. Stars moving on Keplerian orbits around a centre of mass therefore show signature changes in their radial velocity over time. This is most commonly expressed as a semi-amplitude, K, about a systemic RV υ_0, derived from Kepler's laws of motion (specifically the differential of the radial distance with angle):

$$K = \upsilon_0 + \sqrt{\frac{G}{(1-e^2)}} M_2 \sin i (M_1 + M_2)^{-1/2} a^{-1/2} \tag{1.8}$$

The RV amplitude is therefore most heavily dependent on the mass of the secondary object (M_2) and the orbital inclination (i). For example, the RV signal of a 2.0$M_\oplus$ planet on a nearly edge-on orbit ($i = 80°$) around Proxima Centauri (M_s=0.123 $M_\odot$) can be equivalently produced from a 15 $M_\oplus$ planet with a nearly face-on orbit ($i = 5°$), with both producing a 1.45m s^{-1} RV semi-amplitude (Anglada-Escudé et al., 2016). The RV amplitude is also weakly a function of orbital separation ($K \propto a^{-1/2}$) and the orbital eccentricity ($K \propto (1 - e^2)^{-1/2}$).

As was first realised in the 19th century (Secchi, 1863; Pickering, 1880), the absorption lines that litter the spectrum of sunlike stars at extremely well-determined intervals can be used to study their Doppler motion (and hence their companions).

The measurement of radial velocities have steadily improved over time thanks to many key developments. Individual absorption lines have varying degrees of noise and scatter, so using the contribution of the entire spectrum to estimate a radial velocity can increase precision. In the pre-digital era, this meant creating an inverse mask from an initial spectrum such that absorption lines would let light through and continuum levels would be blocked (Griffin, 1967). The mask could then be moved across the spectrum and, where the template matched the real spectrum, they would cross correlate to produce a dip in flux (e.g. Baranne et al., 1979). In the digital era, this cross-correlation function (CCF) is performed computationally by correlating a spectrum with a template (e.g. Simkin, 1974), and can be done even with low-SNR spectra (Queloz, 1995).

The average velocity is then typically measured from the average line profile as computed by the CCF. Other quantities measurable from the CCF include the Full Width Half Maximum (FWHM) - a measure of the average stellar line broadening and/or instrumental dispersion. Also used to study activity such as granulation is the line Bisector values

[5]General relativity requires a more complex formulation of Doppler shift, but this can be neglected for relative Doppler shifts of order m s^{-1}.

(BIS) which is a measurement of the change in the average line mid-point with depth (Gray, 2010). The error in the velocity obtained from a CCF is then a function of both contrast (C, e.g. average line depth), FWHM and the spectrum SNR (Bouchy et al., 2001):

$$\sigma_{\mathrm{RV}} \approx \frac{\sqrt{FWHM}}{C\ \mathrm{SNR}} \tag{1.9}$$

Grating spectrometers gave way to echelle spectrographs, which offered higher angles of incidence, higher diffraction orders and therefore more dispersion and higher resolutions (Chaffee and Schroeder, 1976). Simultaneous observations of absorption lines at known wavelengths, first from telluric contamination (Griffin, 1973) and later from "cells" of gas (eg HF, Iodine, ThAr etc), were used to improve wavelength calibrations (Campbell and Walker, 1979). Photographic plates also made way for digital speedometers and eventually modern CCDs. To reduce systematics from changes in atmospheric conditions, the most recent generation of spectrographs are pressure and temperature controlled to within 0.01° and 0.01 mbar respectively (Pepe et al., 2000), giving RV precision on the order of 1m/s. This has been combined with sophisticated measurements and removal of stellar activity, with the BIS and log R'HK (a measure of emission in the Calcium H and K lines at ~395nm, Baliunas et al. (1995)) used as proxies (e.g. Hatzes et al., 2011; Tuomi et al., 2014; Dumusque et al., 2017).

High-precision RV measurements are an important technique for detecting planets, with more than 500 worlds with minimum masses ($M_p . \sin(i)$) as low as 1.2 $\mathrm{M}_\oplus$ (GJ 273 b, Astudillo-Defru et al., 2017). They are also an important method of characterising planets detected by other methods, especially from the transit technique.

As transit observations produce accurate measurements of the planets orbital inclination (from impact parameter, $b = \frac{a}{R_s}\cos(i)$), this breaks the degeneracy on planet mass in radial velocity. The combination of planetary radius from transit depth and planetary mass from RV semi-amplitude gives direct constrains on planetary composition by way of the bulk density, as discussed in section 1.5.3. The detection of a planetary mass for a transiting object is also the best way of confirming a transiting planet candidate as real.

1.4 Stellar Characterisation

To determine the characteristics of a planet to some level of precision, the physical characteristics of the star must be known at least as well. In the case of transits, the most important parameter is stellar radius ($R_p \propto R_s$). For planets found by Radial Velocities or astrometry, mass is most important ($M_p \propto M_s^{2/3}$). For young directly imaged planets and microlensed planets, stellar age and stellar distance are most important factors (although

we do not consider those here).

1.4.1 Photometric

Industrious all-sky surveys over the past two decades now mean that every bright star in the sky (V<14 mag) has between 5 and 12 photometric observations in different wavelengths. These cover the optical (USNO-B, Monet et al. (2003) and SDSS Fukugita et al. (1996)), the near-IR (e.g. JHK from 2MASS, Skrutskie et al., 2006)) to the mid-IR (W1-W4, WISE, Cutri et al., 2014). The information for each star across different wavelengths can give good information on both the general blackbody shape of a stellar spectrum and second-order variation caused by absorption caused by atoms and molecules present in the stellar atmosphere.

Such photometric surveys also provide estimates of proper motion (p.m.) - the apparent movement of stars with respect to the fixed (e.g. RA and Dec) reference frame. Proper motion is a function of a star's lateral velocity (which follows a known probability distribution which drops of for high velocities) and distance ($\mathrm{p.m._{RA}} = v_{\mathrm{RA}}/d$). Therefore, proper motion is used as a prior for distance and (combined with magnitude) stellar luminosity and spectral type.

The available photometry can be compared with colour tables produced from models of the spectral energy density (SED) and atmosphere of stars of various spectral types (e.g. Fitzgerald, 1970). Alternatively, the photometry can be used to model and constrain a Spectral Energy Distribution. This effectively takes a stellar atmosphere model across a the entire wavelength range and convolves with each photometric filter to produce the expected signal in each band. This can then be minimised to give a best-fit stellar parameters (potentially with MCMC to produce uncertainties).

The method of studying SEDs is especially useful for detecting low-mass stellar companions, and for studying the protoplanetary discs around young stars. The disc absorbs light from the star at its core and re-emits the photons at a wavelength determined by the local temperature of the disc. Hence, studying the change in emission with wavelength gives information into the radial structure of a disc. Self-consistent spectral models of a circumstellar disc can then be fit to the available photometry in the same way to give constraints on stellar and disc parameters. These include the radial extent of the disc in AU, the viscosity (α), the ratio of dust to gas (ε), and grain size distribution (D'Alessio et al., 2006).

1.4.2 Spectral

A better and more detailed way of determining stellar parameters is to study a single, high-SNR optical spectrum of the target. Absorption of specific wavelengths of light by ions, atoms and molecules in the (cooler) stellar atmosphere adds complex fine structure to every stellar spectrum. These take the form of absorption lines at wavelengths determined by the electronic structure of the absorbing atoms and their ionization level. Hence, the abundances of metallic atoms in the stellar photosphere can be determined (usually given as the log of the metallicity compared to solar values, i.e. [Fe/H]).

The amount of absorption by each species is also sensitive to the local temperature of the photosphere, and therefore spectral lines (especially neutral metal lines) encode information about the stellar temperature. The most common technique to characterise a stellar spectrum is to measure the equivalent widths of lines (usually iron) and compare with calibrated models (e.g. Tsantaki et al., 2013). The line widths are also sensitive to the pressure in the photosphere, and therefore give information regarding the surface gravity of the star (translated to log g). Therefore, stellar spectra can provide direct estimates of $T_{\rm eff}$, log g, and [Fe/H].

While photometry is available for almost all bright stars in the sky, using spectra to estimate stellar parameters can only be done on an object-by-object approach. Stellar classification is therefore performed on a per-planet basis, often by different groups with different methods, which has led to discrepancies (Torres et al., 2008).

1.4.3 Stellar Models

Spectral and photometric stellar observations do not directly give the stellar radius, R_s, and mass M_s - the two most important stellar parameters for exoplanet studies. Instead, these must be obtained by using stellar evolution models. As main sequence stars evolve, they pass along specific evolution tracks, growing in radius and decreasing in mass due to the increasing proportion of helium in their core. Many complex models have been performed to track this evolution (e.g. Baraffe et al., 1998; Dotter et al., 2008). Self-consistent models are then generated giving the parameters of stars (e.g. R_s,M_s,rho_s,log g, [Fe/H], $T_{\rm eff}$, & age) within the range of the observed parameters, and then weighted by the frequency of stars with each parameter combination. The posterior of the parameters without priors (e.g. R_s) are therefore constrained from those parameters with priors from observations (e.g. $T_{\rm eff}$), giving estimates for each stellar parameter.

Alternatively, the thin band of the main sequence, where stars spend the majority of their lifecycles, can be approximated from simple fits (Torres et al., 2010; Boyajian et al., 2012). Making the assumption that the target star lies on the main sequence (and it is

not, for example, a giant), one can apply the fits to the observed parameters to derive the unobserved stellar parameters and their uncertainties. While such a method has its caveats, it is far simpler and quicker than performing a full stellar evolution model fit.

1.4.4 Other methods

Astrometric distance The above sections assumed no knowledge of the distance to the observed star. However, an independently determined distance (for example through astrometry, e.g. Astraatmadja and Bailer-Jones, 2016) breaks some of the degeneracy as the luminosity (itself a function of stellar temperature and radius, $4\pi R_s^2 \sigma T_s^4$) can be directly determined.

Interferometry The radii of nearby stars can be studied directly with high angular resolution interferometric observations (e.g. Boyajian et al., 2012).

Asteroseimology The internal oscillations of stars are directly related to the physical size of the vibrating body. Therefore, measurements of these oscillations, combined with spectral derivations of stellar temperature, can provide extremely precise stellar parameters, with radii as precise as 1% (e.g. Gilliland et al., 2010).

1.5 The State of Exoplanetary Science

1.5.1 Planet Formation

Stars are born in the dense, dusty environments of molecular clouds, when regions of the nebulae undergo gravitational collapse. As the gas and dust collapses, its residual angular momentum spins out a disc around the protostar, containing a few percent of the system's mass (Herbig, 1962). These discs continue to accrete material onto the pre-main sequence star - a period known as the T-Tauri phase.

T-Tauris are typified by spectral lines such as H-α in emission, and by large infra-red excesses due to the warm dusty disc which absorbs optical stellar radiation and re-radiates it in the infra-red. These circumstellar discs can be directly studied with high-resolution imaging (in the microwave with e.g. ALMA (Wootten and Thompson, 2009); and the infrared with e.g. Sphere (Beuzit et al., 2008a)), and through their effects on the photometry of young stars (e.g. Dullemond et al., 2003; Cody et al., 2014).

As the star evolves, the optically thick, dusty circumstellar disc gradually disappears as the gas is blown away by stellar UV and the dust accretes into larger bodies. Few objects possess such a disc beyond ~10 Myr (Kennedy and Kenyon, 2008). The timescale

of such discs is inversely proportional to stellar mass, meaning low-mass secondary objects including planets are likely to maintain discs far longer than the primary component.

It is within the circumstellar disc that planet formation occurs. Two schools of thought exist for the formation of planetary mass object. The first suggests that gravitational instability within the circumstellar disc leads to the direct collapse of the disc into massive fragments (Boss, 1997). While such instabilities clearly occurs (as images of spiral structures in circumstellar discs show, e.g. Muto et al. (2012); Benisty et al. (2016)), such a process is predicted to form many high-mass planet cores at large orbital separations (Dodson-Robinson et al., 2009). Such a population is now known to be uncommon (<10% from 100-500AU Chauvin et al. (2015); 2.3% from 8-400AU around low-mass stars, Lannier et al. (2016)). Simulations also suggest more planets at lower stellar metallicities (Boss, 2006) - a hypothesis not yet supported by the data (Buchhave et al., 2012; Courcol et al., 2016).

The more accepted theory (especially for for low-mass and close-in planets) is formation via core accretion (Matsuo et al., 2007). Here, planets build from the accretion of mm-sized dust grains, which grow through the "meter barrier" (Blum and Wurm, 2008), and eventually to km-scale planetesimals which impact and merge to form terrestrial planets (Lissauer, 1993). As the cores grow their gravitational wells deepen, collecting yet more material. For large bodies over $\sim$10 $M_{\oplus}$, this includes gas from the gas disc, allowing the relatively rapid accretion phase from super-Earths to gas giants (Pollack et al., 1996). This rapid accretion phase is stopped once the disk is dissipated, the planet accretes all the gas, or the planet's gravitational torques open a gap in the disc itself. Planets below this limit of $\sim$10 $M_{\oplus}$ may still end up with a thick atmospheres (1-6% by mass) as a result of the out-gassing of volatiles post-accretion (Elkins-Tanton and Seager, 2008).

Our knowledge of planet formation is limited for a number of reasons: Protoplanetary discs are optically thick, obscuring any processes occurring within. The number of young stars either close enough or bright enough to allow detailed study is limited, as is the age range they cover (Hinkley, 2011). Processes of migration and evolution after formation modify planet populations, masking the effects of formation on any statistical study of exoplanets (Lopez and Fortney, 2014). And despite resolution improvements to direct imaging, especially in the sub-millimetre, the structure observable in protoplanetary disks is limited to the scale of AU.

Photometric observations of structure in eclipse, however, can probe scales 100 times smaller as its resolution is chiefly limited by the diameter of the stellar disc across which material may pass. This has previously been used to study a wide range of phenomena. For example, inner ring edges were detected around the circum-secondary discs of ϵ Aur (Carroll et al., 1991), EE Cep (Gałan et al., 2012) and around the binary KH 15D

(Herbst et al., 2002). Gas accretion streams from the circumstellar discs have been observed in eclipse as deep, rapid, aperiodic "dipper" variations (e.g. Bouvier et al., 1999; Cody et al., 2014; Ansdell et al., 2016). Even the structure of a potential circumplanetary disc (J1407 Mamajek et al., 2012) has been modelled, suggesting ring-gaps indicative of sharp exorings and material being cleared by the formation of exomoons (Kenworthy and Mamajek, 2015). However, the J1407 eclipse has never been seen to reoccur, leaving open the interpretation that unbound dust structure caused the eclipses. The discovery of similar but repeating eclipses may improve upon our knowledge of this understudied regime of planet formation.

1.5.2 Planetary Evolution and Migration

No classical planetary formation mechanism predicts Jupiter-mass planets can form at < 0.05AU from their stars. Given the relative lack of rocky and gassy constituents present at such close-in radii, hot Jupiters must have migrated to their present position. Similarly, the high numbers of tightly orbiting, low-mass multi-planet systems found by *Kepler* also suggest that either planet-forming material or the planets themselves migrated to their close-in locations (Rein, 2012).

In the case of hot Jupiters, two solutions became apparent: either the planet migrated after the disc had dissipated, exchanging angular momentum gravitationally with another companion; or it migrated through the circumstellar gas disc, which would allow the exchange of angular momentum with the gas. In the former case, an outer perturber in the form of massive outer planet or unbound star, can cause an inner, low-mass body to librate between highly eccentric and highly inclined orbits - the so-called Kozai-Lidov effect (Kozai, 1962; Lidov, 1962). If the increased eccentricity planet perihelion is close but not inside the tidal disruption (Roche) radius, a planet can exchange tidal forces with the star and gradually circularise (Valsecchi and Rasio, 2014). Some planets would not fully tidally recircularise, leading to a small but significant population of highly-eccentric warm Jupiters (Dawson and Chiang, 2014).

In the case of disc migration, it was realised that planets would naturally migrate towards their star as they grow, either while embedded in the disc (Type I), or once they had grown large enough to open a disc gap (Type II). In fact, these mechanisms appeared to migrate all planets inwards too well, and much theoretical efforts have been extended to slow them down. Planets of all sizes can be captured into resonant orbits (or orbital chains) with one another as they migrate, often slowing or stalling inward migration (Cossou et al., 2013).

Disc migration (especially combined with multiplanet resonant chains) would naturally damp orbits, producing circular, low-inclination orbits. In the alternate case, high-eccentric migration would lead to highly inclined, and non-circular orbits (depending on

the degree of recircularisation). Measurements of both of these properties are possible, and can be used to put a formation history on individual planets. Eccentricities are frequently obtained from RV measurements, but can also be probabilistically determined from the comparison of transit duration and stellar density (Eylen and Albrecht, 2015). The inclination of the planetary orbit with respect to the rotation axis of the star has only been achieved for transiting planets. One method for bright, fast-rotating stars is to take high-resolution spectra during transit and measure the change in radial velocity due to the changing stellar rotation obscured by the transiting body (Rossiter, 1924; McLaughlin, 1924). Alternatively, asteroseismology can resolve the difference between edge-on and pole-on modes, allowing the spin-orbit alignment to be calculated (Van Eylen et al., 2014). This has so far only been achieved in numbers for close-in hot Jupiters, and the detection of amenable long-period planets is required to study the orbital evolution of long period planets.

1.5.3 Planetary Characterisation

Planets can be characterised to a first order by their size and orbit. We can, for example, calculate the surface temperature of a planet from stellar and orbital parameters. This is done by balancing the incoming flux, a function of stellar luminosity through the Stephan Boltzmann law ($L_s = 4\pi R_s^2 \sigma T_s^4$ where R_s is stellar radius, σ is the Stephan Boltzmann constant, and T_s is the stellar effective temperature) and the inverse square law ($F_{\mathrm{p,in}} = L_s/a^2$) to give the flux at the planets orbit. This incoming flux, $F_{\mathrm{p,in}}$, can then be balanced with the planet's outgoing radiation $F_{\mathrm{p,out}}$ (assuming some albedo, A): $F_{\mathrm{p,out}} = L_p/(4\pi R_p^2) = \sigma T_p^4 = 0.25 F_{\mathrm{p,in}}(1-A)$. Therefore, the planetary temperature T_p, is found from the balance of incoming flux and outgoing flux:

$$4\pi R_s^2 \sigma T_s^4 a_p^{-2}(1-A) = 4\sigma T_p^4 \tag{1.10}$$

Surface temperature is therefore dependent on the measurable quantities of stellar radius (R_s), stellar temperature (T_s) and the semi-major axis; and the unknown quantity of planetary surface albedo (A, which is often assumed to be between 0.1 and 0.5 from solar system values).

$$T_p = \left(\frac{\pi R_s^2 T_s^4 (1-A)}{a_p^2} \right)^{\frac{1}{4}} \tag{1.11}$$

The temperature can then be used to first-order classify the planet (e.g. hot Jupiters). Alternatively, it forms the key diagnostic for the Habitable zone - the zone of distances around a star where a planet with earth's mass, radius, atmosphere and geology would maintain 'habitable' surface temperatures capable of supporting liquid water (Kasting et al., 1993; Kopparapu et al., 2013).

-	Brown Dwarfs	Jupiters	Neptunes	super-Earths	Earths
Mass	14 – 65 M_j	0.25-14 M_j	15-60 $M_\oplus$	3-15 $M_\oplus$	<3 $M_\oplus$
Radius	~1 R_j	>0.5 R_j	2.5-5 $R_\oplus$	1.5-2.5 $R_\oplus$	0.8-1.5 $R_\oplus$
Example	WASP-30 b	HD209458 b	GJ 436 b	Kepler-10c	GJ1132b
ref	(Anderson et al., 2010)	(Mazeh et al., 2000)	(Butler et al., 2004)	(Fressin et al., 2011)	(Berta-Thompson et al., 2015)

Table 1.2: First-order planetary classes as defined by radii and masses

The planetary size is also used for first-order characterisation, with the minimum mass (from RVs) or the planetary radius (from transit) giving the rough class of world into which the planet belongs, although no standardised naming convention exist, the rough definitions are shown in table 1.2. A definition not shown is that of "mini-Neptunes" which are defined as being planets that have gaseous envelopes (and therefore do not fit into the "super-Earth" definition), but are far smaller than Neptune in terms of either radius (like K2-110 b Osborn et al., 2017b) or mass (like GJ1214 Charbonneau et al., 2009)).

Bulk composition

Given the precise mass and radius of an exoplanet, we can do more than a simple classification. Planets across the universe, all built by the same mechanism, will contain broadly similar constituents to the solar system planets - siderophilic metals (e.g. iron), silicate rock, water & other volatiles/ices, and gas (e.g. hydrogen and helium). The interactions of these constituents are similarly universal, and therefore can be modelled. This means that the bulk density of extrasolar planets can constrain the possible combinations of these elements extremely well. A high-density planet cannot have large amounts of H/He and may even require a higher core fraction than Earth to produce the observed density. And vice-versa, a low-density planet must H/He-dominated. Modelling such mixtures can therefore give accurate limits on the core-, mantle- and atmosphere-fractions of a planet (e.g. Zeng and Sasselov, 2013).

To perform direct observations of the true bulk elemental abundance of extrasolar rocky material, exoplanets would need to be completely disintegrated. Such a process does occur for tidally disrupted rocky bodies around White Dwarfs, many of which show the presence (and abundance) of exoplanetary material (Gänsicke et al., 2012; Wilson et al., 2016).

As one would expect from formation theory, large planets tend to have a higher fraction of gases, as these can only be accreted from the gas disc once a planet passes $\sim 10M_\oplus$, and as a corollary, small planets are most often rocky. This has been borne out in our observations, even allowing mass-radius relationships to be made, which purport to predict the most likely mass given a radius (and vice versa) (Weiss and Marcy, 2014, ; see dashed line in Figure 3.7).

The transition between the regimes of terrestrial and gas-dominated planets is also

an interesting and chaotic region. They range from low-density Neptunes (e.g. the Kepler-11 system; $0.6 - 1.7 \mathrm{gcm}^{-3}$ Lissauer et al., 2013), to super-Earths with large rocky interiors (e.g. Kepler-10 c; $7 \pm 1 \mathrm{gcm}^{-3}$ Dumusque et al., 2014), to ultra-dense super-Earths that could be evaporated gas giant cores (e.g. K2-38 b; $17.5 \pm 7 \mathrm{gcm}^{-3}$ Sinukoff et al., 2016). To form such a diverse group, more than just diverse initial conditions are needed - there must also be some process sculpting these populations, either by formation (late formation inhibiting gas-accreting) or by evolution (for example, envelope evaporation) (Lopez and Rice, 2016). Statistical studies of exoplanet populations in this region are beginning to reveal answers (Fulton et al., 2017).

Probing population statistics of exoplanets to study their compositional or formational processes is intrinsically biased by the orbital distribution of well-characterised planets. Only 141 planets have both mass and radius determined with errors < 30%, and only 35 of those have radii < 3 $R_\oplus$. Of small (<0.5 R_J) and cool (>0.2AU) planets, only nine have measured densities (Akeson et al., 2013). Hence current populations are dominated by hot planets, which may have had different formation and evolutionary processes to the majority of cooler exoplanets.

Atmospheric composition

The most advanced method of exoplanet characterisation is to directly observe the spectrum of an exoplanet. This can reveal the presence of specific atmospheric molecules, detect the physical characteristics of the atmosphere, and may eventually enable the detection of biosignatures on exo-earths (Seager and Deming, 2010). Atmospheric characterisation can also help pin down differences in initial conditions, planet formation and atmospheric evolution of the planet.

For hot (e.g. young) planets on wide orbits around nearby stars, we can obtain spectra of their emitted flux directly (HR8799 b - Bowler et al., 2010). For close-in transiting planets, spectra can be obtained by comparing spectra during transit to out-of-transit. For a transiting planet with a large atmosphere, the transit depth varies with respect to wavelength due to absorption from atoms (e.g. Sodium, Charbonneau et al., 2002), molecules (e.g. water Tinetti et al., 2007), and from scattering effects (e.g. Rayleigh scattering Des Etangs et al., 2008). This technique has now been performed on dozens of planets (Sing et al., 2016), with hot Jupiters dominating the sample with thanks to being relatively numerous around bright stars, hosting hot atmospheres and inflicting deep transit depths.

The detection of emitted flux during secondary eclipse has also been used to probe the reflected spectrum of some exoplanets, especially in the far-IR where the contrast with the star is reduced (Grillmair et al., 2007). Atmospheric detection of non-transiting hot Jupiters has also been performed by searching for narrow absorption lines in the reflected

light from the planet that are then seen to vary with the planetary radial velocity (Brogi et al., 2012). In both cases, only hot Jupiters and Neptunes have been studied, and the atmospheres of warm and cold giant planets remain out of reach, due in part because of the lack of such planets, and also due to the suppressed atmospheric signal due to their lower temperatures and smaller scale heights.

1.5.4 Exoplanetary Occurrence rates

Determining the number of exoplanets as a function of various properties (eg. stellar spectral type, orbital distance, planet size, etc) is a key goal of modern exoplanetary science. One fundamental requirement is that a large unbiased sample of well-characterised stars are searched for planets with the same method. The number of detected planets must then be de-biased to account for planets that were not detected. This might be because of a weak signal (ie. stars with high noise or planets with low masses/radii), or because of some orbital constraint of the observations (i.e. face-on orbits in the case of RV surveys, or not edge-on orbits in the case of transit surveys).

Radial Velocity surveys, which are capable of detecting most large planets, provided the first such estimates, showing that high-metallicity stars host more giant planets (Fischer and Valenti, 2005), that multiplanet systems are common (Wright et al., 2009), and that low-mass planets (3-10 $M_\oplus$) are far more common than giant planets (Howard et al., 2010; Mayor et al., 2011).

The first transit mission with the sensitivity to survey the occurrence rate of terrestrial-sized planets was *Kepler*. Using the first 6 quarters of data Fressin et al. (2013) computed occurrence rates of planets with orbits < 85d around FGK stars, finding small planets to be the most common size bin, with a frequency of $\sim$ 16.5%. Looking exclusively at M-dwarfs, where the occurrence rate of "habitable" terrestrial planets is easier because they orbit on shorter periods and produce deeper transit depths, Dressing and Charbonneau (2015) found $\sim$2.4 0.5 – 4 $R_\oplus$ planets per star including $\sim$0.15 in the habitable zone, although Kopparapu (2013) found > 0.5. Earthsize planets around FGK stars, with their low SNR, prove the most difficult sample to analyse. Using all 16 quarters of data, Burke et al. (2015) found an occurrence rate of 0.77 ± 0.13 for 0.75-2.5 $R_\oplus$ planets, and an $\eta_\oplus$ (eta-Earth - the number of habitable earths per star) of $\sim$ 0.1, albeit with large uncertainties (0.01 – 2.0). Maintained across many of these results is the trends that small, terrestrial planets are far more common than Neptune- and Jupiter-sized planets, and that beyond very close orbits, planetary occurrence rates are roughly flat when using log P bins (Figure 1.6).

These precise occurrence rates also allow current and future transit survey missions to more accurately determine their potential yield given the sample of stars observed and the recoverability rates as a function of stellar and planet types.

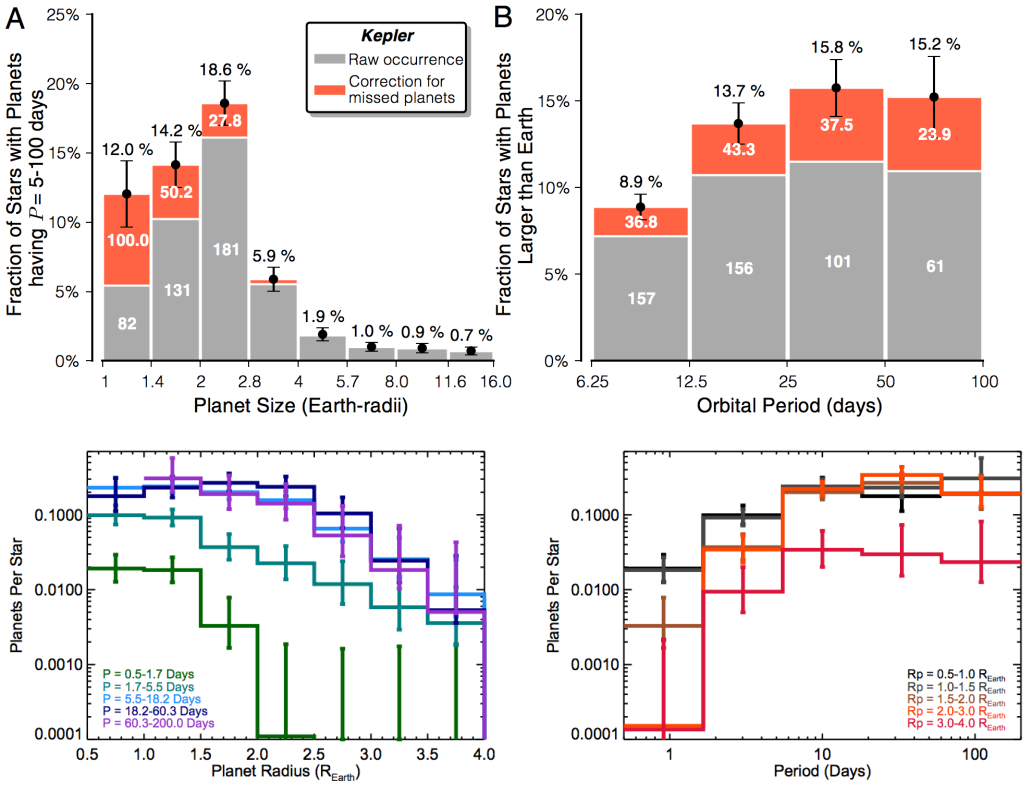

Figure 1.6: Planetary occurrence rates from Kepler. **Above:** results for planets around G and K-type stars from Petigura et al. (2013). **Below:** Results from Dressing and Charbonneau (2015) for planet occurrence as a function of planet radius and period around M-dwarfs.

The poor coverage of long-period planets with *Kepler* photometry places large uncertainties on analysis of long-period planets. However, a systematic (and computational) search of *Kepler* photometry for long-period and single-transiting planet candidates by Foreman-Mackey et al. (2016) revealed a high occurrence rate of planets in the parameter space from 2 to 25 years and $0.1 - 1.0$ $R_\oplus$ of 2.0 ± 0.7. This value was higher than those derived from radial velocity surveys (e.g. Mayor et al., 2011), although the transit searches were able to push to lower planetary size regimes. However, the first study to combine occurrence rate regimes for distant planets (microlensing, RVs and direct imaging), finds a far similarly high frequency (specifically for M-dwarfs), with 2.75 ± 1.5 in the $50 - 600$ $M_\oplus$ mass regime (Clanton and Gaudi, 2016). There still remains much uncertainty on the occurrence of planets in the regime between < 0.5AU where transits are most sensitive, $\sim$ 1AU where RVs dominate for large planets, and $>$ 2AU where microlensing is used.

1.6 Format

Following an exploration of the methods and data sources used in this thesis will be four chapters dedicated to specific research projects.

The first of these (Chapter 3) will explore those methods already frequently used in both ground-based and space-based transit surveys - namely using the phase-folded signals of multiple transits to detect exoplanet candidates, followed by focused stellar characterisation and radial velocity measurements to both confirm and begin to characterise exoplanets.

Chapter 4 develops new methods to search for long-period planets and eclipses from single transit events. This is applied to fields from the ground-based surveys WASP and NGTS, including short-cadence light curves from 38 "Stare" fields in WASP and 36 NGTS fields, and then 2 million WASP objects with nightly-averages light curves to search for deep, multi-night eclipses.

The fifth chapter explores one of these deep, long-duration events in detail, for which a second and near-identical eclipse was found 2.2 years later and which is interpreted in this work as dusty material in the vicinity of a secondary body which could be planetary or brown dwarf in mass.

In the sixth chapter, the search for single transiting planets is applied to space-based K2, detecting dozens of interesting candidates which are likely planetary in nature. To characterise these candidates, a single transit-specific light curve model is developed to provide orbital period, planetary radius and planetary probability estimates. The future detectability of long-period transiting planets (e.g. with the forthcoming TESS, Gaia and PLATO missions) is also discussed.

Chapter 2

Methods

"Space. A fertile subject to get a less than worthless doctorate or professorship, the field hasn't done anything worthwhile since the moon landings. Today its just full of conjecture, artists impressions and VERY blurry pictures described in breathless awe by the aforementioned purporting to be all sorts of ethereal nonsense. The more they extol with authority the more the masses suck it up!"

jackpotseven, bristol, Daily Mail

Note: In the following chapter the methods and data sources used or referred to more than once in this thesis are introduced and explained.

2.1 Uncertainties and their propagation

Incorrect uncertainties can skew data, lead to the wrong conclusions, and generally reduce the quality of scientific observations and analysis. Therefore correctly deriving and propagating uncertainties are key.

Many measured parameters are normally distributed about a mean, with a probability density function (PDF) well approximated by a Gaussian distribution. This includes astronomical measurements of flux, for which the "photon counting" Poisson-distributed shot noise approximated to a Gaussian with a reasonable number of datapoints (e.g. high count rate). In this case, errors can be propagated using the classic rules - adding absolute uncertainties in quadrature for common measured quantities, adding relative uncertainties in quadrature for disparate parameters, etc.

In the case of asymmetric errorbars, or data not well-fitted by a Gaussian distribution, this becomes more tricky. The most logical method of error propagation in this case is to perform the mathematical operations on each member of the posterior PDF of the parameter. This allows any complex shape to be propagated, and new asymmetric uncertainties to calculated on the resulting PDF using the median compared to the 16th and 84th percentile (which enclose 68%, or 1σ of the distribution). For highly asymmetric distributions, the median (e.g. 50th percentile) will not correspond to the peak of the distribution. In this thesis, we consistently use the median, rather than position of the peak (e.g. the mode) as the quoted parameter value.

2.2 Astronomical Magnitudes

In astronomy, the brightnesses of stars are measured on a log scale with base 2.5[1], meaning that a magnitude change of 5 corresponds to a change in intrinsic brightness of 100 (2.5^5), although the scale is such that brighter stars have lower magnitudes. Hence the magnitude of one star compared to another ($m_1 - m_0$) corresponds to the ratio of their fluxes using:

$$m_1 - m_0 = -2.5 \log_{10} \frac{f_1}{f_0} \tag{2.1}$$

Magnitudes are measured for each filter available, with the difference between magnitudes in two bands is known as a colour. The major magnitude systems (UBVRI, JHK, WISE, etc) are computed with respect to the average magnitude of the bright star Vega, which therefore has magnitude and colour close to zero (Bessell et al., 1998). AB magnitudes, on

[1]In actuality this value should be $\sqrt[5]{100}$, although 2.5 is most frequently used despite the 0.5% difference between them

the other hand, are compared with a distribution of constant flux per unit frequency (defined as 3631Jy, where 1Jy=10^{26} W Hz^1 m^2).

Individual telescopes and missions may use their own filter for observations, and will therefore produce a new magnitude for all stars, although it can be estimated using known colours. Kepler observes a broad wavelength band across 430 to 900nm, and gives a unique "Kepler magnitude" to all stars which can be estimated from the g and r magnitudes (which themselves can be approximated from V and R) (Koch et al., 2010). WASP and NGTS cover a regions from 400nm to 750nm (Pollacco et al., 2006) and 520 to 890nm (Wheatley et al., 2013) respectively.

2.3 Fitting models to data

In the case of exoplanetary lightcurves, for each data point we have a single well-constrained datapoint (time, x_i), and a measured quantity (flux, y_i). We may, regardless of the scenario, create a model that we think best describes the physics of the changing light from the system. In a noiseless system, and for a perfect model, all y datapoints could be determined from some function, $f(x)$. However, this is impossible in reality, and we must find a model that fits best given the errors intrinsic to each flux value (Hogg et al., 2010)[2].

In astronomy each flux measurement (y_i) has intrinsic uncertainty ($\sigma_{y,i}$). In most cases this scatter is dominated by the presence of "shot" or "white" noise from the source. This uncertainty comes from the inconsistent nature of "counting" photons, as all photometric equipment including our eyes effectively do, and it can therefore be found from Poisson statistics. This shows that the uncertainty is proportional to the square root of the number of detector counts and therefore that the noise from an astronomical source is proportional to its brightness, $\sigma_w = \sqrt{N} \propto \sqrt{f_0.10^{0.4*(m_*-m_0)}}$. As well as the source itself, all photometry also includes shot noise from the sky coincident with the source, and dark current & readout noise from the detector. Calibrations such as flat fielding, bias and dark frames, also contribute uncertainties. The intrinsic flux from the source may also include uncertainties due to correlated noise between data points, which we explore in section 1.2.5.

To determine the model which most closely predicts the data, the "Chi-Squared" statistic is classically used:

$$\chi^2 = \sum_{i=1}^{N} \frac{(y_i - f(x_i))^2}{\sigma_{y,i}^2} \tag{2.2}$$

This is effectively the squared sum of the difference between y measurements and their model-predicted value, scaled to their individual errors. Minimising the χ^2 through iteration therefore provides the best-fit model for a given set of model parameters and datapoints.

[2]We use the essay of Hogg et al. (2010) extensively for the following section

More comparable to other models is the reduced chi-squared, which is the the chi-squared per degrees of freedom, χ^2_R/ν, where the degrees of freedom are determined by the number of model parameters N_{par} and the number of datapoints N by $\nu = N - N_{\text{par}}$. In the case of simple models with many datapoints, the reduced chi-squared tends to the average model deviation per measurement, scaled to uncertainties. χ^2_R close to 1.0 suggest good model fits. Values less than 1.0 suggest overfitting (e.g. the errorbars are too large). To compare two models of the same data, one can compute the "f-distribution", which simplifies to the ratio of chi squares between each model for equal datasets and similar models. This computes information regarding which is the best-fitting model. Chi-square statistics only hold if the datapoints have Gaussian distributions.

Is it also useful to determine how well a model fits in a probabilistic manner. The frequency distribution for a datapoint, y_i, normally distributed from some model value $f(x)$, is therefore:

$$P(y_i|f) = \frac{\exp -((y_i - f(x_i))^2/2\sigma_i^2)}{\sqrt{2\pi}\sigma_i} \tag{2.3}$$

We seek to know some model parameters that maximise the probability of each of our observations. The "likelihood", which is the probability of obtaining your data y given the model f and the fixed observed values of x_i and σ_i:

$$\mathscr{L} = P(y_{i=1}^N|f, I) = \prod_{i=1}^{N} P(y_i|f) \tag{2.4}$$

Applying a logarithm to remove the exponential term and encapsulating constants into K gives:

$$\ln \mathscr{L} = K - \sum_{i=1}^{N} \frac{(y_i - f(x_i))^2}{2\sigma_{yi}^2} = K - \frac{1}{2}\chi^2 \tag{2.5}$$

Therefore, for well-behaved Gaussian distributions, maximising the likelihood is equivalent to minimising the chi-square. For non-Gaussian statistics, the likelihood formulation can be modified to return the best-fitting model.

For many scenarios, we also have information from past experience or theoretical considerations, about what the eventual parameters should be - these are "priors" on the distribution. To compute the most likely model given the datapoints and the priors, we can turn to Bayes theorem:

$$P(f|y_{i=1}^N, I) = \frac{P(y_{i=1}^N|f, I)P(f|I)}{P(y_{i=1}^N|I)} \tag{2.6}$$

$P(y_{i=1}^N|f, I)$ is the likelihood function, our prior knowledge on the model parameters is $P(f|I)$, and our prior knowledge related to the data (e.g. x_i, σ_i, etc) is I. In most cases

the denominator, $P(y_{i=1}^{N}|I)$ or the probability of the datapoints given their position and error, can be ignored as a constant.

The priors on model parameters are themselves a probability distribution, guided by past experiment or theoretical limits, that are applied to each model parameter. Typical priors include a uniform prior (limited between two end points), a Gaussian prior (normally distributed around expected value μ with standard deviation μ), or more complex distributions. These are normalised such that the total probability for each parameter is one. The result is a posterior probability density function (PDF) that encodes the probability of each model parameter, given the datapoints and the priors.

The former two methods (chi-squared minimisation and log likelihood maximisation) produce, for some given model, the best-fitting parameters. For perfectly gaussian (and uncorrelated) parameters, their uncertainties can be estimated. However, most models will have correlations or asymmetric parameter distributions, and therefore we need an empirical way to estimate for the uncertainties on (and covariances between) model parameters. The most frequent method is to use Markov Chain Monte Carlo (MCMC).

2.4 Markov chain Monte Carlo

Markov chain Monte Carlo, or MCMC, is a procedure that allows the probability distribution of the posterior distributions of a model to be empirically explored. Many methods use similar MCMC techniques, but we describe the Metropolis-Hastings algorithm (MacKay, 2003), as used by `emcee`, the MCMC model developed in Foreman-Mackey et al. (2013b) and used in this thesis.

It works by first creating multiple "walkers". These are chains of model parameters that explore the model parameter space. They do this by computing the likelihood of the model given the datapoints for a new set of model parameters. The likelihood is then compared to the previously generated model. If it is more likely, this new set of parameters is taken. If the likelihood is lower than the last model, the difference between the previous and the newly generated likelihood is used to determine the probability of the new model parameters being taken. Hence each point in a Markov chain depends only on the position of the previous step. The parameters used in each subsequent step are usually generated using parameter-specific step parameter, for example N_p normal distributions each with some σ_p. This must be chosen such that the walker is not so small such that it only explores small parameter regions, nor so large that the walker's next step is in a low-probability region and never accepted. The affinine invariance of Goodman and Weare (2010) is used in `emcee` is such that these multiple step parameters are parameterized by only two hyperparameters.

To ensure the walkers are exploring the full posterior PDF, a burn-in phase is used.

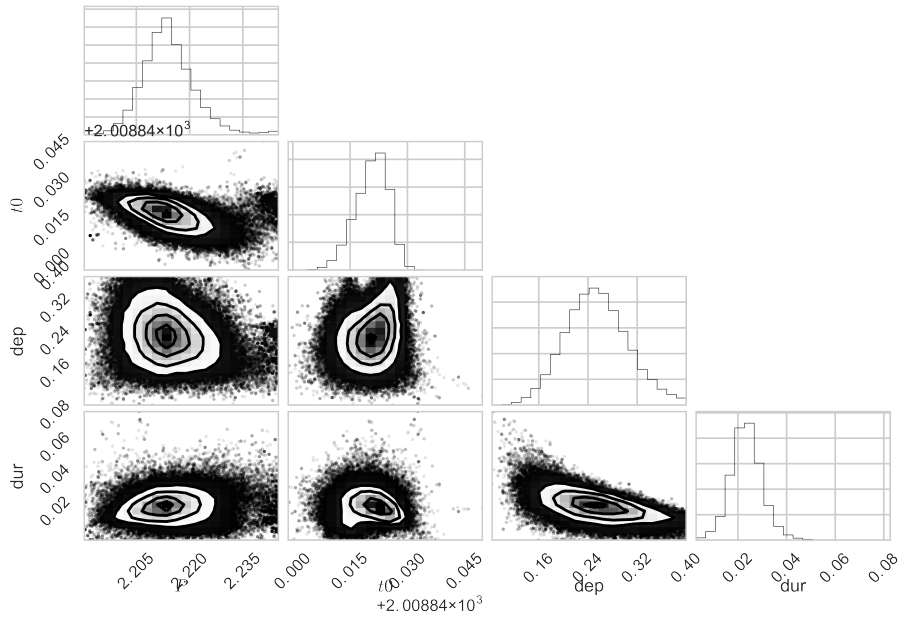

Figure 2.1: An example of the posterior probability density function from an MCMC for a 3-parameter eclipse model. The resulting PDF for each parameter is clearly non-gaussian, and both t_0 and P and dep and dur parameters show some degree of correlation. The graphs at the top show 1D PDFs for each parameter.

This allows any walkers started in a low-probability region to move towards the maximum likelihood estimate. The burn-in phase, usually apparent in the position of walkers against step position, is then cut from the sample to ensure only the maximum likelihood estimation (MLE) is sampled.

Numerous walkers, run for a significant amount of iterations, therefore explore the full parameter space and, their flattened and combined chains give the posterior PDF of the model. This is typically visualised using a "corner plot" which flattens the multi-parameter probability space onto a 2-parameter plane for every possible two-parameter combination. This is a good way of determining if correlations exist between parameters. The 1-d flattened probability distribution of each parameter is also typically shown. An example (see section 5.4.4) is shown in Figure 2.1.

To estimate the value and uncertainties of each parameter, the chain of samples can be flattened on each parameter, giving a 1D PDF. The median and 1-sigma bounds can then be found from the 16th, 50th and 84th percentile (with the 16 to 84th percentile encapsulating 68% of the probability).

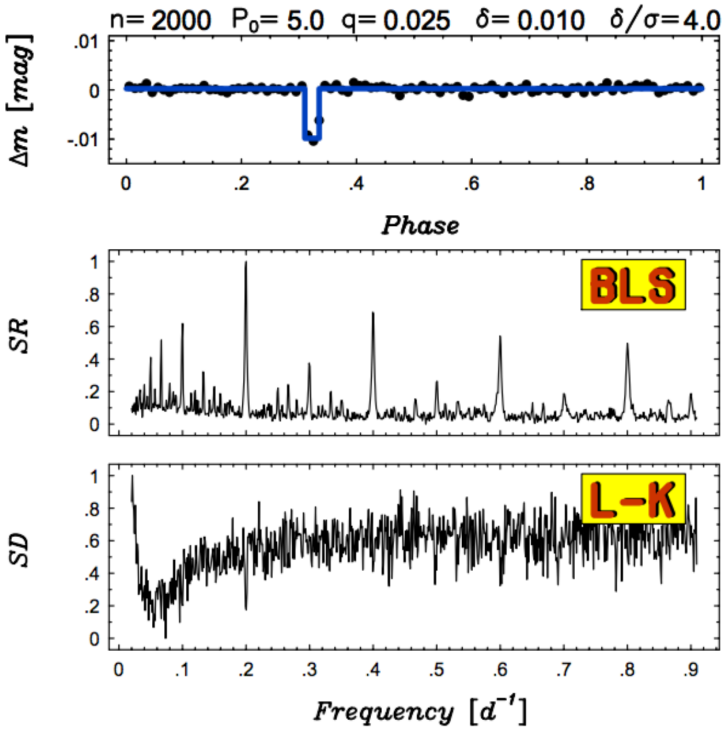

Figure 2.2: Best-fit detection with "box" model (above), BLS periodogram from Kovács et al. (2002) (central), compared to an earlier variable star-finding technique of Lafler and Kinman (1965)(lower).

2.5 Classic Transit detection methods

The most commonly used method for detecting a transit is using the "Box least squared" algorithm (Kovács et al., 2002). This uses a box-like step function with five parameters: Period, P, the fraction of phase in-transit, q, the flux level in-transit, L, the flux-level out-of-transit H, and the epoch of transit, t_0. For each test period, the period is phase-folded such that $\phi =$ mod $(P - t_0)/P$. Then a weighted chi-squared value is computed for each set of start- and end-of-transit phases, i_1 and i_2, which are iterated both over the phase (0 to 1) and up to some limit on their difference (e.g. $q < 20\%$). The parameters which give a minimum value returned across all i_1 and i_2 values are returned for each test period to create a BLS periodogram (see Figure 2.2).

A transit present in the light curve will, for the correct period, produce a BLS peak. It will also produce alias peaks at integer multiples of P, such as $P/2$, $2P$, etc (see Figure 2.2).

A Bayesian tool was also developed by Aigrain and Favata (2002) which modified the Gregory-Loredo method used to search for X-ray pulsars for planetary transits. Unlike

BLS it can use multiple in-transit bins to model transit shape, but maintains a flat out-of-transit light curve. However it proved more computationally intensive for insufficient gains in detection improvement, hence was rarely used (Aigrain and Irwin, 2004).

One problem with the current transit-search mechanism is that detrending the light curve either leaves correlated noise present in the light curve, or reduces the transit depth (and therefore transit signal). BLS can be improved if the detrending described in sections 2.7 and 2.10 are performed simultaneously with the BLS. The application of a probabilistic phase-folded transit search combined with a Gaussian process model for correlated noise will likely be possible in the future, and has briefly been explored for single systems (Kipping et al., 2017).

2.6 Photometric Data Products

2.6.1 WASP

The Wide Angle Search for Planets (WASP, briefly described in Section 1.2.4) is comprised of two outposts, located at the Roque de los Muchachos Observatory on La Palma (WASP-North) and the South African Astronomical Observatory (WASP-South). Each observatory consists of 8 cameras using 200mm f/1.8 lenses and cameras with 2048×2048 pixel CCDs, 7.8×7.8 square degree fields of view, and pixel scales of $13.7''$ (Pollacco et al., 2006).

After being flat-fielded and bias and dark subtracted, photometry is extracted from apertures of 2.5, 3.5, & 4.5 pixels (34", 48" & 62") around each bright star ($V < 15$) in the field of view. Sky background is found from star-free areas of an annulus of 13 to 17 pixels and a background subtraction performed.

The targets are given WASP IDs according to their RA and DEC, which are matched with the 2MASS IDs (Skrutskie et al., 2006), and basic statistics on their flux (median, flat chi-square, rms, etc) are also computed. Detrending using the Sysrem algorithm (Tamuz et al., 2005; Collier Cameron et al., 2006) is then performed on this 2D array of time, flux, flux uncertainties, etc.

For a star-by-star basis, the full WASP light curves of objects were accessed individually from the archive of WASP data stored locally at Warwick and opened with `astropy` (Robitaille et al., 2013). Where entire fields are used, the sysrem output fits file was accessed directly using a python copy of `fitsio` (Pence, 1992).

2.6.2 NGTS

The Next Generation Transit Survey (NGTS, also briefly described in Section 1.2.4) is an observatory in Paranal, Chile composed of 12 independently mounted near-IR telescopes

imaging 96 deg^2 of the Southern sky every 10 seconds. Near-instantaneous monitoring of the shift in star positions enables sub-pixel (rms 0.04px) stability in tracking. After image processing such as de-biasing and flat-fielding, 3-pixel radius apertures are used to extract aperture photometry of the stars in the field (which are pre-determined with a NGTS-specific input catalogue), and a sigma-clipped background level subtracted. Like the WASP data, the NGTS photometry is then detrended with a custom `sysrem` algorithm (Tamuz et al., 2005) to remove trends common to all stars, and custom methods are run to remove moon phase and sidereal day (Wheatley et al., in prep,). After this detrending, the resulting flux of all objects in the field is stored in a single fits file, with time and flux error information which is directly accessed on the NGTS system with, eg, `fitsio` (Pence, 1992).

2.6.3 Kepler and K2

The CCDs on board Kepler observe from 423 to 897nm (to avoid the more variable blue starlight), with the postage stamp images around each target summed into short (9×6s frames/1min) and long (270×6s frames/30min) cadence observations and downlinked for processing (Koch et al., 2010). Despite individual pixels saturating at $Kp \sim 11.5$, charge conservation in nearby pixels meant precise photometry was possible even down to $Kp \sim 7$.

The images were first background-subtracted, cosmic ray-removed, flat-fielded, etc to give calibrated images before aperture photometry was performed (Jenkins et al., 2010). Initially the position of 200 bright stars were used as proxies for spacecraft motion and, combined with onboard instrument readings, used to remove systematics (Twicken et al., 2010). This was updated in Stumpe et al. (2012) to model systematic errors using the correlation between all lightcurves, determined with a maximum a posteriori approach. The result was a median combined differential photometric precision (CDPP = $\sqrt{\sigma^2_{\text{shot}} + \sigma^2_{\text{stellarvar.}} + \sigma^2_{\text{instrumental}}}$) for dwarf stars of less than 50ppm over 6.5hrs for stars brighter than 13th magnitude (Christiansen et al., 2012). K2 data was downloaded by multiple teams (see Section 2.7.1), with light curves made available on the Mikulski Archive for Space Telescopes (MAST)[3] on an object-by-object basis. These were most frequently accessed with `astropy`(Robitaille et al., 2013), or with purpose-made `python` scripts (e.g. everest; Luger et al., 2016), with HJD, detrended flux and flux error arrays compiled into a 3-column light curve for analysis.

[3]https://archive.stsci.edu/k2/

2.7 Detrending lightcurves

To remove the correlated noise described in section 1.2.5, we must attempt to model these trends, and remove (or "detrend") them from the photometric data.

The most basic way of monitoring variations from the latter is to use differential photometry between the target star and a nearby star. This is because the drop in flux due to changes such as airmass, clouds and extinction changes, PSF (point spread function - the 2D shape of each star on the detector plane) changes, etc are common across all objects close together on the sky (Howell, 1992). Performing this for multiple stars in the field increases the number of photons used for such a correction, thereby decreasing any noise, and also reduces the effect of intrinsic variability of a single nearby comparison star. Such a technique is often utilised for follow-up photometric and spectral studies of exoplanetary transits.

For transit surveys, the photometry of all bright stars in the field will be used to search for transits, therefore individual differential photometry detrending becomes inefficient. However, using the same assumption that the majority of trends in stellar flux are common to all stars in a field, techniques exist to detrend all stars. The most commonly used is "sysrem" (Tamuz et al., 2005), which fits and removes series of linear trends across all stars in the field until all trends are removed. This uses a chi square function to minimise the residual of each datapoint from the mean depending on the extinction coefficient c_i of star i and the airmass a_j of image j in

$$S_i^2 = \sum_j \frac{(r_{ij} - c_i a_j)^2}{\sigma_{ij}^2} \tag{2.7}$$

This is then iterated over both i (all stars) and j (all images) until the best fit coefficients of c_i and a_j are found. This is then performed numerous times on the output light curves to remove multiple linear systematic effects until no more effects are present. This method has become vital to transit surveys including SuperWASP, where it is performed on all light curves and significantly reduces "red" (correlated) noise, although much remains (see Section 1.2.5).

Space-based photometry has the bonus of being free of atmospheric effects, and is able to produce continuous phase coverage of stellar variability, the removal of which is discussed in section 2.10. Detector effects also become important, with the flux changes on space-based *K2* dominated by the movement of the spacecraft as the star changes position on the CCD, producing raw flux with an RMS often a factor of ten higher than expected from white noise (Howell et al., 2014).

2.7.1 K2 detrending methods

The shifts in the proportion of starlight spread over different pixels results in a change in flux, as the response of each pixel (as well as the gaps between them) are different and unpredictable. To solve this, numerous teams developed similar models to determine the effect that various shifts in spacecraft pointing have on the flux, and therefore remove effects from this motion. These were, in almost all cases, applied to the raw target pixel files (TPFs) made available by the K2 team on MAST.

The model of Vanderburg and Johnson (2014) uses a fifth-order polynomial along the most common axis of motion. In the case of Armstrong et al. (2015a), a 2D surface fit is performed over the flux as function of both x- and y-axes. In Barros et al. (2016), the flux is binned into a 1D series along the line of stellar motion along the chip, with the resulting flux-position vector divided from the flux. The apertures used by each also differed significantly, with Vanderburg and Johnson (2014) using the lowest-RMS of 30 different aperture sizes, Armstrong et al. (2015a) similarly taking the best-fitting light curve from 4 circular apertures, and Barros et al. (2016) using an asymmetric aperture determined by iteratively adding one pixel until flux rms was minimised. From Campaign 3 onwards, the detrended PDC-SAP light curves of the original Kepler mission (See 1.2.7 Stumpe et al., 2012) were computed and made available.

More complex methods were developed to also account for potential stellar variability during detrending, including Aigrain et al. (2015), Aigrain et al. (2016) and Crossfield et al. (2015). Both methods use the centroid analysis defined above, but create a model of the motion using Gaussian Processes (GPs, explained in section 2.10). In the case of Aigrain et al. (2016), also use a GP to simultaneously model stellar variability. Different still is the method of (Foreman-Mackey et al., 2015), which used the full set of raw light curves for one campaign to produce a series of "eigen light curves" containing information only related to raw flux shifts common to many light curves (and therefore due only to detector-level noise).

The most accurate detrending of K2 data to date, however, comes from the `everest` pipeline (Luger et al., 2016). This, rather than using a model of the centroid position of the star, performs pixel-level-decorrelation (initially applied to Spitzer by Deming et al., 2015). By using the flux in each pixel, normalised to the total flux of the image, as the basis for detrending, and using a gaussian process to model intrinsic stellar noise, `everest` performs better than the majority of other detrending methods, with noise levels extremely close to that of the original *Kepler* mission (Luger et al., 2016, finds equivalent rms to the prime mission for Kp$<$ 13).

2.8 Removing Anomalies

Some datapoints may exhibit extremely large differences from the median flux. These may be due to cosmic rays, the coincidence of rapidly moving bright objects with the star, errors during reduction, etc. The presence of such anomalies could inhibit any model fits, and therefore need to be removed. However, we do not want to remove intrinsic variation of the light curve (especially drops in flux caused by e.g. transits). While other methods such as median filters are frequently used in the literature, we develop a fast and accurate method for removing flux anomalies with no model fitting, no shallowing of real signals, and from only the (time-sorted) flux array.

This "difference product" method uses the assumption that anomalies are typically uncorrelated (e.g. not proceeded or followed by other anomalous points). Using some flux measurement y_i, anomalies can be defined as any point from $i = 1$ to $i = N - 1$ where the following is true:

$$\frac{-(y_i - y_{i-1}).(y_{i+1} - y_i)}{\widetilde{|\Delta y|}^2} > \sigma^2_{\text{thresh}} \tag{2.8}$$

Where σ_{thresh} is a threshold multiple of the white noise. In the numerator, we find the difference between each flux value y_i and both its previous y_{i-1} and subsequent y_{i+1} flux values and multiply the two. In cases where this product is negative, point y_i lies either above or below both its neighbouring values, and hence likely to be an anomaly. We normalise this using the median absolute difference across all flux values squared as the denominator ($\widetilde{|\Delta y|}^2$). This value (mad) tends towards the root mean square (rms) white noise of the data for an uncorrelated normally-distributed series.

This works best with near-continuous data coverage, and can fail for consecutive anomalies and anomalies at the first or last point in the data. It is numerically fast, however, scanning a 100,000-long datapoint light curve in 6.5ms on a 8gb i5 processor. We typically set the threshold as 3.5 in this thesis, as this such that a normally-distributed flux value would occur by chance once in $\sim$ 2150 values - suggesting only one such anomaly per *K2* lightcurve ($\sim$ 3000 points).

2.9 Removing Trends

Search algorithms for transiting exoplanets frequently assume that out-of-transit flux is non-varying and at some constant (normalised) flux level. In the case of real light curves, this is plainly not true, especially at the sub-mmag level probed by space-based telescopes such as Kepler - stellar variability, long-term drifts, etc. all contribute flux. However, these usually vary on timescales far longer than that of exoplanetary transits (typically hours). So they

are in principle removable without affecting the transit search, and many techniques exist for performing this on light curves.

One technique is to use the Fourier technique of high-pass filters, however, this does not perform well with irregularly time-sampled data, and can shallow transit signals, or cause unphysical bumps either side. Another technique is to use median filters over timescales longer than the likely transit duration, thereby ensuring any low in-transit flux does not contribute to the sample. However, these again do not deal with irregular sampling and lightcurve gaps. Gaussian Processes (explained in Section 2.10) might seem the best choice for this, and on an individual lightcurve basis, they are the best method for model variability. However, they are slow to process, and with the iterative techniques of transit detection over period, phase and often many thousands of lightcurves, the implementation of GPs is impossible.

Another method is to iteratively fit segments of lightcurve with a filter excluding any potential transit (a non-linear time-domain filter as described by Aigrain and Irwin (2004, , Section 3.3)). The method adapted in Armstrong et al. (2014a), and used multiple times in this thesis, applies smoothing to a small window which is iterated along the light curve. A weighted polynomial fit is performed on a wide and anomaly-masked timespan either side (but not including) this window to determine long-duration trends. Such a method is excellent at correcting for even relatively short timescale variations, while preserving transit structure and depth. We typically used a 7-day window iterated in steps of 0.3d, with a 3rd order polynomial, and 20 iterations to remove anomalies.

2.10 Gaussian Processes

In almost all time-domain astronomical observations, noise is not exclusively "white", as described in section 2.7. Instead, systematics associated with the instrument, the environment, and variations associated with the observed objects themselves also contribute a signal to the observations, which may typically be attempting to measure another process. In most cases these processes produce smooth, continuous trends that vary over characteristic timescales with characteristic amplitudes, however the exact underlying functions are unknown. In these cases a simple parametric curve (e.g. a polynomial fit) would not be an accurate representation of the timeseries.

Gaussian Processes are a powerful way of modelling such systematics with few prior assumptions on the underlying functions. Originally brought to attention by Williams and Rasmussen (1996) and Rasmussen (1996), Gaussian processes were further explored by Neal (1997) and reviewed by MacKay (1998). Developing on these ideas, exoplanet-specific applications for GPs appeared in the 2010s, including for transit spectroscopy (Gib-

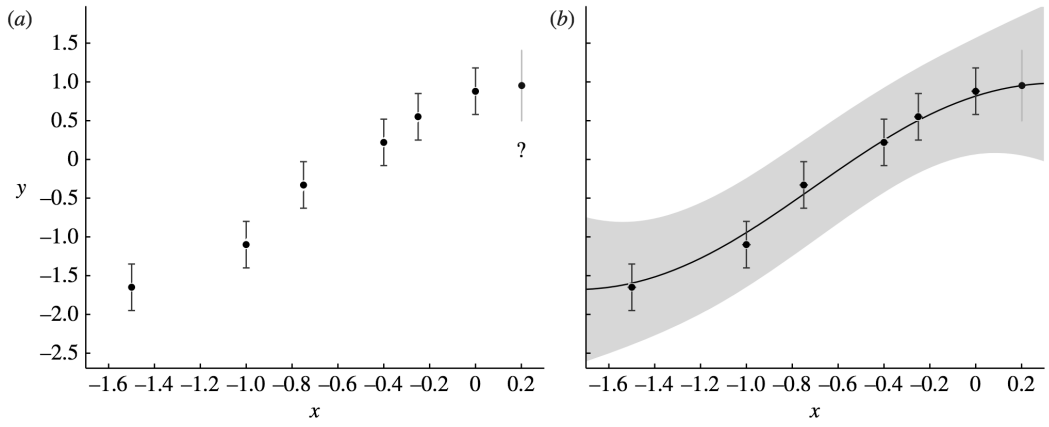

Figure 2.3: Noisy observations with an unknown datapoint (green errorbars) constrained with a Gaussian Process conditioned on the previous 6 data points. Taken from Roberts et al. (2013).

son et al., 2012), and radial velocities (Rajpaul et al., 2015). We recommend the general introduction from Roberts et al. (2013) which has informed the majority of this section. While they can be used for any smoothly varying timeseries, we focus here on modelling stellar flux as a function of time.

The core of Gaussian Processes is covariance. Two subsequent data-points on a time-series are not randomly sampled, but instead the precise measurement of one constrains the position of the next - they have covariance. Alternately, if we have some array of t evenly-sampled datapoints on a timeseries, the flux at position $(t+1)$ is not purely random but can be constrained, along with an uncertainty on its flux, from the fluxes and covariance of the previous datapoints (e.g. Figure 2.10).

The amount of weight a Gaussian Processes gives to any datapoint from all previous (and future) datapoints, is then determined by the covariance kernel function, $k(x_i, x_j)$. This is a matrix which computes the covariance between each point and every other. The probability function of any function is therefore constrained by a Gaussian drawn from the mean value of the timeseries, $\mu(x)$, and the covariance kernel function $\boldsymbol{K}$, $p(\boldsymbol{y}(\boldsymbol{y})) = \mathcal{N}(\boldsymbol{\mu}(\boldsymbol{x}), \boldsymbol{K}(\boldsymbol{x}, \boldsymbol{x}))$. In the case that uncorrelated "white" noise ($\sigma^2\boldsymbol{I}$ where $\boldsymbol{I}$ is an identity matrix) is also present, this becomes $p(\boldsymbol{y}(\boldsymbol{y})) = \mathcal{N}(\boldsymbol{\mu}(\boldsymbol{x}), \sigma^2\boldsymbol{I} + \boldsymbol{K}(\boldsymbol{x}, \boldsymbol{x}))$.

The kernel takes on a functional form that determines how the covariance of two points decays with distance, often defined by one or more "hyperparameter". The most commonly used kernel is that of the squared exponential (SE), given by:

$$k(x_i, x_j) = h^2 \exp\left(-\left(\frac{x_i - x_j}{\lambda}\right)^2\right) \tag{2.9}$$

Where h and λ are hyperparameters governing the amplitude (or magnitude) and timescale of variations. Other kernels include the "Matern" class of kernels, which increase in complexity from $\nu = \frac{1}{2}$ (which is equal to an "exponential" kernel), to $\nu = \frac{3}{2}$, $\nu = \frac{5}{2}$, etc, and tend to the SE kernel as ν increases. These low-order Matern kernels typically are better at modelling more sharp, "choppy" changes gradients. To model variations with covariance timescales falling off more slowly than the SE kernel, the "rational quadratic" kernel uses a beta distribution to model the covariance kernel function. Also possible are kernels with periodic and quasi-periodic functions, which can be formed by multiplying the standard kernels by a periodic component.

While the kernel is often chosen at the onset of modelling, the Gaussian process hyperparameters can be optimised by fitting the data with various functions and maximizing the log-likelihood. Priors may be placed on the hyperparameters based on knowledge of the likely timescales of variation. A number of techniques are also used to stop the GP from overfitting the datapoints. These include adding a parameter that globally rescales errorbars, co-fitting a white noise kernel, and placing a prior on the amplitude hyperparameter in the form of a gamma distribution ($p(Ai) = \Gamma(1, 100)\exp[100Ai]$ (Evans et al., 2015)). These give decreasing probability to increasing covariance amplitude unless justified by the data.

In this thesis the exponential squared kernel was typically used, often with a mean function set from the average flux, and a white noise kernel parameterised from the expected white noise (given the stellar magnitude). The hyperparameters were typically trained using the out-of-transit lightcurve, maximising the log likelihood. The `George` `Python` library (Foreman-Mackey, 2015) was used for this modelling.

2.11 Supervised Machine Learning

Supervised Machine Learning is a technique in which a function is inferred from labelled training data, which can then make predictions for future instances. It is frequently used when datasets are so large that human classification is impossible.

One commonly used form is "Random Forests" of decision trees (Breiman, 2001). This is especially useful for any multi-parameter classification problem. The input parameters should be as numerous and independent as possible, with each plausibly contributing to the classification of the class (e.g. the two-parameter classification detailed in figure 2.11). For example, to use such a method for the detection of different classes of variability, we would use the available stellar information and statistics about the variation of flux such as period, amplitude, phase-folded shape, light curve scatter, etc (as we performed in Armstrong et al., 2016a).

Random forests are, as one might expect, collections of decision trees. These split

the data up along some randomly defined axis of parameter space at each branch junction, and each make a prediction of the class of the input. Given their random nature, most of the decision trees do not predict the data well. Some however, will split the parameter space in such a way that leads to good predictions of the training set. The trees are then ranked according to how well they perform on the training set, meaning that the good trees outweigh the bad trees, and produce a classification of the data (see Figure 2.11).

A test set entirely exclusive of the training set is then used to test the tree (to avoid effects from the over-fitting of the tree to the training data). The output classifications can then be compared to their known classifications to produce a confusion matrix between each class. The contribution of each "feature" (input parameter) to the classification can also be determined from analysing the strength individual trees have in correctly dividing according to the specific parameter used. In the case of Armstrong et al. (2016a), period and light curve shape were the most important for classifying variability. This also enables a probabilistic prediction of class, using the proportion of trees that outputted each output.

In this thesis, the Random Forest implementation in the `scikit learn` python module was used (Pedregosa et al., 2011), as well as the 'tree interpreter' package[4] which allows easy access to the individual decision trees (see chapters 4 and 5).

[4]http://blog.datadive.net/random-forest-interpretation-with-scikit-learn/

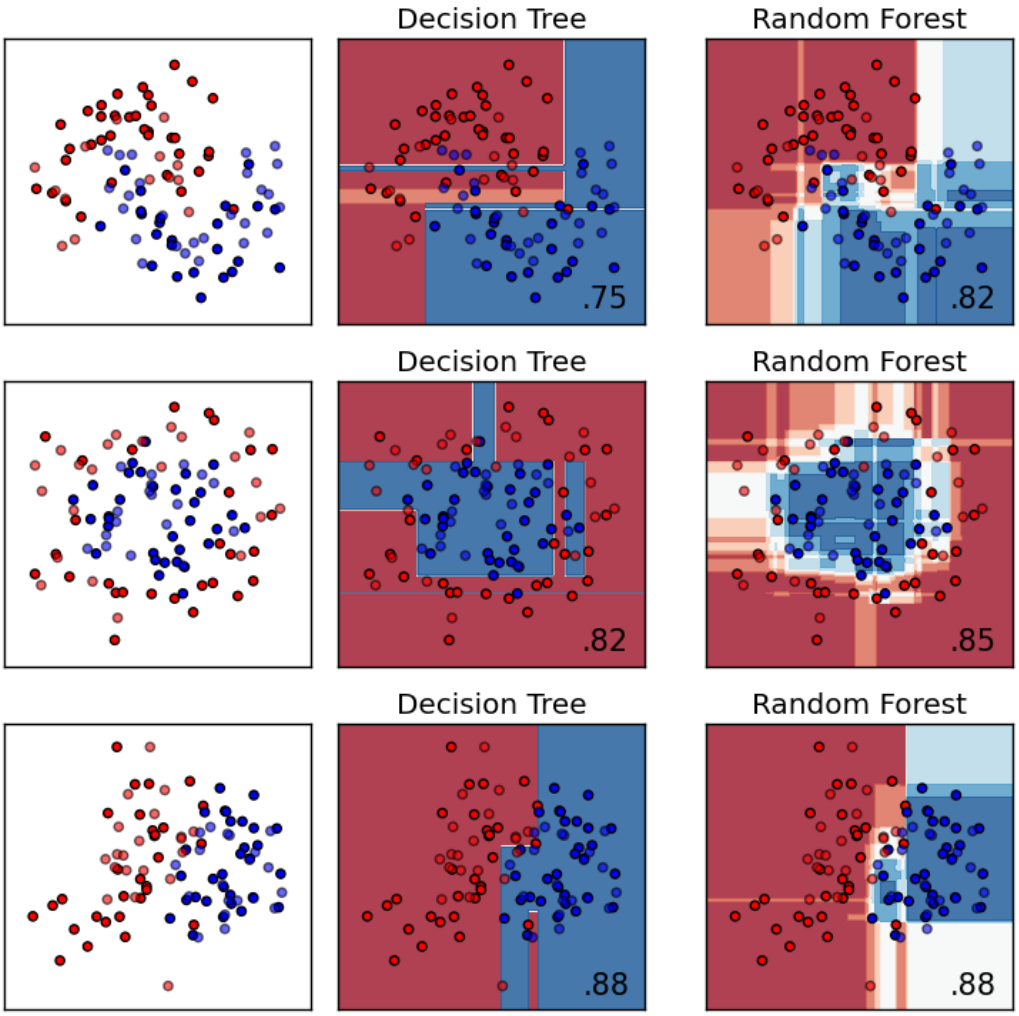

Figure 2.4: An example of a random forest, with two classes of data (red and blue) and two parameters (x- and y-axis) distributed with slightly different parameters. The central panels show the output of a single decision tree whereas the right shows the output of the random forest, which averages over many trees. The number in the bottom right shows the proportion of samples correctly classified. (Figure from http://martin-thoma.com/images/2016/01/ml-classifiers-2.png)

Chapter 3

Periodic Exoplanet Candidates in K2 and Confirmation of the mini-Neptune K2-110b

"No planet was "discovered". Just another theoretical "discovery" like all the rest. Again, no planet outside our system has ever been directly observed."
pete, USA, Daily Mail

Note: The following chapter is partly based on unpublished transit detections, and partly on the paper "K2-110 b – a massive mini-Neptune exoplanet" (Osborn et al., 2017b, ; accepted for publication, April 2017). In the former case, transit searches were led by myself, but contributions of a small team were required. In the case of K2-110b, spectral fitting and the planet confirmation model were performed by collaborators, however the photometric data, the assembly of individual results, and all discussions and conclusions were performed by myself.

3.1 Introduction

Unlike the primary *Kepler* mission, detrended photometry was not initially produced by the mission team, with raw target pixel files (TPFs) released from the engineering campaign (ET) to campaign 3, and detrended PDC-SAP light curves available from then onwards. This led to numerous groups developing light curve detrending techniques, including (see Section 2.7.1 Vanderburg and Johnson, 2014; Armstrong et al., 2015a; Aigrain et al., 2016b; Luger et al., 2016; Barros et al., 2016).

The next step was to search these light curves for the signals of transiting planets. This has also been performed by many groups, producing around 500 planet candidates (Foreman-Mackey et al., 2015; Vanderburg et al., 2015a) and nearly 150 confirmed or validated planets (Montet et al., 2015; Sinukoff et al., 2015; Armstrong et al., 2015b; Barros et al., 2015; Crossfield et al., 2016). K2 has especially contributed new planetary systems around bright stars (V<12), with planets suitable for ground-based follow-up, including radial velocities (RVs), the Rossiter-McLaughlin (RM) effect and atmospheric spectroscopy.

We present in Section 3.2 the detection of 199 multi-transiting exoplanet candidates from a search of these *K2* light curves. In Section 3.3 we describe in detail the detection of a sub-Neptune radius planet around the K field dwarf K2-110 from *K2* photometry and the confirmation and mass measurement of this planet with HARPS and HARPS-N RVs.

3.2 K2 Exoplanet Candidates

3.2.1 Data

K2 Campaigns from 0 through 10 were searched for planet candidates. The number of candidates searched varied campaign by campaign, as did the magnitude limit. We used the detrending technique first of Armstrong et al. (2015a, hereafter DJA15) for campaigns 0 to 3, both DJA15 and PDC_SAP light curves (Stumpe et al., 2012) for campaigns 4-7, and finally the method of Barros et al. (2016, hereafter SB16) for campaigns 7 through 10, as techniques improved (see Section 2.7.1 for details). The total numbers, magnitude limits, and date ranges of the data searched is shown in Table 3.1.

3.2.2 Methods

After detrending, we normalised the light curves by dividing by the median flux, and "flattened" using the method outlined in Armstrong et al. (2014a, described in Section 2.9). Anomalies were also removed with the difference product method described in Section 2.8.

To attempt to de-weight problem regions associated with un-decorrelated spacecraft motion and systematics (eg due to poorly-removed *K2* thruster firings), we globally rescaled

Campaign	t_{start} (KJD)	t_{end} (KJD)	mag limit	N_{stars}	Det. method
0	1892	1971	NA	7244	DJA13
1	1981	2057	NA	21217	DJA13
2	2060	2141	NA	13311	DJA13
3	2143	2223	13.1	5909	DJA13
4	2228	2302	13.1	8032	DJA13 & PDC_SAP
5	2307	2380	12.1	~2000	DJA13 & PDC_SAP
6	2385	2462	13.3	8388	DJA13 & PDC_SAP
7	2466	2549	14.5	13210	SB16 & PDC_SAP
8	2558	2637	14.5	22702	SB16 & PDC_SAP
9	2653	2637	NA	0	SB16 & PDC_SAP
10	2743	2818	13.0	5186	SB16 & PDC_SAP

Table 3.1: Details of the K2 objects searched for planets in each campaign. Kepler Julian Date (KJD) refers to days since the start of the Kepler mission, HJD-2454833. "NA" shows no magnitude limit was applied.

the flux errorbars. This was performed by first finding, for each light curve, the median average deviation (MAD) for each time stamp compared to the median flux of the rest of the light curve. The average relative MAD across all light curves was then calculated for each time stamp in the campaign. Errors were then rescaled by $2.5\left(MAD/\overline{MAD}\right)^2$.

The transit search was done using the BLS algorithm (adapted from Kovács et al. (2002)[1], see section 2.5) with a frequency spacing of $\sim 10^{-5}$ across frequencies from 2 hours to 95% of the light curve duration, for a total of $\sim 10^6$ test periods per light curve. To determine the best candidates in a self-sufficient way and help discard variable or noisy signals, a BLS "signal to noise" for each output was computed with respect to the median of the lowest 98% of the BLS spectral values. Peaks in the BLS spectrum were then detected and sorted by SNR.

Despite de-trending and errorbar-rescaling, spacecraft thruster-firings on a $\sim$ 6hrs still created BLS aliases at this period (and aliases of it). To correct for this, the affected frequencies were found by applying the BLS algorithm to the inverse of the global systematic MAD array, as this formed a global systematic model which maps transit-like features present in multiple light curves. The strongest BLS systematic signals (usually at frequencies at or near the thruster firing timescales and the two strongest aliases) were then discarded from the BLS peaks recovered for each light curve.

Light curves with significant detections were then sorted by the BLS SNR and "eyeballed". Information used for this manual candidate analysis included the BLS power spectrum, the raw light curve, detrended light curve, phase-folded light curves of the top three BLS signals, and a guide to the most common systematic frequencies (on the BLS spec-

[1]https://github.com/dfm/python-bls

trum) and times (on the detrended light curve).

To be designated a good candidate, objects needed to show statistically significant transit-like features in the phase-folded detrended flux, have at least one obvious transit event in non-phase folded detrended flux, have a signal which did not correspond to systematics seen in raw flux (or in other nearby detrended light curves), and show no signs of secondary eclipses (on-off variation in transit depth) or ellipsoidal variation in the phase-folded signal. The period for strong candidates were then recorded from the BLS spectrum, epoch was determined from the raw light curve, and depth was determined by eye using the phase-folded plot.

3.2.3 Planet Candidates

We have detected a total of 199 candidates from Campaigns 0 to 10 of *K2*. EPIC IDs of these candidates are listed in Tables 3.2 to 3.3, along with their best-fitting periods, epochs & depths, the stellar radii, Kepler magnitude of their host stars, and a first-order planetary radius. Figures 3.1 and 3.2 show the parameters of our candidates. The median depth is 1.1ppt, the median period 8.4d and the median *Kepler* magnitude 12.3.

92 of the candidates overlap with other surveys for planets in K2 such as from campaigns 1 (Foreman-Mackey et al., 2015; Montet et al., 2015), 0 to 3 (Vanderburg et al., 2015a), 1 to 5 (Crossfield et al., 2016), 5 & 6 (Pope et al., 2016), 1 to 5 (Adams et al., 2016, $P < 1$d), 1 to 6 (Barros et al., 2016) and 6 to 8 (Jackson et al., 2017, $P < 1$d). These candidates also include some of the first detections published for stars observed in campaigns 7 through 10.

We plot the candidates as a function of their host star brightness, planetary period and planetary radius in figure 3.1. The Kepler survey and other K2 candidate (Campaigns 0-6) are also plotted. We also find far more planets around bright stars than the primary mission.

Where reconnaissance spectra have not been taken, the stellar parameters used in this analysis come from one of two sources. Where available, stellar information was taken from ExoFOP[2], most commonly provided by the Ecliptic Plane Input Catalogue (EPIC, Huber et al., 2016). Where no estimate of stellar temperature existed from this catalogue, a search of NOMAD (Zacharias et al., 2004) and WISE (Cutri et al., 2014) catalogues provided photometric information from visible to infra-red. Colours were then matched against colour-temperature tables from Pecaut and Mamajek (2013) to estimate a stellar temperature, with colour errors propagated into a $T_{\rm eff}$ error. Using the fits of Straižys and Kuriliene (1981), we estimated stellar mass and radii. If no log g estimate was available from ExoFOP or follow-up spectra, a main-sequence fit was performed. Where log g was

[2]Accessed at https://exofop.ipac.caltech.edu

available a 2D fit to both stellar temperature and log g were used to estimate a (model-dependent) stellar radius and mass.

3.2.4 Follow-up

A number of avenues for follow-up were used to characterise these planets:

Imaging - In order to observe or rule out blended stars that could be the source of the transit signal (and therefore rule-out likely astrophysical false positives) high-resolution imaging of the target is required. AstraLux, the lucky-imaging camera on the 2.2m at Calar Alto (Hormuth et al., 2008), was primarily used for this, achieving limits of Δmag$\sim$ 7 at 1$''$in the z- and I-band.

Reconnaissance spectra - High signal-to-noise spectra are the best means of characterising a star, giving information about its surface gravity (log g), temperature ($T_{\rm eff}$) and metallicity ([Fe/H]), and model-dependent information about stellar radius and mass. Ruling out a giant star (primarily with log g) is important to determine if the transit is caused by a planet eclipsing a dwarf star, or a dwarf star eclipsing a giant. We primarily used spectra from CAFE, an echelle spectrograph also on the Calar Alto 2.2m (Aceituno et al., 2013), for this purpose.

High-resolution spectra - To rule out low-mass stars, measure the mass of the planetary candidate, and truly confirm the candidate as a planet, high-resolution spectra and accurate radial velocities are required. We have utilised multiple observatories with this aim, including Sophie (on the 1.95m at the Observatoire de Haute Provence Perruchot et al., 2008), Coralie (on the 1.2m Euler telescope, La Silla Queloz et al., 2000) and HARPS (on the 3.6m at ESO, La Silla Pepe et al., 2000). Follow-up by radial velocity monitoring and stellar characterisation is ongoing for many of these candidates (e.g. ESO LP 198.C-0169).

Candidates detected by our search process and subsequently confirmed with follow-up observations include:

- **K2-19 b and K2-19 c** - Two Neptunes (4.2 and 7.2$R_\oplus$) close to a 3:2 orbital resonance around a 12.8 magnitude K-dwarf (Armstrong et al., 2015b; Barros et al., 2015).
- **K2-30 b and K2-34 b** (EPIC210957318b and EPIC212110888b) - Two hot jupiters with radii 1.2 and 1.22R_{Jup} (Lillo-Box et al., 2016).
- **K2-29 b** - A 1.19R_{Jup} hot jupiter on a 3.25d orbit around a G7 dwarf. (Santerne et al., 2016)
- **EPIC 201702477b** - A 0.76R_{Jup}, 67M_{Jup} brown-dwarf and one of the densest sub-stellar objects ever detected. (Bayliss et al., 2016)

Figure 3.1: Candidates detected by our search in *K2* (in red) are shown as a function of stellar magnitude, period, radius and stellar effective temperature. For comparison, candidates from other *K2* searches are shown in blue, and planets from the *Kepler* primary mission in green (with similar shading due to $T_{\rm eff}$).

Figure 3.2: The parameters of candidates detected by our search in *K2*. a) Number of planet candidates per campaign; b) Planet candidate sky position in RA and Dec (colours are maintained from the plot above); c) Planet candidates by transit depth; and d) Candidates by planetary radius.

Table 3.2: *K2* Candidate List. Stellar information was primarily derived by EPIC (Huber et al., 2016) (accessed from ExoFop at https://exofop.ipac.caltech.edu/k2/). Where certain values were unavailable, other methods were used. † denotes that the main-sequence fits of Straižys and Kuriliene (1981) were used to calculate mass and radius. ‡ denotes that $T_{\rm eff}$ was obtained from all available catalogue colours. * denotes that logg was calculated from a luminosity class given by exofop. ◊ denotes that spectral type and luminosity class were given in exofop. §denotes that the kepmag was calculated from B & V colours obtained with a USNO source match.

EPIC ID	Camp	Kepmag	Period [d]	Depth [ppt]	R_p [$R_\oplus$]	Spec Type	R_s [$R_\odot$]
201092629.01	10	11.86	26.824	1.0	2.6	G8	0.76
201110617.01	10	12.95	0.813	0.3	0.7	K6	0.35
201127519.01	10	11.56	6.179	14.0	9.2	K3	0.71
201130233.01	10	12.6	0.365	0.02	0.4	G5	0.87
201132684.01	10	11.68	10.062	0.7	2.5	G4	0.88
201160662.01	1	12.12	1.54	6.0	10.5	F8	1.24
201208431.01	1	14.41	10.004	0.484	1.6	K7.7V ◊	0.66
201227197.01	10	12.49	3.706	1.0	3.7	G1	1.07
201257461.01	1	11.51	50.268	0.784	14.6	K2	4.79
201295312.01	1	12.13	5.656	0.361	3.3	G0	1.58
201324416.01	10	12.32	1.796	0.06	0.7	G8	0.77
201324549.01	1	12.15	2.52	1.0	5.0	F7	1.45
201338508.01	1	14.36	10.933	0.324	0.9	K7	0.46
201338508.02	1	14.36	5.735	0.324	0.9	K7	0.46
201352100.01	10	12.8	13.384	1.5	3.3	K0	0.79
201357643.01	10	12.0	11.893	1.3	5.3	F8	1.35
201357835.01	10	12.28	11.893	1.2	5.2	F6	1.38
201367065.01	1	11.57	10.054	0.361	1.2	M0.1V ◊	0.56
201367065.01	1	11.57	44.563	0.6	1.5	M0.1V ◊	0.56
201367065.02	1	11.57	24.647	0.196	0.9	M0.1V ◊	0.56
201384232.01	1	12.51	30.938	0.729	3.0	G2	1.01
201393098.01	1	13.05	28.679	0.529	5.3	G3	2.13
201403446.01	1	12.0	19.154	0.324	2.5	F7	1.29
201427874.01	10	12.82	6.673	0.8	2.2	K2	0.7
201433325.01	10	11.99	2.757	0.05	1.2	F7	1.53
201437844.01	10	9.23	9.553	0.3	2.4	F6	1.27
201437844.02	10	9.23	21.057	1.0	4.4	F6	1.27
201445392.01	1	14.38	10.353	0.9	2.6	G9	0.8
201445392.02	1	14.38	5.064	0.576	2.1	G9	0.8
201448860.01	1	11.68	41.4	0.4	6.6	K1	3.04
201454397.01	10	11.52	12.601	20.0	18.2	F8	1.18
201465501.01	1	14.96	18.449	2.809	2.1	M2.8V ◊	0.37
201528828.01	10	11.42	14.098	1.5	3.2	G8	0.77
201549860.01	1	13.92	5.608	0.729	1.8	K4V ◊	0.62
201555883.01	1	15.06	5.797	2.025	2.7	K6	0.54
201565013.01	1	16.91	8.638	11.236	5.1	K8	0.44
201567796.01	1	12.36	5.009	15.0	18.3	F8	1.37
201576812.01	1	10.07	2.864	21.0	13.6	G4	0.86
201577035.01	1	12.3	19.306	1.225	4.1	G4	1.08
201596316.01	1	13.15	39.842	0.676	2.4	G8	0.83
201613023.01	1	12.14	8.282	0.324	2.6	F8	1.31
201617985.01	1	14.11	7.282	1.156	2.2	M0.5V ◊	0.61
201629650.01	1	12.73 §	40.049	0.225	1.8	G3	1.09

Table 3.3: *K2* Candidate List [cont.]

EPIC ID	Camp	Kepmag	Period [d]	Depth [ppt]	R_p [$R_\oplus$]	Spec Type	R_s [$R_\odot$]
201635569.01	1	15.55	8.368	9.604	6.7	M0V ◊	0.62
201702477.01	1	14.43	40.736	4.489	7.2	G1	0.98
201705526.01	1	9.94	18.102	6.0	13.4	F9	1.58
201713348.01	1	11.53	5.34	0.8	2.3	K1	0.75
201736247.01	1	14.4	11.811	1.024	2.7	G7	0.78
201754305.01	1	14.3	19.073	0.676	1.9	K2	0.67
201754305.02	1	14.3	7.62	0.576	1.8	K2	0.67
201828749.01	1	11.56	33.509	0.841	2.8	G3	0.9
201855371.01	1	13.0	17.971	0.784	1.9	K5V ◊	0.63
201912552.01	1	12.47	32.941	1.225	1.6	M3.0V ◊	0.41
202072704.01	0	11.4	2.67	8.0	13.8	F1	1.42†‡
202088212.01	0	11.6	2.62	10.0	15.3	F7	1.4
202088861.01	0	11.6	9.11	0.5	2.5	G3	1.0 †‡
202136063.01	0	12.4	5.21	2.0	2.2	M3	0.46 †‡
202137753.01	0	12.7	2.21	5.0	5.4	K6	0.69 †‡
202138842.01	0	12.2	12.51	2.5	3.8	K6	0.7 †‡
203753577.01	2	11.11	3.4	3.0	9.8	F6	1.64
203771098.01	2	11.65	20.89	2.0	7.4	G5V ◊	1.51
203771098.02	2	11.65	42.36	4.5	11.1	G5V ◊	1.51
204057095.01	2	11.58	23.2	5.0	10.3	G0	1.34
204128016.01	2	12.01	50.75	4.0	14.2	F7	2.05
204129699.01	2	10.61	1.258	6.0	7.6	G5	0.9
204884005.01	2	11.51	46.3	2.0	3.1	K3	0.63
204890128.01	2	11.89	12.2	1.0	2.9	G8	0.85
204991696.01	2	10.53	49.8	0.7	4.0	F7	1.37
205071984.01	2	12.0	8.99	4.0	6.4	G6	0.92
205570849.01	2	12.12	16.85	3.5	6.9	G0	1.07
205924614.01	3	13.09	2.849	4.6	5.7	K4.2V ◊	0.77
205999468.01	3	12.93	12.258	0.5	1.8	G9	0.72
206011496.01	3	10.92	2.368	0.3	1.7	G5	0.91
206011691.01	3	12.32	15.494	1.0	2.5	K7.9V ◊	0.72
206026904.01	3	12.15	7.053	1.3	3.4	G6	0.86
206036749.01	3	13.01	1.131	1.2	5.0	F7	1.32
206038483.01	3	12.59	3.002	4.9	11.2	G2	1.47
206061524.01	3	14.44	5.879	10.0	7.9	M0.7V ◊	0.73
206096602.01	3	12.04	6.67	1.1	2.6	K2	0.73
206103150.01	3	11.76	4.158	12.0	13.2	G0	1.1
206121833.01	3	10.16	41.4	4.0	12.0	F6	1.74
206125618.01	3	13.89	6.531	0.7	2.1	G7	0.73
206144956.01	3	10.4	12.653	0.4	1.8	G8	0.84
206154641.01	3	11.3	2.485	16.2	19.3	F9	1.39

Table 3.4: *K2* Candidate List [cont.]

EPIC ID	Camp	Kepmag	Period [d]	Depth [ppt]	R_p [$R_\oplus$]	Spec Type	R_s [$R_\odot$)]
206155547.01	3	14.62	24.395	21.0	17.7	G0	1.12
206181769.01	3	12.77	13.987	1.4	3.8	G4	0.93
206245553.01	3	11.74	7.495	0.8	3.3	G0	1.06
206247743.01	3	10.58	4.602	0.5	6.3	K1	2.59
206268299.01	3	12.43	19.58	0.6	2.6	F9	0.98
206432863.01	3	13.01	11.994	7.2	11.9	G2	1.28
206500801.01	3	12.19	8.153	25.0	15.8	G4	0.91
210402237.01	4	11.8	10.992	0.9	4.2	G0	1.28
210448987.01	4	13.93	6.101	1.2	2.4	K3V ◊	0.63
210508766.01	4	13.84	10.001	1.6	2.4	M1V ◊	0.55
210512842.01	4	12.11	5.866	0.2	1.8	F9	1.14
210550063.01	4	11.15	2.166	0.5	4.2	F6	1.71
210558622.01	4	12.03	19.573	1.0	2.3	K7V ◊	0.68
210598340.01	4	12.54	3.735	11.3	17.6	F6	1.52
210629082.01	4	11.58	27.31	0.3	2.8	F8	1.48
210667381.01	4	12.67	5.331	0.2	1.4	G3	0.92
210693462.01	4	13.1	31.374	2.3	1.6	M1	0.31
210769880.01	4	11.04	1.438	1.0	1.6	K7	0.47
210776787.01	4	11.87	22.815	2.0	6.8	F7	1.38
210903662.01	4	12.05	2.41	6.0	12.8	F6	1.51
210957318.01	4	13.17	4.098	19.1	13.8	G4	0.92
210968143.01	4	13.72	13.715	1.2	2.4	K5V ◊	0.63
211002562.01	4	12.48	3.348	12.3	15.9	F9	1.31
211009047.01	4	12.54	1.32	1.4	8.4	F6	2.06
211020714.01	4	12.6	44.377	1.1	5.5	F7	1.51
211048999.01	4	12.66	5.171	0.7	2.3	K0	0.8
211089792.01	4	12.91	3.259	20.0	13.1	G7	0.85
211147528.01	4	11.83	2.348	8.5	18.2	F2	1.81
211432103.01	5	10.25	0.933	2.0	3.9	G9	0.81 †‡
212110888.01	5	11.44	2.996	8.0	14.9	F9	1.53
212294561.01	6	13.15	2.763	0.3583	19.1	G8	9.25
212349118.01	6	12.62	2.548	1.0	5.1	F9	1.48
212357477.01	6	10.22	6.33	0.5581	2.8	G1	1.1
212435047.01	6	12.39	1.116	0.1662	2.1	F8	1.5
212440430.01	6	13.27	20	1.0	3.7	G1	1.07
212460519.01	6	12.44	7.388	0.8217	1.9	K7V ◊	0.62
212469831.01	6	13.56	5.075	6.3459	8.3	G3	0.96
212488008.01	6	10.63	5.67	2.0	10.2	G6	2.1
212496592.01	6	12.97	2.858	0.2514	1.5	G8	0.85
212521166.01	6	11.59	13.862	1.5	3.0	K2	0.7
212530118.01	6	13.56	12.837	0.5263	1.1	K6	0.45

Table 3.5: *K2* Candidate List [cont.]

EPIC ID	Camp	Kepmag	Period [d]	Depth [ppt]	R_p [$R_\oplus$]	Spec Type	R_s [$R_\odot$)]
212572439.01	6	12.84	2.582	4.9914	5.7	K1	0.74
212577658.01	6	11.54	14.073	0.3958	1.9	G6	0.88
212580872.01	6	13.05	15.04	1.8	4.0	G5	0.87
212585579.01	6	12.63	3.022	1.3924	5.7	G0	1.4
212586030.01	6	11.69	7.79	0.7	11.4	K2	3.94
212587672.01	6	12.19	23.241	0.5379	3.3	F8	1.29
212645891.01	6	12.64	0.328	1.9529	5.2	G1	1.09
212658818.01	6	12.07	2.321	6.0	7.3	G5	0.87
212661144.01	6	13.6	2.458	0.7972	2.6	G8	0.83 †‡
212672300.01	6	12.85	39.67	1.0	4.9	F7	1.41
212679925.01	6	13.02	1.835	23.9801	10.7	K5	0.63
212689874.01	6	12.33	15.85	1.0	4.4	G1	1.29
212689874.02	6	12.33	28.47	0.8	4.0	G1	1.29
212705192.01	6	11.73	2.269	6.4223	9.4	G1	1.08
212735333.01	6	11.98	8.355	0.5444	2.6	G2	1.04
212779596.01	6	11.93	7.377	2.5	3.8	K3	0.7
212797028.01	6	13.1	14.978	20.0	12.7	G8	0.83 †‡
212803289.01	6	11.01	18.26	2.0	7.8	F8	1.59
213546283.01	7	12.03	9.771	1.0	3.2	G3	0.93
213817056.01	7	12.96	13.612	1.5	3.5	K0	0.82
214965287.01	7	14.09	1.926	0.1	20.0	K5	18.31
215854715.01	7	12.61	11.124	0.5	2.0	G8	0.83
215969174.01	7	14.3	4.175	14.0	17.5	F8	1.35
216166748.01	7	11.88	19.68	0.5	5.7	G2	2.35
216231580.01	7	14.77	3.905	17.0	17.5	F9	1.23
216334329.01	7	12.9	28.073	3.0	10.7	G0	1.79
216405287.01	7	13.0	3.405	0.4	5.1	G8	2.32
216468514.01	7	12.75	3.314	7.0	13.3	G0	1.46
216494238.01	7	12.3	19.899	3.5	11.8	F9	1.82
217192839.01	7	12.6	16.034	1.0	2.2	K4	0.63
217192839.02	7	12.6	26.805	0.6	1.7	K4	0.63
217393088.01	7	15.29	1.319	12.0	15.7	G0	1.31
217977895.01	7	12.74	21.7	0.7	5.0	G3	1.75
218916923.01	7	11.47	28.382	10.0	9.7	G6	0.89
219388192.01	7	12.34	5.293	10.0	12.8	G1	1.17
219703368.01	7	13.22	1.722	0.1	11.7	K3	10.7
220187552.01	8	12.84	17.1	27.0	7.6	M0	0.43
220228500.01	8	13.42§	2.505	1.8	3.5	G8	0.75
220256496.01	8	12.87	0.67	0.3	1.5	G8	0.79
220292715.01	8	12.21	41.6	2.8	4.1	K2	0.71
220294712.01	8	12.26	23.61	0.8	3.7	F9	1.21

Table 3.6: *K2* Candidate List [cont.]

EPIC ID	Camp	Kepmag	Period [d]	Depth [ppt]	R_p [$R_\oplus$]	Spec Type	R_s [$R_\odot$)]
220303276.01	8	10.93	4.046	7.7	15.1	F7	1.58
220376054.01	8	11.6	8.595	0.3	1.9	G3	0.99
220376864.01	8	14.49	60.6	4.5	2.6	M1	0.36
220395416.01	8	11.91	45.6	1.7	4.7	G2	1.04
220400525.01	8	13.75	57.8	7.0	6.9	K2	0.75
220431824.01	8	13.0	9.073	16.0	12.3	G6	0.89
220436208.01	8	13.92	5.236	1.3	3.7	G3	0.94
220503236.01	8	12.71	8.68	0.6	3.0	G1	1.12
220504338.01	8	13.51	5.818	8.0	8.7	G4	0.9
220510874.01	8	13.02	7.475	0.5	3.2	G0	1.29
220522262.01	8	14.76	8.688	11.0	7.5	K4	0.66
220535923.01	8	13.68	57.3	1.5	4.4	G2	1.05
220554210.01	8	13.72	4.171	0.8	2.6	G5	0.84
220565349.01	8	14.12	21.78	25.0	15.1	G8	0.87
220621788.01	8	11.75	13.681	0.5	2.4	G3	0.98
220629489.01	8	14.12	1.921	1.6	3.3	K1	0.76
220674823.01	8	11.96	13.34	1.0	3.4	G2	0.99
220674823.02	8	11.96	0.571	0.3	1.9	G2	0.99
220676213.01	8	10.53	15	2.5	3.9	K2	0.72
220696233.01	8	15.54	57.5	15.0	5.6	M0	0.42
228706256.01	10	12.3	1.364	0.1	1.4	F9	1.31
228735255.01	10	12.48	6.569	15.0	14.6	G3	1.09
228758948.01	10	12.87	12.202	1.7	5.1	G0	1.14
228801451.01	10	10.96	0.584	0.4	1.9	G7	0.85
228801451.02	10	10.96	24.982	0.7	2.5	G7	0.85
228952747.01	10	12.22	1.056	0.1	0.5	K9	0.44
228974324.01	10	12.87	1.606	0.3	0.5	M2	0.28
229004835.01	10	10.15	16.142	0.5	2.5	G0	1.02
229020361.01	10	11.81	1.706	0.05	1.1	F7	1.37
229024057.01	10	12.93	3.151	20.0	18.0	G1	1.16
229049184.01	10	12.0	1.645	0.04	1.0	F6	1.5
229119550.01	10	9.97	3.744	0.1	4.9	K0	4.51
229133720.01	10	11.48	4.036	1.0	8.1	K1	2.34

- **HD 106315b & HD 106315c** - Two sub-Neptune mass planets with very different densities (5.1g.cm^{-3} & 0.9g.cm^{-3}, Barros et al., 2017)

In the following section we study another of these candidates which has been confirmed: K2-110b (Osborn et al., 2017b).

3.3 Observations, data reduction and analysis of K2-110b

3.3.1 K2 Photometry

K2-110 (previously EPIC212521166 or EPIC-1166) was observed during Campaign 6 of the *K2* mission. We initially downloaded the pixel data from the Mikulski Archive for Space Telescopes (MAST)[3] and used a modified version of the CoRoT imagette pipeline to extract the light curve (Barros et al., 2016).

Based on signal-to-noise of each pixel we computed an optimal aperture of 25 pixels. The background was estimated using the 3σ clipped median of all the pixels in the image and subtracted. We also calculated the centroid using the Modified Moment Method by Stone (1989). In order to correct for flux variations due to the star's apparent motion on the CCD we used a self-flat-fielding procedure similar to Vanderburg and Johnson (2014). This assumes the movement of the satellite was mainly in one direction, as described in Barros et al. (2016).

The detection of EPIC-1166 as a candidate is described in Section 3.2.3. It was also independently identified by Aigrain et al. (2016a) & Pope et al. (2016) although no detailed analysis was performed.

Gaussian processes were used to flatten the light curve. A combination of Exponential Square kernel and white noise kernels were applied to a light curve with the 0.15 days around each of the six transits removed to not influence the fit. Hyperparameters were trained by maximizing the likelihood of the Gaussian process on out-of-transit data, with resulting values of mean= 1.000037, white noise kernel amplitude $\ln(\sigma^2_{\rm WN}) = -19.64$ ($\sigma_{\rm WN}$ = 54ppm), exponential squared kernel amplitude $\ln(a) = -15.38$, and exponential squared kernel lengthscale $\ln(l) = 1.636$ Transit fitting was performed jointly with RVs and is described in section 2.4. The final light curve of K2-110 has mean out-of-transit RMS of 134 parts per million (ppm) per 30min cadence.

3.3.2 Radial velocity follow-up

We performed RV follow-up of the target star. A single exposure with the CORALIE spectrograph (Queloz et al., 2000) mounted on the EULER telescope at ESO La Silla obser-

[3] *http://archive.stsci.edu/kepler/data_search/search.php*

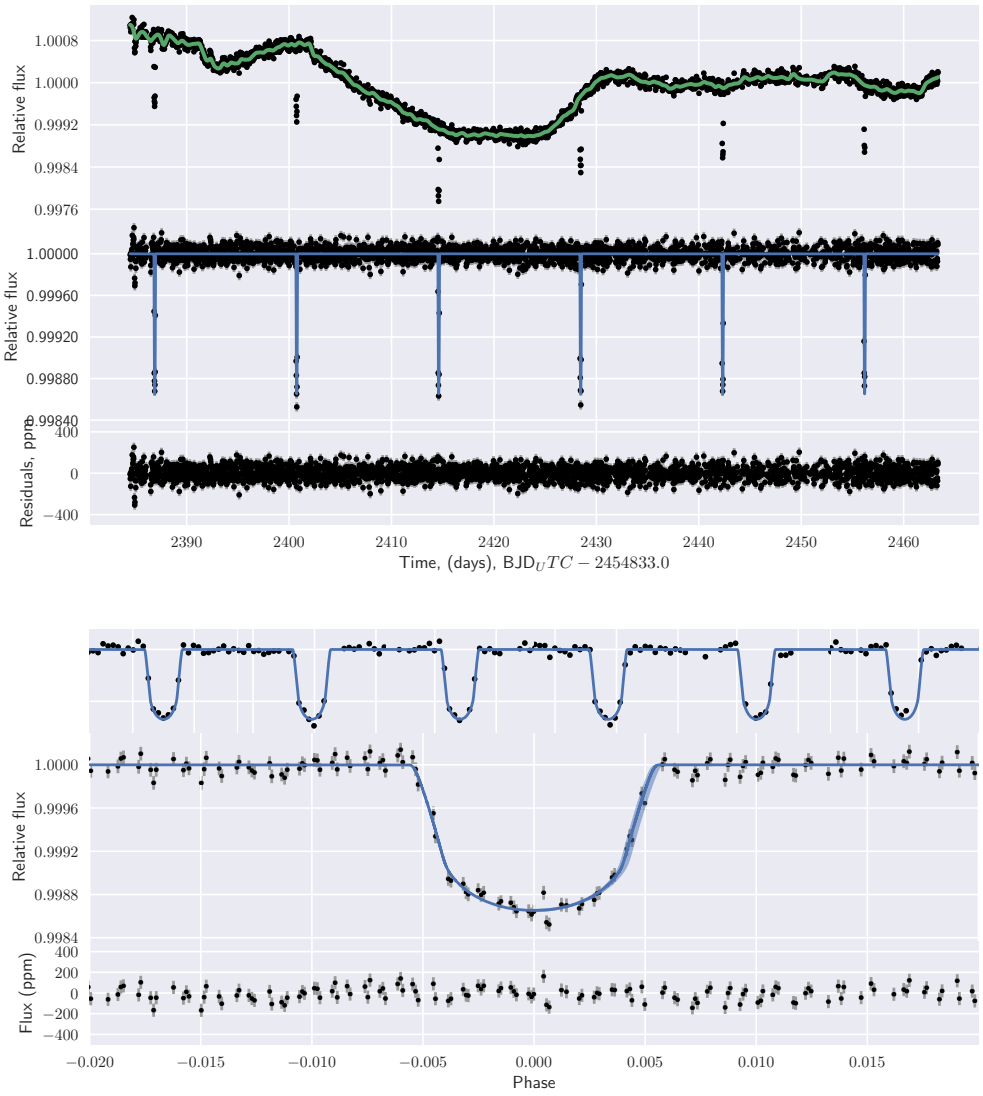

Figure 3.3: Transit light curve and model best-fit for K2-110 b. Detrended *K2* light curve; light curve smoothed with Gaussian Processes; best-fit transit model light curve residuals (upper panels; top from bottom); All six transits; Phase-folded unbinned light curve centred on transit with best-fit model in blue & best-fit region in light blue; Phase-folded model residuals (lower panels; top to bottom).

vatory, Chile confirmed that the target was suitable for precise radial velocities. A second exposure would have ruled out spectroscopic binaries but given the 14-d period of the orbit, this second epoch was not possible between the detection of the candidate in the *K2* data and the telescope scheduling.

The target was then observed with the HARPS spectrograph (Mayor et al., 2003), mounted on the 3.6m telescope at ESO La Silla observatory[4]. Seventeen exposures of 3600s in the obj_AB mode were secured on 13 nights from 2016-03-03 to 2016-08-10, with S/N per pixel at 5500Å from 25 to 57 leading to photon noise uncertainty in the range 1.2 – 3.0 m/s.

Eleven further spectra were also taken with the HARPS-N spectrograph (Cosentino et al., 2012), mounted on the 3.58m Telescopio Nazionale Galileo at ING La Palma observatory. These had a median exposure time of 1800s were secured on 11 nights from 2016-05-12 to 2016-06-25, with S/N per pixel at order $n = 50$ (550nm) from 15 to 37. The HARPS-N exposures suffered from contamination of moonlight. This was corrected by subtracting the CCF of the spectrum of the sky (gathered with fiber B) from the CCF of the target star (gathered with fiber A), after recomputing the former with the same flux correction coefficients of the latter (see Malavolta et al. (2017) for details). Although contamination corrections were applied to all HARPS-N measurements, only six of these had $|\Delta\mathrm{RV}| > \sigma_{RV}$, with four being corrected by more than $2\sigma_{RV}$ (see Table 4)

We computed the RVs from each high-resolution spectrum using weighted cross-correlation with a K5 template (Baranne et al., 1996; Pepe et al., 2000) as implemented by the HARPS and HARPS-N pipelines. RV uncertainties were determined as described in Bouchy et al. (2001). They range from 1.1 to 8.8 ms^{-1}. The pipeline also computed the averaged line profile full-width half maximum (FWHM), bisector span (BIS) and the log R'HK, defined in Section 1.3. All these data are reported with uncertainties in appendix Table 3.10.

3.3.3 Host Star Parameters

Stellar atmospheric parameters and [Fe/H] were derived in LTE using a recent version of the MOOG code (Sneden, 1973) and a set of plane-parallel ATLAS9 model atmospheres (Kurucz, 1993), as described in Sousa et al. (2011). The full spectroscopic analysis is based on the Equivalent Widths (EWs) of 103 Fe I and 15 Fe II weak lines by imposing ionization and excitation equilibrium. The line-list used was taken from Tsantaki et al. (2013), and is adapted for stars with $T_{\mathrm{eff}} < 5200$K. The stellar parameters derived using this methodology were shown to be in line with the ones derived using other methods, e.g. interferometry and Infra-Red Flux Method (IRFM) (see Santos et al., 2013, for details). The methodology

[4]ESO programme ID: 096.C-0657

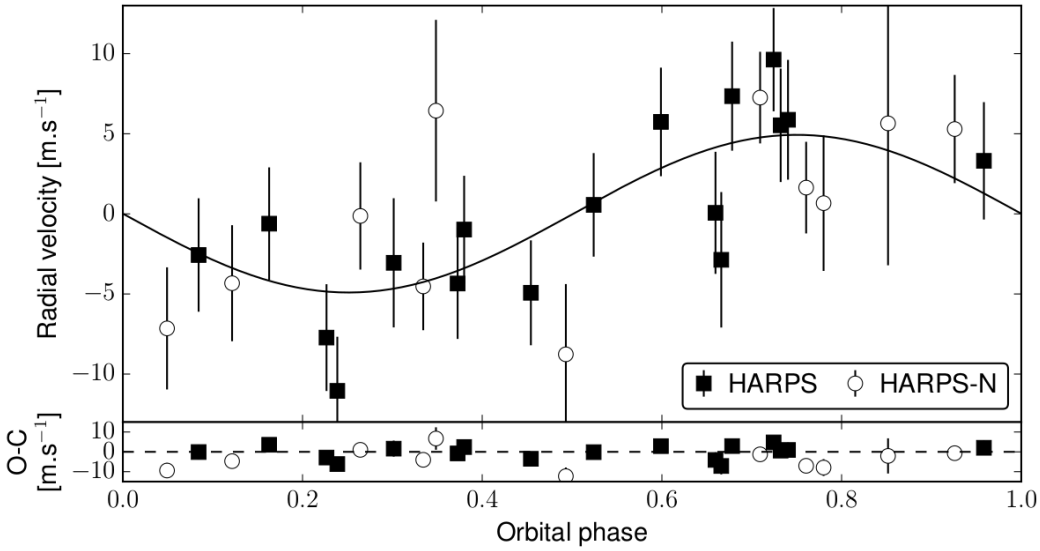

Figure 3.4: RVs taken by HARPS and HARPS-N, phased to the 13.86d period as determined from the *K2* light curve. The best model is also displayed together with the residuals.

is further described in e.g. Adibekyan et al. (2016) and Santos et al. (2015). Our derived values of Teff (4960 ± 60K), log(g) (4.58 ± 0.13) and [Fe/H] (-0.34 ± 0.03) are used as priors in `PASTIS` (see Section 2.5 and Table 5) and therefore are re-derived in a self-consistent manner with all observed stellar information. We also find a log R'HK of -4.992+/-0.002. Results are shown in Table 3.9 and chemical abundances for different species are shown in Table 3.7.

3.3.4 PASTIS Analysis

We jointly analysed the HARPS/HARPS-N RVs, *K2* photometric light curve within 3h of the transit midtime and the spectral energy distribution (SED) as observed by the APASS, 2-MASS and WISE surveys (Munari et al., 2014; Cutri et al., 2014) using the `PASTIS` software (Díaz et al., 2014; Santerne et al., 2015). It models the light curve using the `jktebop` package (Southworth, 2008) assuming an oversampling factor (Kipping, 2010) of 30 to account for the long integration time of the K2 data. The SED was modeled using the BT-SETTL library of stellar atmosphere (Allard et al., 2012). The RVs were modeled with a Keplerian orbit. A Markov Chain Monte Carlo (MCMC) method was used to analyse the data. The results from the spectral analysis described in Section 3.3.3 were used as priors for the host star. The spectroscopic parameters were converted into fundamental stellar parameters in the MCMC using the Darthmouth evolution tracks (Dotter et al., 2008). For detail on the priors used see Table 3.11.

Table 3.7: Stellar abundances. [Cr/H] & [Ti/H] are the average abundance of neutral and ionized lines. Mg/Si = $10^{A(Mg)-A(Si)}$. A(Li)=log $[N(Li)/N(H)]$ + 12.

Elem	[X/H]	error	Elem	[X/H]	error
O I	0.009	0.080	Mn I	-0.331	0.077
Na I	-0.334	0.046	Co I	-0.272	0.031
Mg I	-0.274	0.060	Cu I	−0.305	0.048
Al I	-0.157	0.035	Zn I	−0.323	0.101
Si I	-0.260	0.039	Sr I	−0.338	0.050
Ca I	-0.223	0.062	Y II	-0.425	0.093
Sc II	-0.276	0.064	Zr II	−0.290	0.080
Ce II	−0.131	0.327	Ba II	−0.452	0.010
Cr	-0.279	0.074	Ti	-0.205	0.092
[Fe/H]	-0.343	3.2×10^{-2}	[O/Fe]	0.35	0.08
Mg/Si	1.191	–	A(Li)	< 0.2	–

Parameter	value and uncertainty
Stellar Information	
EPIC	212521166
R.A.	13h 49m 23.890s
Dec	-12d 17m 04.16s
2MASS ID	2MASS J13492388-1217042
$\mu_{\text{R.A.}}$	42.6 ± 1.1 mas/yr
μ_{Dec}	−101.2 ± 1.4 mas/yr
Photometric Magnitudes	
B	12.834 ± 0.05
V	11.91 ± 0.07
Kep	11.59
J	10.184 ± 0.022
H	9.641 ± 0.023
K	9.607 ± 0.024
WISE 3.4μm	9.521 ± 0.024
WISE 4.6μm	9.577 ± 0.020
WISE 12μm	9.479 ± 0.038
WISE 22μm	8.695

Table 3.8: Stellar Information for K2-110. Magnitudes from ExoFOP-K2.

Parameter	value and uncertainty
Stellar parameters	
Stellar mass $M_\star$ [$M_\odot$]	0.738 ± 0.018
Stellar radius $R_\star$ [$R_\odot$]	0.713 ± 0.020
Stellar age τ [Gyr]	8 ± 3
Distance d [pc]	118.0 ± 3.6
Reddening E(B-V) [mag]	$0.019^{+0.019}_{-0.013}$
Systemic RV υ_0 [km.s^{-1}]	-21.6331 $\pm 9 \times 10^{-4}$
Effective temperature Teff [K]	5010 ± 50
Surface gravity log$g$ [g.cm^{-2}]	4.60 ± 0.03
Iron abundance [Fe/H] [dex]	-0.34 ± 0.03
Spectral type	K3V
Orbital parameters	
Period P [d]	$13.86375 \pm 2.6\times10^{-4}$
Transit epoch T_0 [BJD_{TDB}]	$2457275.32992 \pm 6.1\times10^{-4}$
Orbital eccentricity e	0.079 ± 0.07
Argument of periastron ω [°]	90^{+180}_{-64}
Inclination i [°]	$89.35^{+0.41}_{-0.24}$
Semi-major axis a [AU]	$0.1021 \pm 8\times10^{-4}$
Transit & radial velocity parameters	
System scale $a/R_\star$	30.8 ± 1.0
Impact parameter b	$0.34^{+0.14}_{-0.22}$
Transit duration T_{14} [h]	3.22 ± 0.03
Planet-to-star radius ratio k_r	$0.0333 \pm 6.6\times10^{-4}$
Limb darkening u_a	$0.5322 \pm 1.2 \times 10^{-2}$
Limb darkening u_b	$0.1787 \pm 8 \times 10^{-3}$
RV amplitude K m.s^{-1}]	5.5 ± 1.1
HARPS-N RV jitter [m.s^{-1}]	3 ± 2
HARPS RV jitter [m.s^{-1}]	3.1 ± 1
Instrument offset [m.s^{-1}]	4.2 ± 1.8
K2 contamination [flux, ppt]	3.4^{+4}_{-2}
K2 jitter [flux, ppm]	40 ± 4.6
SED jitter [mag]	0.02 ± 0.02
Planet parameters	
Planet mass M_p [$M_\oplus$]	16.7 ± 3.2
Planet radius R_p [$R_\oplus$]	2.592 ± 0.098
Planet density ρ_p [g.cm^{-3}]	5.2 ± 1.2
Equilibrium temperature T_{eq} [K]	640 ± 20

Table 3.9: Physical parameters of the K2-110 system. All the uncertainties provided here are only the statistical ones. Errors on the models are not considered, as they are unknown. Stellar parameters are derived from the combined analysis of the data and not from the spectral analysis. We assumed $R_\odot$=695 508km, $M_\odot$=1.98842×10^{30}kg, $R_\oplus$=6 378 137m, $M_\oplus$=5.9736×10^{24}kg, and 1AU=149 597 870.7km.

We used uninformative priors for most of the parameters. Exception include the stellar atmospheric parameters, for which we used the inputs of Section 3.3.3; the orbital eccentricity, for which we choose a Beta distribution (Kipping, 2013); and the orbital ephemeris, for which we choose uniform distributions centered on the values found by the detection pipeline. Table 3.11 shows the priors on all parameters in the model.

We ran 20 independent MCMCs of 3×10^5 iterations randomly started from the joint prior distribution. We then removed the burn-in phase before merging the converged chains. The residuals of the RV have a RMS at the level of 3.0ms^{-1}, which is about twice the median photon noise.

Initially, HARPS RV residuals were seen to exhibit a clear correlation with the Mount Wilson S index with a Pearson correlation coefficient of $\rho_{S_{\rm MW}} = 0.74 \pm 0.07$, although no correlation was found between the radial velocity residuals and the FWHM or the bisector with Pearson test values of $\rho_{\rm FWHM} = -0.24 \pm 0.07$ and $\rho_{\rm BIS} = 0.06 \pm 0.04$. We corrected the RVs for this correlation effect, similarly to that described by Tuomi et al. (2014). However, on collecting more data and adding the HARPS-N observations, the significance of the correlation was reduced, and we removed this correction for RVs based on S-index.

Complete stellar and planetary outputs of `PASTIS` are reported in Table 3.9 and the priors used are reported in 3.11.

3.4 Discussion of EPIC-1166b

3.4.1 Validity

The presence of a RV signal in-phase with (and at a similar amplitude to) that expected from the transit detection is extremely strong evidence for a planet. However, we also performed additional tests to ensure that the signal was not due to, e.g. a blended eclipsing binary.

Using the cross-correlation function with which we computed RVs, we can exclude to 3-sigma all secondaries with $\Delta mag < 6.5$, assuming the companion is spectrally resolved (ie $v_0 > 2.7\text{kms}^{-1}$), and has a similar Teff, metallicity, and rotation (Santerne et al., 2015). We can also rule out close companions within 3 arcsec from archival survey data (Cutri et al., 2003; Zacharias et al., 2004). Although *K2*'s pixel drift is significant, we compared the median in-transit centroid positions with the median out-of-transit (after correcting for pixel drift). We used bootstrapping on 200 randomly-selected transit positions to generate uncertainties on any centroid shift, finding no centroid shift in the x & y directions of more than 0.86" and 0.28" (2-sigma limits, Fig. 3.5). Hence, this further reduces the likelihood that we are observing a blended eclipsing binary.

The BIS and FWHM (defined in Section 1.3) do not exhibit significant variation

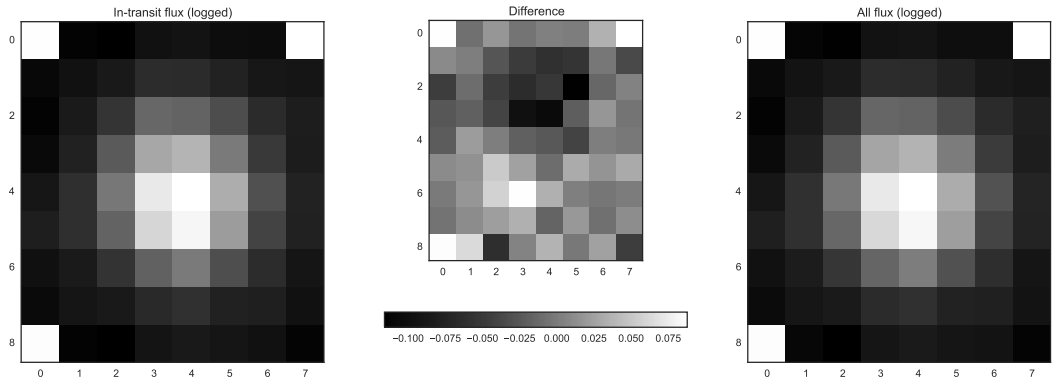

Figure 3.5: In-transit and out-of-transit median flux from the Target Pixel File compared. The central panel difference image has rescaled, but shows no significant deviation during transit.

with RMS at the level of 6ms^{-1} and 5ms^{-1}, respectively. No significant correlation is found between these spectroscopic diagnoses and the radial velocity with a Pearson test of 0.01 ± 0.02, and 0.13 ± 0.02, respectively. This strongly supports the planetary nature of the detection (Santerne et al., 2015). Small Neptunes also exhibit the lowest false positive rates (6.7% in *Kepler*, Fressin et al. 2013).

Together all these are extremely good evidence that the signal is planetary rather than from a false positive, and enables us to designate this planet as confirmed.

3.4.2 Age & Rotation

From the joint orbital analysis of RVs, photometry and stellar evolution tracks, with posterior samples cut such that age < 13.5Gyr, we derived a stellar age of 8 ± 5 Gyr.

No clear rotational signal is detected in the light curve, although variation on the order of weeks is seen (see Fig. 3.3) which could be suggestive of slow starspot rotation. Using the candidate 50 ± 5d signal seen in the Lomb-Scargle periodogram of the light curve as the stellar rotation period, the gyro-chronology relation of Angus et al. (2015) would suggest an age of 11 ± 5Gyr. A slow stellar rotation and old age are also supported by the upper limit of v_{rot} measured from HARPS spectra (< 2.7kms^{-1}, P_{min} > 9.2d), and the non-detection of Lithium ([Li/H]< 0.2).

Recently, Nissen (2015) showed that [Y/Mg] ratio can be used to estimate stellar ages. This result was later confirmed by Tucci Maia et al. (2016), the age relation from which suggests an age of 8.1 ± 2.8 Gyr for K2-110. Hence, all methods point this star being an old field star, which may also explain its low metallicity.

3.4.3 Stellar Composition

The low metallicity of K2-110 is in agreement with the hypothesis that small planets are more likely to form around metal-poor host stars (Buchhave et al., 2012). However, the large ($16M_\oplus$) interior mass appears anomalously large for such a metal-poor star, sitting on the mass-metallicity upper boundary as found by Courcol et al. (2016) for Neptunian exoplanets. Unusually, K2-110 doesn't show an enhancement in α-elements (e.g. Si, Mg, etc) as compared to other metal-poor planet hosts (Adibekyan et al., 2012) though it does show enhancement in the pure α-element oxygen ([O/Fe]=0.35).

3.4.4 TTVs and other planets

Using a transit model generated from our `PASTIS` best fit, we searched for transit timing variations by iteratively shifting the flux model over each individual transit with a resolution of 2.6s. We detect no significant TTVs and are able to rule out their presence above an amplitude of 6 minutes to 3σ (see Fig. 3.6).

We also searched for potential other transiting planets in the system but found no significant signal. Injection & retrieval tests enable us to rule out to > 90% confidence the presence of co-planar planets with orbits < 30d and radii > $1R_\oplus$ (see Fig. 3.6). This, along with its location at the metallicity-mass upper limit, may suggest that K2-110 b is a solitary planet containing the majority of K2-110's protoplanetary disk mass.

3.4.5 Composition and Formation

With a mass of $16.7 \pm 3.2M_\oplus$ and a radius of $2.6 \pm 0.1R_\oplus$, this planet stands out as being one of the most massive exoplanets with a sub-Neptune radius (Fig. 3.7) detected so far.

Despite an Earth-like density of 5.2 ± 1.2 gcm^{-3}, a 2-layer iron-silicate composition model is unable to explain the density of K2-110 b. Instead, either low-density volatiles such as water, an H-He atmosphere, or a combination of both must be present. We explore the possibility of these degenerate compositions here. Using the 3-layer solid exoplanet composition model of Zeng and Sasselov (2013)[5], we compute that a $9M_\oplus$ Earth-like interior of $\sim$ 70% $MgSiO_3$ and $\sim$ 30% Fe covered by $8.7M_\oplus$ of H_2O can explain the mass and radius of K2-110 b. As well as surface molecular water, such a model would also require high-pressure water phases Ice VII, Ice X and superionic fluid (Zeng and Sasselov, 2014).

In the alternate and more likely case, the models of both Adams et al. (2008) and Lopez and Fortney (2014) show that an earth-like $16.5M_\oplus$ interior of iron core and silicate mantle can host a $0.2M_\oplus$, $\sim 0.4R_\oplus$ H-He atmosphere to produce the equivalent bulk density. Intermediate compositions between these two boundary models are also possible. This

[5]Accessed from https://www.cfa.harvard.edu/ lzeng/

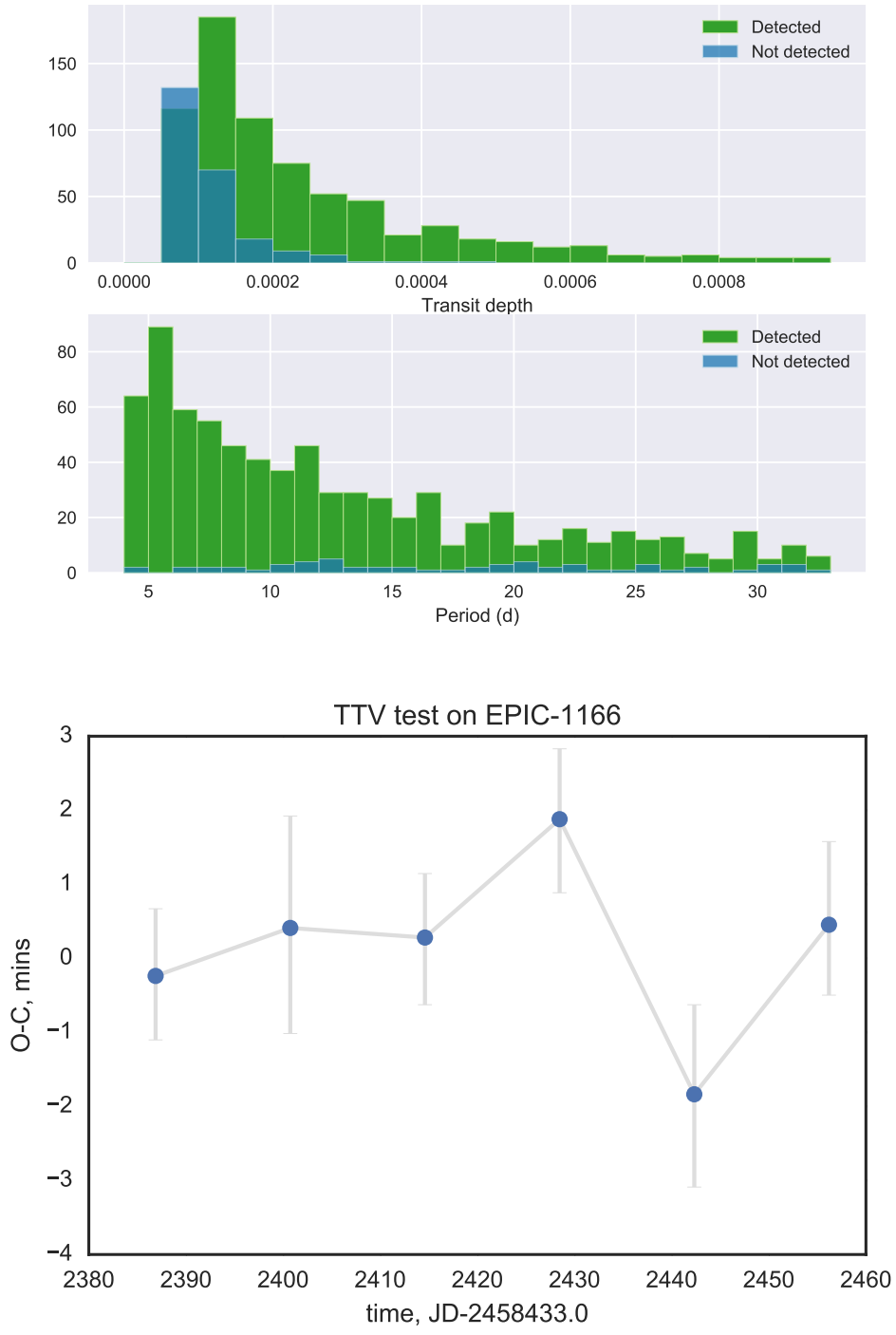

Figure 3.6: **Above:** Histograms of the 750 planet injection and retrieval tests as a function of transit depth and planet period. **Below:** Best-fit transit times for K2-110 show no TTVs at the level of 5 minutes.

suggests the mass fraction of hydrogen is likely ≤1% for K2-110 b. This places it firmly in the mini-Neptune regime (2-3$R_\oplus$) which Fulton et al. (2017) found to be a distinct and numerous population of planet, with around 22% ± 6% of FGK stars hosting such a planet on orbits <100d.

The growing population of high-density planets in the regime from 10 to 20 $M_\oplus$ also suggests that planets can exist in this region without accreting significant hydrogen. This may therefore suggest that the minimum core accretion mass of $\sim 10M_\oplus$ is underestimated, the planet formed after the disc was dissipated, or that processes exist to remove gaseous atmospheres post-accretion. The unusual density of this planet also suggests that mass-radius relations (e.g. Weiss and Marcy, 2014), should be used with extreme caution in the regime between terrestrial planets and gas giants (e.g. Figure 3.7).

To investigate whether K2-110 b could have been formed with a substantial atmosphere that later evaporated, we looked at the potential mass loss from EUV. We use the calculations of Lecavelier des Étangs (2007) to calculate a mass loss rate (equation 15):

$$\dot{m}_{\rm EUV} = 3.7 \times 10^7 {\rm gs}^1 \left(\frac{F_{\rm EUV}(1{\rm AU})}{4.6{\rm ergcm}^{-2}s^{-1}}\right)\left(\frac{R_p}{R_{\rm Jup}}\right)^3 \left(\frac{M_p}{M_{\rm Jup}}\right)^{0.5} \left(\frac{a}{1AU}\right)^{-2} \tag{3.1}$$

Where $F_{\rm EUV}$ was that of the most EUV-luminous K-type star in the sample ($14.7 erg{\rm cm}^{-2}{\rm s}^{-1}$), and the planetary parameters from the PASTIS best-fit, we obtain a value of $2 \times 10^9 {\rm gs}^{-1}$ (eq. 15), which corresponds to an upper limit of $0.13M_\oplus$ over 10Gyr. An estimate of X-ray mass-loss rate computed from Eq. 16/Fig. 8 of Owen and Jackson (2012) suggests $4 \times 10^{10} {\rm gs}^{-1}$ which, over the likely 100Myr period after formation when K2-110 would have been producing X-rays (Jackson et al., 2012), could only have evaporated as much as 0.21 $M_\oplus$. Therefore, using the Hydrogen atmosphere models mentioned previously, the host star is likely incapable of evaporating more than $0.3M_\oplus$ of Hydrogen from K2-110 b (which is equivalent to less than $0.3R_\oplus$). Thus evaporation is unlikely to have significantly contributed to the high density we see today and K2-110 b likely formed dense.

However, to form K2-110 b *in situ* at 0.1 AU would require a disc mass enhanced by 50 compared to solar values (Schlichting, 2014). Hence, either material from more distant parts of the disk migrated inwards to build K2-110 b (e.g. Chatterjee and Tan, 2013; Hansen and Murray, 2012), or the planet itself formed far out in the disc and migrated inwards (e.g. McNeil and Nelson, 2010; Kley and Nelson, 2012).

In the latter case, migration could have occurred through dynamic scattering, or through disc migration. Better constraints on orbital eccentricity ($e = 0.08 \pm 0.07$ in this analysis) could help point such an orbital migration mechanism, however we can rule out high eccentricities ($e > 0.25$) typical of warm exoplanets caused by Kozai migration (Dawson and Chiang, 2014). On its relatively wide orbit of 14d, K2-110 b is also unlikely to

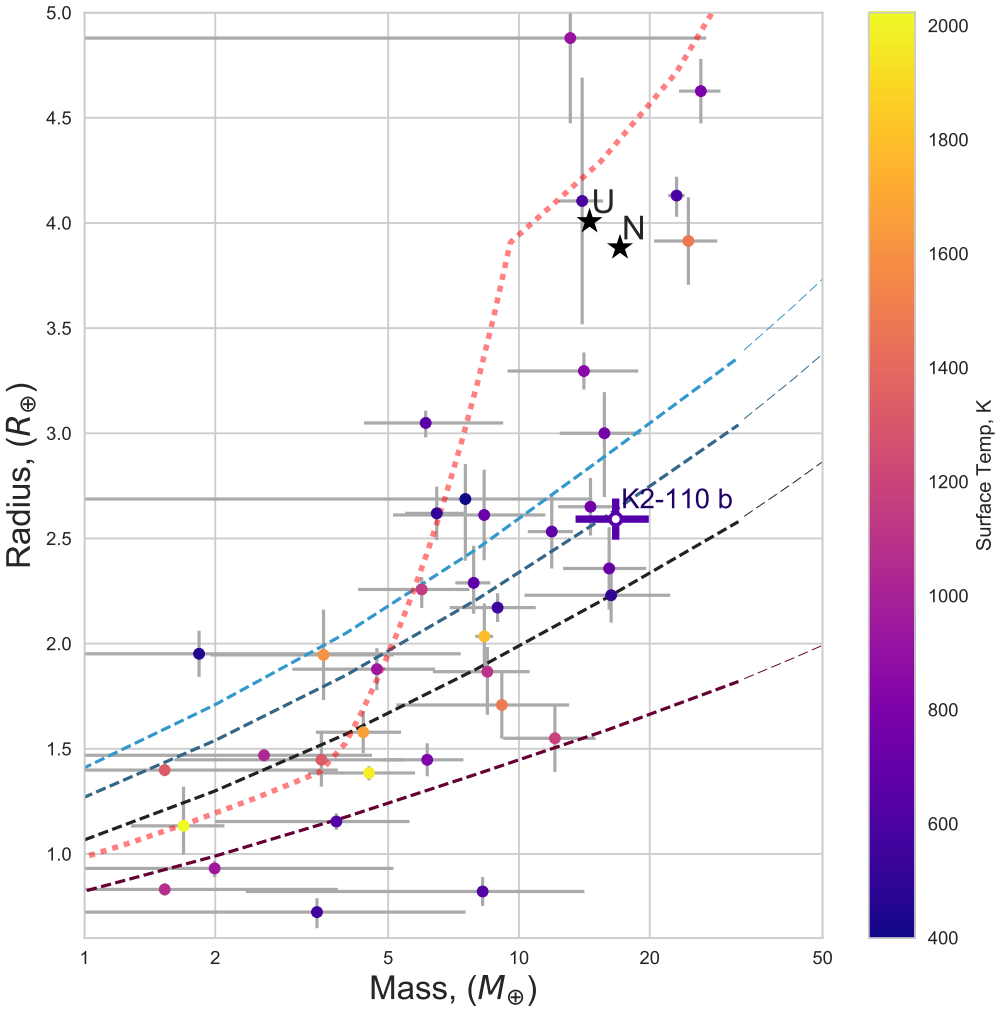

Figure 3.7: K2-110 b (solid cross, right) compared to other super-Earth and Neptunian planets (data from Han et al. (2014); Marcy et al. (2014)). Mass-radius relations adapted from Zeng and Sasselov (2013) for 100%-Fe, Earth-like, 50%-water and 100% water compositions (dashed lines from bottom to top). A mass-radius relation for small exoplanets (Weiss and Marcy, 2014) is also show (fine dashes).

have been to acted on by stellar tidal forces; a necessary component of dynamic migration (Fabrycky and Tremaine, 2007). Therefore, if K2-110 b migrated to its current position low-eccentricity disc migration is more likely. However, the lack of a thick H atmosphere on K2-110 b is at odds with the migration of a > 10 $M_\oplus$ planet through a gaseous disc.

On the other hand, models of the migration, impact and accretion of systems of compact planets or planetary embryos (Ida and Lin, 2008; Boley et al., 2015) are able to explain both K2-110 b's orbit and its lack of significant hydrogen atmosphere (Liu et al., 2015; Inamdar and Schlichting, 2016). Improved orbital parameter measurements (e.g. misalignment & eccentricity) and statistical analyses of exoplanet populations could disentangle which scenario occurred.

3.5 Conclusion

We have detected 199 exoplanet candidates from eleven campaigns of *K2*, including 9 which were confirmed as a direct result, and many more for which follow-up is ongoing. Unlike from the *Kepler* primary mission, we have detected a large number of planets around relatively bright (V< 13) stars in *K2*. These could enable a range of follow-up precise mass measurements, atmospheric characterisation, orbital studies (e.g. Rossiter-McLaughlin and Doppler tomography), etc.

One such planet is the 2.6 ± 0.1 $R_\oplus$ K2-110b. RV observations with HARPS have confirmed this object, on a 13.9d orbit around an early K-dwarf, as a planet and measured its mass to be 16.7 ± 3.2 $M_\oplus$. The corresponding bulk density suggests K2-110b has a large rocky interior and is hydrogen-poor, with <1% of it's mass in a hydrogen atmosphere. Alternatively, the planet could be volatile-rich, with up to 9 $M_\oplus$ of H_2O. Our analysis means K2-110b is now one of the best-characterised sub-Neptune planets with a radius and mass constrained to 4% and 20% respectively. Future observations will improve our understanding of the bulk composition and migration history of this planet.

Table 3.10: Raw radial velocity data from HARPS (upper section) and HARPS-N (lower section). Typical errors on the FWHM and BIS were 2-5m.s^{-1}for HARPS and 4-10m.s^{-1}for HARPS-N. Typical log R'_{HK}errors were 0.02-0.05 for HARPS and 0.05-0.11 for HARPS-N.

Time [UTC]	RV [m.s^{-1}]	σ RV [m.s^{-1}]	FWHM [m.s^{-1}]	BIS [m.s^{-1}]	log R'_{HK} [dex]	S/N 50 [dex]	Texp [s]	ΔRV_{moon} [m.s^{-1}]
57451.737	-21623.6	1.2	5940	19	-4.940	68.1	3600	-
57457.817	-21633.8	1.8	5936	6	-5.027	45.9	3600	-
57458.702	-21640.9	1.5	5942	12	-4.994	56.1	3600	-
57458.869	-21644.2	1.6	5937	18	-5.029	53.8	3600	-
57459.739	-21636.2	2.7	5930	16	-4.985	33.5	3600	-
57460.725	-21637.5	1.7	5946	23	-4.980	48.5	3600	-
57460.826	-21634.2	1.5	5943	26	-4.993	54.9	3600	-
57461.855	-21638.1	1.3	5943	15	-5.034	65.2	3600	-
57462.825	-21632.6	1.2	5944	22	-4.995	70.3	3600	-
57463.862	-21627.4	1.6	5939	18	-5.006	54.2	3600	-
57464.704	-21633.1	2.4	5935	14	-5.103	36.9	3600	-
57464.793	-21636.1	3.0	5947	24	-5.132	30.3	3600	-
57465.710	-21627.7	1.9	5946	23	-5.017	44.0	3600	-
57465.823	-21627.3	2.2	5947	7	-4.978	38.0	3600	-
57478.825	-21625.8	1.6	5936	14	-5.037	52.7	3600	-
57567.639	-21635.8	1.9	5984	19	-5.094	48.3	3600	-
57607.484	-21629.9	2.1	5948	22	-4.959	42.4	3600	-
57521.558	-21635.3	2.7	5867	15	-4.856	36.6	1800	0.18
57525.560	-21644.1	3.7	5849	21	-4.921	28.2	1800	2.99
57526.564	-21641.3	3.5	5841	22	-4.972	29.2	1800	2.05
57528.543	-21637.1	3.2	5908	82	-5.000	32.9	1800	28.34
57529.513	-21641.5	2.5	5879	42	-4.945	38.5	1800	10.55
57557.437	-21630.5	5.6	5899	-19	-5.007	20.5	1800	-36.54
57559.442	-21645.7	4.3	5903	6	-4.862	25.8	1800	-31.28
57562.439	-21629.7	2.7	5867	5	-4.943	37.1	1800	-4.07
57563.419	-21636.3	4.1	5860	13	-4.882	26.2	1800	-1.42
57564.413	-21631.3	8.8	5836	42	-4.802	15.3	1800	15.07
57565.442	-21631.6	3.2	5857	5	-5.001	32.1	1800	0.9

Parameter	Prior	Posterior
Orbital parameters		
Orbital period P [d]	$\mathscr{U}(13.8; 13.9)$	$13.86375 \pm 2.6\times10^{-4}$
Transit epoch T_0 [BJD_{TDB}] - 2.45×10^6	$\mathscr{U}(7275.2; 7275.5)$	$7275.32991 \pm 6.3\times10^{-4}$
Orbital eccentricity e	$\beta(0.867; 3.03)$	0.091 ± 0.089
Argument of periastron ω [°]	$\mathscr{U}(0; 360)$	90^{+180}_{-64}
Inclination i [°]	$\mathscr{S}(70; 90)$	$89.35^{+0.41}_{-0.24}$
Planetary parameters		
Radial velocity amplitude K [$m.s^{-1}$]	$\mathscr{U}(0; 1000)$	5.5 ± 1.1
Planet-to-star radius ratio k_r	$\mathscr{U}(0; 1)$	$0.0333 \pm 6.6 \times 10^{-4}$
Stellar parameters		
Effective temperature T_{eff} [K]	$\mathscr{N}(4960 : 60)$	5010 ± 50
Surface gravity log g [$g.cm^{-2}$]	$\mathscr{N}(4.58; 0.13)$	4.60 ± 0.03
Iron abundance [Fe/H] [dex]	$\mathscr{N}(-0.34; 0.03)$	-0.34 ± 0.03
Reddening E(B-V) [mag]	$\mathscr{U}(0; 1)$	$0.019^{+0.019}_{-0.013}$
Systemic radial velocity υ_0 [$km.s^{-1}$]	$\mathscr{U}(-25, -15)$	$-21.6331 \pm 9 \times 10^{-4}$
Distance to Earth d [pc]	$\mathscr{P}(2; 10; 1000)$	118.0 ± 3.6
Instrumental parameters		
HARPS radial velocity jitter [$m.s^{-1}$]	$\mathscr{U}(0; 1000)$	3.1 ± 1.0
HARPS-N radial velocity jitter [$m.s^{-1}$]	$\mathscr{U}(0; 1000)$	3.2 ± 2.3
HARPS – HARPS-N radial velocity offset [$m.s^{-1}$]	$\mathscr{U}(-100; 100)$	-4.2 ± 1.8
SED jitter [mag]	$\mathscr{U}(0; 1)$	0.021 ± 0.019
K2 jitter [ppm]	$\mathscr{U}(0; 10000)$	41.2 ± 4.6
K2 contamination [ppt]	$\mathscr{N}_{\mathscr{U}}(0; 5; 0; 100)$	$3.4^{+3.6}_{-2.4}$

Table 3.11: List of free parameters used in the PASTIS analysis of the light curves, radial velocities and SED with their associated prior and posterior distribution. $\mathscr{N}(\mu; \sigma^2)$ is a normal distribution with mean μ and width σ^2, $\mathscr{U}(a; b)$ is a uniform distribution between a and b, $\mathscr{N}_{\mathscr{U}}(\mu; \sigma^2, a, b)$ is a normal distribution with mean μ and width σ^2 multiplied with a uniform distribution between a and b, $\mathscr{S}(a, b)$ is a sine distribution between a and b, $\beta(a; b)$ is a Beta distribution with parameters a and b, and $\mathscr{P}(n; a; b)$ is a power-law distribution of exponent n between a and b. The choice of prior for the orbital eccentricity is described in Kipping (2013).

Chapter 4

The Detectability of Single Transiting Exoplanets and Deep Eclipses with WASP and NGTS Photometry

"Astronomers must have the easiest job on the plant; convincing the gullible of alleged findings that they can never in our life times ever quantify, or have to prove. With the aid of some pretty "artist interpretations", and few statements riddles with could, might and possibly suggests, and the next 10 years of funding is in the bag! Nice work if you can get it!!!!!!"

The Good Doctor66, Daily Mail

Note: The following chapter details the creation of a detection code for single transits, injection and retrieval results in both WASP and NGTS datasets with that code, and the detection of candidate transits in WASP and NGTS photometry. It is entirely the author's work and has yet to be published.

4.1 Introduction

While space-based missions such as Kepler or K2 have the benefit of nearly 100% phase coverage and operate above the atmosphere and its negative effects on photometry, ground-based photometry has produced many transiting planets orbiting a far brighter population of stars and from observatories with far lower costs. Where they are lacking, however, is in long-period planets, with the median orbital period of such worlds only 3.25 days and the longest transiting planet detected from the ground only 16.2d (HATS-17 b Brahm et al., 2016). This is firstly due to the poor phase coverage from wide-field, ground-based transit surveys, which means that both the longer transits are less likely to be fully covered by observations, but also that observations of multiple transits require far longer baselines than with continuous observations. This is coupled with higher levels of correlated noise (see Section 1.2.5) which both mimic transit signals, and reduce the multiplicative gains that multiple transits provide (e.g. in BLS searches, see section 2.5). Hence, ground-based transit surveys are classically limited short-period planets that transit often.

The most precise observatories have the ability to detect the transits of giant planets from only a single transit. This includes more advanced surveys like NGTS and MEarth (Wheatley et al., 2013; Irwin et al., 2014). Surprisingly, older generation surveys are also able to reach this limit. In the case of WASP, moving from scanning multiple fields simultaneously to continuously "staring" at single fields has increased the number of datapoints (and therefore increased the signal-to-noise ratio) enough to detect exoplanets from single transits in the best cases. For example, a 12th magnitude star in WASP produces white noise of $\sim$1% per observation. In the classical observing mode of $\sim$8 observations per hour, a 2-hour transit has photometric uncertainty of 2.5ppt - enough to detect a 1% transit to only 4σ. Increasing the cadence by a factor of six improves the SNR by a factor of $\sqrt{6}$, or ~ 2.5, allowing 10σ detections of 1% transits, and much better limits on the shape and position of in- and egress.

In fact, the ability of ground-based surveys to detect and follow-up long-period planets has already been shown by MEarth. The 24.7 day period of LHS 1140 b was detected after follow-up of a single transit event (STE) found with MEarth in 2013 (Dittmann et al., 2017).

Phase coverage and precision are problematic for exoplanetary transits, which last for only a few hours and are typically close to the noise level of the telescopes. For events lasting longer than $\sim$1 night, and deeper than a few percent, ground-based transit surveys have far more capability than space-based surveys, covering more of the sky and often with multi-year baselines. Deep, long-duration eclipses are amenable to discovery by ground-based data, as has been shown with the detection of eclipsing circumstellar material (e.g.

Scott et al., 2014; Rodriguez et al., 2013, 2016a, , etc.). The objects can even be of planetary (J1407 Mamajek et al., 2012) or completely unknown (KIC 8462852 Boyajian et al., 2016) origins.

In this chapter I undertake a search of 36 fields of NGTS data taken from 2015 to 2017 and 38 fields of WASP Stare data taken from 2010 to 2013 for transiting planets. Further to this, 2 million lightcurves of WASP objects are searched for long-duration eclipses.

4.2 Methods

4.2.1 WASP Planet search data

The WASP survey and its data products are described in Section 2.6.1.

We performed the search on WASP Stare fields, which we defined as having an average of more than 240 points per night. WASP observes with a cadence of 1 point per 40 seconds. The stare fields gain signal to noise both due to the (up to 8x) increase in sampling and photometric stability as the telescopes maintain pointing better, reducing some of the systematic noise associated with the PSF moving on the detector. We accessed the photometry of all stars brighter than 12.25mag. This marks the limit for which, given only white (uncorrelated) noise, a 1%,1-hour long transit would be detectable to 7-σ. WASP stars typically have saturation problems for V<7.5, although few such stars existed in this dataset. In total, the search was run on 136,000 stars in 38 fields.

The light curves of each object were accessed from the sysrem output files and cleaned, first by normalising it to a median flux, then by cutting extremely high and low values (such that $0.025 > f_i > 50.0$). Anomalies were then removed according to the method described in section 2.8 and with a threshold of 3.5σ. Finally, artificially small errorbars ($\sigma_i <$ 2mmag) were scaled to the median of the absolute difference between datapoints (a proxy for white noise, σ_w), and points with errors larger than 99% of the rest of the lightcurve were also cut. To speed up the scan process, the lightcurves were then binned to 15 minute bins using a weighted average for each 15 minute segment with data in between the first measurement and the last. Bins with artificially small errorbars were once again scaled to the median absolute difference between binned flux values.

4.2.2 NGTS data

The NGTS survey and its data products are described in Section 2.6.2.WaspDefSec We used data from all 36 NGTS fields observed so far, accessing the files outputted from the `sysrem` detrending algorithm (see section 2.7). We derived a magnitude limit of R=14.25, fainter than WASP due to the increased collection area of the NGTS survey telescopes and

corresponding increased precision. 135,000 stars across all fields were searched for single transits.

The cuts and 15-minute binning performed for WASP were applied nearly identically, although with artificially small errorbars instead defined as $\sigma_i < 0.5$mmag.

4.2.3 Planetary Injections

We injected transiting planetary signals into 40% of all lightcurves. Periods were distributed between 12.2 and 665 days, with an exponential decay in likelihood such that the median period was 90 days. We assume the signals of planets with periods $<$ 12.2days will be detected with classical transit search techniques (eg BLS). Transit injection depths were chosen with a gamma distribution with k=1.0 and θ=0.0 scaled by 0.005, meaning the median injected depth was 2.6ppt and only 10% of injections had depths greater than 10ppt. These were chosen such that injections at and below the likely detection threshold (i.e. shallow depth and short duration) dominate, allowing the precise threshold to be studied, and mimicking the likely real distribution of signals. Transit timing centres were distributed randomly over a timescale far longer than the periods (10 years).

For ease of comparison both NGTS and WASP were injected with the same planet distribution. The above distributions were intended to mimic the true variation in planet frequencies, with the caveat of being more than 10 times as numerous as the real signals, allowing higher confidence in their detectability.

4.2.4 Transit Detection - `steve`

Our single transit detection method, which we named `steve`, can be summed up in three simple steps - find all the dips, characterise them, then sift out those that aren't exoplanet transits. We did this by first iterating a box-function over all the lightcurves, by model-fitting, and finally by random forest classification.

Box method

Firstly, the depth of a "box" with given transit centre and duration was compared to out-of-transit data. In- and egress were masked to remove effects from an off-centre transit. Where the depth was greater than some threshold (set in this search as 4σ), the eclipse time was stored in an array, along with depth, duration, signal-to-noise, the fraction of the 'box' covered by the photometry and the ratio of errors in the dip compared to the out-of-transit. This was iterated along the lightcurve in steps 0.13 times the transit duration, and the duration was scaled up from 1.95 hours to 1.2 days, increasing by 25% each time. The

red noise was calculated by binning the lightcurve to each transit duration timescale and calculating the RMS, enabling the depth to be compared to the correlated noise in the data.

Once box detections had been run on the entire lightcurve, the positions of concurrent detections within 2 hours of each others (but at different durations) were combined into a single detection, taking that with the largest SNR.

Model Fit

Two models were then run on each detection higher than some threshold of SNR_r. After performing machine learning on the box-search detections (without fitting), we determined $\mathrm{SNR}_r = 1.5$ to be the best threshold, as below this level false positives dominated real injections by a ratio $> 1000 : 1$.

The first model was a transit with depth, centre, duration and transit shape found by chi-square minimisation. In real transits, the lightcurve shape is a function of both limb darkening (which varies with stellar type) and impact parameter. To encapsulate this as a single one dimensional "shape" parameter, an array of transit models were created using the `transit` python package [1] for a range of stellar types (limb darkening found using the V band and the models of Claret and Bloemen (2011), see Figure 4.1). The transits were then normalised to have a depth (found as the median of the central 40% of transit compared to the out-of-transit normalised flux) and duration of unity. After stacking according to the flux at at arbitrary phase of 15% of T_d (which aligns the transits mostly by impact parameter), the models were interpolated in 2D both for each of 400 phases across transit and against normalised phase. This resulted in a continuous 2D surface of normalised flux vs. normalised phase and transit shape. Hence transit shape gives a slice in flux and phase space which can be compared directly with the transit once it has been shifted for depth, duration and transit centre. This is performed with:

$$\mathrm{model}_i = \left(\left(\mathscr{M}\left(\frac{t_i - t_{\mathrm{cen}}}{2T_D}, t_{\mathrm{shape}}\right) - 1\right)\Delta F\right) + 1.0 \tag{4.1}$$

Where $\mathscr{M}$ is the 2D model transit array, t_i is the individual time, t_{cen} the transit centre, T_D the duration, t_{shape} the shape parameter and ΔF the depth. Testing has shown that the resulting 4-parameter transit model produces adequate fits for any and all transits in photometry with reasonable levels of noise (SNR$<$ 10).

In the case of the long-duration eclipse search, models for transiting planets do not adequately represent the likely eclipse shapes caused by large dusty bodies. To correct for this, we adapted the model to include Gaussian dips, adding a Gaussian of $\mu = 0.0$ and $\sigma = 0.4$ in a smooth transition (using interpolation) from the most V-shaped high-impact

[1] https://github.com/dfm/transit

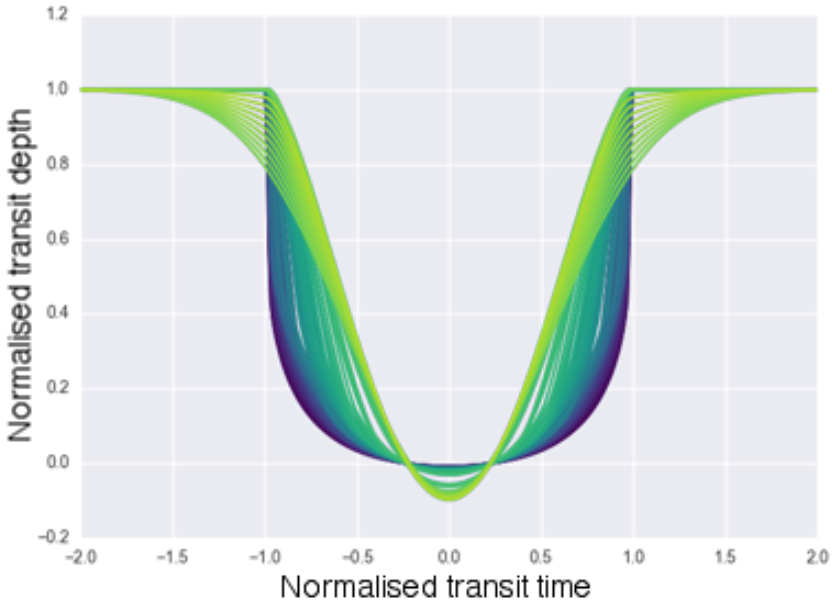

Figure 4.1: 1D shape parameter used in injections and fitting for `steve` Long-duration planet search. Light green models represent the added Gaussian-dip models for the long-duration eclipse search.

parameter fit used in the transit model (models in green in Figure 4.1). Modifications of depth and duration therefore produce any possible symmetrical Gaussian dip.

To model non-transiting phenomena, we used a two-line model with a "step", similar to the non-transiting models used by Foreman-Mackey et al. (2016) to distinguish between real and unreal signals. This was physically motivated by looking at false-positive signals, which often show only a trend at the end-of-night (and therefore best fit by a straight line), a V-shape from variability or grazing eclipsing binaries, a flux drop with no in- or egress, etc. Fitting this model involved minimising five parameters - the gradient and intercept of each line and the position of the "step".

In both the transit and the step function case, we performed minimisation with `scipy`'s "optimize" tool, starting at with three different central starting positions across the initially detected 'duration', to allow any off-centre step or transit to find the best fit. The lowest reduced chi-square of each minimised model was then used to determine the best fit. The ratio of these minimum reduced chi-squares (which approximates to the "f-distribution" between the models) was then calculated and used as a parameter in the Random Forest Classifier (RFC).

Machine Learning

Machine learning is an excellent method of recovering known signals from a large dataset with minimal human involvement, (see section 2.11). We applied this method to detect single transit events from the large number of candidate signals detected by the *steve* transit search (Section 4.2.4).

The Random Forest Classifier package of scikit learn (Pedregosa et al., 2011) was used, with 500 trees and 16 jobs. We initialised the detection array with the known classifications by comparing the position of the injections with the detections of `steve`'s box search and model fit sections. We determined an injection recovery to be any detection within ±0.3 transit durations of the transit centre, and with more than 3 in-transit lightcurve points. The detection array was then split into two with one set used to initially train the random forest, followed by a test set to determine how well the RFC would perform on unseen data. To utilise the most of the low numbers of detected injections, we performed training and testing on both halfs and predicted the opposing half of the data in an isolated manner.

17 different statistics were used, generated from the transit-fitting procedure. These were:

- Recovered eclipse depth (both from the initial box-model, "dep", and from the secondary transit-fit, "fit_tr_dep")
- The SNR with respect to both the white noise of the out-of-transit data ("snr_w") and the red noise of the whole lightcurve at that duration ("snr_r").
- "dur" - The recovered eclipse duration from the initial box-model,.
- "Nconc_all" - The number of concurrent transits detected globally within 2 hours of the detected $t_{\rm cen}$
- "SIGMA_XS" - the weights from the sysrem run, which uses the variance of stellar photometry as a function of image, star and field to use the most stable photometry and down-weight the most variable (e.g. clouds and stellar variability).
- "MAG_MEAN" - Stellar magnitude
- "tran_cover" - The proportion of the initial box model dip that was covered by data.
- "err_ratio" - The ratio of the median in-transit errorbar with the median out-of-transit errors, .
- "n_conc" - The number of detections at that transit centre (but different transit durations) from the box model

- "S_max" - The maximum detection of all transits SNR multiplied by the square root of the number of detections
- "fit_f_ratio" - The ratio of box-model fit to the systematic step-model.
- "fit_tr_conv" - whether the transit model converged during transit fitting.
- "fit_tr_dep_offset", "fit_tr_dur_offset" & "fit_tr_tcen_offset" are the offsets in depth, duration and centre between the initial box model and the latter transit model.

Once trained on the data, we predicted the classifications of the test set in order to determine the recovery rate. The RFC is such that the probability of class membership can be determined from the number of different tree iterations that produced each classification. Hence, it is possible to tweak this probability to include more detections, but also more false-positives. For example, setting $P_{transit}$=0.5 as a threshold may substantially increase the number of detections compared to $P_{transit}$=1.0, while only marginally increasing the ratio of real signals to false positives.

The long-duration eclipse search was performed almost identically to that described above for the Single Transits. Both injections and the fitting procedure were modified to also including non-transit shaped gaussian dips (see Figure 4.1).

4.2.5 Estimating Stellar & Planetary Sample

To perform a simulation of the frequency of transiting planets as a function of duration, period, magnitude, etc. we need to simulate the likely stellar and planetary population of stars observed by both WASP and NGTS.

To estimate the sample of stars in the fields observed, the TRILEGAL galactic stellar population model was used (Girardi et al., 2012). This stellar sample was complete to 18th magnitude, and used for 10 square degree fields of view at the centre of 20 random WASP and NGTS fields. Stellar radius was calculated from the output log luminosity and log effective temperatures. To replicate the missing fields, these stellar samples were randomly duplicated until the number of target stars matched the number scanned. The WASP and NGTS bandpasses were approximated as V and R bands respectively. The deeper magnitudes, redder colours, and higher average galactic latitudes meant the stellar population observed by NGTS included fewer giant stars and more main sequence stars.

To estimate the planetary population, occurrence rates of Fressin et al. (2013) were used and extended to long-periods ($< 10^4$d) with a distribution flat in ln P. The stellar sample was then iterated, generating planetary radii and periods as per Fressin et al. (2013), planetary eccentricities as Kipping (2013) and impact parameter from a flat random distribution. The argument of periastron was generated consistent with Barnes (2007) such

that the periastron of transiting eccentric planets was more likely at periasteron (using $\phi = 1 + e\cos(\phi)$). Using the eccentricity, semi-major axis (calculated from period, (Kepler, 1609)) and eccentricity (using the formulation of Barnes, 2007, and described in 1.2.3), the probability of transit was calculated and used to determine if each planet transited. This was performed ten times for the stellar target list, giving a simulated catalogue of transiting planets in both the NGTS and WASP fields.

The resulting distributions of planets produced multi-dimensional histograms with the probability of transit as a function of planet and stellar parameters. The left-hand panels of figures 4.3 and 4.9 show the corresponding number for the WASP and NGTS samples. They show that shallow planets are far more frequent, with only a few dozen planets causing dips deeper than 10ppt (1%). These populations can then be directly compared to the recovery fractions from transit searches.

4.2.6 Predicting Number of Detections

We have a simulation of the likely frequency of transiting planets as a function of depth, duration, period, etc and an estimate of the detection efficiency of transiting planets from the recovery rate of the injected planets and the RFC. Using this it is possible to estimate the likely number of detectable planets in each sample (WASP Stare data and NGTS data).

For some parameter space of the planetary injection (e.g. eccentricity, duration, depth and stellar magnitude mag) and for some class probability threshold ($P_{\rm class}$), we want to determine how many planets we would be able to detect, $N_{\rm det}$. To do this, we can use the proportion of injections within that parameter space detected, the number of expected planets in the parameter region ($P(\mathrm{pl}|e, t_d, \mathrm{dep}, \mathrm{mag})$) given the stellar sample and occurrence rates defined in section 4.2.5, and the number of stars observed, N_s:

$$N_{\rm det}(e, t_d, \mathrm{dep}, \mathrm{mag}, P_{\rm class}) = \frac{N_{\rm inj,det}(e, t_d, \mathrm{dep}, \mathrm{mag}, P_{\rm class})}{N_{\rm inj}(e, t_d, \mathrm{dep}, \mathrm{mag})}.P(\mathrm{pl}|e, t_d, \mathrm{dep}, \mathrm{mag}).N_s \quad (4.2)$$

This allows us to predict the number of detectable planets as a function of planetary parameter space

We set every detected signal that was not an injection as a false positive. The number of false positives is constant across the scanned light curves (e.g. do not vary as a function of the number of detected planetary signals). This means, to estimate the false positive rate per detection, we must estimate the number of detectable planets at some class probability of the RFC.

4.2.7 Deep Eclipse Search

We also attempted to use the same method to search for long-duration eclipses in WASP light curves.

To aid in the search for long-duration eclipses, the flux files output from `sysrem` were split into individual nights and a weighted mean for each night taken. These were compiled for every object in the WASP database, giving 35 million nightly average light curves over 850 arrays (each corresponding to a single WASP North or WASP South field). However, many of these objects were duplicates, giving ~7million stars in total. NaNs ("not-a-number"s) and anomalies (computed with the method described in section 2.8 with a threshold of 4.2 was used here.) were removed, and the flux and flux errors were normalised to the median flux. To reduce processing time, a cut of 13.5 magnitude was used. On average, stars were observed for 300 nights over a median baseline of 2.5 years.

Injections of eclipses were used with depths determined by a gamma distribution with mean 0.1, $k = 0.8$ and $\theta = 1.0$ (5^{+9}_{-4}%); durations were set according to a to a normal distribution with $\mu = 6$ and $\sigma = 2$ with the exponent of 1.5 ($11.4^{+13.9}_{-6.3}$d); eclipse epochs were picked randomly between the start and end of the light curve; and eclipse shapes were picked randomly according to our 1D transit-shape model that varies from Gaussian to U-shaped.

Unlike for planetary companions, the occurrence rates of such long-duration eclipses are unknown, therefore we make no effort to predict the number of likely detections. Instead we use the detection efficiency to directly predict the occurrence rate of these eclipses themselves.

4.3 Results

4.3.1 WASP - Planets

Recovery rate

Of the 55,000 injections in the 136,000 light curves searched (see the left-hand panels of Figure 4.3), only 15,500 modified the light curve at all, and fewer than 1500 caused flux changes greater than 1%. 716 of those were detected by the initial box search, which detected 218,000 dips in total. We trained the RFC on these detections with two simple classes of "single transit" and "false positive". The feature importances of the RFC are shown in Figure 4.2, and the number and detection rate of the injections is shown in Figure 4.3. The data was split into bins of eccentricity, duration, depth and magnitude to show differences in these key parameters. The recovery rate for each bin was then computed

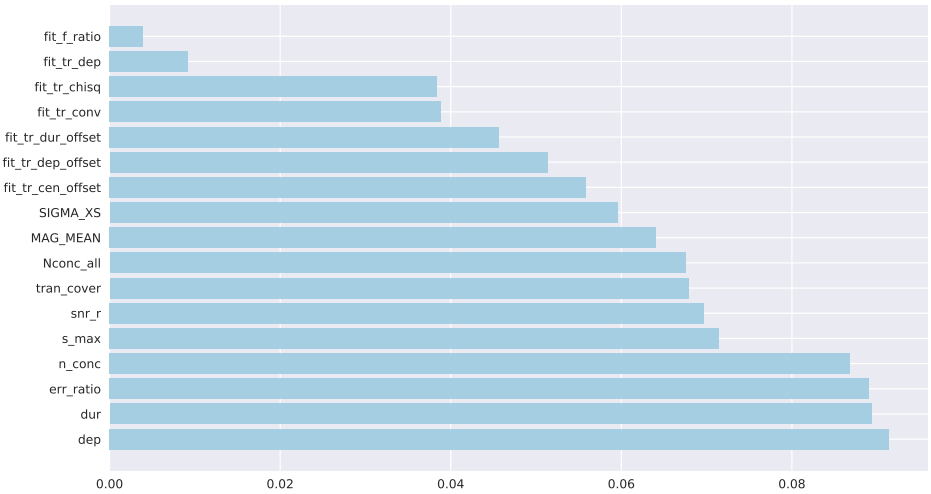

Figure 4.2: Feature importances of the RFC for WASP data.

using the number of detected injections. The corresponding detections per year (24 Stare fields, as opposed to the 38 studied here), this drops to only 1.43 ± 0.15.

Expected Number of Detectable Planets

Figure 4.4 shows the expected number of transiting planets across all 136,000 search stars per parameter bin. By multiplying these by the recovery rate for each bin, we can compute the expected planet haul. For the case of WASP, with the RFC classifier probability threshold (P_{STE}) of 0.03, we find 2.27 ± 0.2 detectable planets.

False Positive Rate

While the detectability of planetary signals likely remains constant between the injection test and searches for real planets, the number of false positives scales only with the number of light curves searched. Therefore, any real planet search will see a substantially higher false positive rate than the injections, as real planets are spread far more thinly within the data. Figure 4.5 shows the change in both expected planet haul and the ratio of planet to false positive as a function of the RFC STE classification probability. As can be seen, using a higher probability results in more planets per false positive, but fewer overall planets. For example, with a threshold of 0.1 on ProbPL, we should expect ~1.7 transiting planets but a real to false positive ratio of only ~ 0.004 (e.g. ~250 FPs per detection).

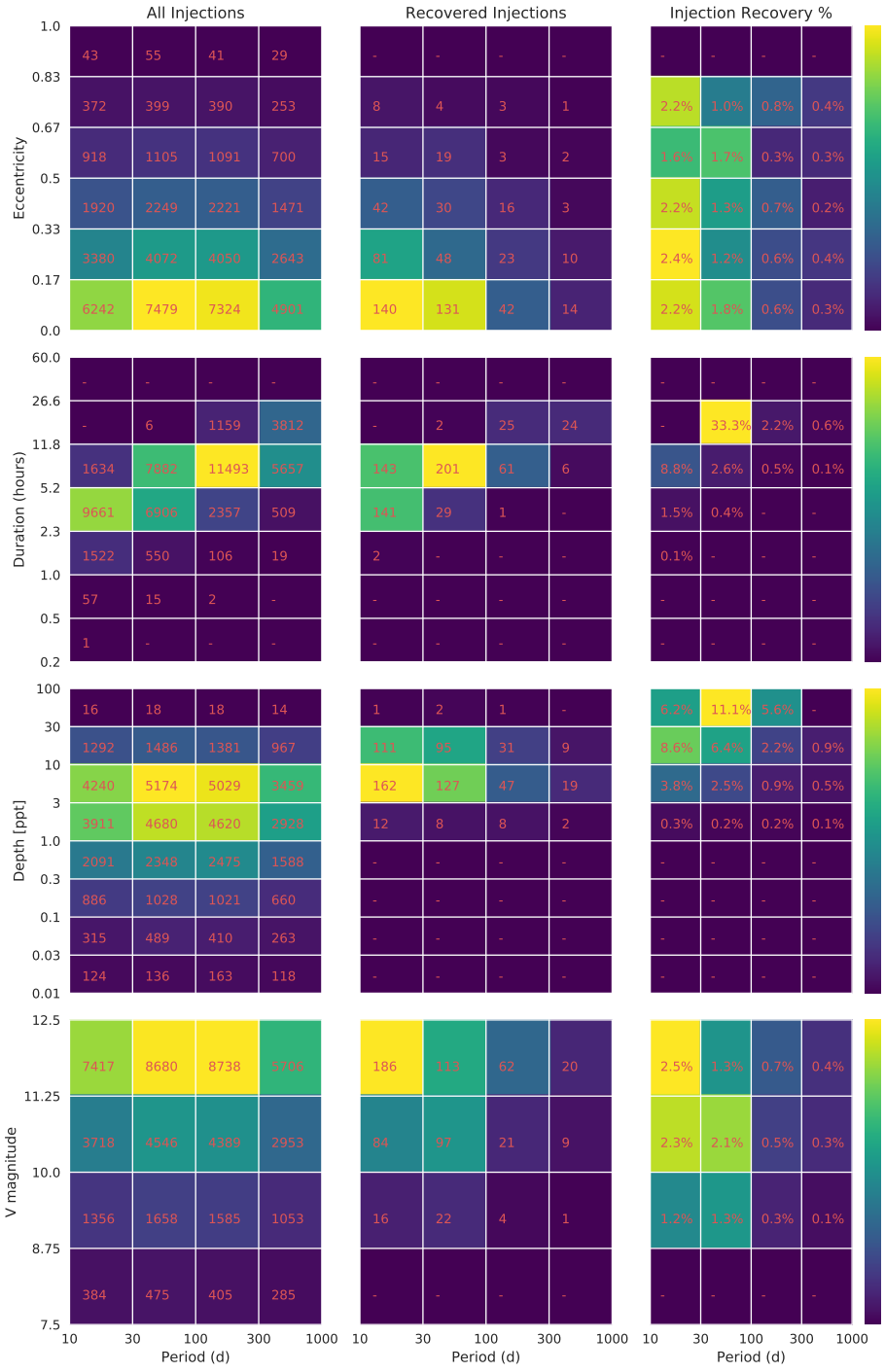

Figure 4.3: Injected signals (left), recovered injections (centre) and the detected fraction (right) as a function of orbital period (x-axes, all panels), eccentricity, duration, transit depth and magnitude (y-axes, top to bottom) for injections into WASP data. The class probability threshold was set to $P(\mathrm{STE}) > 0.03$.

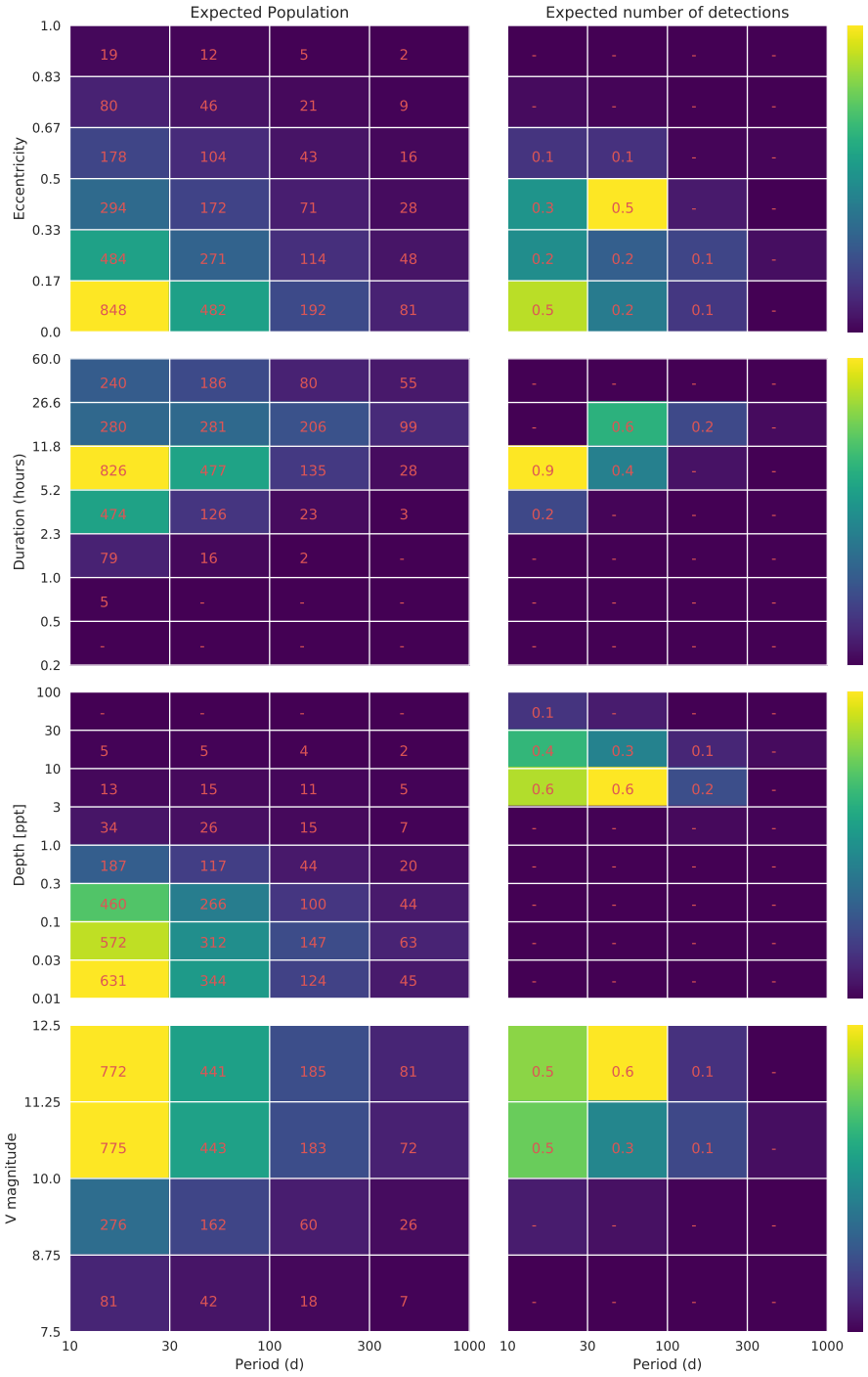

Figure 4.4: **Left:** Expected planets in all stars in the scanned WASP Stare fields as a function of orbital period (x-axes, all panels), eccentricity, duration, depth and V magnitude (y-axes, top to bottom); **Right:** Expected detectable planets as a function of the same planet parameters for a class probability of $P(\text{STE}) > 0.03$.

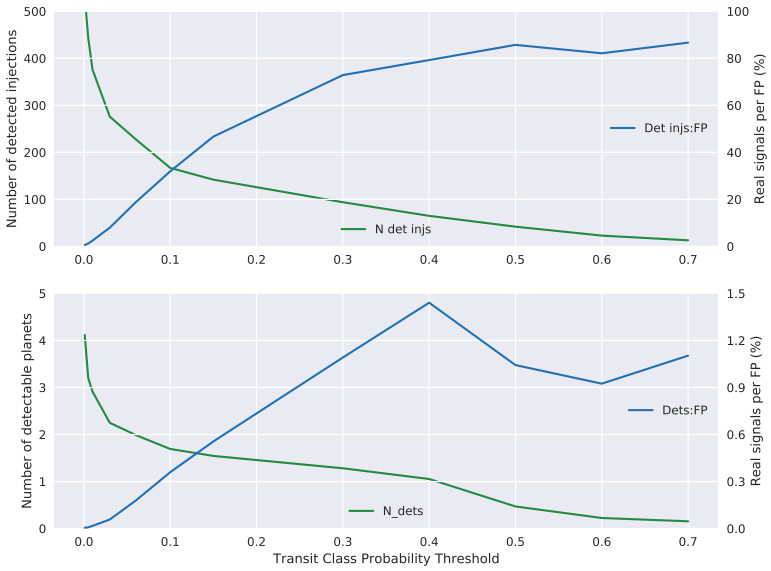

Figure 4.5: Variation in number of detected injections (top) and then detectable single transiting planets (bottom) detectable with WASP as a function of the single transit class probability and the false positive rate.

Candidate Signals

The trained Random Forest was used to search for single transiting exoplanets within the data. Among the detections with the highest probabilities, as predicted by the RF, was a single eclipse of the known exoplanet HAT-P-33b (Hartman et al., 2011), showing that the search was performing well. It also detected 214 eclipses of eclipsing binaries, including some with depths below 2% (classified as Low Mass Eclipsing Binaries, or EBLMs). The majority of detections with lower transit probabilities were noise signals which were not adequately filtered out by the random forest. Events at MJD=5811, 5820, and 5882 proved particularly common detections. Many potential in- or egresses were found for which the origin of the signal is unclear. Follow-up in necessary to determine if these are the result of planets.

4.3.2 NGTS

Recovery rate

We ran the search on 126,000 light curves in total, creating 50,300 random injections. 20,000 of those actually cause any effect to the lightcurve, substantially higher than WASP thanks to improved phase coverage from a location with better weather. Just over 1000 of

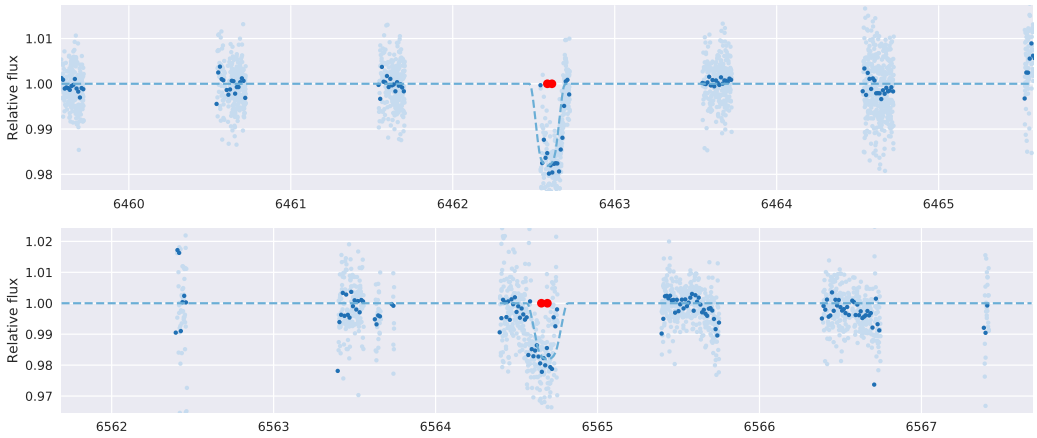

Figure 4.6: Known EBLMs with depth<2% detected with *steve* in WASP photometry

those detected in the initial box search, higher than with WASP data. In total, we estimate that 4.14 ± 0.16 planets can be detected from this sample above an RFC class probability of 0.03.

This marks an improvement on WASP data due to the improved recovery rate of NGTS. Indeed, even transiting planets with depths below 1ppt could be detected by NGTS (0.4 with current sample).

False Positive Rate

NGTS has a similar false positive ratio to WASP, with a $P(\text{STE}) \sim 0.1$ corresponding to a real to false positive ratio of ~ 0.004, or ~250 FPs per detection (Figure 4.10).

Candidates

A review of the top 100 non-injected "detections" sorted by transit class probability revealed many strong planet candidates, as well as many clear false positives. Four good candidates are shown in Figure 4.12. Figure 4.13 shows the detections of two known objects - a known EBLM with depth of 32ppt and WASP-68 b with a depth of only 6ppt.

4.3.3 WASP - Deep Eclipses

Of the 2 million lightcurves currently searched, eclipses were injected into 35%. The dip method detected 13 million dips within those lightcurves, suggesting it may be overly zealous with dip detection. However, the RFC performed remarkably well, recovering more than 50% of the injections with a false positive rate of only 2%. This was especially true for deep and long eclipses, for which the recovery rate of detections found by the initial

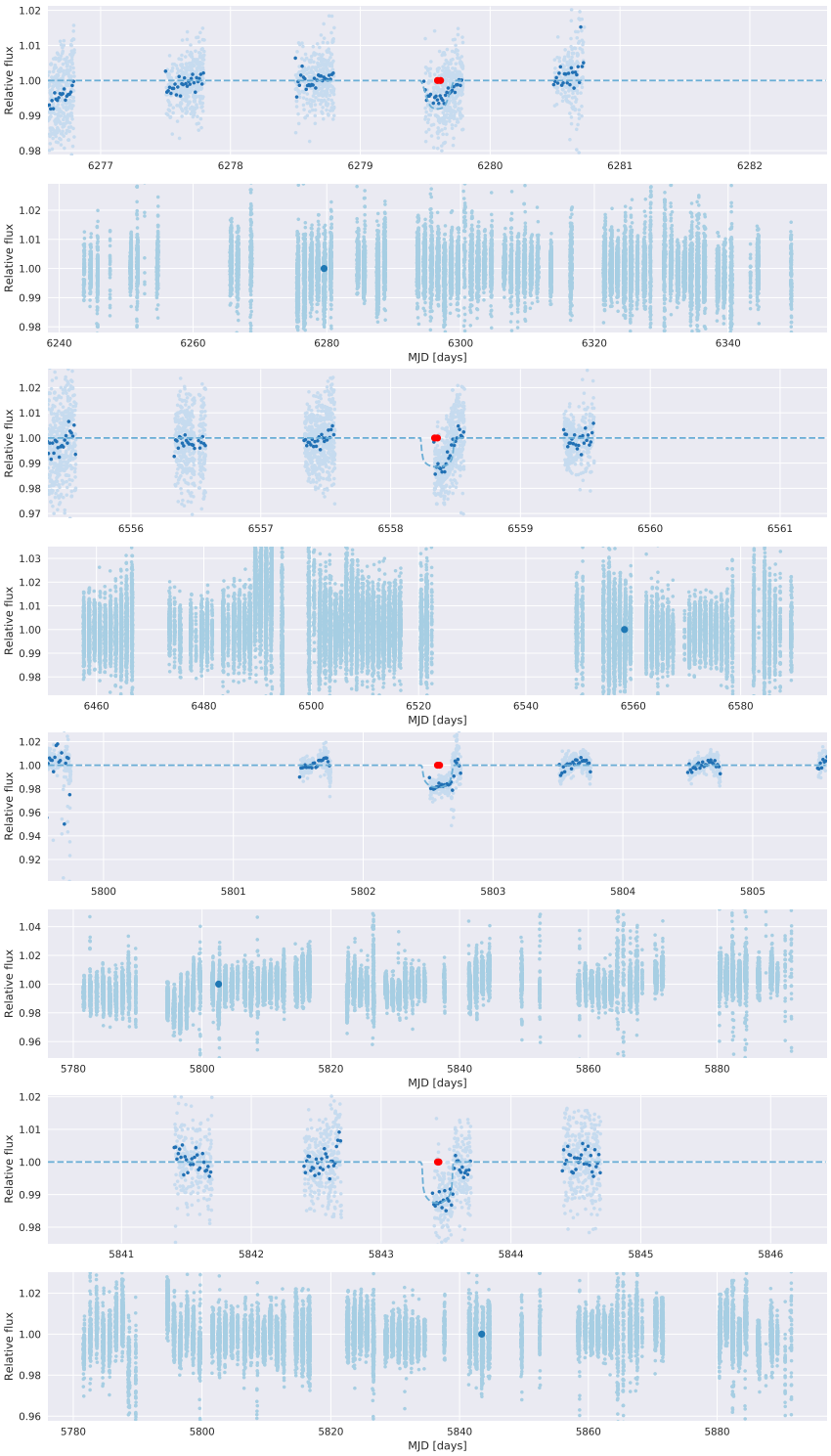

Figure 4.7: New candidate long-period planets detected in WASP stare photometry. Upper panels show raw (light blue) and binned (dark blue) photometry spanning the closest 6 days, with the initial and post-model fitting transit centre shown as a red dot and the transit model as an blue dashed line. Lower panels show only binned photometry (blue) across the entire season, with the detected location shown as a red dot.

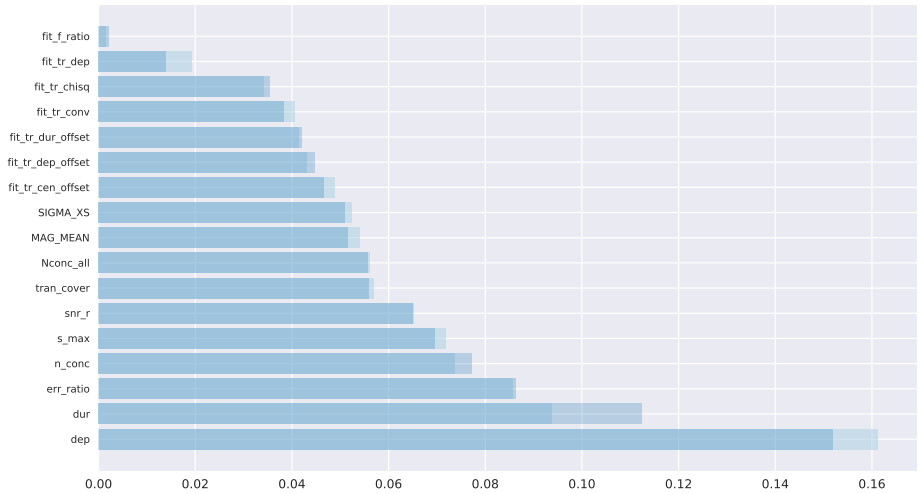

Figure 4.8: Feature importances of the RFC applied to NGTS single transit detections. The two bars represent the value for each half of the data, which were trained and tested independently.

box search was $\sim 60\%$. Figure 4.14 shows injection and recovery rates as functions of detection parameters, although the sheer number of detections at short-durations and shallow depths means that the rates for long-duration injections are dominated by (poorly recovered) shallow eclipses, and vice-versa.

From the number of deep eclipses detected and the rate of injection recovery we are able to place upper limits on the occurrence rate of eclipses. We use the bounds of 10% in depth and 15d in duration, as regions above these bounds have excellent detection recovery rates. Of the ~40% of eclipses injected actually occurring during WASP observations, 21% of those were detected by the initial box search, and 60% of those were found by the RFC. Hence, the probability of detecting a once-per-decade eclipse of any given star in the WASP field with this method is $10.1 \pm 0.3\%$. However, from analysis of the candidates, fewer than 20 such candidate eclipses were found in the 2 million lightcurve sample. Hence, we can state that fewer than < 10 per million stars per year undergo such eclipses (to 1σ).

Candidate Signals

By applying the light curves (and box detections) that were not consistent with injections to the random forest identified 300 new eclipse candidates. The majority were systematics. Similarly to the planet search, systematic drops in flux across whole fields and for entire

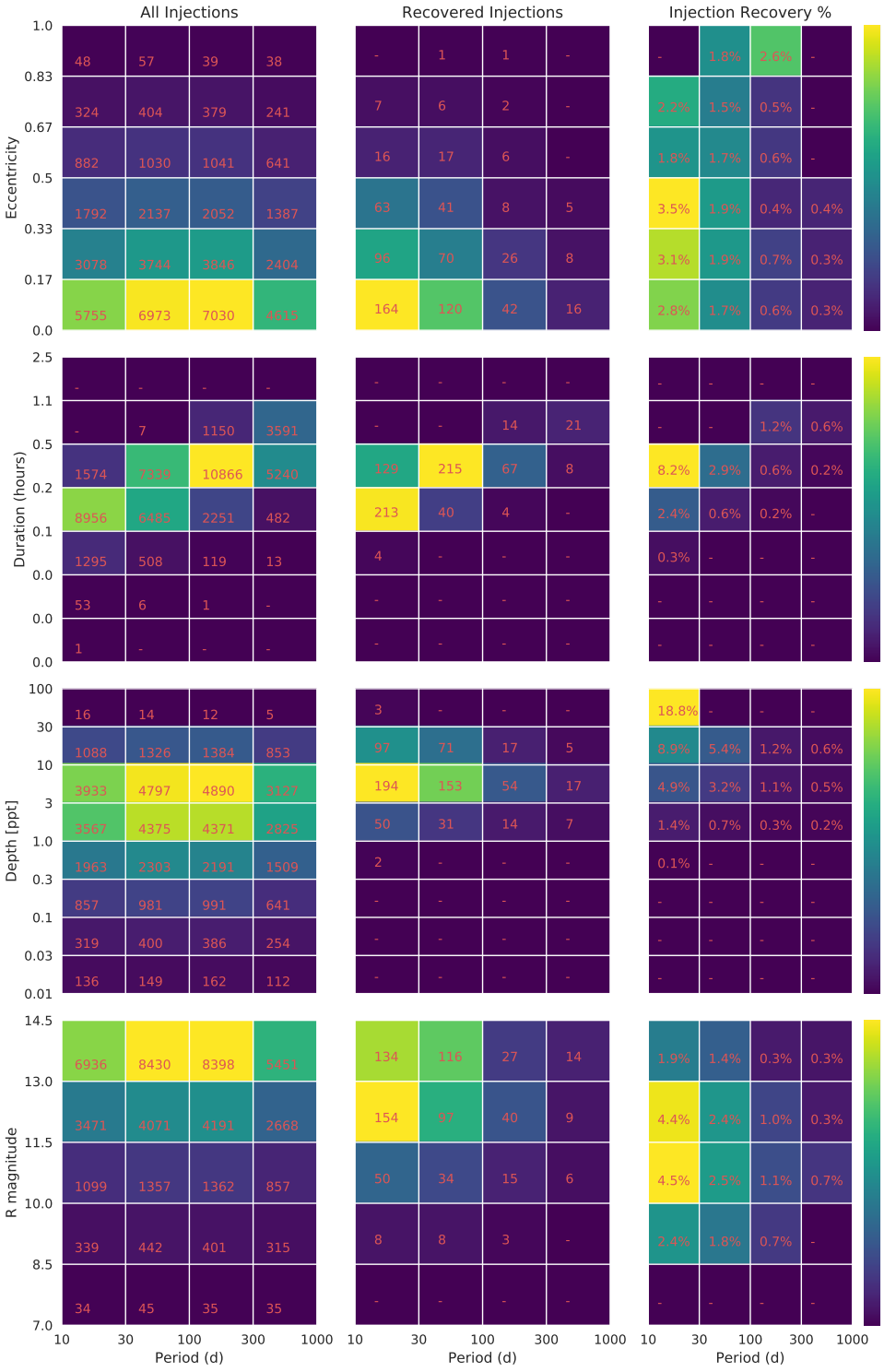

Figure 4.9: Injected signals (left), recovered injections (centre) and the detected fraction (right) as a function of orbital period (x-axes, all panels), eccentricity, duration, transit depth and magnitude (y-axes, top to bottom) for NGTS planet injections. The class probability threshold was set to $P(\mathrm{STE}) > 0.03$.

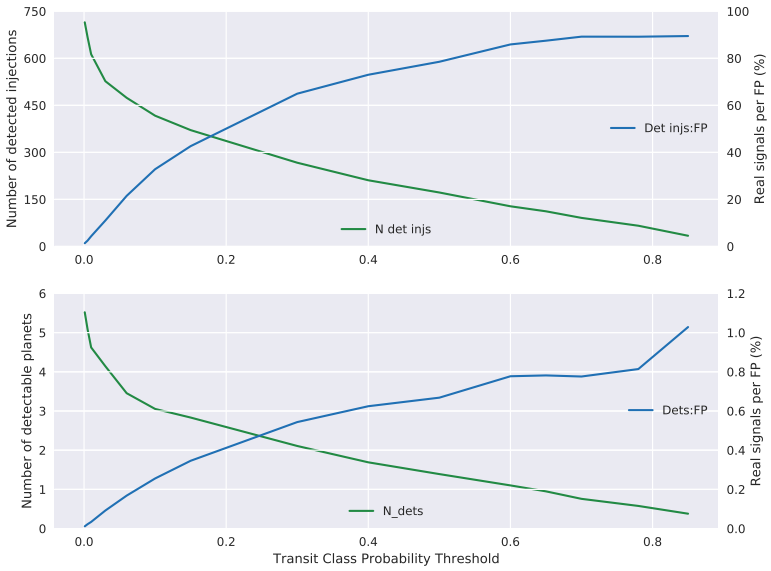

Figure 4.10: Variation in number of detected injections (top) and detectable transiting planets (bottom) with NGTS and the ratio of real transits to false positives as a function of the single transit class probability.

weeks dominate the number of detections. Eclipsing binaries with periods close to one day (which produces an alias in nightly-averaged data at $1/(1 - P_{EB})$ days) also caused false positives. Long-period variability (e.g. Miras) were also detected at their lowest flux levels. In some faint light curves, changes in background levels due to the moon also caused systematic drops in flux.

Four apparently real eclipses are shown in Figure 4.15.

4.4 Discussion

4.4.1 Assumptions

In an ideal case transits would be injected into the raw pixel data from each survey and put through the same aperture photometry and detrending process as the data, which are likely to shallow the flux drop compared to a transit injected in simply the raw photometry. We would also correct for the influence of stars contributing flux within the aperture. However, this is a very slow and computer-intensive process, hence, we make no attempt to correct for the likely shallowing of transits from blending or lightcurve processing.

By randomly injecting a population of planet-star parameter combinations, we assume differences in stellar parameters are independent of the planetary detectability. It is

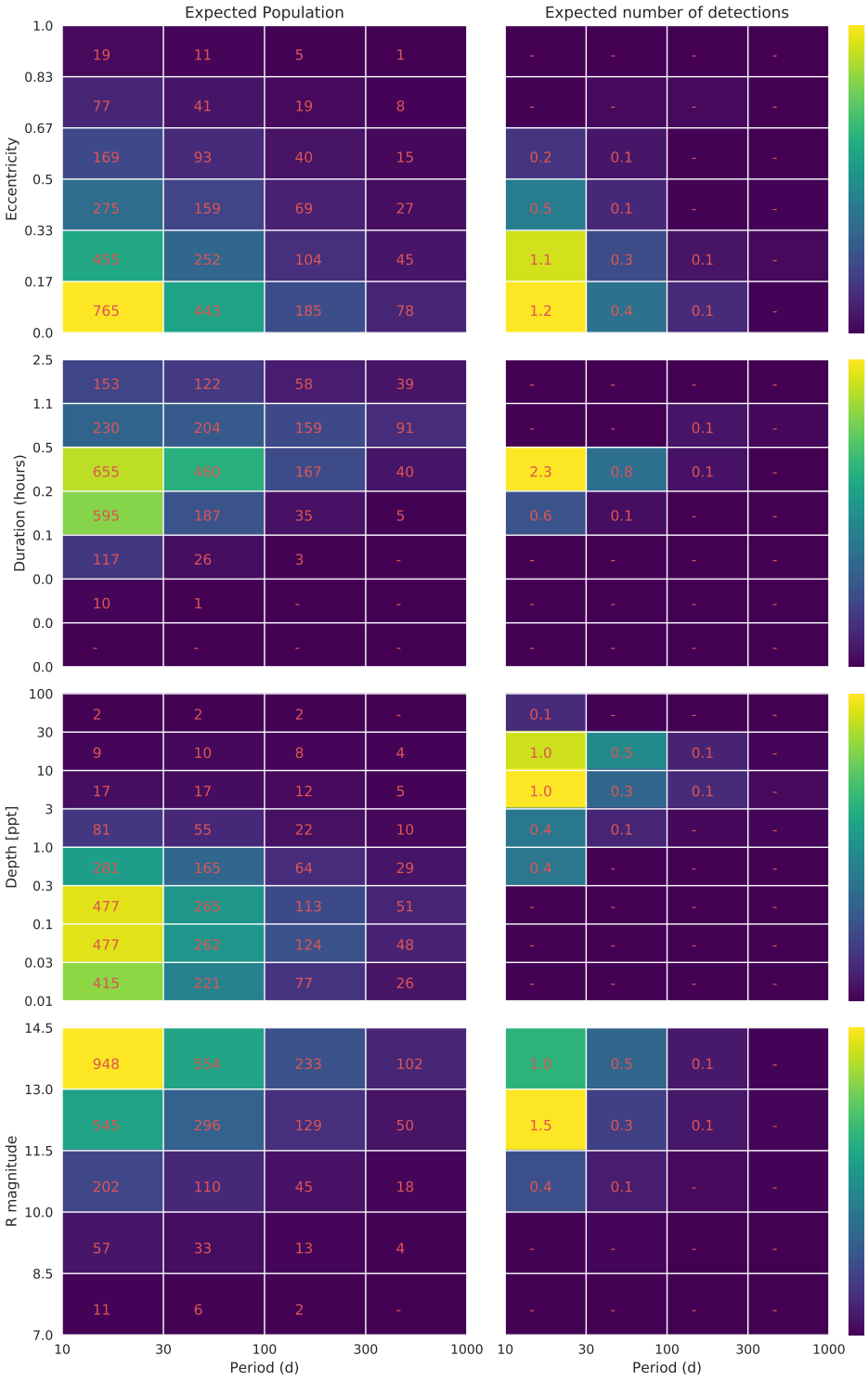

Figure 4.11: **Left:** Expected planets in all stars in the scanned Stare fields as a function of orbital period (x-axes, all panels), eccentricity, duration, depth and V magnitude (y-axes, top to bottom); **Right:** Expected detectable planets as a function of the same planet parameters for a class probability of $P(\text{STE}) > 0.03$.

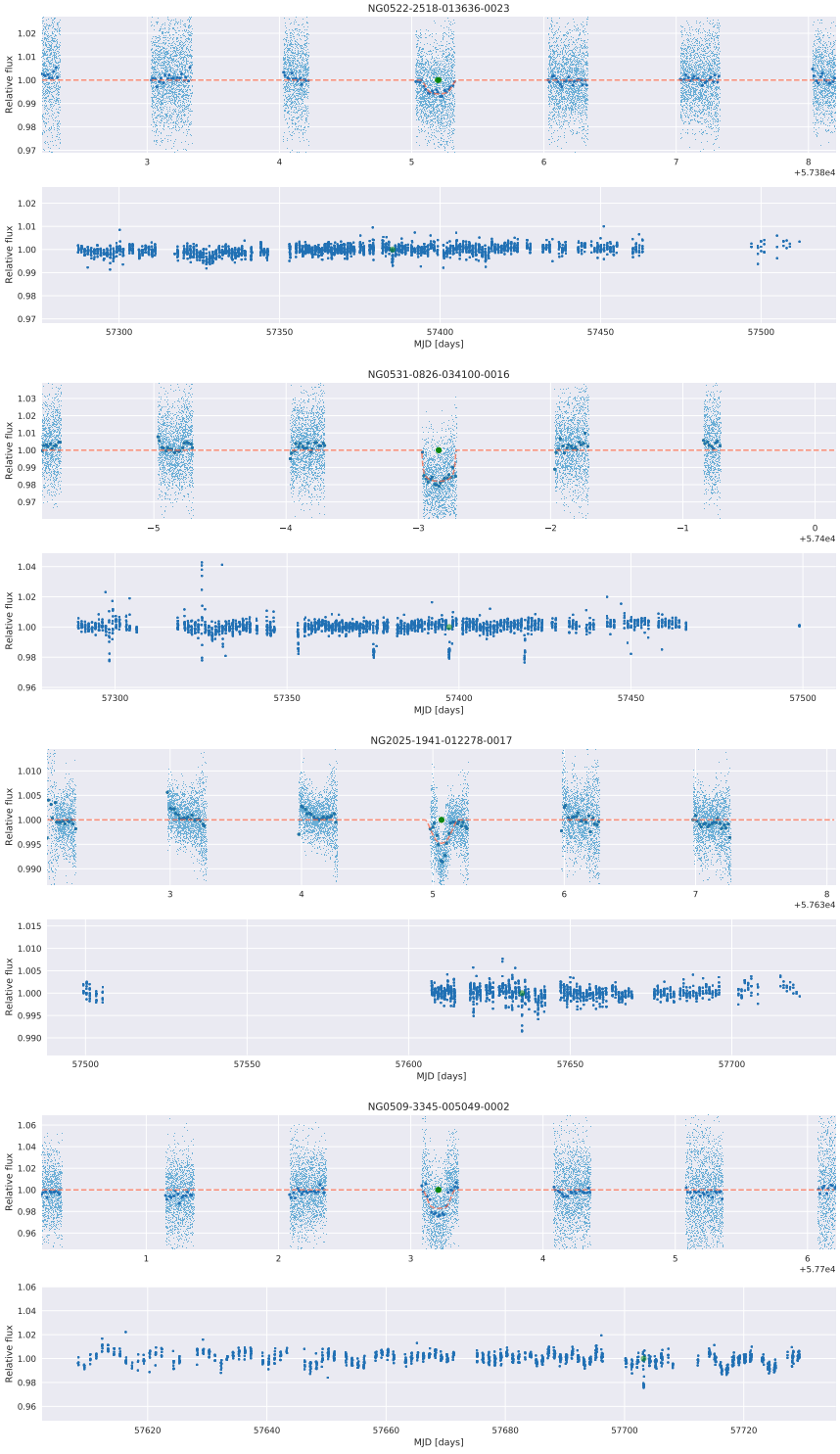

Figure 4.12: New candidate long-period planets detected in NGTS. Upper panels show raw (light blue) and binned (dark blue) photometry spanning the closest 6 days, with the initial and post-model fitting transit centre shown as a green dot and the transit model as an orange dashed line. Lower panels show only binned photometry (blue) across the entire season, with the detected location shown as a green dot.

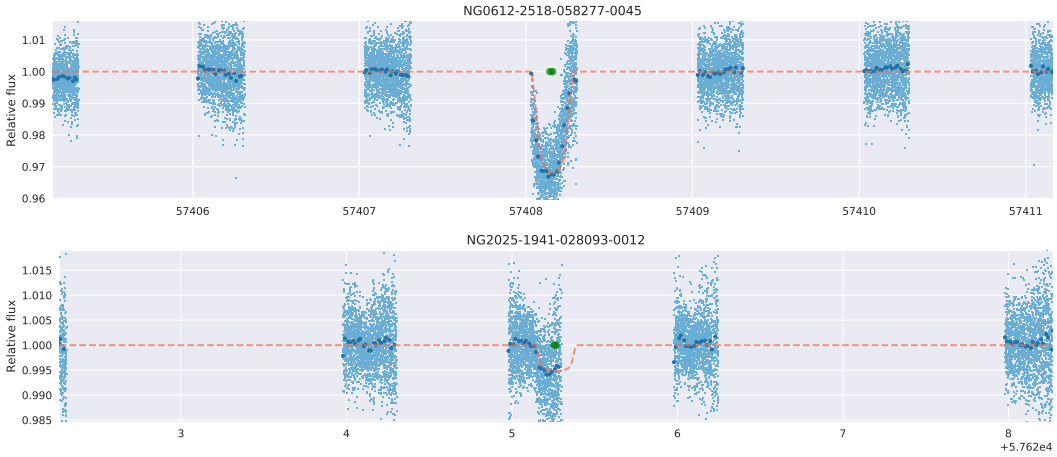

Figure 4.13: A known EBLM (top) and WASP-68 b (bottom) detected from a single transit in NGTS photometry.

possible, for example, that certain stars such as spotty K- and M-dwarfs (Basri et al., 2013) are more likely to have intrinsic variability which inhibits planet detection.

4.4.2 Blends

The large aperture size of WASP photometry (on average with a radius of 45") means that blending is an issue for both shallowing exoplanet transits, and providing a potential source of false positives as blended eclipsing binaries. Analysis of the TRILEGAL stellar data suggested 10% of the bright stars searched were blended with a companion brighter than 15th magnitude, and therefore capable of producing a blended eclipsing binary signal as deep as ~5% (assuming a 50% eclipse and a V=12 primary star). In the case of NGTS, the smaller aperture for photometry (15") means a lower chance of blending, with only 7% probability of a blend with Δmag< 3. We have not accounted for the presence of blending or BEBs in this analysis, therefore these could potentially increase the already high FP rate.

4.4.3 False Positives

We initially determined false positives to be any detected signal that did not correspond to the precise detection of an injected transit signal. In reality these are not all true false positives, but often interesting astrophysical signals in their own right.

One major source of false positives was from low-flux events occurring on many stars across the entire field. Although we hoped the "N_conc" factor would adjust for this, many such events still remain. By more strictly discarding nights and fields with a high number of concurrent transits, the false positive signal could be reduced. In many cases, false positives were also introduced by the injected transits, which were not adequately

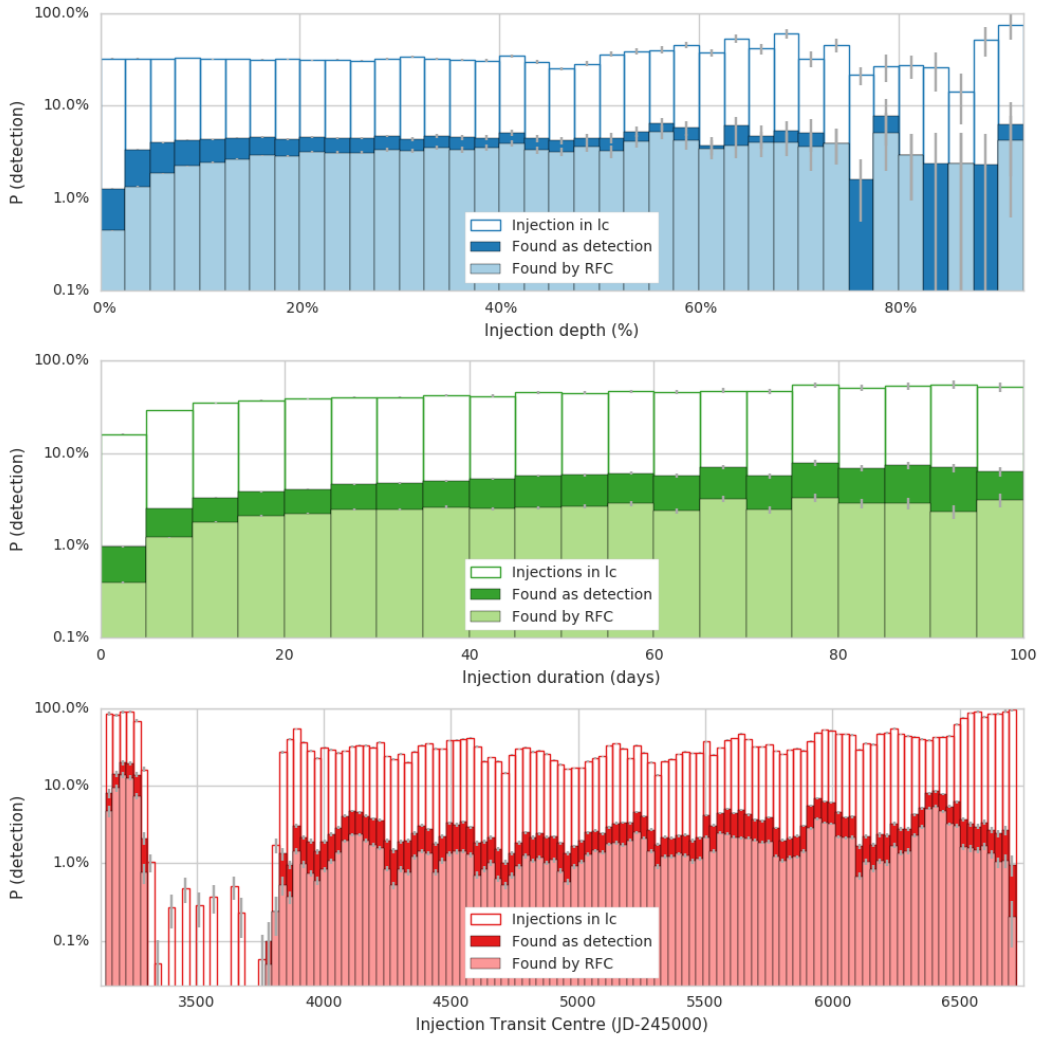

Figure 4.14: Injections into nightly averaged WASP data as a function of depth, duration and transit centres.

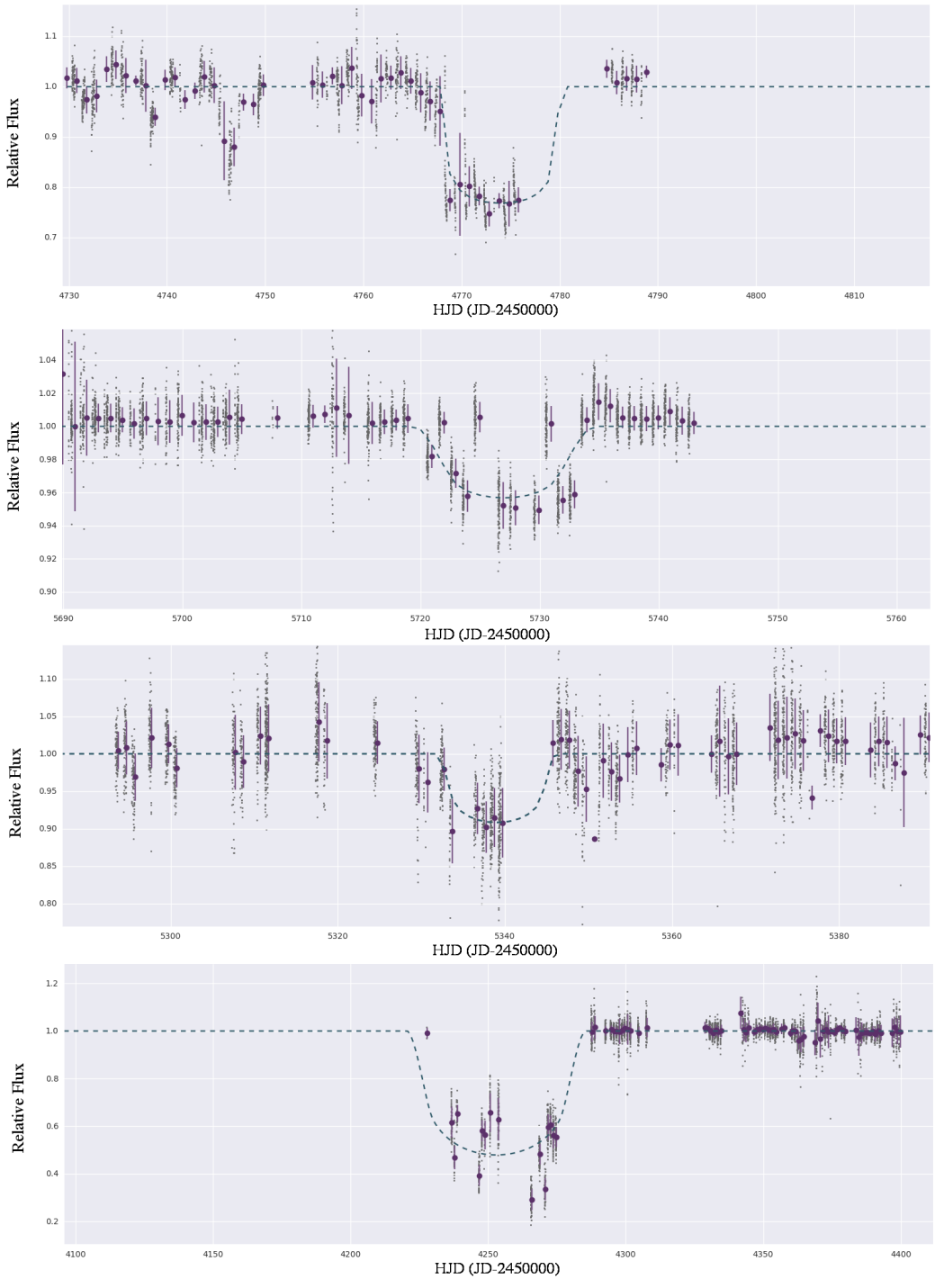

Figure 4.15: Candidate long-duration eclipses from WASP photometry.

detected (e.g. because the full transit was not covered by data, and the resulting "detected" transit centre was distant from the expected "injected" transit centre). These false positives would not be present in the injection-free searches of WASP data, therefore lowering the FP rate. Similarly, in the injection/recovery process, signals from the real long-period planets that we want to detect form part of the false positive sample, thereby artificially increasing the number of FPs. Eye-balling the first 100 significant detections also revealed that EBs, variable stars, short-period planets, and known planets also formed as much as 30% of the FP list. These can themselves be excluded once identified, or even added as an "injection" to help train the RFC. Alternatively, further classes of variables and EBs could be added to the RFC to reduce confusion, although this may require period-space analysis (e.g. Lomb-Scargle, auto-correlation function, or BLS periodograms), thereby further slowing down the analysis.

The lack of significant numbers of candidates from either photometric data can also be attributed to the intrinsic number of planets as a function of depth and period. As the lower-left panels of Figures 4.4 and 4.11 show, the number of planets drop off both with period (primarily due to transit probability, $P_{\rm pl} \propto P^{-0.67}$ and poor time coverage), and with depth (primarily due to the low numbers of giant planets). If ground-based transit surveys were sensitive to transits deeper than 1ppt instead of 3ppt, they could anticipate a 3-fold increase in total detectable planets.

4.4.4 Follow-up

After candidate transits have been found, the first step is to use the remaining photometry to constrain the possible orbital period. In the case of WASP this may include many past seasons as well as the rest of the Stare light curve. This would give an estimated period, or give probabilistic limits on the minimum orbital period.

Radial Velocities could also be utilised to confirm the object as planetary, and to predict its orbital period. In the future, any single transiting planets could be followed-up with TESS. Given the majority of detected planet candidates are in the 10-30d region, the 27d observing windows of TESS would almost certainly spot at least one transit and constrain both period and radius.

Similarly, TESS and future ground-based survey data would monitor the stars seen to have long-duration eclipses, potentially detecting repeated, or periodic signals.

4.4.5 Future implementation and changes

Improvements to the current transit detection could involve adding specific classes for specific noise sources, such as EBs, global flux-drops, etc. Also useful would be a metric

of what proportion of in- and egress are covered, as false positive detections are frequently missing large segments of both, whereas the strongest detections cover the full transit range.

Despite analysing the likely planetary population, the expected number of EBs or BEBs which may act as false positives in this search were not analysed. Any future analysis of the single transit yield should take this into account (e.g. Günther et al., 2017).

NGTS will observe 36 fields per year, suggesting that similar numbers of single transiting planets on orbits >12 days could be discovered every year during NGTS's observations.

WASP has observed 96 more Stare fields since 2013. If false-positives can be suppressed, this could provide as many as a 8 new long-period planets across all new fields.

4.4.6 Discussion - Deep Eclipse Search

The full (non-stare) WASP data set, while not amenable to the detection of planetary transits with dips on the order of $\sim 1\%$, should be highly amenable to the detection of longer-duration and deeper eclipses. As this search has shown, WASP is indeed capable of detecting some such eclipses, but that they are rare in the majority of the WASP stellar sample. Therefore, the number of false positives, usually due to various different forms of systematics, dominate the number of real signals, except in specific groups (such as young disc-hosting stars, as Chapter 5 will show). One way to ameliorate this would be to use more than a single flux point per night, which may allow sharp drops in flux (e.g. due to pixel systematics) to be more easily removed. This would also allow shorter-duration signals to be detected. However, the information gain for long duration (e.g. weeks) eclipses is likely not worth the increase in required processing power. The problems of large-duration flux drops could also be improved by re-processing the full WASP data set in a fully self-consistent manner (rather than season-by-season and camera-by-camera). However, such a reprocessing is beyond the scope of this work.

4.5 Conclusion

High-quality photometric data from the ground has the potential to detect long-period exoplanets, with up to 4 planets per year being detected in NGTS photometry, and ~2 per year from WASP Stare fields. And initial searches of 36 and 38 felds of NGTS and WASP data respectively has revealed dozens of potential candidate single transits. None have yet been confirmed however, follow-up is ongoing. Despite being plagued by systematics, deep and long-duration eclipses are detectable with WASP, although we show such events are rare in the WASP field, with < 10 per million stars per year.

The biggest hurdle in the way of detecting single transiting exoplanets in numbers is the quantity of false positives. With more advanced techniques for suppressing common noise (e.g. detrending improvements), the flagging of variables, EBs & known planets, and improvements to the current search algorithms, numerous long-period planets may be found with high levels of confidence.

Chapter 5

Periodic Eclipses of the Young Star PDS 110 Discovered with WASP and KELT Photometry

"Hilarious how people get exited by Fantasies We can't even get clear pictures of Saturn yet lol NASA "scientists" lol" - - JEFF, USA, Daily Mail

Note . The following chapter is heavily based on the paper "Periodic Eclipses of the Young Star PDS 110 Discovered with WASP and KELT Photometry" (Osborn et al., 2017a, ; accepted in MNRAS, April 2017). The detection, compilation of photometric data, simple eclipse model, ISIS spectral analysis, as well as all introduction, discussion and conclusion were performed by the author. TRES spectra analysis, HR Diagram position, SED model, and the circumplanetary ring eclipse model were performed by collaborators.

5.1 Introduction

The transit of dusty circumstellar material in front of a star provides a unique opportunity to resolve the structure of circumstellar and circumplanetary material at a resolution far below the classical limits of direct imaging. Eclipses include circum-secondary discs (ϵ Aur, Carroll et al. (1991); EE Cep, Gałan et al. (2012); KH-15D, Herbst et al. (2002)), gas accretion streams from the circumstellar disc (e.g. Bouvier et al., 1999; Cody et al., 2014; Ansdell et al., 2016), unexplained dimmings from circumstellar dust (around young stars; UX Oris e.g. Dullemond et al. (2003), around main sequence stars, e.g. Boyajian et al. (2016)), and even ring gaps in putative circumplanetary discs (e.g J1407; Mamajek et al., 2012; Kenworthy and Mamajek, 2015).

Unfortunately, these events are rare, with only a dozen or so such eclipsing objects currently known. However, projects like the Wide Angle Survey for Planets (WASP; Pollacco et al., 2006) and the Kilodegree Extremely Little Telescope (KELT; Pepper et al., 2007, 2012) provide long baseline, high-precision time series photometry for a large portion of the entire sky. The combination of baseline, cadence, precision, and sky coverage make these surveys well-suited to search for these "Disk Eclipsing" systems. The Disk Eclipse Search with KELT (DESK) survey has been conducting an archival search for these unique systems in the ~4 million KELT light curves (Rodriguez et al., 2016a) and has already led to the discovery and analysis of 6 previously unknown large dimming events including the periodic dimming events around V409 Tau (Rodriguez et al., 2015), DM Ori (Rodriguez et al., 2016c), and a ~69 year period analogue to ϵ Aur, TYC 2505-672-1 (Rodriguez et al., 2016d). The OGLE survey of the galactic bulge (Udalski, 2003) has also discovered young eclipsing candidates that require follow up (e.g. Scott et al., 2014).

In this paper, we present the light curve of PDS 110, a young star in the Ori OB1 association, which shows two extended, deep dimming events over durations of ~25 days, separated by about 808 days. We interpret these eclipses, the first detected with WASP, as due to the transit of a circumsecondary matter associated with an unseen companion PDS 110b (or B), in a bound Keplerian orbit about PDS 110.

5.2 PDS 110 - Background on the star

PDS 110 (also known as HD 290380, IRAS 05209-0107, GLMP 91, 2MASS J05233100-0104237 and TYC 4753-1534-1) has been observed in many photometric (Garcia-Lario et al., 1990; Alfonso-Garzon et al., 2012; Hernández et al., 2005) and spectroscopic (MacConnell, 1982; Torres et al., 1995; Miroshnichenko et al., 1999; Gregorio-Hetem and Hetem, 2002; Rojas et al., 2008) studies.

Table 5.1: Observational Information about PDS 110

Parameter	Description	Value	Source	Reference(s)
α_{J2000}	Right Ascension (RA)	05:23:31.008	Tycho-2	Høg et al. (2000)
δ_{J2000}	Declination (Dec)	-01:04:23.68	Tycho-2	Høg et al. (2000)
SpT	Spectral Type	keF6 IVeb	...	Miroshnichenko et al. (1999)
U	Johnson U	11.02	PDS	Gregorio-Hetem and Hetem (2002)
B	Johnson B	10.934 ± 0.005	...	Miroshnichenko et al. (1999),Pojmanski (2002)
B_T	Tycho B_T magnitude	11.093 ± 0.058	Tycho-2	Høg et al. (2000)
V	Johnson V	10.422 ± 0.002	ASAS	Pojmanski (2002)
V_T	Tycho V_T magnitude	10.476 ± 0.048	Tycho-2	Høg et al. (2000)
g'	Sloan g'	10.693 ± 0.032	APASS	Henden et al. (2015)
R	Cousins R	10.10	PDS	Gregorio-Hetem and Hetem (2002)
r'	Sloan r'	10.285 ± 0.01	APASS	Henden et al. (2015)
I	Cousins I	9.77	PDS	Gregorio-Hetem and Hetem (2002)
i'	Sloan i'	10.174 ± 0.017	APASS	Henden et al. (2015)
J	2MASS magnitude	9.147 ± 0.021	2MASS	Cutri et al. (2003)
H	2MASS magnitude	8.466 ± 0.042	2MASS	Cutri et al. (2003)
K_s	2MASS magnitude	7.856 ± 0.021	2MASS	Cutri et al. (2003)
WISE1	WISE 3.4 μm band mag	6.941 ± 0.035	WISE	Cutri et al. (2012)
WISE2	WISE 4.6 μm band mag	6.474 ± 0.019	WISE	Cutri et al. (2012)
WISE3	WISE 12 μm band mag	4.512 ± 0.016	WISE	Cutri et al. (2012)
WISE4	WISE 22 μm band mag	1.809 ± 0.021	WISE	Cutri et al. (2012)
IRAS 12μm	IRAS Flux Density (Jy)	0.558 ± 0.056	IRAS	Helou and Walker (1988)
IRAS 25μm	IRAS Flux Density (Jy)	1.68 ± 0.10	IRAS	Helou and Walker (1988)
IRAS 60μm	IRAS Flux Density (Jy)	2.13 ± 0.15	IRAS	Helou and Walker (1988)
IRAS 100μm	IRAS Flux Density (Jy)	1.68	IRAS	Helou and Walker (1988)
μ_α	Proper Motion in RA (mas yr^{-1})	1.146 ±1.067	Gaia	Gaia Collaboration et al. (2016)
μ_δ	Proper Motion in DEC (mas yr^{-1})	-0.338 ± 1.076	Gaia	Gaia Collaboration et al. (2016)
Distance	pc	335 ± 13	Hipparcos	Hernández et al. (2005)

It was also found to have a signficant infrared excess (Garcia-Lario et al., 1990), representing roughly 25% of the total luminosity (Rojas et al., 2008), which likely has comparable contributions from a disk and a more spherical envelope (Gregorio-Hetem and Hetem, 2002). Table 1 summarizes the photometry we will use here. Spectroscopically, it shows Hα in emission with an equivalent width of roughly 6Å and LiI 670.7 nm in absorption with an equivalent width of 0.08mÅ (Gregorio-Hetem and Hetem, 2002). A range of spectral types have been assigned to it (F0 Cannon and Pickering (1949), keF6IVeb Miroshnichenko et al. (1999), F7e Miroshnichenko et al. (1999)). Rojas et al. (2008) made estimates of the luminosity, mass and age, but used a distance of 600 pc which is significantly larger than its measured distance (Gaia Collaboration et al., 2016), leading to overestimates of the mass and luminosity and underestimates of the age. The foreground extinction is small, with $E(B-V) = 0.05$ mag (Miroshnichenko et al., 1999).

PDS 110 has a GAIA parallax of 2.91 ± 0.34 mas, corresponding to a distance of 345 ± 40 pc, and a negligible proper motion (1.15 ± 1.07, −0.34 ± 1.08) mas/year (Gaia Collaboration et al., 2016). This distance makes PDS 110 consistent with being a member of the Ori OB1a association which has an estimated distance of 335 ± 13 pc and similarly small mean proper motion of 0.75 ± 0.29,−0.18 ± 0.22 (Wu et al., 2009). The Ori OB1 association has an estimated age of 7-10 Myr (Briceño et al., 2007; Van Eyken et al., 2012; Ingleby et al., 2014; Ciardi et al., 2014). The group contains numerous B stars, but not

earlier than B1 (Brown et al., 1994) suggesting that the age may be slightly higher (10-15 Myr).

5.3 Data

A 0.3-mag deep eclipse of PDS 110 was first identified in 4.5 seasons of WASP photometry (2007-2012; All photometry is shown in Figure 5.1) during a search of young stellar object light curves. The eclipse was seen from both WASP locations (WASP-N, La Palma and WASP-S, Sutherland), suggesting a real event rather than systematic source.

The validity of this eclipse was further confirmed by inspecting simultaneous ASAS photometry (covering years 2000-2009). Subsequent examination of KELT photometry (4.5 seasons from 2010-2015) identified a second and near-identical eclipse in 2010. ASAN-SN (2011-2016) and IOMC (2006-2008) data was then obtained to search for more eclipses, although extrapolation from the two known events mean subsequent eclipses occurred when PDS 110 was unobservable. However, photometry from KELT and ASAS-SN data from 2010 onwards help rule out interval periods and explore the out-of-eclipse variability.

For KELT and WASP, which have non-conventional passbands and potential offsets, we normalised the median (out-of-eclipse) magnitude of each to the median photometric magnitude of ASAS photometry, which is calibrated to Johnson-V and has the longest-term observations. The combined photometry allows us to rule out integer fractions of the observed eclipse period.

In this section we briefly introduce the origin and analysis of the photometric and spectroscopic data obtained for PDS 110. Figure 5.1 shows full and phase-folded light curves along with views of eclipses observed in 2008 (observed by WASP-North, WASP-S and ASAS) and 2011 (observed by KELT). Figures 5.2 and 5.3 show optical and IR spectroscopy and best-fit models.

5.3.1 WASP

PDS 110 was observed by both WASP-North and WASP-South (described in section 2.6.1) with exposure times of 30s and a cadence of 8-10 minutes. In total 49558 observations were taken, between UT 2008 January 25 and 2013 February 23.

Light curves were further cleaned, initially by removing 3-sigma anomalies and regions with high hourly scatter (e.g. with hourly RMS scatter above 3%). To remove trends present in all nearby stars but not removed by `sysrem` detrending, nightly linear trends were fitted to the median-divided fluxes of 100 bright and non-varying stars within a 25 arcminute aperture. The target light curve was then divided by these residual trends, improving the average flux rms from 6% to 3%.

5.3.2 KELT

The Kilodegree Extremely Little Telescope (KELT) is an all sky, photometric survey of bright stars ($8 < V < 11$) designed to detect transiting planets around bright stars (Pepper et al., 2007, 2012). The project has comprised of two telescopes, KELT-North in Sonoita, AZ, USA and KELT-South in Sutherland, South Africa. Both telescopes have a 42 mm aperture, a broad R-band filter, and observed with a 10-20 minute cadence. Using a Mamiya 645-series wide-angle lens with an 80mm focal length (f/1.9), the telescopes have a $26^\circ \times 26^\circ$ field-of-view, and a $23''$ pixel scale.

PDS 110 is located in KELT-South field 05 (α = 06hr 07m 48.0s, $\delta = +3^\circ\ 00'\ 00''$). The KELT-South telescope observed PDS 110 from UT 2010 February 28 to UT 2015 April 09, obtaining 2892 observations. For a detailed description of the KELT data acquisition and reduction process, see Siverd et al. (2012); Kuhn et al. (2016). The typical per point error is ~0.02 %.

5.3.3 All-Sky Automated Survey (ASAS)

With the goal of finding and cataloging bright variable stars, the All-Sky Automated Survey (ASAS) obtained photometric observations of a large fraction of the sky. The survey observed simultaneously in two bandpasses (V and I) from two observing sites, Las Campanas, Chile and Haleakala, Maui. A detailed description of the survey set up, data acquisition, and reduction pipeline is presented in Pojmanski (1997). At each location are two wide-field Minolta 200/2.8 APO-G telephoto lenses and a 2K×2K Apogee CCD. The telescope and camera set up corresponds to a $8.8^\circ \times 8.8^\circ$ field-of-view and a pixel scale of $13.75''$. PDS 110 was observed from 2001 until 2010[1]. There are 488 ASAS epochs with a typical per-point flux error of 3%.

Both KELT and WASP have non-conventional passbands and potential zero point magnitude offsets. Therefore, to compare them with photometry from other surveys, the out-of-eclipse photometric median was normalised to the out-of-eclipse median of ASAS (Johnson V-band). ASAS photometry confirms the 2008 eclipse seen by WASP.

5.3.4 All-Sky Automated Survey for SuperNovae (ASAS-SN)

The All-Sky Automated Survey for SuperNovae (ASAS-SN) is monitoring the entire sky every two days down to a V-band magnitude of 17. The survey has two separate observing sites, each with four 14 cm Nikon telephoto lenses and 2k × 2k thinned CCD. The FOV is 4.5×4.5 degrees and the pixel scale is $7\farcs8$. PDS 110 was observed 559 times from 2012

[1] ASAS data from http://www.astrouw.edu.pl/asas/?page=aasc

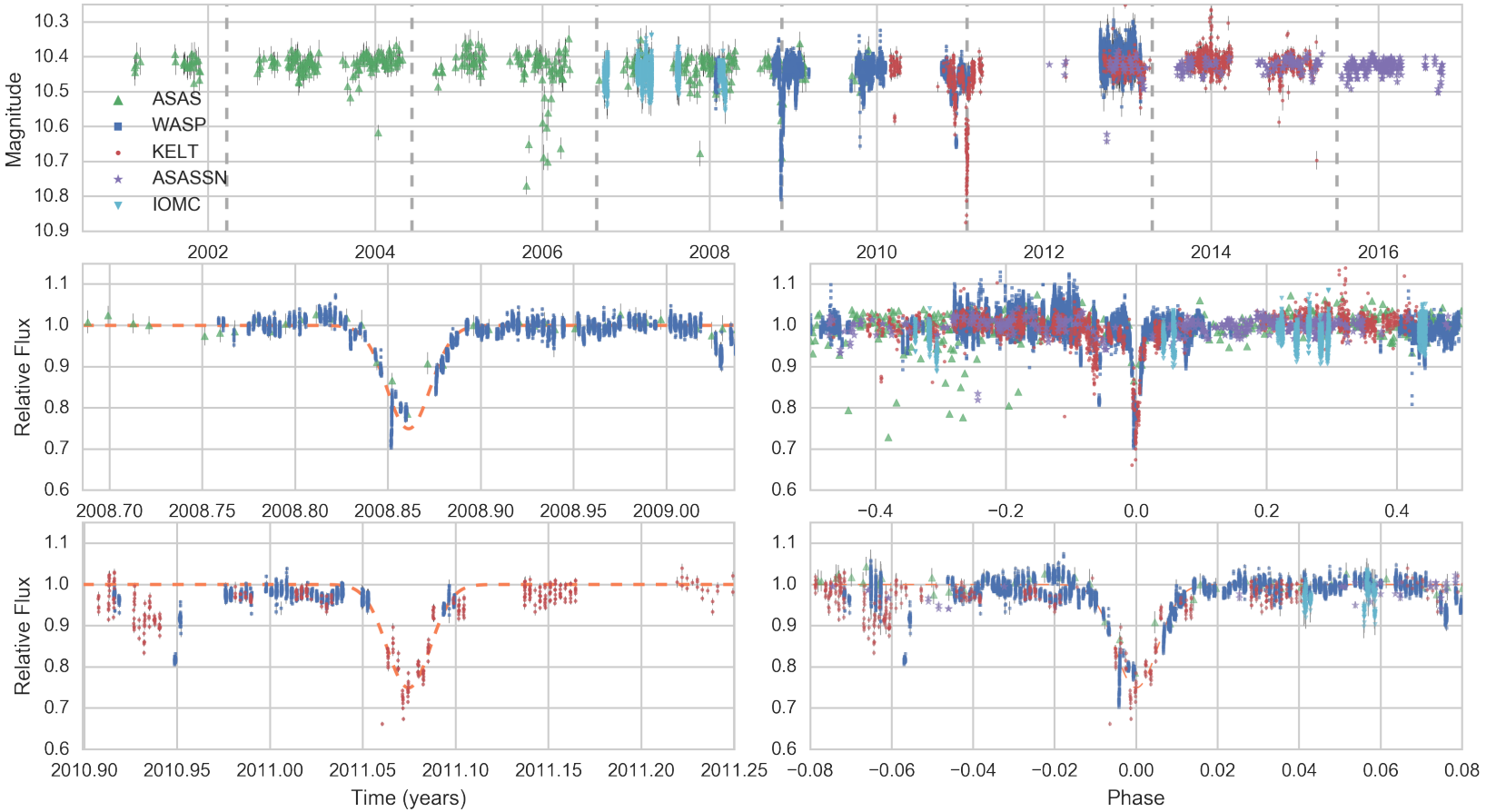

Figure 5.1: WASP (blue squares), KELT (red circles), ASAS (green triangles), ASAS-SN (purple stars) and IORC (turquoise triangles) observations. Upper figure: plotted from 2002 to 2016. Eclipse times are shown with dashed vertical lines. Lower left figures: individual eclipses in 2008 (upper) and 2011 (lower). Lower right figures: phase-folded light curve with full phase coverage (upper) and zoomed to the eclipse (lower). The best-fit eclipse model (see section 4.3) is overplotted in orange in these cases. In all cases we have applied a vertical offset to the KELT and WASP data to match the quiescent magnitude seen in the ASAS *V*-band data. However, there has been no attempt to place all the data on the same absolute scale.

until 2016 with an average per-point rms of 1%. For a complete description of the observing strategy and reduction process, see Shappee et al. (2014).

5.3.5 INTEGRAL-OMC

The INTErnational Gamma-Ray Astrophysics Laboratory (INTEGRAL) (Winkler et al., 2003) is an ESA satellite in orbit since 2002. As well as performing gamma ray and X-ray observations, INTERGRAL possesses an Optical Monitoring Camera (OMC, Mas-Hesse et al. (2003)), a V-band (500-600nm) imager designed to measure the target's optical brightness and position. It observed PDS-110 on 14 occasions from 2006 to 2008, taking over 2000 individual flux measurements with an average cadence of 2.7 minutes and a median precision of 1.4% (Alfonso-Garzon et al., 2012)[2].

5.3.6 Optical spectrum

A low-resolution (R∼3000) spectrum of PDS 110 was taken with the ISIS spectrograph in the R600B and R600R modes on the 4.2-m William Herschel Telescope at the ING, La Palma (shown in Figure 5.2). The spectrum exhibits a strong Hα emission line, moderate emission in the Ca H & K line cores, and Li I absorption at λ = 670.8 & 610.3 nm – all consistent with previous measurements (Torres et al., 1995; Rojas et al., 2008). To characterise the spectra, a grid of 1200 synthetic spectra were generated with the Python package iSpec (Blanco-Cuaresma et al., 2014) using the MARCS model atmospheres (Gustafsson et al., 2008) and compared with the optical spectrum. The best-fit models had $T_{\rm eff}$ = 6500 ± 250, $\log(g) \simeq 3.8$ and [Fe/H] = -0.5 ± 0.2, in agreement with previous estimates of the stellar parameters (e.g. 6653 K, Gregorio-Hetem and Hetem, 2002)

5.3.7 TRES spectra

We have taken seven spectra of PDS 110 with the Tillinghast Reflector Echelle Spectrograph (TRES, Fűrész et al. (2008); Szentgyorgyi and Furész (2007)) on the 1.5 m telescope at the Fred Lawrence Whipple Observatory (FLWO), Arizona. The TRES spectra have resolution R ∼ 44000 and were reduced, extracted, and analysed with the Spectral Parameter Classification (SPC) procedure of Buchhave et al. (2012). We ran this without priors for each spectrum (with an average SNR of 53.5) and took a weighted average of the resulting stellar parameters. These give an effective temperature of $T_{\rm eff}$ = 6360 ± 110K, a log g of 3.89 ± 0.17 and [Fe/H]=0.06 ± 0.06. Only metallicity shows a significant difference from previous estimates of stellar parameters. The higher precision of the TRES spectrum

[2]IOMC data accessed from Vizier at http://vizier.cfa.harvard.edu/viz-bin/VizieR?-source=J/A+A/548/A79

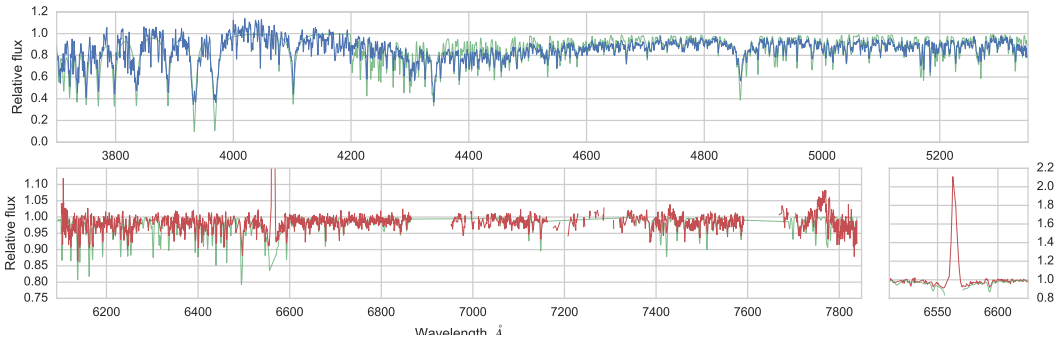

Figure 5.2: Red and Blue spectra of PDS 110 taken with the WHT/ISIS. The best-fit synthetic spectrum is shown in green. H-alpha emission is shown in a separate plot in the lower right.

suggests this value is more precise, and we adopt it here. The star is rapidly rotating with $\upsilon \sin i_\star$ of 64.3 ± 0.9 km.s^{-1}

5.4 Analysis

5.4.1 HR Diagram Position

Previously published spectral types span F5-F7 (Miroshnichenko et al., 1999; Suárez et al., 2006; Rojas et al., 2008). Based on the $T_{\rm eff}$ scale for pre-MS stars from Pecaut and Mamajek (2013), a spectral type of F6 (±1 subtype) translates to a $T_{\rm eff}$ estimate of 6250 ± 140 K (also consistent with the $T_{\rm eff}$ estimate with larger uncertainty derived from the optical spectrum). Based on these estimates, we adopt a mean $T_{\rm eff}$ estimate of 6450 ± 200 K.

On the scale of Pecaut and Mamajek (2016), this temperature translates to a V-band bolometric correction of $BC_V \simeq -0.02 \pm 0.02$ mag. Fitting the UBV photometry listed in Table 1 alone, the range of quoted spectral types translates to a reddening of $E(B-V) \simeq 0.09$ mag. Combining this estimate along with the two previous independent reddening estimates from §2, we adopt a mean reddening estimate of $E(B-V) \simeq 0.07 \pm 0.02$ and V-band extinction of $A_V \simeq 0.24 \pm 0.07$ mag.

Adopting the mean distance to the Ori OB1a from Hernández et al. (2005) as representative for PDS 110, we can now calculate stellar parameters like absolute magnitude ($M_V = 2.54 \pm 0.11$), apparent bolometric magnitude ($m_{\rm bol} = 10.14 \pm 0.08$), absolute bolometric magnitude ($M_{\rm bol} = 2.52 \pm 0.11$), luminosity ($\log(L/L_\odot) = 0.89 \pm 0.05$ dex), and radius ($R = 2.23 \pm 0.18\ R_\odot$). Interpolating between the pre-MS isochrones from Siess et al. (2000), one estimates a mass of $1.6\,M_\odot^N$ and age of ~11 Myr, consistent with the rest of Ori OB1a.

Table 5.2: Determined Stellar Parameters for PDS 110

M_V	2.54 ± 0.11	Teff	6450 ± 200 K
$E(B-V)$	0.09mag	$\log g$	3.8 ± 0.3
A_V	0.24 ± 0.07	[Fe/H]	-0.5 ± 0.2
$\log(L/L_\odot)$	0.89 ± 0.05	R_s	$2.23 \pm 0.18 R_\odot$
age	~ 11 Myr	M_s	$\sim 1.6 M_\odot$

5.4.2 SED Disk model

To model the SED of PDS 110, we used the self-consistent irradiated, accretion disk models of D'Alessio et al. (2006) to create a model grid using the stellar parameters of PDS 110 in Table 2. We adopted a dust sublimation temperature of 1400 K to set the inner radius of the disk. We included outer disk radii of 50 AU, 150 AU, and 300 AU, viscosity parameters (α) of 0.01, 0.001, and 0.0001 and dust settling parameters (ε; i.e. the dust-to-gas mass ratio in the upper disk layers relative to the standard dust-to-gas mass ratio) of 1.0, 0.5, 0.1, 0.01, 0.001, and 0.0001. The minimum grain size in the disk atmosphere was held fixed at 0.005 μm while we varied the maximum grain size between 0.25, 1.0, and 2.0 μm to reproduce the 10 μm silicate emission feature. The inclination angle was fixed at 60 degrees.

Based on χ-squared values, the best fitting model has $a_{\max}$=0.25, ε=0.5, α=0.01, and an outer radius of 300 AU. Uncertainties are beyond the scope of this analysis. This disk model has a mass of 0.006 $M_\odot$ using Equation 38 in D'Alessio et al. (1999). While there are no millimeter data available to provide spatial constraints, a large outer radius of 300 AU is consistent with the significant MIR and FIR excess of this object given that the strength of the disk emission is related to the disk mass which in turn depends on radius (D'Alessio et al., 1999). We also note that ε=0.5 corresponds to a relatively flared disk. Here we measure a disk height at 2 AU of 0.3 AU.

5.4.3 Photometry

Some out-of-eclipse variability is seen with peak-to-peak amplitudes on the order of ~3%. From the measured $v \sin(i)$ (64km.s^{-1}) we would naively estimate a P_{rot} of ~1.7d. However, searches with lomb-scargle periodograms (Press and Rybicki, 1989) on both the entire dataset and shorter segments do not detect any coherent period of variation attributable to rotation, with the signals dominated by day- and month- aliases from the ground-based surveys. This suggests variations are stochastic or quasi-periodic, as has been seen for T-Tauri stars before (Rucinski et al., 2008; Siwak et al., 2011). The (space-based) IOMC light curves show candidate signals at 1.11d and 0.304d, with an amplitude of around 3%. However, like the ground-based data, the time coverage is non-continuous. The KELT light curves alone show a possible signal with P=67d.

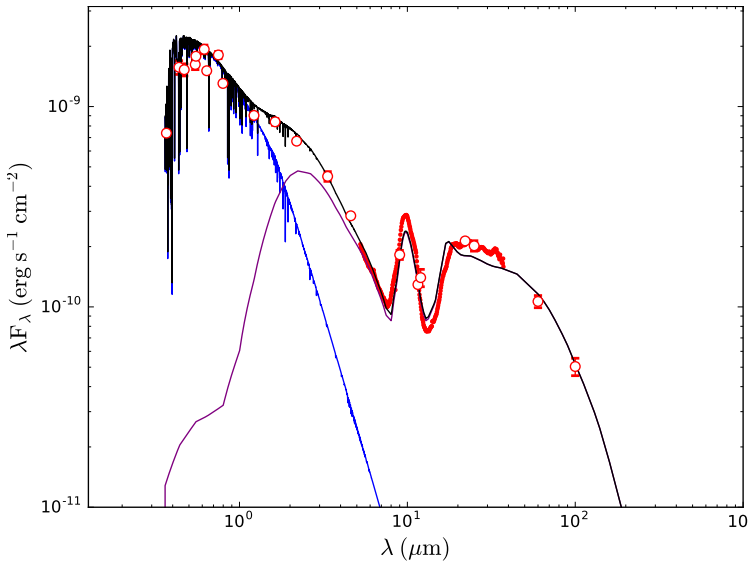

Figure 5.3: Best-fitting model (black) to the SED of PDS 110. Photometry (red) are from Table 1 and *Spitzer* IRS (Werner et al., 2004; Houck et al., 2004) low-resolution spectra are from the Cornell Atlas of SpitzerIRS Sources (CASSIS Lebouteiller et al., 2011). The best-fitting model includes emission from a NextGen stellar photosphere (Hauschildt et al., 1999) (blue) and disk emission (purple).

Some dimmings, slightly shallower in depth and shorter in duration than the eclipses (only 3 to 4 points, or 9 to 12 days long) are also seen in ASAS data in 2006. These are inconsistent with the proposed period (see section 4) seen and the lack of simultaneous data also means we are unable to rule out whether these are caused by systematics or from a genuine drop in stellar flux.

All observations thus far have also been monochromatic, with the ASAS, KELT and WASP data all focused on the V/R bands, and showing little differences in variability between one another in- or out-of-eclipse.

5.4.4 Simple Eclipse Model

We fit a simple Gaussian model to the phase-folded combined photometry to estimated physical parameters of the eclipse. An MCMC model was run to determine uncertainties on the best-fit with `emcee` (Foreman-Mackey et al., 2013a) in `Python`, using a total of 1 million steps across numerous walkers. The result of the model, and output posteriors, are shown in Figure 5.4. We find the period to be 808 ± 3 days with an eclipse centred at HJD=2454781 ± 2, depth of $26 \pm 6\%$ and full-width half maximum of 7 ± 2 days. The residuals show that the in-transit variability increases substantially compared to out-of-transit, indicative of finer structure in the eclipse light curve (see Figure 5.4).

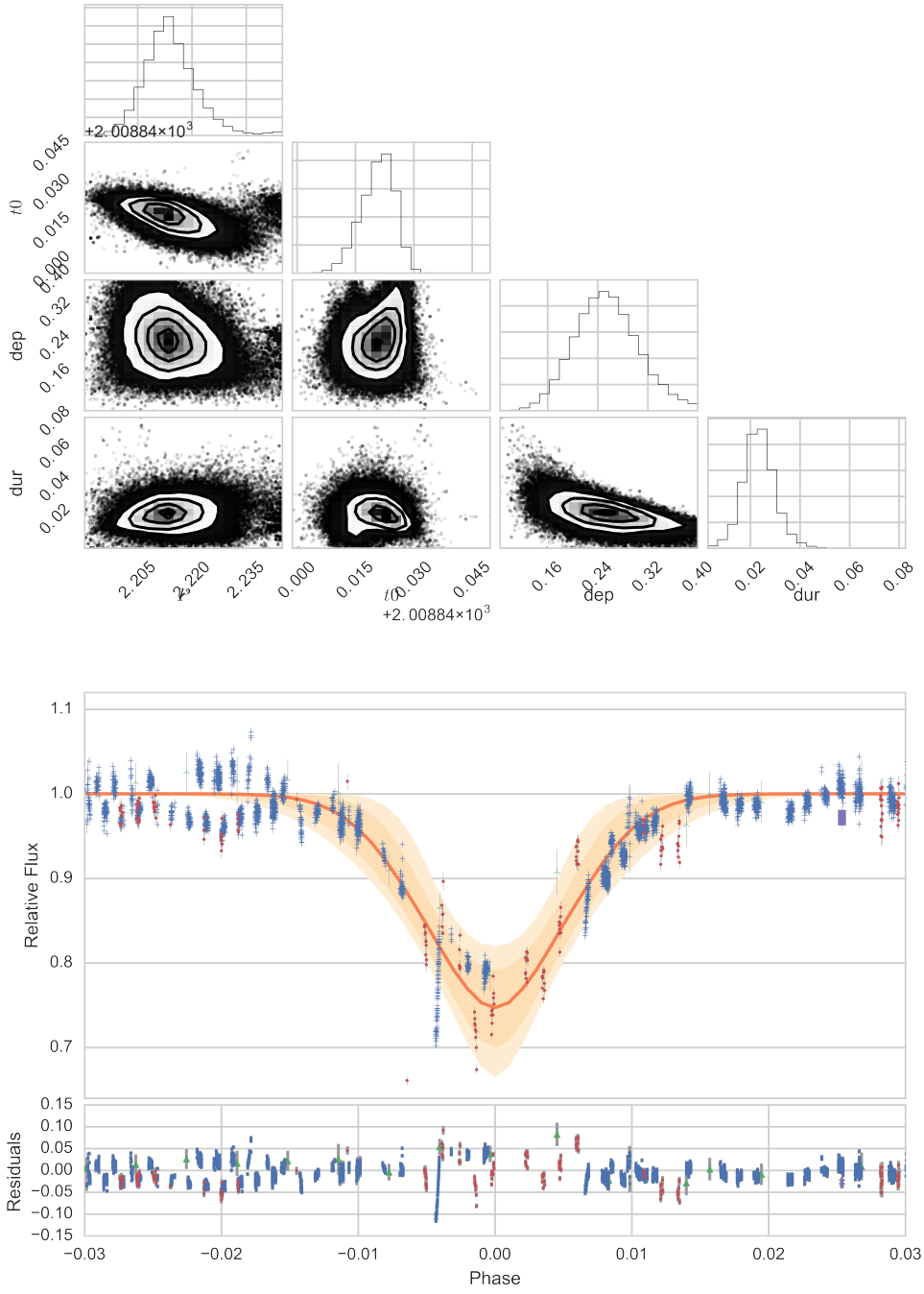

Figure 5.4: **upper:** MCMC posteriors for the gaussian fit model: duration (or FWHM), depth, and t0). **lower**: A best-fit Gaussian model compared to phase-folded data with 1-/2-sigma error regions in orange/yellow. Blue and red points show measurements from WASP and KELT respectively and have been phase-folded on the median period value.

5.5 Interpretation and Discussion

5.5.1 Summary of Information

We have detected two near-identical eclipses of the bright (V=10.4 mag), young (~10Myr) star PDS-110 in the OB1a association with WASP, KELT and ASAS photometry. The two events are separated by 808 ± 2 days and have nearly identical shapes, durations (~ 25 days) and depths (~ 26%). Sharp in-eclipse gradients of up to than $0.5L_{\rm star}$/day (5 of the 6 nights with gradients > $0.1L_{\rm star}$/day observed by WASP occur in-eclipse) suggest fine structure in the eclipsing material.The similarities of the eclipses strongly suggest that they are periodic. Unfortunately, despite 25 seasons of data across 15 years and five surveys, all other predicted eclipses lie in observing gaps.

A study of the star and disc suggest that PDS-110 is a young Ge/Fe star surrounded by a thick protoplanetary disk which contributes to as much as ~25% of the total luminosity. Since we see significant optical emission and negligible extinction, we must be viewing the star at a significant inclination relative to the stellar disc. Hence any eclipsing material must reside at a significant altitude above the disk midplane.

For any eclipse hypothesis we must take into account the shallow depth of this eclipse, its interesting substructure, and whether the material is optically thick or thin. The most probable explanation is that the occulting object entirely crosses the star, but is optically thin. In this case, the slow and Gaussian-like in- and egress gradients are the result of density gradients within a diffuse occulting dust cloud. Sharp features during the eclipse can be explained as regions of sharply varying density within the cloud, such as gaps, clumps, thicker rings or ring gaps. This would appear the most plausible scenario, although a mix of sharp optically thick regions and low-opacity dust regions, as has been proposed for the J1407b ring system, may also work. These scenarios can be disentangled with multiband photometry during eclipse (see Section 6).

There exist two potential mechanisms for the eclipses. First that circumstellar dust caused the eclipse; and second that the eclipse of a secondary body caused the eclipse. We explore these hypothesis in detail here.

5.5.2 Circumstellar structure scenario

Many processes within the large circumstellar dust disc could disturb dust above the midplane and into eclipse. One possibility is from a spiral arm or a vortex. However, such scenarios are likely concentrated in the disk midplane, have significant azimuthal extent (of order radians), and move much more slowly than the material itself, hence not conducive to short, deep eclipses.

KH-15D-like dimmings, in which one member of a binary pair passes behind the circumstellar disc each orbit is another possibility. However, a binary on a 2 year orbit would clear the entire inner disc region - inconsistent with the disc model needed to explain the SED. If the total obscuration of a companion star leads to a ~30% dip during eclipse, it must be less than $-2.5 \log 0.3/0.7$ or only ~0.9 magnitudes fainter. Hence such a bright companion would likely have been detected in either the CCF of the optical spectra or in the SED model.

Although the mechanism of eclipse remains unsolved, the deep and aperiodic dimmings or UX Ori stars (known as UXOrs), which are seen around many Herbig Ae/Be stars (Bertout, 2000) are similar to the eclispes seen in PDS-110. Some eclipses resemble a single PDS-110 eclipse in depth or duration (e.g. Caballero, 2010). However, these dimming events tend to be deeper (often several magnitudes), longer-duration (weeks to years) and are aperiodic. Lightcurves of those UXOrs found also tend to exhibit many events, usually with differing depths and durations.

The proposed mechanisms for UXOr-like dimming include hydrodynamical fluctuations at the inner edge of self-shadowed circumstellar disks (Dullemond et al., 2003), occultations of dust clumps in their circumstellar disk (Grinin, 1988; Voshchinnikov, 1989; Grady et al., 2000, etc.), and the eclipsing debris of planetesimal collisions in young asteroid belts (Kennedy et al., 2017). As an F-type star there is no guarantee that the self-shadowing proposed as a cause of UXOr behaviour is present for PDS-110. Our tentative SED fit also suggests an unsettled (ϵ=0.5) and moderately turbulent (α=0.01) disc - atypical for UXOrs (Dullemond and Dominik, 2004). Regardless, the inferred period for the events, and their rarity, suggests the occulting material lies well beyond the disk's inner edge at the sublimation radius. The lack of other significant variability suggests that the occulting material lies well above the "main" disk, and that the disk structure may be relatively unimportant for determining the nature of the eclipses.

While this style of eclipse does not fit what is observed for PDS-110, it is possible that we could be observing a new UXOr-like eclipse behaviour.

Regardless of the formation mechanism, any diffuse clumps would be subject to shear. The angular shear rate is $R d\Omega/dR = -3\Omega/2$, so across a clump of radius $R_{\rm cl}$ the shear velocity is $v_{\rm sh} = 6\pi R_{\rm cl}/P$ (where P is the orbital period). That is, a clump of any size will be sheared out by a factor of 6π after one orbit, and the radial and vertical optical depth will be roughly 6π times lower. Any disk structure will shear out rapidly, and on successive orbits will have a very different azimuthal extent. Thus, the similar shapes of the eclipses mean that if they were caused by the same clump, an additional means to maintain the concentration of this clump is needed.

5.5.3 Circumsecondary structure scenario

We have therefore established that the eclipsing object is highly likely to be periodic, and unlikely to be formed of streams or clumps of dust. The simplest way of concentrating material is with the gravitational attraction of a massive body. This is the established interpretation for many long-duration young star eclipses in young systems, with orbits from 48d (Herbst et al., 1994) to ~70 years (Rodriguez et al., 2016b). We explore here the likely characteristics of such a body by considering its Hill Sphere.

Hill Sphere Considerations

With an orbital period of 808 days, and the total mass of the system of 1.6 solar masses, we derive a circular Keplerian velocity of 27km.s^{-1}. By assuming an eclipse is caused by an optically-thick knife-edge moving across the star, the gradient of the steepest slope can be used to give a minimum velocity of the eclipsing object. For the sharp flux increase seen at 2008.85 (~20% in 6 hours) in WASP data (Figure 1), this gives $v_{\rm min}$ = 13km.s^{-1}. An optically thin or angled structure could produce faster velocities for a given slope, this is consistent with the implied orbital motion of 27km.s^{-1}. From the Keplerian orbital speed and eclipse duration (~21 days), we can derive the diameter of the eclipsing object to be ~0.3 au, or about 50 million km. A lower limit on the mass of the secondary companion can be derived assuming that the cloud is within the Hill sphere of the secondary.

The Hill radius can be approximated as: $a_H \approx a\,(1-e)\,(m/3M_s)^{1/3}$ where a is the orbital semi major axis, e is the orbital eccentricity, m is the mass of the secondary and M_s is the primary (stellar) mass. If the duration of the eclipse is $t_{\rm ecl}$ days, then the diameter of the disk $d_{\rm disk} = v_{\rm circ}.t_{\rm ecl}$, where the circular velocity of the companion $v_{\rm circ} = 2\pi a/P$ and $t_{\rm ecl}$ the duration of the eclipse. Combining these expressions with Kepler's third law, the mass of the secondary companion is: $m = 2M_s\,(\pi t_{\rm ecl}/\xi P)^3$ where P is the orbital period of the secondary companion and $0 \leqslant \xi \leqslant 1.0$ is the fraction of the Hill sphere that the disk fills. $\xi = 0.3$ is typical for a prograde rotating disk (Nesvorný et al., 2003).

Assuming $M_s = 1.60 M_\odot$ and $t_{\rm ecl}$ = 21 d and P = 808 d gives: $m = 1.8{\rm M_{Jup}}\,(1/\xi)^3$ Using the prograde stability criterion of $\xi = 0.3$ (Quillen and Trilling, 1998), the mass is 68 $\rm M_{Jup}$ and for $\xi = 0.6$, this becomes 8.5 $\rm M_{Jup}$. Increasing the eclipse duration (for example, by including the shallow dips seen 15-20 days before and after) will substantially increase this mass limit (to > 20$\rm M_{Jup}$ in the case of a 40 day eclipse).

Such a body would likely also perturb a gap in the circumstellar disc at 2.2AU. We recomputed the SED model with a narrow gap at this radius and found it to be consistent with the data, with negligible difference to a gapless model.

Inclination Considerations

The two eclipses have similar duration of ~25 days and so we assume that the cloud has a constant size. We hypothesize that the eclipse is caused by the passage of a large optically thin cloud that contains an unseen secondary companion which holds the cloud together in dynamic equilibrium, and that the companion and cloud orbit around the primary.

In the cases of KH-15D, ϵ Aur and EE Cep the secondaries are stars, whereas for J1407 the massive body at the centre of the disc appears to be of planetary or brown dwarf mass. In order to cause the eclipse, either:

(1) The secondary body is large and on an orbit with low mutual inclination to the disc, but with highly inclined (Uranus-like) circumsecondary material which protrudes above the circumprimary disc and passes our line-of-sight of the primary star. If, as our lack of reddening suggests, we are viewing PDS-110 at an angle moderately inclined from edge-on ($\sim 30°$), the eclipsing secondary disc must be greater than ~1AU in radius, hence stellar in mass. This, it would likely be detected as anomalous flux in the optical spectra and SED fit.

(2) The secondary body is small but has significant orbital inclination with respect to the disc. Such an orbital scenario could occur due to scattering. This is our favoured scenario, and would be invisible except during eclipse. A figure representing this scenario PDS 110 system is shown in Figure 5.6.

Circumplanetary Ring Model

The WASP eclipse shows substructure over individual nights in the form of steep gradients similar to those seen towards J1407 (Mamajek et al. 2014). While the interpretation is uncertain, we briefly consider the implications of a circumplanetary ring model using the framework of Kenworthy and Mamajek (2015). The rapid changes seen in eclipse, reminiscent of J1407 (Mamajek et al., 2012), could be interpreted as the passage of a Hill sphere filling ring system around a secondary companion, passing across the line of sight of the star. To explore whether such a mechanism could explain the PDS 110 eclipse, we applied the exoring fitting method of Kenworthy and Mamajek (2015) to the WASP eclipse light curve.

We consider the light curve slopes in the WASP and KELT light curves separately. We set the midpoint of the WASP eclipse as 2454780.7 days, as determined by the Gaussian fit carried out in Section 4.2, and we take the centre of the KELT eclipse to be at 2455590.4 days, determined by visual inspection of the two light curves and adjusting them so that the photometry of the different epochs gives the most consistent match in both photometry and in the matching of the light curve gradients. This result suggests a period of 809.7d, within

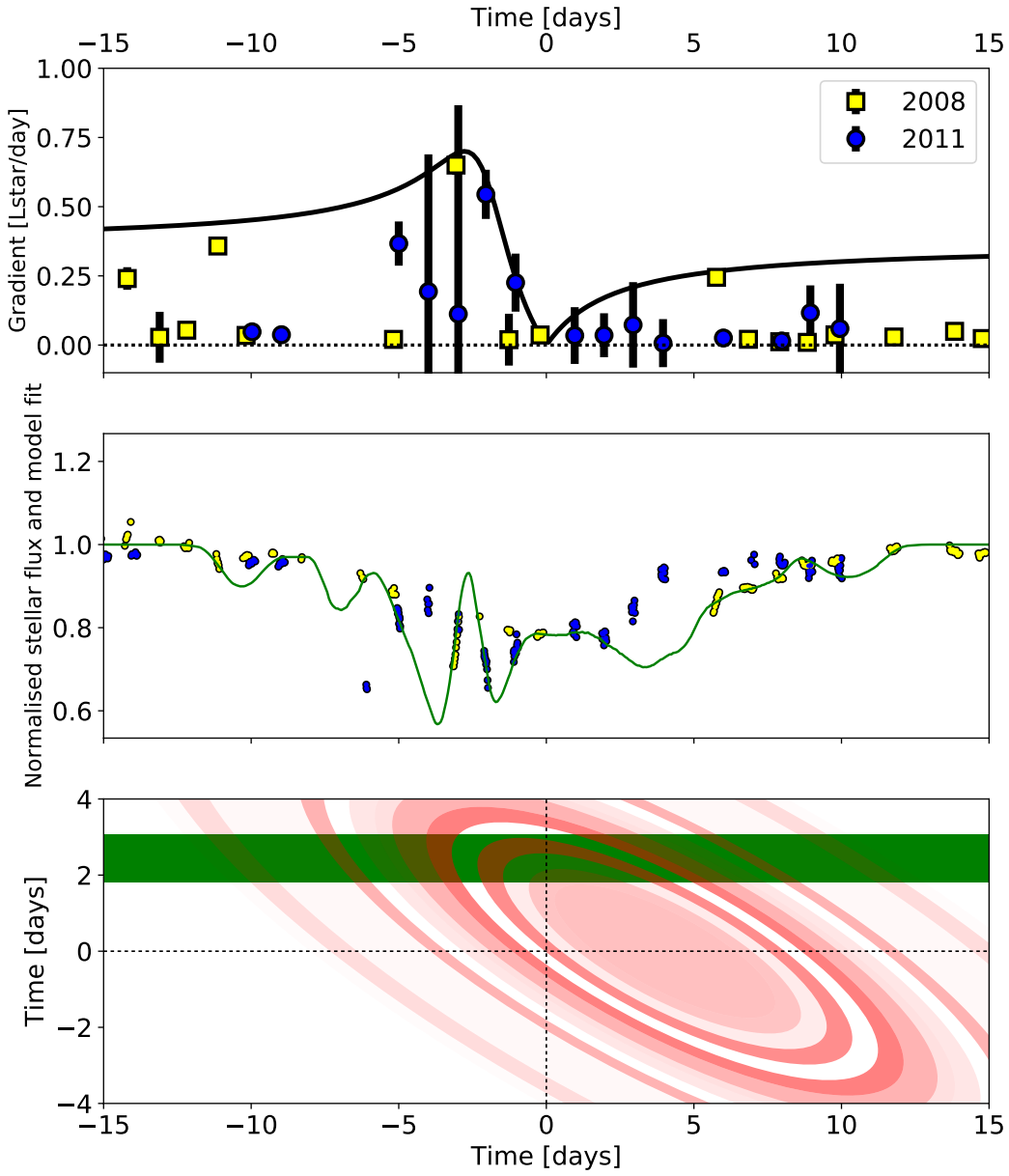

Figure 5.5: The circumsecondary ring model. **Upper panel:** Absolute light curve gradients in stellar luminosity per day seen in WASP photometry (yellow squares) and KELT (blue circles), and a maximum fit line (black) from which the macro parameters of the system is interpreted (e.g. disc orientation). **Central panel**: The photometric prediction of one best-fitting symmetrical ring model (green line) with WASP & KELT photometry (yellow & blue points). **Lower panel**: A schematic view of this model ring system (red) crossing the stellar disc (green band).

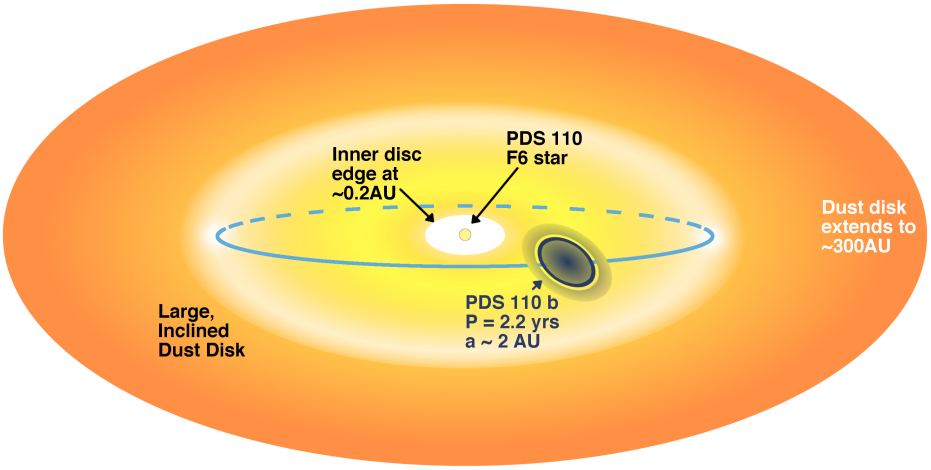

Figure 5.6: A sketch of the PDS 110 system. The primary star is surrounded by a warm disk of dust inclined away from edge-on. Orbiting around the primary star is a secondary companion with an extended disk which eclipses the primary every 808 days.

uncertainty of the analysis performed in Section 5.4.4.

The measurements of light curve gradient as a function of time from the centre of the respective WASP and KELT eclipses are shown in Figure 5.5. The figure shows that there are seven light curve gradients above 0.1 Lstar/day during the ingress of PDS 110b, compared to only one during egress. WASP detects 5 slopes and KELT detects three significant slopes (best-fit slope gradient and $1-\sigma$ uncertainty > 0). From this we conclude that many more steep gradients are seen during ingress in both eclipse events, and in the context of the ring models, this implies an eclipsing object with small spatial scale structure similar to that seen in J1407b. These gradients are used to determine the orientation of the ring system following the method of (Kenworthy and Mamajek, 2015, Section 3.1). By fitting the measured gradients g(t) to the model gradients G(t) we achieve the fit shown in the upper panel of Figure 5.5 as the solid black curve. All gradients must lie on or below this curve for there to be a consistent ring model. The macro-scale disc parameters determined from this fit are an Impact parameter of 2.45 d, a ring centre offset of 4.02 d (both in velocity space), an apparent disk inclination of 74°, and total obliquity of the disk plane to the orbital plane of 26°.

We then model the ring radii and transmissions as the convolution of the stellar disc (R=2.23$R_{\odot}$) with the ring parameters. Minimization of ring transmissions produced the ring model as seen in lower panels Figure 5.5

The incomplete coverage of both eclipse events leads to several plausible ring solutions, of which we show just one in Figure 5. The ring model fits both epochs well in several places, and shows deviations in others. From the plot of light curve gradients, where we

can see several high gradients on the ingress of the transit in both epochs, we conclude that a tilted disk containing azimuthal structure at high spatial frequencies is a reasonable fit to the data. There isn't a unique solution using azimuthally symmetric structures, which may be due to several causes: (i) We are seeing at different clocking angles in successive transits (eg from a spiral pattern), (ii) the intrinsic stochastic variability of the parent star is affecting the derived photometry and light curve gradients, (iii) precession of the disk between successive transits, (iv) the eclipses are instead aperiodic dimmings caused by unexplained dust disc processes. A comprehensive photometric monitoring campaign during future eclipses will help resolve these ambiguities in the interpretation of this object.

5.6 Future Observations

While we favor the presence of dust structure around a periodic secondary companion as the cause of the eclipses, additional data is needed to test it. In particular, the next eclipse will take place on HJD=2458015.5 ± 10 (Sept 9-30 2017). Unfortunately, it will only be observable for a few hours each night from the ground, and space based observations may be needed for better temporal coverage of the event. The presence or absence of an eclipse will immediately settle the question of periodicity.

High cadence and low noise light curves during the eclipse will better constrain the presence of any smaller scale structures in the eclipsing material, potentially confirming the hypothesis that it is a disk of material with gaps and other structures orbiting a low mass secondary. Color information during the eclipse can determine if the obscuration is due to small dust grains or larger bodies that produce more achromatic absorption. The continuing out-of-eclipse monitoring by photometric surveys may detect other eclipsing structures and further characterize any other variability.

We have received 40 hours of time with the 0.4m telescopes of the Las Cumbres Observatory (Shporer et al., 2010), a multi-longitudinal network of robotic telescopes that will allow us to observe between 3 to 9 flux measurements per day, with gaps as short as ~6 hours (proposal ID: "Gomez_345_2017AB").

A secondary should produce radial velocity variations in the primary of $\sim$ 200 m/s (for a $10 M_{\rm Jup}$ companion) that may be measurable. The difficulty is that the fast rotation and variability of the primary will limit the precision of radial velocity measurements. While the scales corresponding to the orbit of the potential secondary ($\sim$ 2 AU) cannot be resolved in sub-millimeter observations, they can characterize the disk on larger scales (10s of AU) and search for distortions or gaps in the outer disk that might indicate the presence of other massive bodies in the system.

5.7 Conclusions

We have detected two near-identical eclipses of the bright (V=10.4 mag), young (~10Myr) star PDS-110 in the OB1a association with WASP, KELT and ASAS photometry. Further ASAS-SN and IOMC photometry of the star have increased the photometric coverage of this star to 25 seasons of data across 15 years. We interpret these eclipses to be caused by the same optically-thin clump of material on a 808 ± 2 day orbit around the star.

Despite a large circumstellar disc around PDS-110, such a scenario cannot be caused by lose clumps of dust above the disc plane, as shearing forces would not maintain eclipse depth and duration across 2.2 years. Therefore, we interpret the eclipse structure to be gravitationally bound around a companion body, which must have mass > $1.8 M_{Jup}$.

Such a body much be significantly inclined from the circumstellar disc to eclipse the star. The body may be surrounded by rings, as has been hypothesised for J1407, with the sharp photometric gradients seen at t_0 ± 5 days being the result of the transit of a ring gap. This hypothesis can be tested, and the orbiting body studied in much greater detail, in September 2017 when we predict the next eclipse to take place.

Chapter 6

Single Transiting Exoplanet Candidates from K2

"Funny how these new planets are trillions of miles away where the can't be reached te be full proven,and we only have the words of these people. Makes me think they make stuff up just to keep the space programme and jobs."

YorkshireLass, Daily Mail, Feb 2017

Note: The following chapter is heavily based on the paper "Single transit candidates from K2: detection and period estimation" (Osborn et al., 2016, ; publised in MNRAS, 2016). All analysis was performed by the lead author. The searches for candidate planets were led by myself, but involved the help of a team of people at Warwick, who also contributed ideas and discussions. An external collaborator also contributed candidates, many of which were found contemporaneously in our search, but some of which were previously undetected.

6.1 Introduction

The occurrence rates of transiting planets with periods on the order of months (most precisely determined by *Kepler*, e.g. Fressin et al., 2013) suggest that there exist a large number of long-period planets. With K2 observing with a reduced mission duration of 80 days since 2014 (compared to 1400 days for the primary mission), such planets are likely to only transit once. With typical photometric precision of 150ppm hr^{-1}, planets with transit depths over $\sim$ 1ppt offer the potential for discovery from just a single event. Such signals may then constitute strong planetary candidates with undefined orbital parameters, similar to those detected by microlensing surveys (e.g. Bennett and Rhie, 1996).

The detection of single transits was speculated upon prior to the launch of *Kepler* (Yee and Gaudi, 2008), and many long-period planet candidates were subsequently detected from single transits during the 4-year primary mission. These included Wang et al. (2015), Uehara et al. (2016) and Foreman-Mackey et al. (2016), giving a total of 67 single transit candidates. In the first two studies, orbital periods were estimated for these candidates using a non-specific transit model. Three of the the systems found by Wang et al. (2015) were subsequently validated through probabilistic methods.

The first example of the detection and subsequent confirmation of a single transiting exoplanet occurred during K2's engineering test campaign. During the 6.5 days of stable photometry, a single transit of K2-2 b was spotted (Vanderburg et al., 2015b). Subsequent follow-up with both spectroscopy (HARPS) and photometry (MOST) determined that the planet was a $2.5R_{\oplus}$ mini-Neptune on a 9.12d orbit. However, the longer duration of subsequent campaigns means planets capable of being detected in a single transit will likely have orbital periods of 50 days or more. This makes follow-up more challenging as RV signals are weaker (equation 1.8), and the absolute period uncertainty needed to reobserve a transit is comparatively large.

Here we perform a search for the transits of long-period planets in 12 campaigns of K2 (Engineering campaign and fields 0 to 10), detecting 71 new candidate events. We also develop the Bayesian fitting tool `Namaste` to estimate orbital parameters specifically for single transiting planets. We show that, provided the host star can be characterised, the information contained within a single transit allows an accurate estimate of a planet's orbital period. We obtain period estimates for six *Kepler* planets as proof of concept and apply the technique to our long-period planet candidates.

6.1.1 Single Transit Event Occurrence Rate

To assess the number of potential single transits detectable with *K2* three separate simple analyses were performed - studying the detectability of confirmed *Kepler* planets, with giant

planet occurrence rates from both RVs and transit, and finally from occurrence rates of all transiting planets. In all cases, we assume gapless K2 data with white noise uncertainties, rather than performing injection/recovery in genuine K2 data.

From its initial sample of $\sim$ 150,000 stars, *Kepler* detected 101 planets and 828 planet candidates with periods longer than 50 days. Using values from the exoplanet archive (Akeson et al., 2013, - accessed 2015-11-14), we calculated the SNR of the Kepler candidates to determine how many might be detectable from a single transit:

$$\mathrm{SNR} = \frac{\Delta F}{\sigma_w}\sqrt{t_{\mathrm{dur}}} \tag{6.1}$$

from Howard et al. (2012). The white noise can be found using:

$$\sigma_w = p.\frac{\sqrt{f_{12}.10^{-0.4(K_p-12)}t_{\mathrm{int}} + n_a.N_R^2}}{\sqrt{n_{\mathrm{frames}}}f_{\mathrm{kep}}t_{\mathrm{int}}} \tag{6.2}$$

where p is a value accounting for other noise sources, f_{12} is the flux at $K_p = 12$, t_{int} is the integration time, N_R is the readout noise, n_a is the number of pixels in the aperture, n_{frames} is the number of frames per cadence, and K_p is the magnitude in the Kepler bandpass. Using typical values for long cadence gives:

$$\sigma_{\mathrm{w,cad}} = 1.2\frac{\sqrt{1.74\times10^5\times10^{-0.4(K_p-12)}\times6 + 20\times120^2}}{\sqrt{270}1.74\times10^5\times10^{-0.4(K_p-12)}\times6}\,[1] \tag{6.3}$$

Using this formulation, and assuming only white noise, 53% of Kepler planets exhibit deep enough transits to allow their detection from a single transit ($> 5\sigma$).

Both RV surveys and *Kepler* have estimated occurrence rates for long-period (>50d) planets. We compare these here to explore both the number of likely planets and any discrepancies between the samples. Using occurrence rates from 0.8 to 85 days (Fressin et al., 2013), and assuming a flat distribution in $ln(P)$ beyond 85d, suggests that 15% of FGK stars should have a large Neptune or Jupiter on $0.8 < 3000$ day orbits. This is similar to the giant planet occurrence rates found by (Mayor et al., 2011), with 14 ± 2% of FGK stars hosting planets larger than $50M_\oplus$ (see Figure 6.1). Accounting for transit probability (which scales with stellar radius and semi major axis by $\frac{R_\star}{a}$) and timing probability (which scales with observation campaign duration and orbital period by $\frac{t_{\mathrm{obs}}}{P}$) gives detectable multi- and single-transiting planets around 0.15% & 0.03% of stars from Fressin et al. (2013), and 0.09% & 0.02% from Mayor et al. (2011). Hence one in every few thousand FGK stars observed by K2 should have a detectable giant planet observable with a single transit, although

[1] https://keplergo.arc.nasa.gov/CalibrationSN.shtml

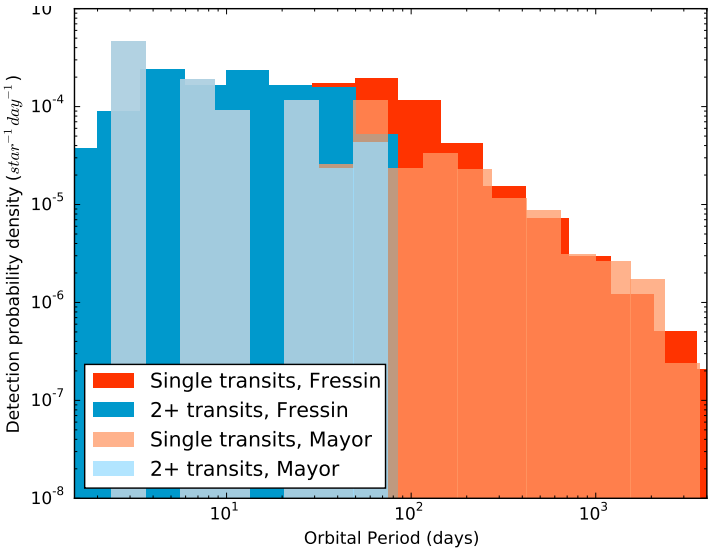

Figure 6.1: Comparing the detectability of a planet around a sun-like star with K2. Blue: multiple transits detectable. Red: Only single transits detectable

this should increase with the inclusion of smaller radii planets.

An analysis of Kepler results also suggests that, at long periods (> 50d), a similar number of planets and eclipsing binaries exist (Planets:EBs = 292:276). Similarly, the number of confirmed planets & unconfirmed candidates is comparable to the number of false positives for deep signals with 500-15000ppm (PLs:FPs = 493:449). Therefore we would naively expect a false positive rate of less than 50% for objects detected in this regime.

However, the previous analysis assumes a Kepler-like stellar sample, and does not use small planet sizes (e.g. small Neptunes and superEarths) which may be detectable with K2 as single transits. To analyse the full planet sample, a (purely theoretical) analysis of K2 stars was performed, using the stars characterised by Huber et al. (2016) in fields 0 to 10 of K2, combined with planets using the full occurrence rates of Fressin et al. (2013) and purely white noise statistics (increased by a factor of 20% higher than the Kepler sample to account for stronger systematics). This revealed that, from the 94,000 stars in that sample, we should expect as many as 320 ± 50 single transiting planets to be detectable at > 7σ, with typical periods from 50 to 500 days (see Figure 6.2). Occurrence rate estimations for the long period regime are, at present, extremely poorly constrained. Hence the detection and subsequent follow-up of monotransiting planets in this regime will allow improved occurrence rates for this relatively unexplored parameter space.

The three analyses used here all predict that a large number of single transits should be detectable with K2.

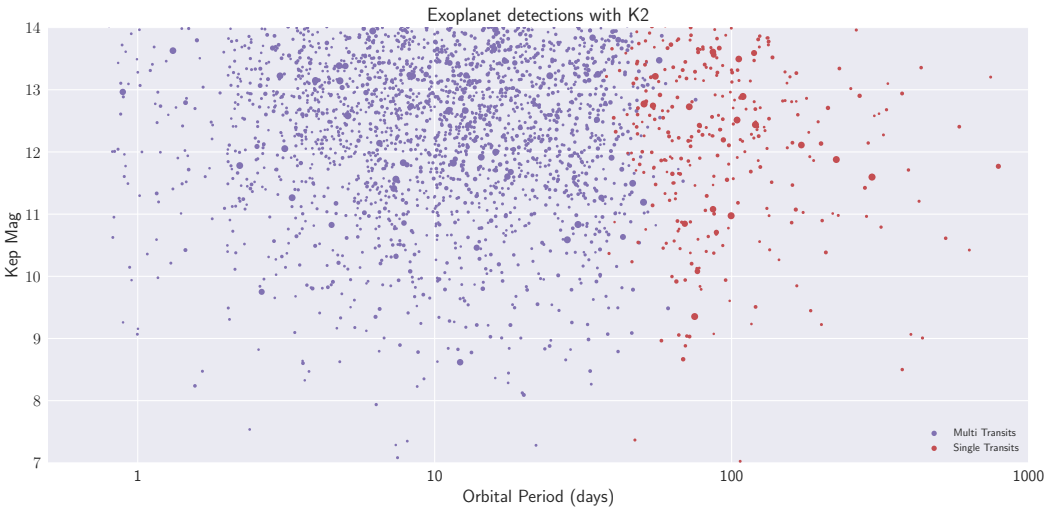

Figure 6.2: A simulation of planet detections from 96,000 K2 targets in Huber et al. (2016). They are plotted as a function of period (x-axis), magnitude (y-axis) and size (marker diameter), with purple and red points showing multi- and single-transiting planets respectively.

6.2 Methods

6.2.1 Transit Search

Long-duration variability was removed from the detrended lightcurves (see section 6.2.2) by fitting 3rd order polynomials to 3-day windows either side of a rolling untouched 4hr central window as detailed in Section 2.9 and in Armstrong et al. (2014a) Anomalies were also removes according to the method described in Section 2.8.

A search for transit signals was then performed on the lightcurves. Least-square minimisation was used to fit pre-generated transit models (developed from the Mandel and Agol (2002) small planet, quadratic limb-darkened model) to a lightcurve window of 6 times the transit duration (T_D). This was repeated for transit models with durations from 1.5 to 24hrs in increasing T_D steps of 25%, with each fitting window shifted by 25% of the targeted T_D each time. Models with depths greater than 2.5σ from the out-of-transit RMS were recorded. A combination of highest SNR and lowest reduced χ^2_R value ($SNR/\log(\chi^2_R)$) was used to select the best transit fit when multiple durations and transit centres were flagged on the same region of lightcurve.

To reduce false positive detections caused by residuals from thruster firings, the SNR of detections with above-average numbers of events occurring concurrently were suppressed. Lightcurves were then sorted by the total SNR of detected signals and manually 'eyeballed' by at least two independent observers, leaving only the best candidate events. This was performed alongside the eyeballing required for the planet search documented in

Chapter 3. All lightcurves were also searched independently by collaborators who detected a similar number of single transits, though there were varying amounts of overlap between the candidate lists for different campaigns.

6.2.2 Lightcurves

Engineering Campaign

The ~2000 stars observed in this initial testing campaign had 6.5 days of stable photometry, and were only available with the detrending of (Vanderburg and Johnson, 2014).

Campaigns 0-6

We primarily used lightcurves detrended by the technique of Armstrong et al. (2015a) for transit searches in the first few campaigns. This method is described in more detail in Section 3.2 and in Armstrong et al. (2015a)[2].

Campaigns 3-10

Detrended lightcurves from the Kepler team (the "PDC_SAP" technique, Stumpe et al. (2012)) were downloaded and searched alongside the Armstrong and later LAM lightcurves from C7 onwards. The presence of two lightcurves during the vetting process enabled rapid analysis of false positives caused by flux dropouts (e.g. due to poorly corrected thrust firing systematics).

Campaigns 7-10

From Campaign 7 onwards, the Armstrong et al lightcurves were no longer used in the primary search, and were replaced by those generated at LAM (see Section 3.2 Barros et al., 2016). The PDC_SAP lightcurves continued to be displayed alongside the LAM during the transit detection and vetting process.

Validation with multiple lightcurves

Lightcurves with detected single transit candidates were later checked on multiple detrending methods, including (where available) those by Vanderburg and Johnson (2014), the Kepler PDC pipeline (Stumpe et al., 2012), and the Everest pipeline (Luger et al., 2016). Variations in transit depth and shape between different detrending methods proved a good diagnostic for the source of the eclipse as false positives caused merely by noise (eg flux

[2]Detrended lightcurves are publicly available on MAST at https://archive.stsci.edu/prepds/k2varcat/

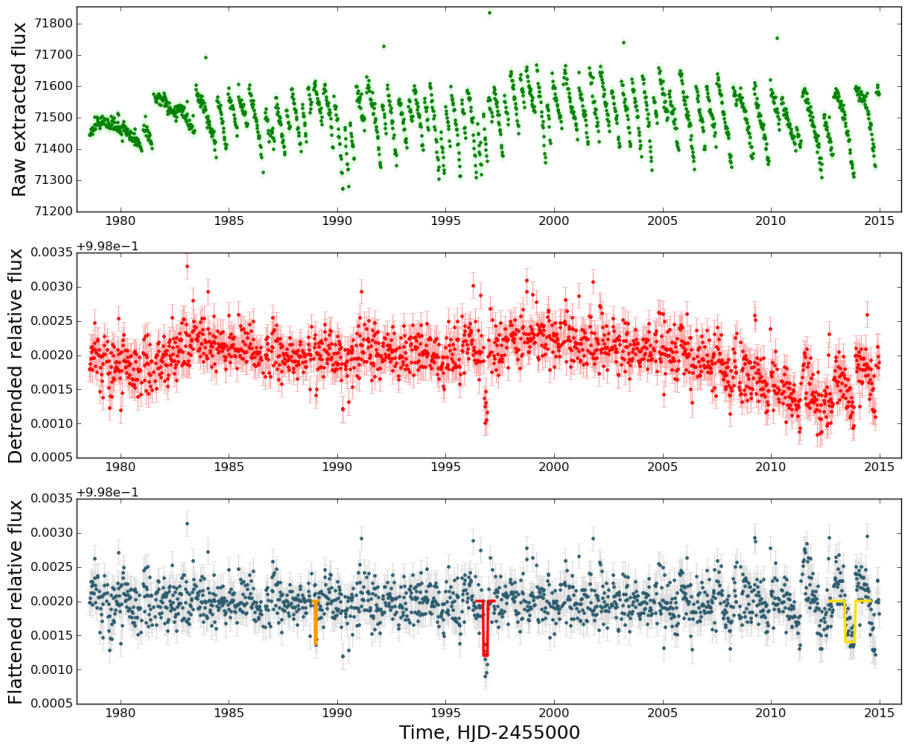

Figure 6.3: Example of the detection process for a single transit of the validated planet K2-11 b (EPIC 201596316 b) using one half of the C1 lightcurve (Montet et al., 2015). (a) Raw aperture-extracted flux; (b) Relative flux after de-trending for pixel motion with the method of Armstrong et al. (2015a); (c) An example of the lightcurve and transit-searched lightcurve seen during eyeballing, with potential detections in red/orange/yellow, where the colour strength is determined using $SNR/\log\chi^2_R$.The red detection corresponds to a significant single transit of K2-11b. All other (less significant) detections are spurious.

drops) were not consistent across all detrending methods. Similarly, false positives caused by blended signals displayed different depths across different lightcurves, enabling fast filtering of e.g. blended EBs.

6.2.3 Transit Fitting - `Namaste`

Modelling transit lightcurves has been explored by numerous authors (e.g. Mandel and Agol, 2002; Seager and Mallen-Ornelas, 2003; Collier-Cameron et al., 2007), but the majority of full transit models rely on knowledge of the period (often scaled to transit duration) or semi-major axis (scaled with stellar radii). In the case of a single transit, these approximations cannot be used as they rely on fitting both the period and semi-major axis scaled to stellar radius (a/R_s). Instead, we develop "`Namaste`: An Mcmc Analysis of Single Transit-

ing Exoplanets" (hereafter, `Namaste`[3]). This technique estimates a planetary velocity scaled to stellar radius (v') in place of a velocity calculated from the planetary period. This velocity can be geometrically defined from impact parameter(b), planet-to-star ratio ($R_p/R_\star$) and transit duration (T_D) using:

$$v' \equiv \frac{v_{\rm pl}}{R_\star} = \frac{2\sqrt{(1+R_p/R_\star)^2 - b^2}}{T_D} \tag{6.4}$$

The scaled velocity of a small planet crossing the centre of the stellar disc ($b = 0$) is therefore twice the inverse of the transit duration ($\sim 2/T_D$).

Velocity, impact parameter & radii ratio can be estimated geometrically from fitting the transit shape. We adapt the transit fitting regimes of Ian Crossfield[4] and the Monte Carlo Markov chain implementation `emcee` (Foreman-Mackey et al., 2013b), to estimate posterior probability distributions for each monotransit signal. Quadratic limb darkening parameters adapted for the *Kepler* bandpass were interpolated from stellar temperature and log g(Sing, 2010). A Gaussian prior distribution was applied to these limb darkening parameters with values and errors set from the temperature probability distribution.

If eccentricity is assumed to be zero, a circular planetary period ($P_{\rm circ}$) can be estimated from the scaled transit velocity (v') and stellar density ($\rho_\star$) using *Kepler*'s laws:

$$P_{\rm circ} = \frac{8\pi^2 G}{3}\frac{\rho_\star}{v'^3} = 2\pi\frac{g}{R_\star v'^3} \tag{6.5}$$

Or, using non-SI units:

$$\left(\frac{P_{\rm circ}}{d}\right) = \frac{18226\left(\frac{\rho_\star}{\rho_\odot}\right)}{\left(\frac{v'}{d^{-1}}\right)^3} = \frac{0.67439\times 10^{\log g}}{\left(\frac{R_\star}{R_\odot}\right)\left(\frac{v'}{d^{-1}}\right)^3} \tag{6.6}$$

Longer period orbits (and hence lower-velocity fits) are probabilistically less likely due to transit probability ($p_{\rm tr} \approx \frac{R_s}{a_{\rm pl}} \approx \frac{v'}{\rho_\star}$). We discourage longer-period fits (and encourage faster-velocity fits) with a linear prior on transit velocity ($P(v) \propto v$). In the case of multi-planet systems, the probability of a subsequent planet transiting does not simply scale with transit probability $R_\star/a$, as co-planar orbits are favoured. Hence, in these cases, the forcing of fits to shorter orbits by a linear prior may not be valid. However, the increase in transit probability for a planet at distance x given transiting exoplanets on orbits y,z, etc. is a complex problem beyond the scope of this work.

The non-detection of subsequent transits in the light-curve can also be used to set a lower limit on the orbital period, and hence an upper limit on velocity. We apply this

[3]Publicly available at https://github.com/hposborn/namaste

[4]Accessed from http://www.lpl.arizona.edu/ ianc/python/

minimum period ($P_{\min}$) as a secondary prior on the velocity distribution using:

$$v_{\max} = \left(\frac{8G\rho_s\pi^2}{3P_{\min}}\right)^{\frac{1}{3}} \tag{6.7}$$

We apply this in the form of a cumulative normal distribution, with value and errors from the distribution of $v'_{\max}$. This prior knowledge makes the assumption that the orbit is circular, which we discus the validity of in section 6.2.4. As period and velocity are related by a constant and the stellar density, this is the only fitting prior that is dependent on stellar parameters.

The impact parameter was limited with a uniform prior between -1.2 to 1.2 to avoid the model (specifically the "walkers" as defined in section 2.4) artificially building up at $b = 0$. Planet-to-star radius ratios were limited to 0.25, as at high values the assumption that the transiting object is fully opaque and covering a uniform region of stellar surface breaks down (Mandel and Agol, 2002).

Planetary orbital velocity is directly linked to stellar density (Seager and Mallen-Ornelas, 2003) (see section 1.2.2). For the best constrained transit models, stellar density is likely to prove the largest uncertainty. Characterising the star, therefore, is key to accurately estimating orbital period. Such characterisation is best performed with asteroseimology, or less accurately, with spectral fitting and stellar models.

Large radii planets which spend longer crossing the rim of the stellar disc are most suitable to `Namaste` fitting as the impact parameter can be more easily distinguished. Price et al. (2015) showed that for smaller and lower signal-to-noise planet transits the uncertainty on impact parameter increases linearly, causing poor determination of perpendicular velocity and therefore eccentricity. For less well-defined fits, parameters such as impact parameter, planet-to-star ratio and velocity become correlated, as can be seen in their posterior distributions of figure 6.5. This is especially true for eclipses that cannot be constrained to an impact parameter less than 1.0. In these cases the fit cannot distinguish between planetary, high-velocity, disc-crossing transits and lower-velocity grazing eclipses. As impact parameter increases beyond 1.0, velocity stabilises to a minimum value determined by transit duration. However, even for correlated and non-gaussian parameters, `Namaste` allows us to put probabilistic constraints on the transit fit.

To model variations in the lightcurve from stellar activity and correlated noise, we co-fit the planetary model with a gaussian process model (as described in Section 2.10)[5]. The majority of smoothly-varying stellar activity is best represented by an exponential-squared kernel, whereby the covariance is proportional to the exponential of the distance

[5]We used the development branch of publicly available `george` package available at https://github.com/dfm/george/tree/1.0-dev (Foreman-Mackey, 2015)

Parameter	Definition	Uniform Prior	Other prior
$T_{\rm cen}$	Transit centre (days)	$\mathscr{U}(T_{\rm cen} \pm 2T_{\rm dur})$	-
b	impact parameter (ratio)	$\mathscr{U}(-1.2, 1.2)$	-
v'	Velocity (R_s/d)	$\mathscr{U}(0.0, 100.0)$	$\mathscr{C}(v'_{\rm max}; \sigma'_v{\rm max}^2)_{\mathscr{L}}(v')$
R_p/R_s	Radius ratio	$\mathscr{U}(0.0, 0.3)$	-
u_1	Quadratic LD parameter 1	$\mathscr{U}(0.0, 1.0)$	$\mathscr{N}(u_1; \sigma^2_{\rm u1})$
u_2	Quadratic LD parameter 2	$\mathscr{U}(0.0, 1.0)$	$\mathscr{N}(u_1; \sigma^2_{\rm u1})$
$\log(\sigma_{\rm white})$	White noise amplitude	$\mathscr{U}(-10^6, 10^6)$	$\mathscr{N}(\sigma_{\rm white}; \sqrt{\sigma_{\rm white}}^2)$
$\log(\tau)$	GP lengthscale	$\mathscr{U}(-10^6, 10^6)$	$\mathscr{N}(\log(\tau); \sqrt{\log(\tau)}^2)$
$\log(a)$	GP amplitude	$\mathscr{U}(-10^6, 10^6)$	$\mathscr{N}(\log(a); \sqrt{\log(a)}^2)$

Table 6.1: The nine parameters used in each `Namaste` fit, with priors. $\mathscr{N}(\mu; \sigma^2)$ is a normal distribution with mean μ and width σ^2, $\mathscr{U}(a; b)$ is a uniform distribution between a and b and $\mathscr{C}(\mu; \sigma^2)_{\mathscr{L}}(a)$ is an inverse cumulative distribution with mean μ and width σ^2 multiplied with a linear distribution with variable a.

between points. This kernel uses two parameters: the lengthscale dominating the data (τ), and the average variance or amplitude of the variation (a), or more strictly their natural logs. We also know the intrinsic photon noise of any star in the field, given its magnitude. To parameterise this (and thereby inhibit the gaussian process defined above from over-fitting white noise), we also define a white noise kernel (σ_w).

Ideally, any fit would use the full out-of-transit lightcurve to constrain the GP hyperparameters. However calculating the covariance of a series of N points requires N^2 calculations. With more than 3000 points in a K2 light curve, this would seriously limit the computational speed of `Namaste`. Instead, we determine the best-fitting hyperparameters from the whole lightcurve by minimising the log-likelihood of the GP and use a Gaussian Prior in the MCMC fitting (with μ set as the square root of the parameter) to constrain the GP hyperparameters. The light curve is then cut to 8 transit durations either side of the transit centre, or 2.0 days if t_D is less than 0.25.

We show two examples of the resulting posterior distributions between parameters (along with model fit and residuals) in figures 6.4 and 6.5. The fit for EPIC229021605 shows a well-constrained fit with b<1.0, whereas that of EPIC212459241 shows shows a less well-constrained grazing fit with b∼1.0 and correlations between b, v & R_p/R_s.

6.2.4 Eccentricity

For exoplanets on non-circular orbits, the circular velocity estimated by `Namaste` ($v_{\rm circ}$) depends strongly on eccentricity and the argument of periastron (equation 6.8, Barnes 2007):

$$V_\theta = V_{\rm circ} \frac{1 + e\cos\theta}{\sqrt{1 - e^2}} \tag{6.8}$$

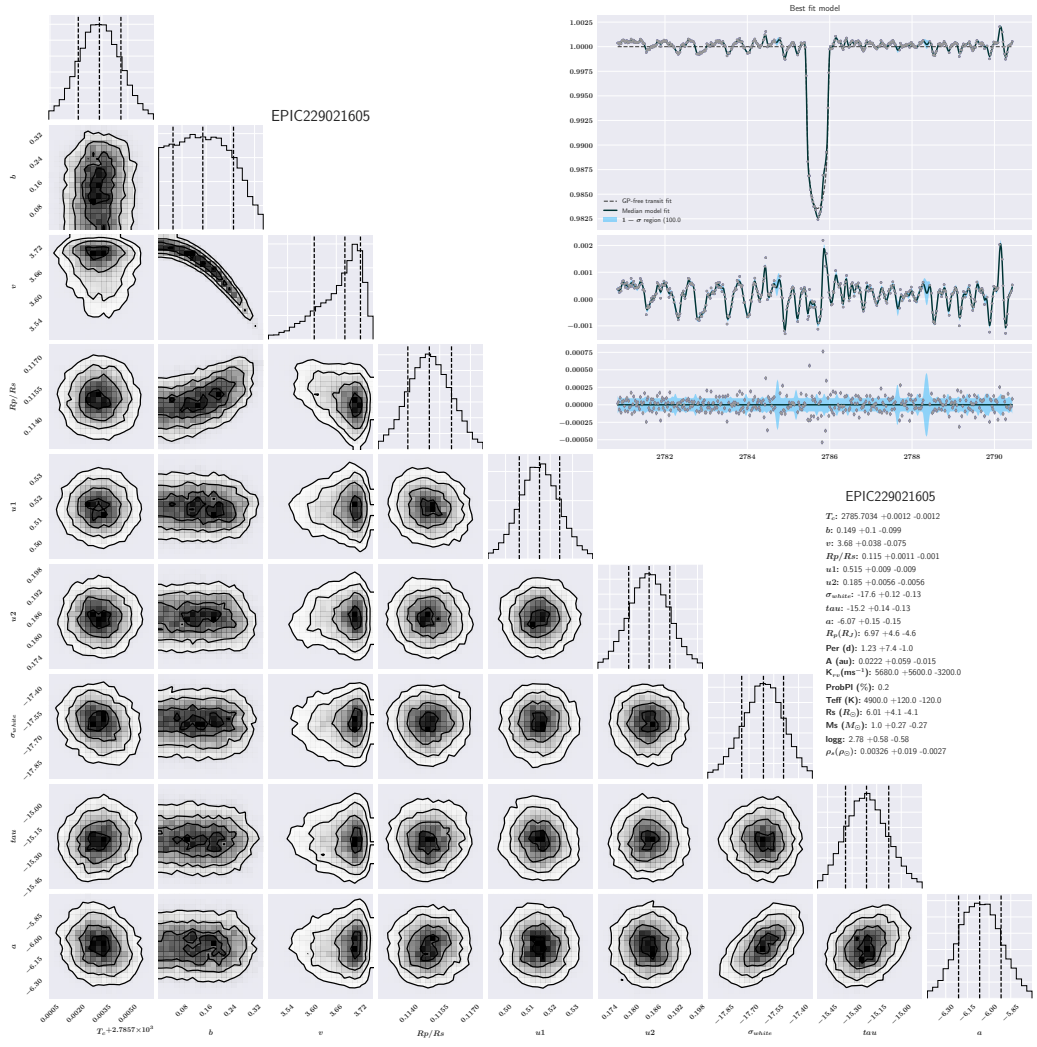

Figure 6.4: Well-fitted `Namaste` model for EPIC229021605. Bottom left plots show the posterior PDF flatten to each possible 2D combination of fit parameters. Diagonal plots show a 1D histogram of the PDF flattened on individual model parameters. Upper right figure shows the detrended lightcurve (grey points) with GP+Transit model in grey, and just the transit model shown with a dashed line. Centre-right panels show the residuals for just the transit model removed (upper) and with the GP+transit model removed (below). Parameters (displayed on the right with 1-sigma uncertainties) are ordered as stated in Table 6.1.

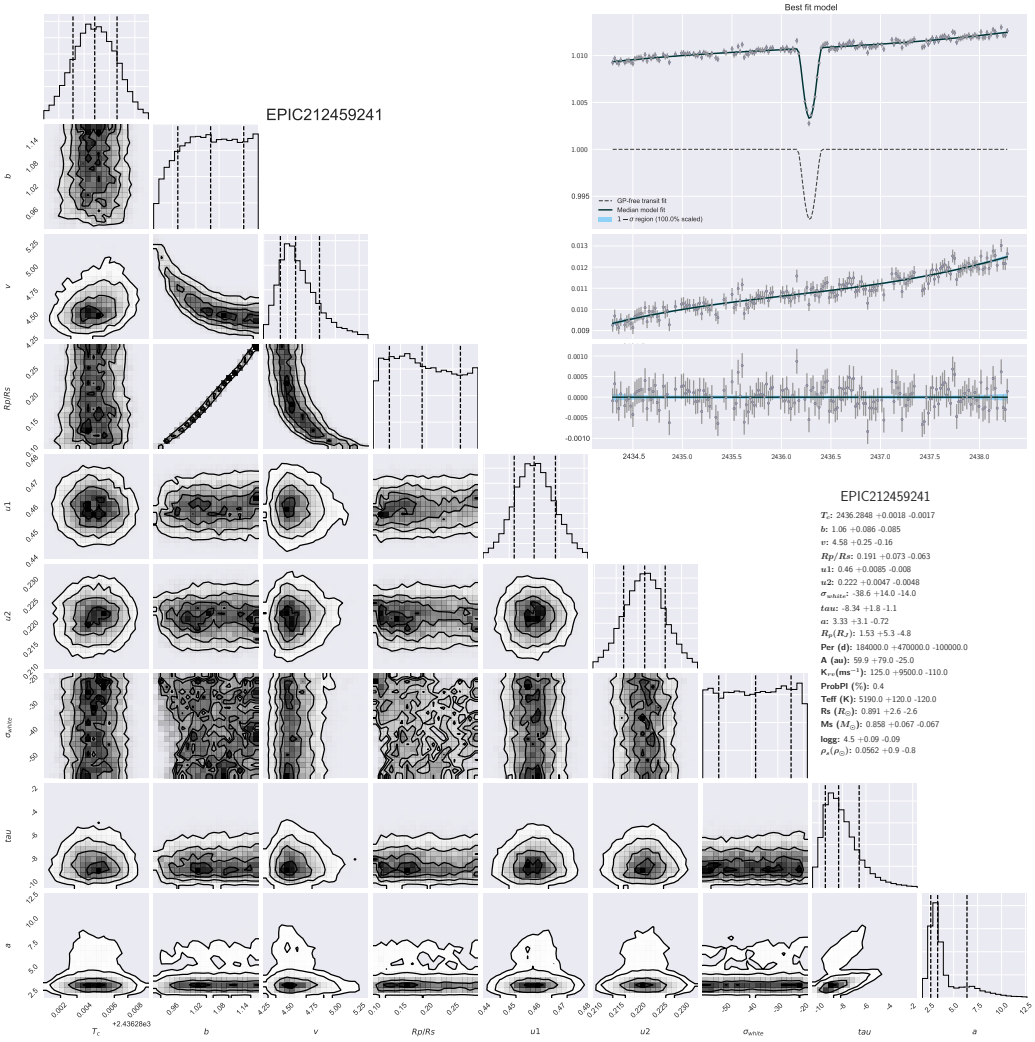

Figure 6.5: Highly correlated `Namaste` model for EPIC212459241. Figure as 6.5

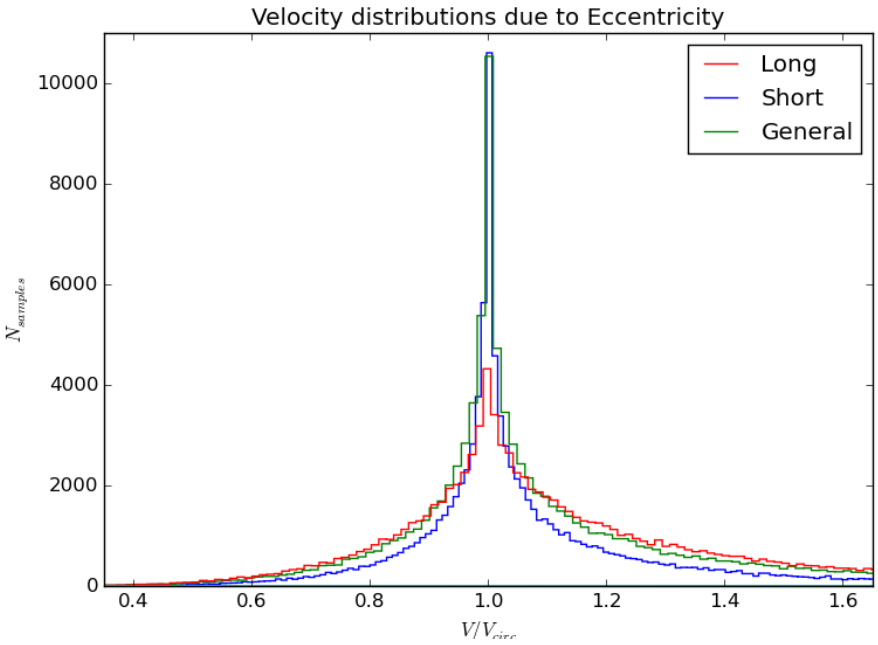

Figure 6.6: Distribution of the ratio of true velocity and circular velocity for three different eccentricity distributions from Kipping (2013).

As the solid angle swept out by an eccentric planet's shadow is greater than that from an equivalent circular orbit, eccentric planets are also more likely to transit (see section 1.2.3). Transit probability is especially raised near periapse, suggesting circular period estimates will on average underestimate the true period. Kipping (2013) used RV planets to study the distribution of exoplanet eccentricities and showed that close-in planets (defined as $P < 382$d) have a more circular distribution than long-period planets. We use these distributions to study eccentricity's effect on transit velocity (Figure 6.6). We find that eccentricity increases the median velocity and its $1-\sigma$ confidence intervals by $1.3^{+21}_{-7}\%$ in the short-period (< 382d) case, and by $3^{+35}_{-9}\%$ in the general case.

Eylen and Albrecht (2015) studied the discrepancy between *Kepler* planet densities determined by asteroseismology and those found from transit duration to determine their eccentricities. This method is analogous to the comparison of true period with those from single transit fits, and suggests `Namaste` could be useful for determining the eccentricities of polytransiting planets.

In this study, we note that eccentricity can add significant uncertainty to our results, but limit ourselves to estimations of circular periods ($P_{\rm circ}$) which are good approximations for the majority of cases. For the short-period regime, two-thirds of planets orbit with eccentricities less than 0.2 Kipping (2013), causing substantially lower increased uncertainties. Hence, in the majority of cases, the small increase in velocity uncertainty is negligible

compared to the large uncertainties from stellar density.

6.2.5 Stellar Parameters

We used three techniques to estimate stellar parameters. Firstly, we used information obtained from spectra. In the cases of stars with published planets, we used the stellar information derived in those publications.

We also obtained 23 spectra with the Echelle spectrograph on the 2.3m ANU Telescope at Siding Spring, Australia. These gave typical uncertainties of 250K on the T_{eff}, 0.5 on the log g and 0.5 on the metallicity.

Where stellar parameters from spectra are unavailable, we turned to the Ecliptic Plane Input Catalogue (EPIC) for stellar information (Huber et al., 2016). Here, Huber et al. (2016) classified the 138,600 stars to be observed by K2 using their colours from multiple all-sky catalogues, their proper motions and stellar population models. This produced typical uncertainties of ~3% in T_{eff}, ~0.3 dex in log g, ~ 40% in radius, and ~10% in mass. We accessed this information from the ExoFOP K2 archive[6].

In the case where no information was available in EPIC (six candidates), we performed a search of nearby sources in NOMAD (Zacharias et al., 2005) and WISE (Cutri et al., 2014) catalogues using the astroquery package (Ginsburg et al., 2013). We then used photometric colours to approximate the stellar effective temperatures using the tables of Pecaut and Mamajek (2013)[7], under the assumption that only the target star contributed to stellar flux. From this temperature, and making the assumption that the star is on the main sequence, stellar models allow a stellar radius & mass to be estimated (Torres et al., 2010; Straižys and Kuriliene, 1981). Temperature uncertainties were estimated from the RMS of the temperature from each colour estimate, or set to 150K if the RMS was smaller than this value. Mass and radius uncertainties were taken from the propagation of temperature uncertainties through the stellar radius and mass relations down to a minimum relative error of 10%.

6.2.6 Prob(PL)

We define a simple statistic related to the probability that the eclipsing object is planetary, using the proportion of the posterior PDF of planetary radii below $1.5R_{Jup}$.

Due to radius degeneracy in the substellar mass regime, Brown-dwarfs and late (>M6) M-dwarfs are also likely to have radii at, or below, this boundary. However, the occurrence rate of objects in this regime (The "Brown Dwarf Desert") is far lower than that

[6] https://exofop.ipac.caltech.edu/

[7] Accessed from www.pas.rochester.edu/~emamajek/EEM_dwarf_UBVIJHK_colors_Teff.txt

of exoplanets (Grether and Lineweaver, 2006), and therefore objects of $\sim 1R_{Jup}$ are much more likely to be planetary.

We split the detected events into three categories: Planetary-radius candidates, Ambiguous candidates, and Eclipsing Binary candidates. Candidates for which the 1-sigma radii boundaries (e.g. >84% of the posterior distribution in planetary radius) is below the predefined boundary of $1.5R_{jup}$ are classed as Planetary-radius candidates (e.g. $0.9 \pm 0.4 R_j$). Candidates with 1-sigma radii limits above $1.5R_{jup}$ are classed as EB candidates, and those with uncertainties spanning this threshold as ambiguous.

However we cannot, with current measurements, determine whether the target is significantly blended below a separation of 1", although we expect the proportion of stars having significant blends to be low. Therefore, a more complete analysis of the planetary probability would include high-resolution imaging and a complete probabilistic exploration of the potential of a blended eclipsing binary (e.g. Morton, 2012; Díaz et al., 2014). Such a probabilistic validation has been performed on a handful of single transiting exoplanets detected in the Kepler primary mission (Wang et al., 2015), although whether such objects can be validated as planets to the same degree as multi-transiting planets is an open question.

6.2.7 Centroid Shifts

Unfortunately, K2 centroids are dominated by changes in the position of the field due to spacecraft drift and thruster firings. Even though the motion is tracked and corrected for by the majority of K2 detrending pipelines, the corrected centroid is dominated by systematics from this effect. This was enhanced by using the PDC_SAP flux Stumpe et al. (2012), which has one of the worst noise levels amongst K2 lightcurves (e.g. Luger et al., 2017), but is the only detrending method to have centroid position and centroid correction to hand. We did, however, search for centroid motion during our single transits in an attempt to identify false positives. We did this by comparing the in-transit corrected centroid position with the median out-of-transit position. We then iteratively chose 1000 random transit centres of the same duration (effectively the boot-stapping method of error analysis) to give the uncertainty in centroid position. For any significant ($> 1\sigma$) centroid shifts, we plotted the corrected centroid positions by eye to determine if the in-transit points occupied their position as a result of systematic offsets, or if they occupied a unique position in the centroid diagram

6.2.8 Eclipsing Binaries

Single eclipsing binary candidates (which likely also populate the planetary candidate population as false positives) are deeper, providing higher SNR, and therefore are a by-product

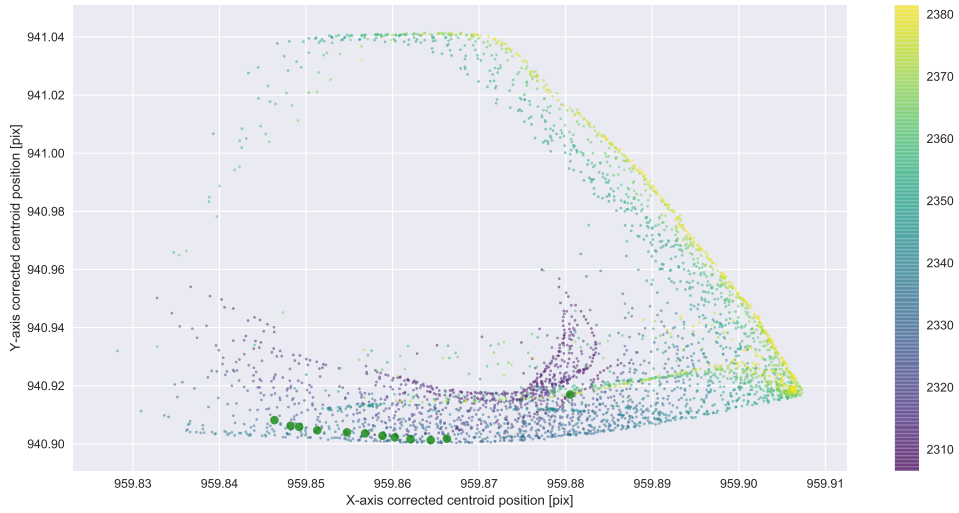

Figure 6.7: An example centroid position for EPIC212485410 from the detrended PDC_SAP centroid, with transit points shown as large green circles and out-of-transit points as dots coloured according to time (colour-bar in time [JD-2454833.0]). The median out-of-transit centroid position is 1.7σ offset from in-transit median position. However, the centroid shift is instead co-incident with (and consistent with) pixel drift from spacecraft motion rather than from a blended EB.

of any search for single transiting planets.

A number of factors make the modelling of the eclipses of stellar companions more difficult. Firstly, the contribution of luminosity from the secondary object means that eclipse depth loses an uncorrelated association with radius, instead becoming primarily a function of the ratio in surface brightness ratios between the two objects. The closer radius ratios between two stellar objects also means that a far higher proportion of such eclipses are grazing, therefore making parameter combinations like the period and the transit duration degenerate. Finally, the presence of flux from a second stellar body, and its contribution to stellar colours and the SED, reduces the precision on derived stellar parameters, which assume a single star model.

However, even without detailed modelling, eclipsing systems can provide information unavailable from planetary transits. The presence of a visible secondary eclipse can precisely estimate a circular period for the system. Alternatively, in such cases where a circular orbit is ruled out by the lack of a primary transit at the next integer position of the primary-secondary spacing, the ratio of the minimum period to primary-secondary separation gives a minimum eccentricity, $e_{\rm min}$, defined as:

$$e_{\rm min} = \frac{1}{2\pi}\left(\frac{(ts - tp)}{P} - \frac{1}{2}\right)$$

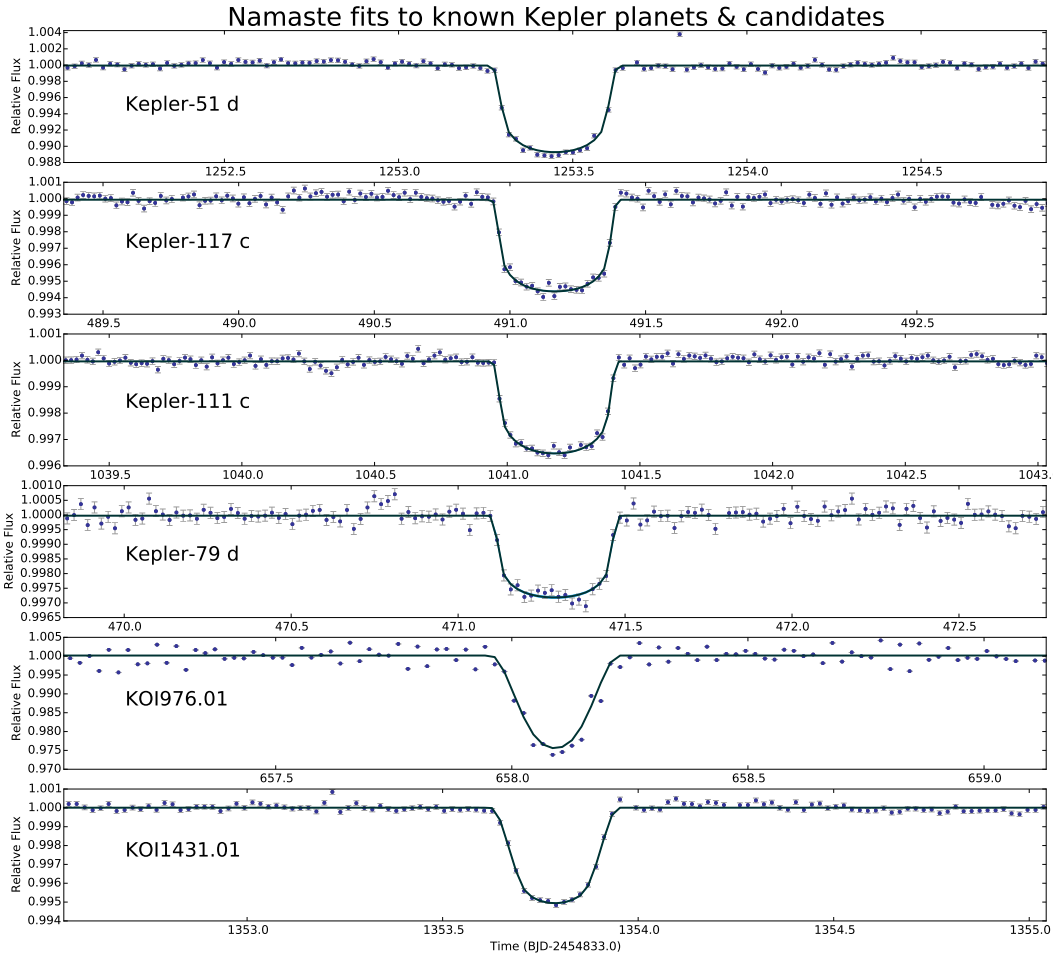

Figure 6.8: Six long-period *Kepler* planets with `Namaste` fits. Best-fit models are in black, while $1-\sigma$ error regions are in blue. x-axis is scaled to 8 transit durations, whereas the y-axis is unconstrained. Note the different y-axis extents, which show the varying depth of these transits.

(Matson et al., 2016, - Appendix A)

(6.9)

This assumes eclipse times happen at a longitude of periastron, ω, of π & $-\pi$, which produces the maximum possible difference in eclipse timing discrepancy.

	Kepler-51 d	**Kepler-117 c**	**Kepler-111 c**	**Kepler-79 d**	**KOI976.01**	**KOI1431.01**
KIC	11773022	10723750	8559644	8394721	3441784	11075279
$T_{\rm cen}(d)$	1253.4490 ± 0.0006	491.16605 ± 0.0009	$1041.17996 \pm 9 \times 10^{-4}$	471.290 ± 0.001	$658.09145 \pm 2 \times 10^{-5}$	1353.7881 ± 6.6^{-4}
$T_{\rm cen,true}$	1253.454 ± 0.05	491.164 ± 0.03	1041.210 ± 0.07	471.290 ± 0.04	658.093 ± 0.05	1353.788 ± 0.06
b	$0.18^{+0.13}_{-0.11}$	$0.32^{+0.12}_{-0.19}$	$0.56^{+0.10}_{-0.29}$	0.43 ± 0.23	$0.8420 \pm 7 \times 10^{-4}$	0.872 ± 0.006
$b_{\rm true}$	0.094 ± 0.08	$0.20^{+0.05}_{-0.14}$	$0.787^{+0.007}_{-0.02}$	$0.02^{+0.15}_{-0.02}$	$1.29^{+0.34}_{-0.17}$	$0.869^{+0.005}_{-0.007}$
$v(R_\star d^-1)$	$6.1215^{+0.090}_{-0.21}$	$4.51^{+0.20}_{-0.25}$	$3.85^{+0.48}_{-0.34}$	$5.2^{+0.4}_{-0.9}$	6.191 ± 0.006	$4.03^{+0.10}_{-0.09}$
$R_p/R_\star$	$0.0943^{+0.0007}_{-0.0005}$	$0.0690 \pm 6 \times 10^{-4}$	0.0560 ± 0.001	$0.049^{+0.002}_{-0.001}$	0.165 ± 0.0002	$0.0759 \pm 7 \times 10^{-4}$
$R_p/R_{\star,\rm true}$	$0.11^{+0.015}_{-0.08}$	$0.057^{+0.03}_{-0.015}$	$0.06^{+0.03}_{-0.02}$	$0.0372^{+0.02}_{-0.005}$	$0.5^{+0.1}_{-0.4}$	$0.076^{+0.04}_{-0.03}$
F	$0.99994 \pm 2 \times 10^{-5}$	$0.99994 \pm 1.3 \times 10^{-5}$	$0.9999617 \pm \times 10^{-6}$	0.99997 ± 1.0^{-5}	$1.0001733 \pm 1.3 \times 10^{-6}$	$0.999958 \pm 8 \times 10^{-6}$
$u1$	0.389 ± 0.004	$0.33^{+0.003}_{-0.004}$	0.363 ± 0.006	0.327 ± 0.003	0.2616 ± 0.003	0.421 ± 0.006
$u2$	0.264 ± 0.0025	0.297 ± 0.002	0.280 ± 0.003	$0.298^{+0.002}_{-0.003}$	0.3468 ± 0.0015	0.245 ± 0.004
$R_P(R_{\rm Jup})$	0.84 ± 0.41	0.99 ± 0.17	0.63 ± 0.07	0.7 ± 0.1	2.7 ± 1.1	0.70 ± 0.06
$R_{p,\rm true}$	$0.96^{+0.39}_{-0.09}$	$0.8^{+0.5}_{-0.1}$	$0.67^{+0.15}_{-0.07}$	$0.51^{+0.2}_{-0.05}$	8^{+7}_{-1}	$0.71^{+0.11}_{-0.03}$
$P(d)$	138^{+20}_{-10}	$53.0^{+5.3}_{-18.7}$	240^{+130}_{-90}	$55.3^{+71}_{-3.1}$	25^{+100}_{-17}	340^{+110}_{-80}
$P_{\rm true}$	130.1775 ± 0.0001	$50.79035 \pm 2 \times 10^{-5}$	224.7782 ± 0.0003	$52.09082 \pm 4 \times 10^{-5}$	$52.56899 \pm 6 \times 10^{-5}$	$345.1599 \pm 4 \times 10^{-4}$
$s.m.a.$(AU)	$0.5^{+1.4}_{-0.3}$	$0.36^{+0.17}_{-0.10}$	$0.80^{+0.27}_{-0.21}$	$0.3^{+0.2}_{-0.1}$	$0.20^{+0.42}_{-0.11}$	$0.98^{+0.20}_{-0.17}$
$s.m.a._{\rm true}$	0.5121	0.2858	0.7469	0.2807	0.321	0.9809
$T_S(K)$	5800 ± 110	6170 ± 100	5952 ± 74	6174^{+83}_{-117}	7200^{+310}_{-240}	5600^{+110}_{-90}
$R_{star}(R_\odot)$	0.91 ± 0.5	1.61 ± 0.05	1.16 ± 0.14	$1.302^{+0.026}_{-0.027}$	$1.66^{+0.2}_{-1.4}$	$0.95^{+0.05}_{-0.14}$
$M_\star(M_\odot)$	1.04 ± 0.12	$1.13^{+0.13}_{-0.02}$	1.17 ± 0.03	$1.165 + \{0.044\}_{\{} - 0.045\}$	$1.59^{+0.18}_{-0.4}$	$1.054^{+0.08}_{-0.06}$
$\rho_S(\rho_\odot)$	1.72 ± 0.12	$0.29^{+0.01}_{-0.02}$	0.75 ± 0.16	$0.526^{+0.018}_{-0.024}$	$0.35^{+0.29}_{-0.30}$	$1.22^{+0.27}_{-0.47}$

Table 6.2: `Namaste` results for 4 *Kepler* planets and 2 KOI candidates, compared with published parameters from traditional analyses.

6.3 Results

6.3.1 Application to Known *Kepler* Systems

To test the accuracy of `Namaste`, we applied it to single transits from the lightcurves of 6 long-period *Kepler* planets and KOI candidates. Figure 6.8 shows the `Namaste` model fits to these transits, and Table 6.2 gives the output parameters compared to their published values.

6.3.2 Application to K2 Single Transit Candidates

We applied `Namaste` to the 72 candidate transiting exoplanets we detected across eleven campaigns of K2. The fits are shown in Figures 6.3.3 to 6.3.3. The input stellar parameters from EPIC and, where unavailable, multiband colours are shown in Tables 6.5 and 6.6, with stellar parameters from spectroscopy shown in Table 6.7. Truncated output parameters from Namaste are shown in Table 6.8.

Our centroid analysis gave a median shift of only 0.08", and showed no candidates to be obviously the result of blended eclipsing binaries (BEBs). The lack of BEBs is likely the result of an earlier vetting process in which we removed a handful of candidates with highly varying depth between lightcurves detrended by different methods (and with varying aperture sizes).

6.3.3 Eclipsing Binaries

We detected 48 EB-like objects with a single deep eclipse. These are detailed in Table 6.3 including an estimate of stellar effective temperature from either EPIC or photometric colours, the eclipse epoch, the eclipse depth, and the minimum period. 24 objects were found to have both primary and secondary eclipses. Table 6.4 shows the vital parameters for these systems, including colour temperature, eclipse epoch, eclipse depth, minimum period and minimum eccentricity. The lightcurves of these can be found in the CD-only Appendix section C. EBs with more than a full phase covered by the K2 data were also found but are excluded from this analysis as they are characterised in, e.g., Armstrong et al. (2015a); LaCourse et al. (2015).

6.4 Discussion

6.4.1 Known Kepler Planets & Candidates

All Kepler planets shown reasonable fits to their correct orbital parameters. We used values from Masuda (2014) for Kepler-51 d, Bruno et al. (2015) for Kepler-117 c, Rowe et al.

EPIC	Camp	T_{eff}[K]	Epoch [MJD]	Depth [%]	Dur [d]	Min P
60024244	ET	~ 4220	56699.99	11.0	0.25	4.5
202065269	C0	3400 ± 50.0	56740.16	1.5	0.2	65.0
202071902	C0	6200 ± 50.0	56791.56	11.0	0.2	63.0
202072917	C0	8250 ± 120.0	56786.6	25.0	0.3	58.1
202085278	C0	~ 5540	56780.99	0.8	1.0	52.5
202137190	C0	~ 6320	56804.12	13.0	0.22	75.6
202137580	C0	~ 6320	56795.7	6.5	2.1	67.2
201635132	C1	~ 8500	56826.98	3.1	0.2	63.4
201668035	C1	4220 ± 70.0	56832.68	1.65	0.25	57.7
201775904	C1	6100 ± 180.0	56835.55	1.5	0.17	54.8
202772183	C2	~ 4330	56929.78	6.0	0.25	42.3
203011840	C2	~ 6520	56913.3	42.0	0.8	58.7
204634789	C2	6030 ± 300.0	56921.01	0.7	0.1	51.0
204776782	C2	~ 6200	56959.95	26.0	0.35	66.7
204918110	C2	~ 4980	56944.85	11.0	0.95	51.6
205272592	C2	~ 4990	56935.35	34.0	0.5	42.1
205666907	C2	5350 ± 100.0	56970.15	12.0	0.15	76.9
205936222	C3	~ 3600	56985.78	32.0	0.25	60.5
205966706	C3	~ 4050	57017.78	12.0	0.3	40.7
206008070	C3	~ 3590	57005.0	11.75	4.0	41.3
206253908	C3	~ 5870	56983.66	10.0	0.27	62.6
210673168	C4	~ 3530	57123.08	36.0	0.2	61.3
210760314	C4	~ 6090	57081.2	29.0	0.3	51.5
210823406	C4	~ 6210	57090.35	17.0	0.2	42.3
210857749	C4	~ 5210	57085.0	18.0	0.55	47.7
211075893	C4	~ 4890	57086.8	18.0	0.45	45.9
211498244	C5	~ 5050	57154.52	10.0	0.25	59.9
211703878	C5	~ 4790	57146.34	13.0	0.4	68.1
211894612	C5	~ 6110	57182.9	4.5	0.35	43.3
211995462	C5	~ 4980	57203.3	39.0	0.5	63.7
212012030	C5	~ 5770	57174.47	26	0.2	40.0
212152316	C5	~ 5190	57207.2	6.5	1.3	67.6
212325089	C6	~ 5840	57274.25	10.0	2.2	56.8
212549089	C6	~ 5460	57245.03	5.5	0.6	51.3
212554009	C6	~ 4190	57295.25	14.0	1.0	77.8
212715204	C6	4190 ± 400.0	57232.34	17.0	0.15	64.0
212776371	C6	~ 5130	57268.34	10.0	0.2	50.9
213332545	C7	~ 4540	57338.58	10.0	0.15	44.3
215067200	C7	~ 5950	57326.8	15.0	1.65	56.0
220194833	C8	~ 6000	57415.44	12.0	0.12	55.3
220515668	C8	5380 ± 110.0	57432.45	15.0	0.2	40.4
220604429	C8	5320 ± 130.0	57433.75	4.5	0.15	41.7
201093731	C10	6130 ± 120.0	57634.8	3.8	0.25	45.0
201208775	C10	5000 ± 100.0	57622.65	4.0	0.15	32.9
201479221	C10	5700 ± 140.0	57620.35	16.0	0.4	31.3
201496916	C10	3830 ± 690.0	57632.6	21.0	0.3	42.8
201510813	C10	5740 ± 170.0	57635.0	16.0	0.2	45.2
228891397	C10	5090 ± 80.0	57613.25	24.0	1.9	38.4

Table 6.3: Eclipsing binary candidates detected in K2 form only a primary eclipse.

EPIC	Camp	T_{eff}[K]	Epoch [MJD]	Depth [%]	Dur [d]	Min P	min e
202084447 A	C0	4140 ± 480.0	56730.5	8.0	0.2	74.7	–
202084447 B	-	-	56788.8	3.3	0.2	-	0.0
202135247 A	C0	~ 3670	56768.5	3.2	1.8	68.3	–
202135247 B	-	-	56796.8	8.5	1.75	-	0.134
201663371 A	C1	4180 ± 100.0	56812.72	4.6	0.3	77.6	–
201663371 B	-	-	56884.74	0.12	0.2	-	0.0
204521712 A	C2	~ 3710	56939.5	2.4	0.3	68.8	–
204521712 B	-	-	56962.08	0.6	0.15	-	0.27
204546592 A	C2	~ 5580	56900.0	2.3	0.85	72.0	–
204546592 B	-	-	56936.8	0.35	0.65	-	0.0
205000535 A	C2	~ 5800	56960.05	6.0	1.65	66.8	–
205000535 B	-	-	56907.75	10.0	0.75	-	0.0
205207894 A	C2	4930 ± 50.0	56911.5	10.0	0.4	73.3	–
205207894 B	-	-	56966.6	1.5	0.4	-	0.0
206109641 A	C3	~ 3930	57011.17	45.0	0.4	41.8	–
206109641 B	-	-	57018.88	40.0	0.4	-	0.496
206241558 A	C3	~ 3570	56993.28	28.0	0.3	53.0	–
206241558 B	-	-	57005.6	5.2	0.4	-	0.42
210725198 A	C4	~ 3840	57091.15	10.5	0.75	64.9	–
210725198 B	-	-	57067.75	1.0	0.6	-	0.219
211489484 A	C5	~ 5600	57192.62	19.0	0.2	69.0	–
211489484 B	-	-	57208.6	10.0	0.2	-	0.422
211490542 A	C5	~ 5600	57183.8	9.0	0.35	44.2	–
211490542 B	-	-	57176.18	1.0	0.3	-	0.515
212109135 A	C5	~ 5100	57198.13	33.0	0.35	58.5	–
212109135 B	-	-	57173.96	24.0	0.5	-	0.137
212332380 A	C6	~ 5800	57282.83	23.0	0.5	65.4	–
212332380 B	-	-	57246.1	13.0	1.3	-	0.0
212343520 A	C6	~ 5830	57284.02	8.0	0.2	78.6	–
212343520 B	-	-	57296.1	1.8	0.4	-	0.544
212516916 A	C6	5760 ± 230.0	57284.13	1.5	0.2	66.7	–
212516916 B	-	-	57271.85	1.5	0.2	-	0.496
212732378 A	C6	~ 4880	57229.8	6.0	0.2	66.6	–
212732378 B	-	-	57277.66	0.8	0.15	-	0.0
212805678 A	C6	~ 5160	57293.5	6.0	0.8	76.0	–
212805678 B	-	-	57225.1	3.0	0.9	-	0.0
213455199 A	C7	~ 5680	57381.9	50.0	1.25	81.6	–
213455199 B	-	-	57373.07	40.0	1.2	-	0.616
213832800 A	C7	~ 5970	57321.48	11.5	0.3	75.9	–
213832800 B	-	-	57376.12	0.4	0.3	-	0.0
215307988 A	C7	~ 5380	57322.4	40.0	0.7	60.4	–
215307988 B	-	-	57348.2	32.0	0.3	-	0.115
220352451 A	C8	5680 ± 110.0	57428.4	7.0	0.4	65.5	–
220352451 B	-	-	57457.6	4.5	0.23	-	0.085
220559378 A	C8	5090 ± 120.0	57401.5	14.0	0.3	69.3	–
220559378 B	-	-	57430.8	2.4	0.25	-	0.121
201225735 A	C10	5030 ± 100.0	57638.55	4	0.4	57.0	–
201225735 B	-	-	57646.75	0.4	0.35	-	0.559

Table 6.4: Eclipsing binaries with both primary and secondary eclipses detected.

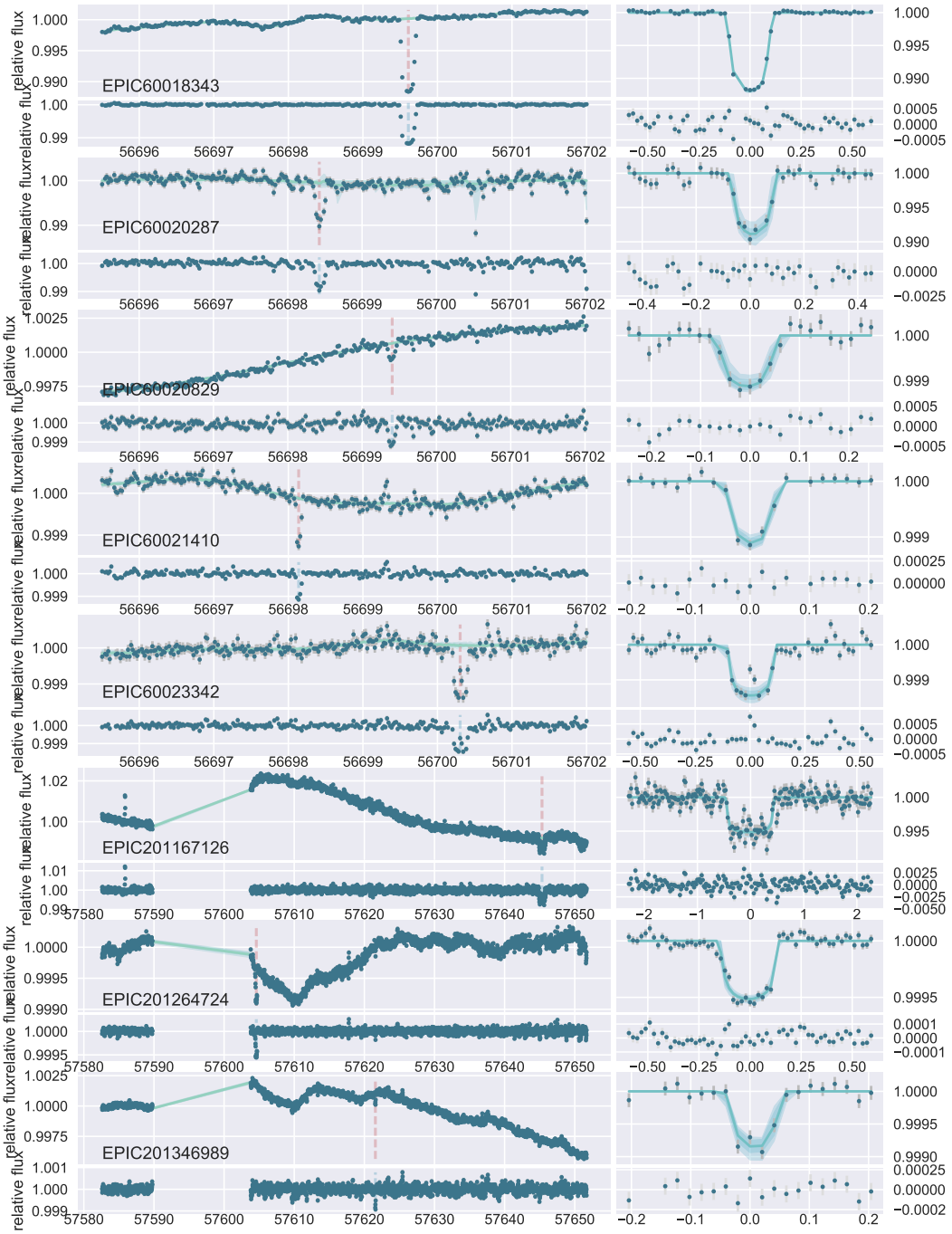

Figure 6.9: K2 STE Candidates. For each candidate: **Upper left:** Detrended K2 lightcurve. GP model is shown in green. The transit position is marked with a red dashed line. **Lower left:** GP-subtracted K2 lightcurve; **Upper right:** A zoom into the GP-flattened K2 lightcurve with transit model over-plotted in light blue; **Lower right:**, residuals to the single transit model.

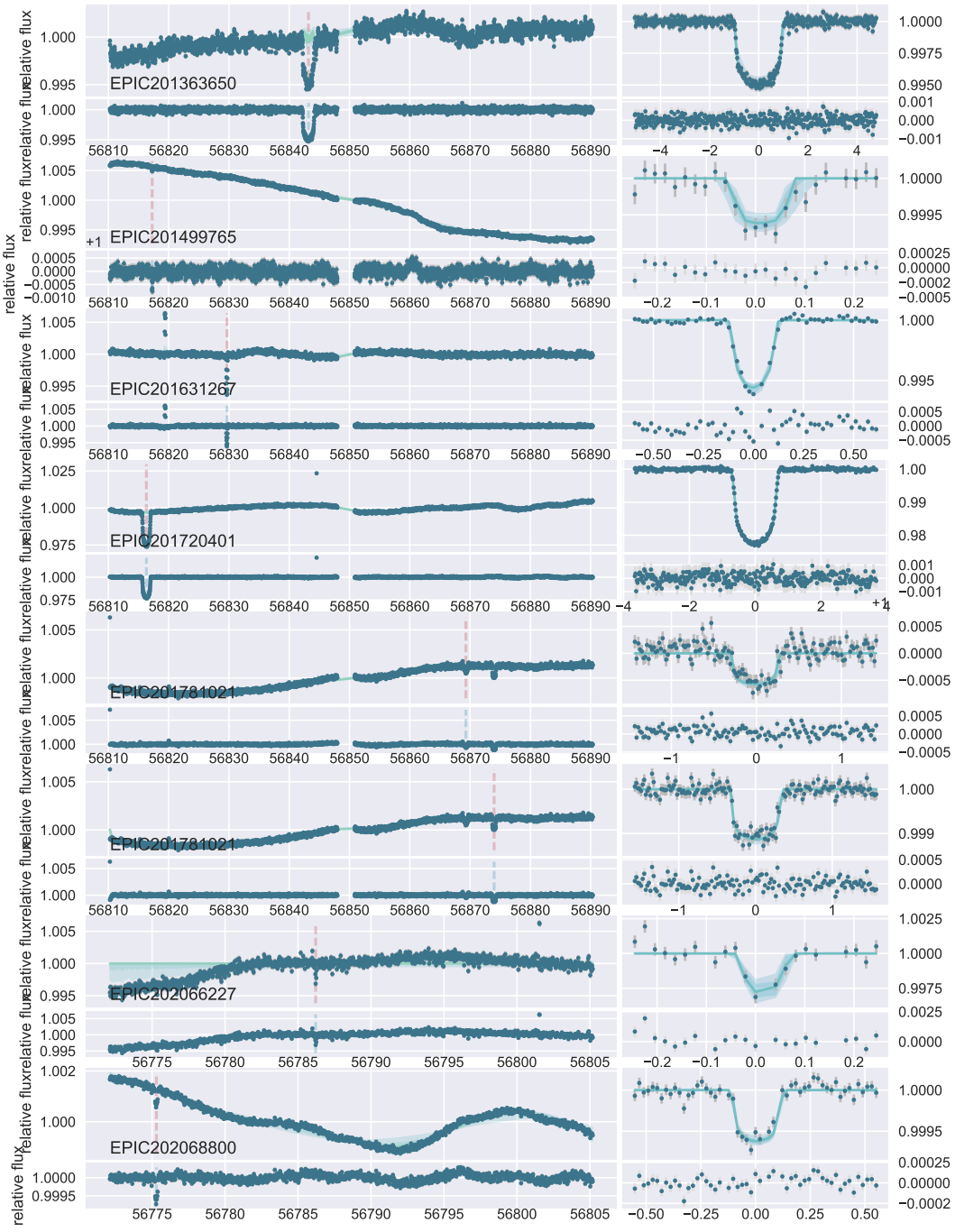

Figure 6.10: K2 STE Candidates [cont.]

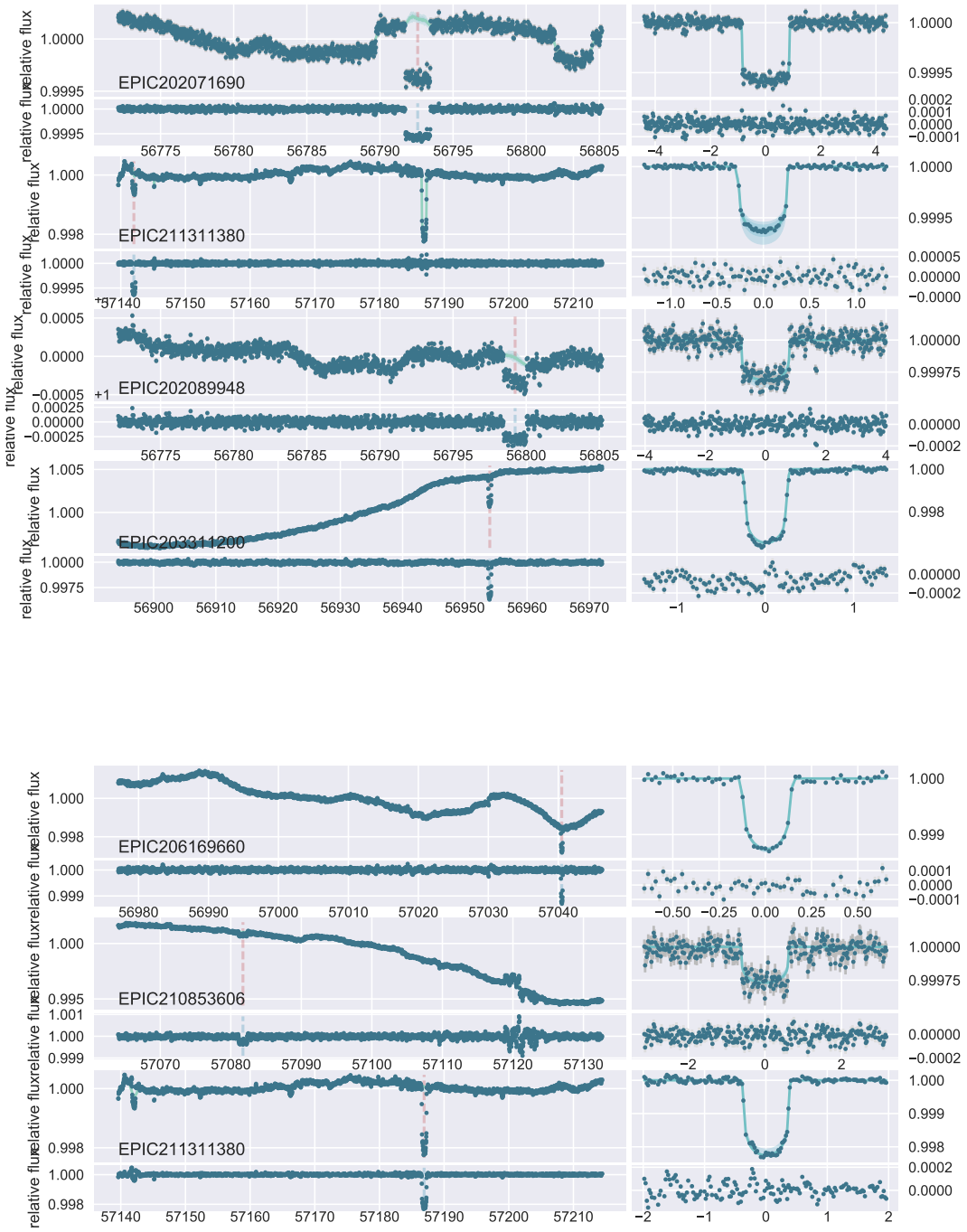

Figure 6.11: K2 STE Candidates [cont.]

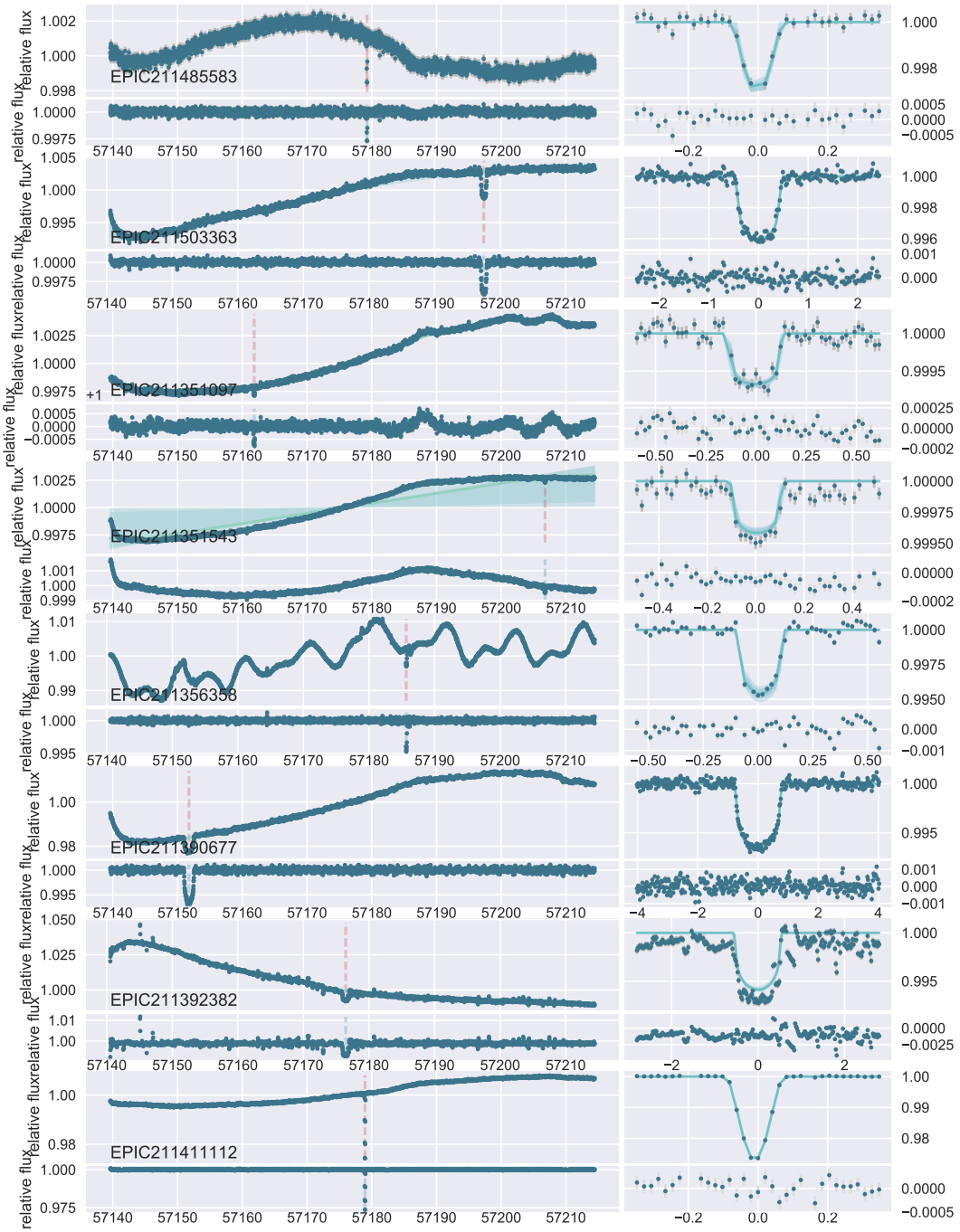

Figure 6.12: K2 STE Candidates [cont.]

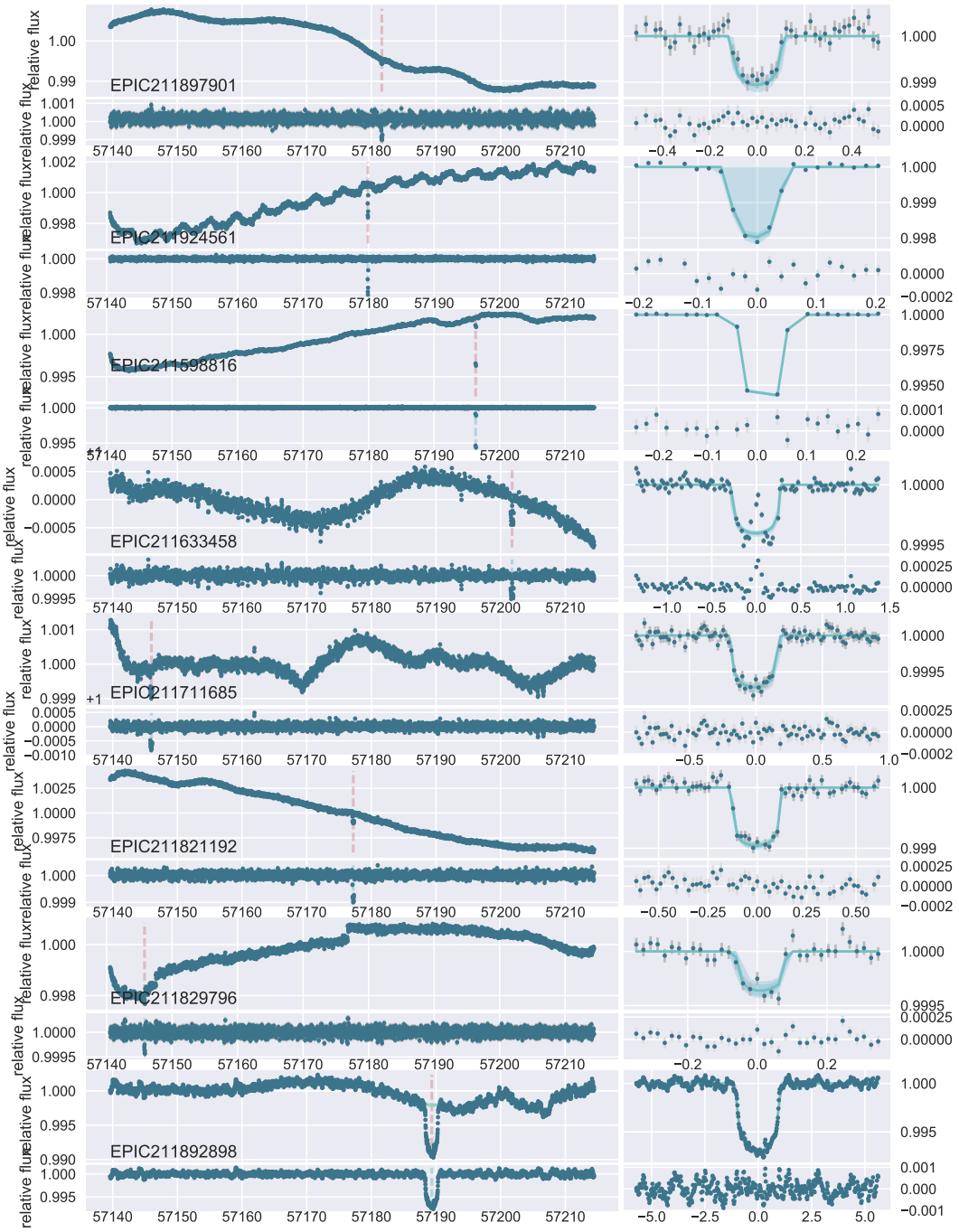

Figure 6.13: K2 STE Candidates [cont.]

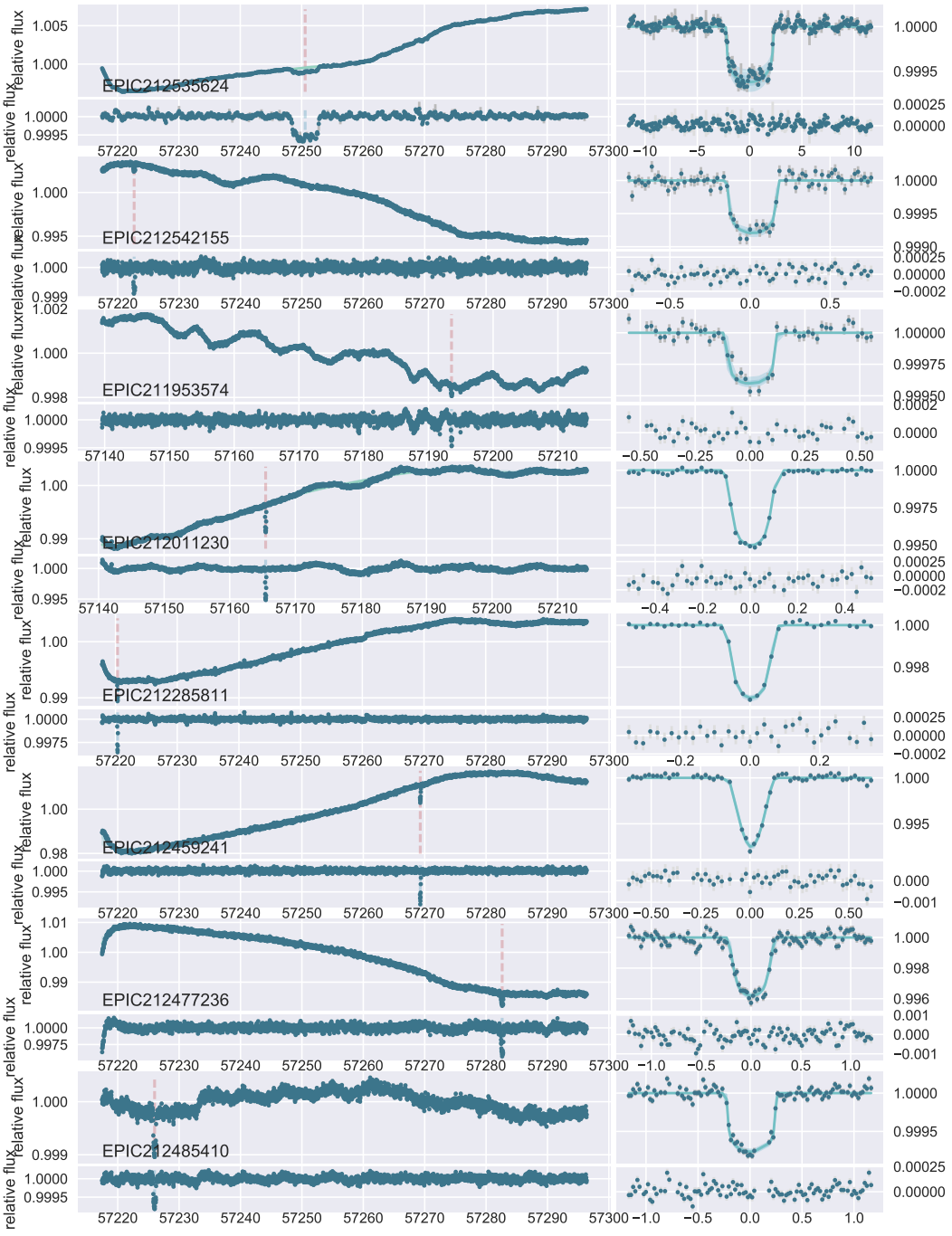

Figure 6.14: K2 STE Candidates [cont.]

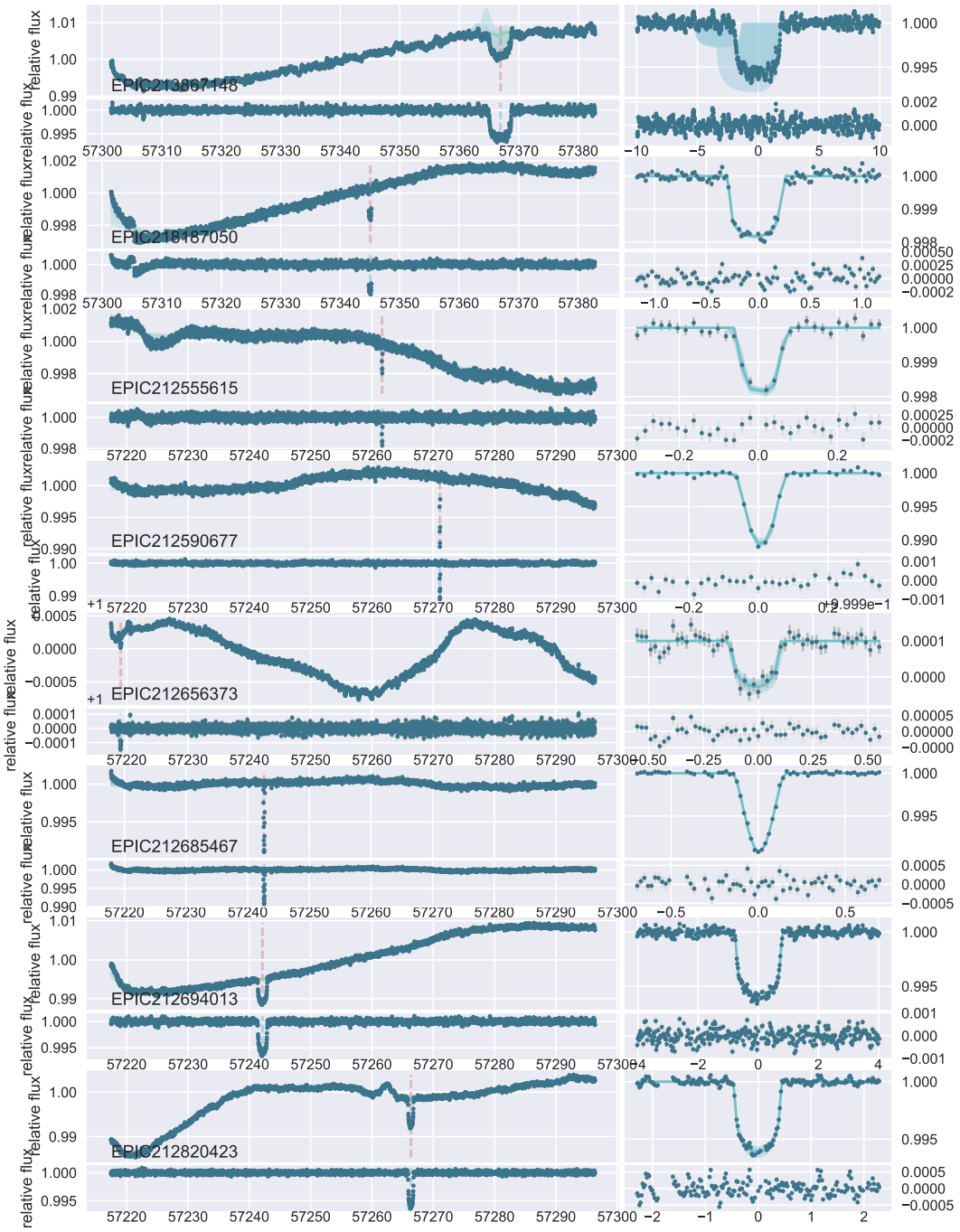

Figure 6.15: K2 STE Candidates [cont.]

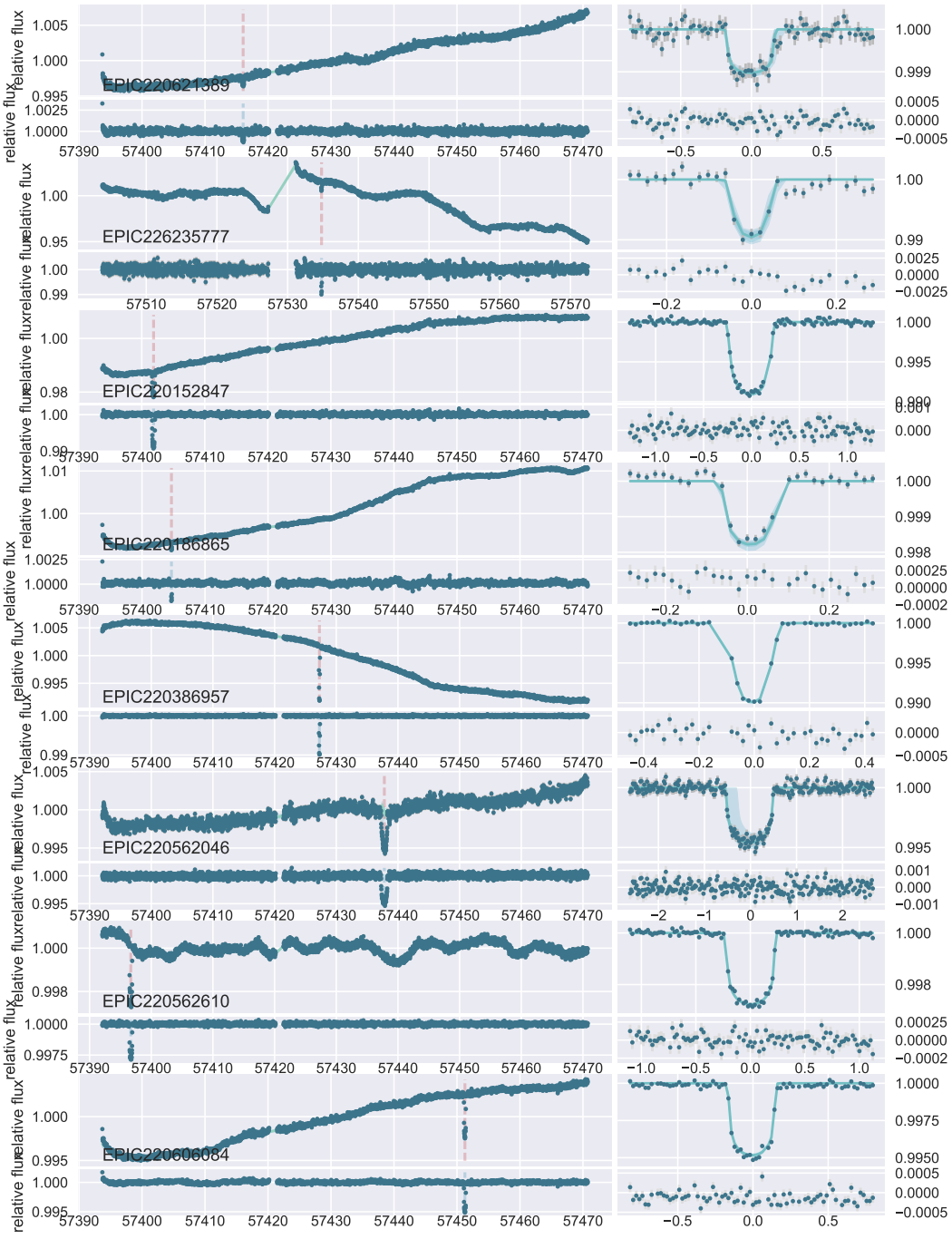

Figure 6.16: K2 STE Candidates [cont.]

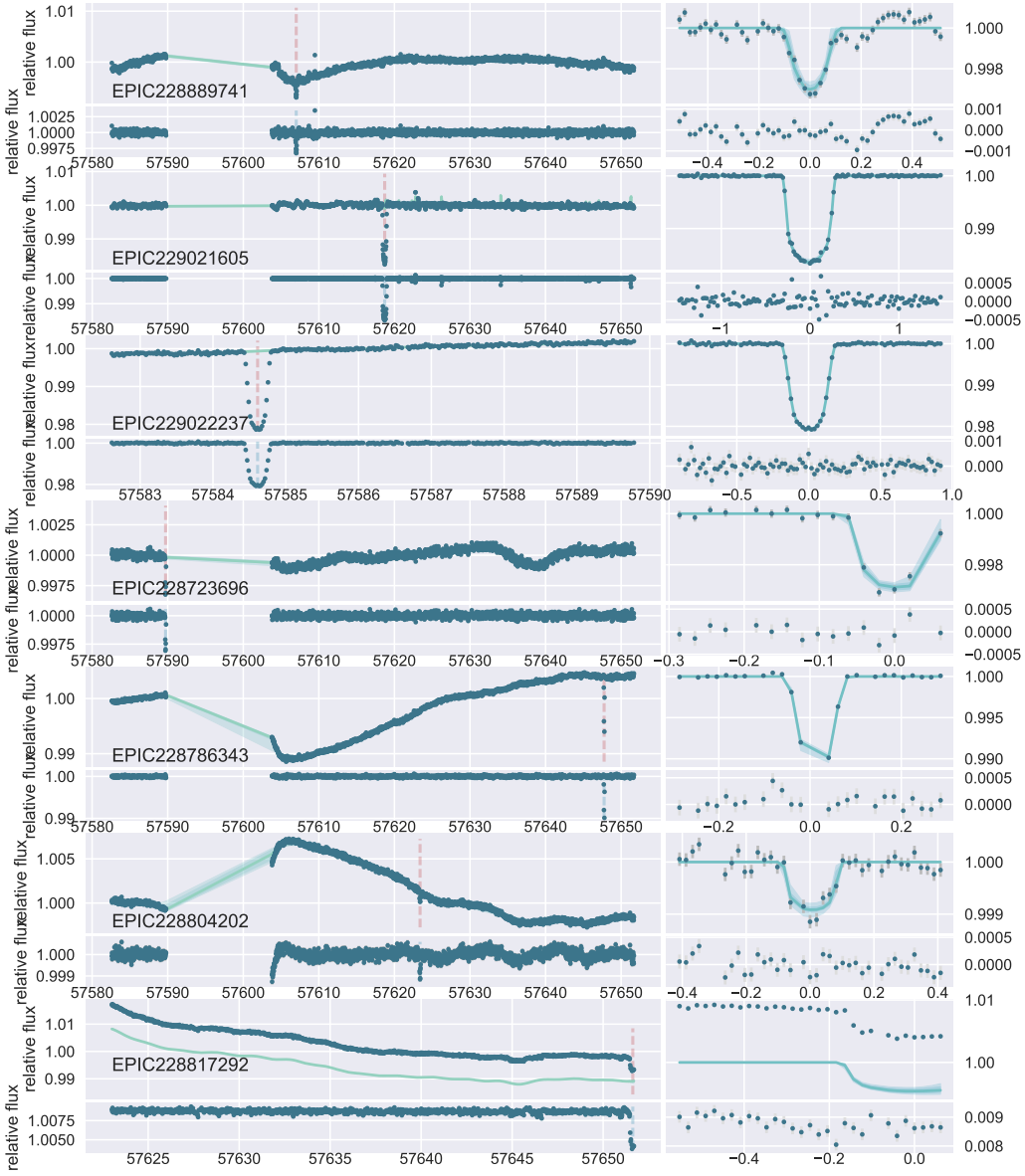

Figure 6.17: K2 STE Candidates [cont.]

EPIC	C	KepMag	RA	Dec	T_{eff}	R_s [$R_\odot$]	M_s [$M_\odot$]	log g[cgs]	ρ_s [$\rho_\odot$]
60018343	E	10.05	00h08m57.98s	+02d56m42.0s	6500 ± 220	$1.3^{+0.1}_{-0.18}$	$1.212^{+0.072}_{-0.085}$	$4.285^{+0.098}_{-0.05}$	$0.55^{+0.15}_{-0.12}$ †
60020287	E	14.9	23h42m59.26s	-09d00m17.9s	3580^{+220}_{-260}	$0.5^{+0.13}_{-0.44}$	0.47 ± 0.12	$4.68^{+0.43}_{-0.18}$	3.2 ± 3.0 †
60020829	E	13.844	23h51m43.76s	-00d28m08.1s	3570^{+220}_{-270}	$0.51^{+0.13}_{-0.47}$	0.47 ± 0.12	$4.68^{+0.45}_{-0.17}$	3.1 ± 3.0 †
60021410	E	9.507	23h35m49.28s	+00d26m43.9s	5089.0 ± 50.0	0.716 ± 0.024	0.775 ± 0.027	4.59 ± 0.026	2.02 ± 0.18 *
60023342	E	11.368	23h31m05.47s	+00d55m49.8s	6040^{+140}_{-160}	$1.13^{+0.09}_{-0.16}$	1.079 ± 0.039	4.36 ± 0.08	0.74 ± 0.18 †
202066227	0	13.7	06h43m33.04s	+28d02m46.6s	8390^{+290}_{-390}	$1.69^{+0.14}_{-0.19}$	1.83 ± 0.13	$4.225^{+0.062}_{-0.051}$	0.365 ± 0.078
202068800	0	11.4	06h20m29.68s	+23d04m27.9s	4780 ± 250	$0.704^{+0.041}_{-0.045}$	$0.766^{+0.045}_{-0.035}$	4.5 ± 0.5	2.1 ± 1.1
202071690	0	10.7	06h36m43.31s	+20d42m12.8s	7930 ± 250	$2.7^{+0.8}_{-1.6}$	$2.01^{+0.31}_{-0.55}$	3.8 ± 0.5	$0.095^{+0.074}_{-0.095}$
202072507	0	11.2	06h31m34.90s	+21d03m54.2s	7690 ± 250	$2.6^{+0.6}_{-1.5}$	$1.9^{+0.29}_{-0.54}$	3.7 ± 0.5	$0.087^{+0.069}_{-0.087}$
202089948	0	10.9	06h30m50.07s	+23d16m35.3s	6280 ± 250	$5.1^{+2.1}_{-3.5}$	$2.13^{+0.55}_{-0.74}$	3.6 ± 0.5	0.02 ± 0.019

Table 6.5: Stellar Information for K2 targets.

EPIC	C	KepMag	RA	Dec	$T_{\rm eff}$	R_s [$R_\odot$]	M_s [$M_\odot$]	log g[cgs]	ρ_s [gcm^{-3}]
201363650	1	13.792	11h24m59.40s	-01d30m13.3s	4912.0 ± 97.0	$2.4^{+2.9}_{-2.4}$	0.86 ± 0.14	3.6 ± 1.0	$0.017^{+0.047}_{-0.017}$
201499765	1	12.766	11h30m56.99s	+00d31m08.0s	6105.0 ± 97.0	1.32 ± 0.39	1.07 ± 0.12	4.19 ± 0.17	$0.45^{+0.2}_{-0.45}$
201631267	1	12.78	11h34m47.15s	+02d31m37.4s	4417.0 ± 99.0	2.64 ± 0.49	1.17 ± 0.11	3.663 ± 0.065	$0.063^{+0.019}_{-0.031}$
201720401	1	14.74	11h56m39.96s	+03d59m11.2s	5230 ± 140	$3.8^{+5.1}_{-3.8}$	0.888 ± 0.055	5.0 ± 0.5	$0.02^{+0.13}_{-0.02}$
201781021	1	12.603	11h16m14.77s	+05d01m25.8s	5540 ± 170	1.83 ± 0.33	1.05 ± 0.13	3.9 ± 0.26	0.17 ± 0.1
203311200	2	11.896	16h03m54.33s	-26d33m13.5s	6830 ± 250	1.95 ± 0.52	1.54 ± 0.2	4.03 ± 0.17	$0.21^{+0.09}_{-0.19}$
206169660	3	11.024	22h14m38.28s	-10d19m34.7s	4992.0 ± 99.0	2.49 ± 0.34	1.1 ± 0.13	3.685 ± 0.09	$0.071^{+0.019}_{-0.028}$
210853606	4	11.27	03h52m52.31s	+20d40m51.4s	5870 ± 180	1.0 ± 0.62	0.865 ± 0.061	4.38 ± 0.17	$0.78^{+0.55}_{-0.78}$
211311380	5	9.128	08h26m27.85s	+10d04m49.4s	6199.0 ± 50.0	1.4 ± 0.19	1.15 ± 0.064	4.18 ± 0.1	$0.4^{+0.11}_{-0.16}$
211351097	5	12.329	08h26m27.85s	+10d04m49.4s	6210 ± 190	1.42 ± 0.47	1.18 ± 0.15	4.18 ± 0.14	$0.4^{+0.19}_{-0.4}$
211351543	5	11.383	08h49m54.95s	+10d50m04.3s	6250 ± 190	1.66 ± 0.81	1.27 ± 0.29	4.04 ± 0.25	0.25 ± 0.2
211356358	5	13.593	08h37m20.04s	+10d50m33.9s	5210 ± 120	0.79 ± 0.12	0.859 ± 0.044	4.562 ± 0.045	$1.7^{+0.43}_{-0.67}$
211390677	5	13.313	08h48m50.83s	+10d55m42.1s	4886.0 ± 97.0	4.9 ± 5.2	0.99 ± 0.21	2.99 ± 0.38	$0.0035^{+0.0074}_{-0.0035}$
211392382	5	8.25	08h30m48.91s	+11d29m40.5s	4902.0 ± 77.0	0.762 ± 0.015	0.83 ± 0.1	4.592 ± 0.02	$1.87^{+0.15}_{-0.15}$
211411112	5	13.405	08h39m50.79s	+11d31m21.6s	6030 ± 210	1.25 ± 0.39	1.06 ± 0.11	4.25 ± 0.14	$0.54^{+0.25}_{-0.54}$
211485583	5	14.237	08h50m26.99s	+11d48m31.3s	5150 ± 140	0.702 ± 0.075	0.728 ± 0.083	4.608 ± 0.054	$2.1^{+0.45}_{-0.56}$
211503363	5	13.221	08h36m03.55s	+12d55m50.7s	4988.0 ± 78.0	4.3 ± 3.5	0.93 ± 0.14	3.08 ± 0.42	$0.0077^{+0.0066}_{-0.0077}$
211598816	5	10.75	08h30m01.63s	+13d11m11.6s	7440 ± 300	2.19 ± 0.91	1.78 ± 0.24	3.96 ± 0.21	$0.16^{+0.09}_{-0.16}$
211633458	5	10.728	09h08m27.29s	+14d31m24.9s	4830 ± 150	10.6 ± 1.0	1.2 ± 0.54	2.48 ± 0.4	$0.00101^{+0.00055}_{-0.00096}$
211711685	5	12.372	08h16m35.05s	+15d00m21.3s	5600 ± 170	0.934 ± 0.074	0.977 ± 0.049	4.476 ± 0.045	1.18 ± 0.21
211821192	5	12.581	08h54m03.43s	+16d04m17.3s	5770 ± 160	0.95 ± 0.25	$0.911^{+0.095}_{-0.095}$	4.444 ± 0.05	$1.06^{+0.38}_{-0.76}$
211829796	5	11.682	08h27m05.68s	+17d37m05.6s	5930 ± 140	1.51 ± 0.63	1.06 ± 0.16	4.05 ± 0.3	$0.29^{+0.18}_{-0.29}$
211892898	5	11.773	08h52m16.71s	+17d44m24.0s	4787.0 ± 77.0	8.7 ± 2.7	0.93 ± 0.12	2.45 ± 0.52	0.0013 ± 0.0011
211897901	5	13.742	08h43m34.63s	+18d37m19.9s	4296.0 ± 68.0	0.52 ± 0.072	0.58 ± 0.1	4.755 ± 0.066	4.0 ± 1.2
211924561	5	10.751	08h38m03.64s	+18d41m45.6s	6980 ± 140	1.79 ± 0.54	1.53 ± 0.16	4.09 ± 0.14	$0.26^{+0.11}_{-0.26}$
211953574	5	11.319	08h50m36.61s	+19d05m28.9s	6027.0 ± 95.0	1.55 ± 0.83	1.18 ± 0.26	4.07 ± 0.27	$0.28^{+0.18}_{-0.28}$
212011230	5	12.375	08h41m31.36s	+19d31m34.8s	4856.0 ± 78.0	4.2 ± 3.9	0.97 ± 0.21	3.08 ± 0.62	0.0065 ± 0.0062
212285811	5	11.803	09h04m57.84s	+20d26m26.9s	6090 ± 150	1.4 ± 0.66	1.18 ± 0.22	4.13 ± 0.2	$0.37^{+0.22}_{-0.37}$
212459241	6	14.074	13h36m17.25s	-17d57m43.2s	5190 ± 120	$0.9^{+2.6}_{-0.9}$	0.858 ± 0.067	4.498 ± 0.09	$0.06^{+0.8}_{-0.06}$
212477236	6	13.936	13h13m34.08s	-13d36m15.8s	5020 ± 120	3.3 ± 1.5	0.93 ± 0.3	3.3 ± 1.2	0.025 ± 0.023
212485410	6	11.193	13h41m58.99s	-13d13m28.6s	5990 ± 140	1.08 ± 0.28	0.892 ± 0.099	4.3 ± 0.16	$0.69^{+0.3}_{-0.65}$
212535624	6	11.417	13h30m42.05s	-13d02m56.5s	5840 ± 180	0.91 ± 0.37	0.835 ± 0.084	4.433 ± 0.085	1.08 ± 0.46
212542155	6	12.52	13h54m42.83s	-11d58m32.4s	5800 ± 140	0.98 ± 0.19	0.966 ± 0.088	4.424 ± 0.055	$0.99^{+0.3}_{-0.5}$
212555615	6	13.424	13h27m09.01s	-11d50m33.9s	5610 ± 220	$2.1^{+5.1}_{-2.1}$	0.874 ± 0.052	3.62 ± 0.67	$0.005^{+0.069}_{-0.005}$
212590677	6	14.449	13h51m37.30s	-11d33m21.2s	5200 ± 160	$2.0^{+4.1}_{-2.0}$	0.89 ± 0.055	3.68 ± 0.9	$0.008^{+0.099}_{-0.008}$
212656373	6	11.378	13h50m53.05s	-10d47m54.2s	4480 ± 220	$14.0^{+22.0}_{-14.0}$	0.96 ± 0.28	2.03 ± 0.74	$6^{+34}_{-6} \times 10^{-5}$
212685467	6	13.264	13h40m20.07s	-09d17m56.2s	5250 ± 130	$0.83^{+0.12}_{-0.3}$	0.916 ± 0.039	$4.55^{+0.25}_{-0.12}$	$1.58^{+0.86}_{-0.69}$
212694013	6	13.364	13h51m51.74s	-08d36m52.5s	4913.0 ± 79.0	5.0 ± 5.0	0.95 ± 0.1	2.95 ± 0.42	$0.0037^{+0.0035}_{-0.0037}$
212820423	6	11.95	13h19m15.45s	-08d24m28.2s	4820.0 ± 78.0	5.1 ± 5.1	1.12 ± 0.2	2.99 ± 0.35	$0.0041^{+0.0055}_{-0.0041}$
213867148	6	13.144	13h41m56.13s	-04d53m41.2s	5150.0 ± 51.0	16.29 ± 0.33	0.804 ± 0.016	1.92 ± 0.21	$0.000184^{+3.2e-05}_{-5e-05}$
218187050	7	12.294	19h22m52.87s	-28d02m21.5s	5380 ± 130	8.75 ± 0.7	0.89 ± 0.25	2.5 ± 1.3	0.0013 ± 0.0011
220152847	7	13.199	18h54m50.16s	-19d15m18.9s	5130 ± 120	0.8 ± 1.0	0.855 ± 0.084	4.559 ± 0.025	$0.5^{+2.2}_{-0.5}$
220186865	8	12.009	01h10m55.35s	-01d47m31.0s	5160 ± 130	$0.9^{+1.8}_{-0.9}$	0.92 ± 0.24	4.521 ± 0.06	$0.3^{+1.4}_{-0.3}$
220386957	8	13.098	01h13m45.63s	-00d30m32.2s	6160 ± 150	1.28 ± 0.3	1.08 ± 0.095	4.24 ± 0.13	$0.5^{+0.2}_{-0.38}$
220562046	8	13.952	00h52m51.48s	+04d27m13.8s	4885.0 ± 98.0	$4.7^{+6.7}_{-4.7}$	0.93 ± 0.1	2.9 ± 1.3	$0.0013^{+0.0065}_{-0.0013}$
220562610	8	12.513	00h37m08.71s	+08d10m26.2s	5920 ± 140	1.4 ± 0.62	1.11 ± 0.11	4.14 ± 0.23	$0.38^{+0.22}_{-0.38}$
220606084	8	13.004	01h14m06.97s	+08d11m15.7s	5760 ± 140	1.5 ± 0.39	0.96 ± 0.11	4.09 ± 0.36	$0.29^{+0.16}_{-0.29}$
220621389	8	13.579	01h02m43.61s	+09d09m35.8s	6000 ± 120	1.24 ± 0.34	1.06 ± 0.12	4.27 ± 0.13	$0.56^{+0.24}_{-0.52}$
226235777	8	13.836	01h09m52.20s	+09d30m30.2s	3510 ± 150	0.5 ± 0.15	0.47 ± 0.15	4.68 ± 0.5	$3.6^{+2.3}_{-3.6}$
228723696	9	12.158	17h35m08.46s	-20d59m56.2s	6610 ± 140	1.44 ± 0.39	1.18 ± 0.42	4.16 ± 0.11	$0.35^{+0.14}_{-0.35}$ †
228786343	10	12.728	12h27m13.71s	-10d10m25.8s	6140 ± 150	1.19 ± 0.17	1.05 ± 0.11	4.28 ± 0.1	$0.6^{+0.17}_{-0.26}$
228804202	10	13.452	12h43m28.81s	-07d20m44.0s	5720 ± 160	0.946 ± 0.079	0.94 ± 0.068	4.46 ± 0.5	$1.09^{+0.47}_{-0.92}$
228817292	10	13.055	12h27m30.65s	-06d36m09.1s	5280 ± 180	0.75 ± 0.1	0.78 ± 0.1	4.573 ± 0.063	1.79 ± 0.62
228889741	10	14.214	12h25m14.71s	-06d03m33.9s	5310 ± 190	0.798 ± 0.081	0.85 ± 0.088	4.552 ± 0.056	$1.64^{+0.33}_{-0.43}$
229021605	10	10.471	12h40m36.90s	-03d27m23.3s	4900 ± 120	6.0 ± 4.1	1.0 ± 0.27	2.78 ± 0.58	0.0033 ± 0.003
229022237	10	13.607	12h43m58.55s	-01d04m21.4s	5170 ± 190	$1.8^{+2.7}_{-1.8}$	0.886 ± 0.086	3.8 ± 0.86	$0.03^{+0.15}_{-0.03}$
201167126	10	15.654	12h18m45.50s	-04d53m16.1s	4560 ± 250	0.412 ± 0.055	0.468 ± 0.052	4.877 ± 0.072	6.7 ± 2.0
201264724	10	10.102	12h08m28.78s	-02d59m05.8s	6100 ± 180	1.31 ± 0.2	1.13 ± 0.12	4.24 ± 0.13	$0.49^{+0.16}_{-0.26}$
201346989	10	12.417	12h13m14.45s	-01d45m05.2s	5370 ± 130	2.0 ± 2.0	0.9 ± 0.12	3.79 ± 0.79	$0.052^{+0.066}_{-0.052}$

Table 6.6: Stellar data; continued from Table 6.5. * targets for which stellar parameters were taken from the discovery paper. †targets without EPIC info for which stellar information required a main-sequence approximation to colour temperature.

EPIC	KepMag	RA	Dec	$T_{\rm eff}$	R_s [$R_\odot$]	M_s [$M_\odot$]	log g[cgs]	ρ_s [$\rho_\odot$]
201631267	12.78	11h34m47.15s	+02d31m37.4s	4420 ± 250	$29.0^{+12.0}_{-19.0}$	$2.52^{+0.61}_{-0.97}$	2.3 ± 0.5	$0.22^{+0.19}_{-0.85}$
201720401	14.74	11h56m39.96s	+03d59m11.2s	5230 ± 250	$0.752^{+0.05}_{-0.062}$	$0.902^{+0.04}_{-0.024}$	5.0 ± 0.5	3400^{+1100}_{-8500}
201781021	12.603	11h16m14.77s	+05d01m25.8s	5540 ± 250	$0.97^{+0.13}_{-0.28}$	$0.97^{+0.025}_{-0.047}$	5.0 ± 0.5	2300^{+1400}_{-6800}
201781021	12.603	11h16m14.77s	+05d01m25.8s	5540 ± 250	$0.97^{+0.13}_{-0.28}$	$0.97^{+0.025}_{-0.047}$	5.0 ± 0.5	2300^{+1400}_{-6800}
202068800	11.4	06h20m29.68s	+23d04m27.9s	4780 ± 250	$0.705^{+0.042}_{-0.046}$	0.766 ± 0.04	4.5 ± 0.5	2900 ± 1600
202071690	10.7	06h36m43.31s	+20d42m12.8s	7930 ± 250	2.7 ± 1.0	$2.01^{+0.3}_{-0.57}$	3.8 ± 0.5	130^{+90}_{-200}
202072507	11.2	06h31m34.90s	+21d03m54.2s	7690 ± 250	$2.6^{+0.6}_{-1.5}$	$1.9^{+0.3}_{-0.55}$	3.7 ± 0.5	120^{+90}_{-200}
202089948	10.9	06h30m50.07s	+23d16m35.3s	6280 ± 250	$5.1^{+2.1}_{-3.6}$	$2.11^{+0.53}_{-0.78}$	3.6 ± 0.5	$28.0^{+24.0}_{-100.0}$
203311200	11.896	16h03m54.33s	-26d33m13.5s	6830 ± 250	$1.304^{+0.066}_{-0.032}$	1.287 ± 0.072	4.7 ± 0.5	900^{+200}_{-2500}
211351097	12.329	08h26m27.85s	+10d04m49.4s	6110 ± 250	$1.085^{+0.027}_{-0.051}$	$1.095^{+0.035}_{-0.038}$	5.0 ± 0.5	1300^{+300}_{-6600}
211356358	13.593	08h37m20.04s	+10d50m33.9s	4910 ± 250	0.719 ± 0.041	$0.785^{+0.032}_{-0.078}$	5.0 ± 0.5	3300^{+900}_{-8900}
211390677	13.313	08h48m50.83s	+10d55m42.1s	4940 ± 250	0.717 ± 0.041	$0.786^{+0.033}_{-0.076}$	4.3 ± 0.5	2700^{+1800}_{-1000}
211503363	13.221	08h36m03.55s	+12d55m50.7s	5230 ± 250	$0.751^{+0.047}_{-0.063}$	$0.902^{+0.04}_{-0.023}$	4.4 ± 0.5	2700^{+1700}_{-1100}
211633458	10.728	09h08m27.29s	+14d31m24.9s	5800 ± 250	$2.37^{+0.59}_{-0.7}$	$1.25^{+0.11}_{-0.17}$	4.0 ± 0.5	160^{+100}_{-350}
211711685	12.372	08h16m35.05s	+15d00m21.3s	5780 ± 250	$2.37^{+0.6}_{-0.7}$	$1.25^{+0.12}_{-0.18}$	3.6 ± 0.5	110^{+70}_{-190}
211821192	12.581	08h54m03.43s	+16d04m17.3s	6260 ± 250	$1.119^{+0.044}_{-0.069}$	$1.119^{+0.036}_{-0.049}$	5.0 ± 0.5	1300^{+300}_{-6300}
211892898	11.773	08h52m16.71s	+17d44m24.0s	5020 ± 250	3.0 ± 1.2	$1.28^{+0.2}_{-0.31}$	3.5 ± 0.5	60^{+40}_{-150}
211924561	10.751	08h38m03.64s	+18d41m45.6s	7320 ± 250	1.338 ± 0.01	1.432 ± 0.071	5.0 ± 0.5	900^{+100}_{-5800}
211953574	11.319	08h50m36.61s	+19d05m28.9s	6520 ± 250	1.21 ± 0.073	$1.191^{+0.06}_{-0.071}$	5.0 ± 0.5	1200^{+300}_{-6200}
212011230	12.375	08h41m31.36s	+19d31m34.8s	4840 ± 250	$0.706^{+0.043}_{-0.046}$	$0.766^{+0.05}_{-0.036}$	4.8 ± 0.5	3200^{+1000}_{-4600}
212485410	11.193	13h41m58.99s	-13d13m28.6s	5530 ± 250	0.846 ± 0.076	0.946 ± 0.02	4.4 ± 0.5	2000 ± 1200
212542155	12.52	13h54m42.83s	-11d58m32.4s	6110 ± 250	$2.1^{+0.41}_{-0.7}$	$1.29^{+0.11}_{-0.15}$	4.1 ± 0.5	240^{+150}_{-400}

Table 6.7: Spectral information for a subset of *K2* targets, from data taken on the ANU 3.2m telescope.

(2014) for Kepler-111 c, Jontof-Hutter et al. (2014) for Kepler-79 d, and the published KOI catalogue for KOI976.01 and KOI1431.01.

Initially, we used transit data for 102 confirmed *Kepler* planets with stellar radius and mass measurements available from the NASA Exoplanet Archive (Akeson et al., 2013)[8]. From transit duration, impact parameter, planetary radii and stellar radii, a circular transit period was estimated and compared to the known period. In the case of eccentric planets, as was detected by (Eylen and Albrecht, 2015), the period estimate is likely to be significantly offset from the circular period.

Intriguingly, stellar densities derived from stellar surface gravities for a wider range (660) of *Kepler* planets showed a correlation between estimated period and impact parameter for grazing transits ($b > 0.6$). This effect is likely due to overestimation of the duration and impact parameter of the shortest transits, for example due to smeared TTVs, which would cause an increase in the estimated period. Such effects would only be present for phase-folded transits, hence unlikely to present problems for `Namaste` analysis.

To avoid this issue, we compared only the better constrained densities from $R_\star$ and $M_\star$ estimates, or directly from asteroseismology. Parameters from the 101 and 69 planets, respectively, were resampled 500 times from a Gassian distribution derived from their uncertainties to produce a cumulative probability distribution of the estimated period compared to the true period. We found that the less-precise density estimates from $R_\star$ & $M_\star$ gave a less precise distribution of orbital period estimates. However both distributions

[8]http://exoplanetarchive.ipac.caltech.edu/

EPIC	Epoch [M<JD]	b	ν' [R_sd^{-d}]	(R_p/R_s)	R_p [$R_{\rm Jup}$]	Per [d]	P(PL)
60018343.1	6699.60635 ± 0.00041	0.738 ± 0.014	$6.89^{+0.16}_{-0.15}$	0.1081 ± 0.00084	$1.39^{+0.15}_{-0.16}$	$30.5^{+6.8}_{-8.4}$	0.6
60020287.1	6698.4358 ± 0.0026	0.43 ± 0.29	$11.5^{+1.4}_{-2.7}$	$0.0866^{+0.0067}_{-0.0052}$	$0.42^{+0.26}_{-0.24}$	34^{+230}_{-60}	1.0
60020829.1	$6699.3998^{+0.0045}_{-0.0046}$	0.42 ± 0.31	$15.7^{+2.8}_{-4.1}$	$0.0306^{+0.0025}_{-0.0021}$	$0.155^{+0.096}_{-0.091}$	14.3^{+170}_{-31}	1.0
60021410.1	6698.1409 ± 0.0018	$0.56^{+0.21}_{-0.36}$	21.0 ± 4.2	0.0313 ± 0.002	$0.223^{+0.018}_{-0.014}$	$7.14^{+7.5}_{-2.9}$	1.0
60023342.1	$6700.3111^{+0.0035}_{-0.0034}$	0.38 ± 0.28	$8.8^{+0.8}_{-1.8}$	$0.0329^{+0.0018}_{-0.0014}$	$0.371^{+0.045}_{-0.044}$	$18.5^{+24}_{-6.5}$	1.0
201167126.1	$7645.3263^{+0.0066}_{-0.0063}$	$0.21^{+0.21}_{-0.15}$	$2.26^{+0.07}_{-0.15}$	0.0686 ± 0.0026	0.28 ± 0.039	5100^{+1200}_{-450}	1.0
201264724.1	7604.5897 ± 0.0037	$0.54^{+0.2}_{-0.35}$	6.1 ± 1.2	0.0213 ± 0.0014	0.278 ± 0.048	40^{+60}_{-20}	1.0
201346989.1	7621.5808 ± 0.0032	0.43 ± 0.32	$21.8^{+3.4}_{-6.2}$	$0.0274^{+0.0026}_{-0.0018}$	$0.53^{+0.58}_{-0.55}$	290^{+2400}_{-250}	0.8
201363650.1	6843.195 ± 0.013	$0.21^{+0.21}_{-0.15}$	$1.032^{+0.029}_{-0.078}$	0.0633 ± 0.0021	1.5 ± 1.8	$1000000^{+18000000}_{-1000000}$	0.6
201499765.1	$6817.2826^{+0.006}_{-0.0043}$	$0.4^{+0.36}_{-0.28}$	$15.2^{+2.7}_{-4.4}$	0.0239 ± 0.0019	$0.317^{+0.099}_{-0.094}$	$2.7^{+6.6}_{-1.6}$	1.0
201631267.1	6829.6742 ± 0.0012	$0.97^{+0.13}_{-0.05}$	$3.77^{+0.29}_{-0.25}$	$0.12^{+0.1}_{-0.03}$	$3.3^{+2.5}_{-0.9}$	22.0 ± 9.0	0.0
201720401.1	$6816.3138^{+0.0025}_{-0.004}$	0.13 ± 0.11	$1.5^{+1.0}_{-0.0}$	$0.134^{+0.001}_{-0.061}$	$0.97^{+0.09}_{-0.44}$	10400^{+3700}_{-8200}	1.0
201781021.1	$6869.3002^{+0.018}_{-0.011}$	$0.51^{+0.38}_{-0.35}$	$3.04^{+0.6}_{-1.4}$	$0.0224^{+0.034}_{-0.011}$	$0.219^{+0.055}_{-0.048}$	1250^{+6700}_{-930}	1.0
201781021.2	6873.9915 ± 0.0036	$0.36^{+0.29}_{-0.25}$	$3.0^{+0.2}_{-0.57}$	0.0311 ± 0.001	$0.3^{+0.07}_{-0.063}$	1200^{+3100}_{-800}	1.0
202066227.1	$6786.2246^{+0.0035}_{-0.0041}$	$0.5^{+0.41}_{-0.34}$	$20.2^{+4.2}_{-9.9}$	$0.052^{+0.012}_{-0.005}$	$0.88^{+0.23}_{-0.12}$	$0.8^{+4.8}_{-0.4}$	0.8
202068800.1	6775.3045 ± 0.002	0.38 ± 0.28	$8.5^{+0.6}_{-1.8}$	0.023 ± 0.0009	0.162 ± 0.012	$65.0^{+60.0}_{-37.0}$	1.0
202071690.1	6792.5897 ± 0.0014	0.1 ± 0.09	$1.16^{+0.006}_{-0.018}$	0.02326 ± 0.00048	0.63 ± 0.24	1100^{+1700}_{-800}	1.0
202072507.1	6790.7145 ± 0.0032	$0.32^{+0.28}_{-0.22}$	$4.84^{+0.25}_{-0.75}$	$0.01833^{+0.00076}_{-0.00067}$	0.47 ± 0.19	22000^{+42000}_{-17000}	1.0
202089948.1	$6799.2414^{+0.0042}_{-0.0047}$	0.23 ± 0.18	$1.233^{+0.029}_{-0.096}$	0.01672 ± 0.00074	0.85 ± 0.48	$500000^{+1400000}_{-400000}$	0.8
203311200.1	6954.01453 ± 0.0008	0.753 ± 0.021	2.75 ± 0.1	0.05834 ± 0.00048	0.757 ± 0.029	$499.0^{+92.0}_{-79.0}$	1.0
206169660.1	$7040.51052^{+0.00083}_{-0.00094}$	0.38 ± 0.3	$7.1^{+0.5}_{-1.5}$	$0.0324^{+0.0023}_{-0.0007}$	0.82 ± 0.12	$4.1^{+4.1}_{-1.4}$	1.0
210853606.1	7081.7202 ± 0.006	0.3 ± 0.2	$1.55^{+0.08}_{-0.21}$	0.0153 ± 0.0006	0.15 ± 0.1	490^{+310}_{-480}	1.0
211311380.1	7186.9143 ± 0.0011	$0.59^{+0.056}_{-0.078}$	$2.18^{+0.14}_{-0.12}$	$0.0452^{+0.0053}_{-0.0077}$	$0.629^{+0.085}_{-0.084}$	703^{+340}_{-480}	0.8
211311380.2	7142.0168 ± 0.0018	0.25 ± 0.18	$3.67^{+0.14}_{-0.38}$	0.0229 ± 0.0012	0.315 ± 0.05	$159.0^{+90.0}_{-49.0}$	1.0
211351097.1	7161.8378 ± 0.0032	0.42 ± 0.3	$7.2^{+0.7}_{-1.7}$	0.0245 ± 0.0011	$0.266^{+0.017}_{-0.014}$	$41.0^{+52.0}_{-11.0}$	1.0
211351543.1	7206.7745 ± 0.0032	0.45 ± 0.32	$8.9^{+1.0}_{-2.6}$	0.019 ± 0.001	0.32 ± 0.16	$8.0^{+32.0}_{-6.0}$	1.0
211356358.1	7185.6965 ± 0.0033	$0.52^{+0.27}_{-0.37}$	$8.7^{+1.4}_{-2.5}$	$0.0636^{+0.0085}_{-0.0036}$	$0.459^{+0.058}_{-0.039}$	60^{+100}_{-20}	1.0
211390677.1	$7151.7759^{+0.0035}_{-0.0033}$	$0.36^{+0.13}_{-0.2}$	$1.268^{+0.072}_{-0.081}$	$0.0733^{+0.0018}_{-0.0015}$	0.524 ± 0.032	17000 ± 10000	1.0
211392382.1	7176.4432 ± 0.0074	0.26 ± 0.21	$1.84^{+0.07}_{-0.18}$	$0.0685^{+0.0022}_{-0.0014}$	0.519 ± 0.017	5500^{+2000}_{-800}	1.0
211411112.1	$7178.95345^{+0.00015}_{-0.00016}$	$1.018^{+0.022}_{-0.032}$	$9.576^{+0.066}_{-0.054}$	0.276 ± 0.02	3.4 ± 1.1	11.0 ± 8.0	0.2
211485583.1	7179.2668 ± 0.0021	$1.02^{+0.11}_{-0.18}$	$6.1^{+3.2}_{-0.6}$	$0.11^{+0.096}_{-0.052}$	$0.77^{+0.67}_{-0.36}$	160 ± 100	0.8
211503363.1	7197.5175 ± 0.0032	$0.79^{+0.04}_{-0.2}$	$1.44^{+0.4}_{-0.11}$	$0.064^{+0.0016}_{-0.0046}$	0.471 ± 0.042	9500^{+7800}_{-6400}	1.0
211598816.1	7196.36134 ± 0.00013	$1.098^{+0.048}_{-0.068}$	$10.16^{+0.23}_{-0.13}$	$0.241^{+0.041}_{-0.053}$	5.0 ± 2.3	$2.6^{+4.8}_{-1.5}$	0.2
211633458.1	7201.76 ± 0.009	$0.35^{+0.3}_{-0.23}$	$3.52^{+0.24}_{-0.64}$	$0.01853^{+0.00085}_{-0.00053}$	0.44 ± 0.12	60^{+160}_{-40}	1.0
211711685.1	7145.979 ± 0.009	$0.52^{+0.33}_{-0.35}$	$4.8^{+0.8}_{-1.8}$	$0.0252^{+0.003}_{-0.0011}$	0.61 ± 0.17	$17.0^{+59.0}_{-12.0}$	1.0
211821192.1	7177.2005 ± 0.0019	0.43 ± 0.29	$7.5^{+0.7}_{-1.7}$	$0.029^{+0.0017}_{-0.0009}$	0.278 ± 0.074	24^{+7}_{-4}	1.0
211829796.1	7145.8128 ± 0.004	$0.46^{+0.35}_{-0.32}$	$13.0^{+1.9}_{-4.3}$	$0.0186^{+0.0017}_{-0.0013}$	0.28 ± 0.12	31^{+22}_{-7}	1.0
211892898.1	7189.322 ± 0.013	$0.65^{+0.08}_{-0.2}$	0.76 ± 0.1	$0.0804^{+0.003}_{-0.0041}$	7.0 ± 2.2	50^{+120}_{-30}	0.0
211897901.1	$7181.6166^{+0.0047}_{-0.0042}$	0.37 ± 0.28	$8.9^{+0.8}_{-1.8}$	0.0293 ± 0.0018	0.153 ± 0.023	110^{+120}_{-40}	1.0
211924561.1	7179.8988 ± 0.0011	$0.71^{+0.28}_{-0.47}$	$16.1^{+6.0}_{-9.7}$	$0.044^{+0.033}_{-0.003}$	$0.86^{+0.58}_{-0.3}$	$2.0^{+18.0}_{-1.0}$	0.8
211953574.1	$7193.5762^{+0.0038}_{-0.0029}$	0.41 ± 0.31	$8.3^{+0.8}_{-2.3}$	0.0188 ± 0.0009	0.29 ± 0.16	16000^{+40000}_{-10000}	1.0
212011230.1	7165.48317 ± 0.00067	$0.847^{+0.014}_{-0.019}$	$5.79^{+0.3}_{-0.23}$	0.0753 ± 0.0012	3.1 ± 2.8	1200^{+6100}_{-900}	0.4
212285811.1	7220.32726 ± 0.00067	$0.87^{+0.03}_{-0.16}$	$8.1^{+2.6}_{-0.8}$	$0.0623^{+0.0023}_{-0.0055}$	0.85 ± 0.4	$11.0^{+26.0}_{-7.0}$	0.8
212459241.1	7269.2849 ± 0.0017	1.06 ± 0.087	$4.58^{+0.26}_{-0.16}$	$0.193^{+0.073}_{-0.065}$	1.5 ± 5.1	$180000^{+470000}_{-100000}$	0.4
212477236.1	$7282.6256^{+0.0044}_{-0.0034}$	$0.86^{+0.04}_{-0.56}$	$2.6^{+2.0}_{-0.3}$	$0.065^{+0.003}_{-0.01}$	2.0 ± 1.0	500^{+6300}_{-400}	0.4
212485410.1	7226.0177 ± 0.0026	0.44 ± 0.29	$3.88^{+0.39}_{-0.83}$	0.0259 ± 0.0009	0.279 ± 0.073	250^{+350}_{-130}	1.0
212535624.1	7250.605 ± 0.027	$0.53^{+0.29}_{-0.37}$	0.38 ± 0.09	$0.0234^{+0.0026}_{-0.0014}$	$0.219^{+0.084}_{-0.089}$	$370000^{+770000}_{-180000}$	1.0
212542155.1	$7222.6897^{+0.0024}_{-0.0025}$	0.38 ± 0.27	$6.1^{+0.4}_{-1.1}$	0.0261 ± 0.0009	0.256 ± 0.051	$87.0^{+81.0}_{-34.0}$	1.0
212555615.1	7261.6643 ± 0.0018	$0.73^{+0.25}_{-0.49}$	$12.8^{+5.3}_{-7.3}$	$0.043^{+0.022}_{-0.003}$	1.0 ± 2.5	1000^{+13000}_{-1000}	0.6
212590677.1	7271.0849 ± 0.00078	$0.95^{+0.13}_{-0.45}$	$8.5^{+7.9}_{-0.5}$	$0.143^{+0.094}_{-0.05}$	$2.8^{+7.1}_{-5.8}$	2000^{+23000}_{-2000}	0.4
212656373.1	7219.025 ± 0.0042	0.4 ± 0.29	$8.4^{+0.8}_{-1.9}$	$0.01045^{+0.00084}_{-0.00066}$	1.6 ± 2.3	10^{+100}_{-10}	0.4
212685467.1	$7242.66163^{+0.00075}_{-0.00076}$	1.03 ± 0.11	$3.94^{+0.33}_{-0.09}$	$0.19^{+0.074}_{-0.06}$	$1.52^{+0.77}_{-0.52}$	440 ± 230	0.4
212694013.1	7242.1581 ± 0.0032	$0.46^{+0.09}_{-0.15}$	$1.19^{+0.084}_{-0.066}$	0.0715 ± 0.0013	$3.6^{+3.5}_{-3.5}$	$90000^{+270000}_{-70000}$	0.4
212820423.1	7266.3447 ± 0.0022	0.36 ± 0.19	$2.17^{+0.12}_{-0.17}$	$0.0709^{+0.0025}_{-0.002}$	3.5 ± 3.7	18000^{+41000}_{-12000}	0.4
213867148.1	$7366.88^{+0.017}_{-0.031}$	$0.19^{+0.16}_{-0.13}$	$0.529^{+0.011}_{-0.045}$	0.0705 ± 0.0039	11.41 ± 0.71	$24.0^{+15.0}_{-5.0}$	0.0
218187050.1	$7345.0334^{+0.0067}_{-0.0047}$	0.45 ± 0.29	$3.6^{+0.41}_{-0.78}$	$0.0399^{+0.0022}_{-0.0009}$	3.51 ± 0.32	760^{+830}_{-320}	0.0
220152847.1	7401.8668 ± 0.0011	$0.57^{+0.08}_{-0.24}$	$3.63^{+0.44}_{-0.25}$	$0.0895^{+0.0019}_{-0.0041}$	0.7 ± 1.1	180^{+920}_{-780}	0.6
220186865.1	$7404.682^{+0.0018}_{-0.0014}$	0.38 ± 0.29	$14.4^{+1.2}_{-3.0}$	$0.0388^{+0.0025}_{-0.0011}$	0.33 ± 0.69	10000^{+31000}_{-6000}	0.8
220386957.1	7427.26466 ± 0.00049	$0.8724^{+0.0055}_{-0.0067}$	6.37 ± 0.13	0.10616 ± 0.00084	1.35 ± 0.32	$35.0^{+27.0}_{-14.0}$	0.6
220562046.1	$7437.7766^{+0.0066}_{-0.0051}$	$0.24^{+0.26}_{-0.17}$	$1.95^{+0.05}_{-0.14}$	0.0611 ± 0.0023	2.8 ± 4.1	$20000^{+420000}_{-20000}$	0.4
220562610.1	7396.6903 ± 0.0011	$0.44^{+0.18}_{-0.27}$	$4.11^{+0.4}_{-0.51}$	0.049 ± 0.0012	0.69 ± 0.3	110^{+230}_{-70}	1.0
220606084.1	7451.25239 ± 0.0008	0.38 ± 0.23	$6.06^{+0.44}_{-0.77}$	$0.0644^{+0.002}_{-0.0009}$	$0.97^{+0.25}_{-0.25}$	$26.0^{+43.0}_{-15.0}$	1.0
220621389.1	7416.0492 ± 0.0048	0.42 ± 0.3	5.5 ± 0.9	$0.0301^{+0.0017}_{-0.001}$	0.37 ± 0.1	70^{+120}_{-40}	1.0
226235777.1	7534.7937 ± 0.0026	0.43 ± 0.29	$18.3^{+2.5}_{-4.3}$	$0.09^{+0.0064}_{-0.0054}$	0.45 ± 0.14	$13.0^{+43.0}_{-9.0}$	1.0
228723696.1	7589.7253 ± 0.0013	0.44 ± 0.3	$16.3^{+1.7}_{-4.0}$	$0.0508^{+0.0026}_{-0.0015}$	0.73 ± 0.2	$1.8^{+3.4}_{-0.9}$	1.0
228786343.1	$7647.76119^{+0.00033}_{-0.00038}$	0.97 ± 0.1	$10.2^{+1.3}_{-0.4}$	$0.169^{+0.078}_{-0.048}$	$2.02^{+0.95}_{-0.69}$	9.4 ± 5.0	0.4
228804202.1	7623.3981 ± 0.003	0.47 ± 0.32	$11.0^{+1.4}_{-3.3}$	$0.0286^{+0.0022}_{-0.0013}$	0.272 ± 0.028	$17.0^{+34.0}_{-9.0}$	1.0
228817292.1	$7651.63^{+0.028}_{-0.018}$	0.29 ± 0.23	$5.85^{+0.93}_{-0.97}$	0.0622 ± 0.0024	$0.463^{+0.068}_{-0.063}$	160 ± 100	1.0
228889741.1	7607.0082 ± 0.0038	1.044 ± 0.097	$3.84^{+0.75}_{-0.39}$	$0.132^{+0.085}_{-0.064}$	$1.05^{+0.68}_{-0.51}$	520^{+270}_{-230}	0.6
229021605.1	7618.7034 ± 0.0013	0.15 ± 0.1	$3.679^{+0.04}_{-0.076}$	0.115 ± 0.001	7.0 ± 4.7	$1.2^{+7.0}_{-1.0}$	0.2
229022237.1	7584.61346 ± 0.0004	0.707 ± 0.011	$4.778^{+0.067}_{-0.064}$	$0.14167^{+0.00074}_{-0.00078}$	2.5 ± 3.7	$30000^{+240000}_{-20000}$	0.4

Table 6.8: Planetary data for the 70 exoplanet candidates detected in K2. MJD is HJD-2450000

peak at the true value, and suggest that the analytical technique is valid.

To show the accuracy to which lightcurve-derived planet parameters can predict the orbital period, we used data from the California-Kepler Survey (Johnson et al., 2017, ; CKS) and computed periods using the formulas derived in Section 6.2.3. These show extremely precise agreement between estimated planetary period (from transit-derived parameters), and the real planet period (left-hand panels of Figure 6.18). In this case, the major deviation from a perfect Gaussian comes from eccentricity, with the median deviation comparing almost exactly with that expected from the general eccentrcitiy distribution in figure 6.6.

However, these transit parameters were derived from dozens of phase-folded transits, and are therefore not accurate estimations of the information in a single transit. Using Yee and Gaudi (2008) (Eq 13 & 28), we calculated the contribution to period uncertainty from a single transit from the Kepler lightcurve, given the observed planet parameters. This was then propagated into the density- and eccentricity- dominated distributions shown in the left of Figure 6.18 to give an accurate representation of the likely period uncertainties from single transits alone. As expected, this shows good agreement only for large planets on long periods, where single transit SNR is high; for example planets on > 100d orbits and with radii > $5R_{\oplus}$ have median uncertainties of only ∼10%, as the six examples of Kepler planets showed earlier in this section.

6.4.2 K2 Single Transit Events

In total, we detected 72 single transit candidates in K2, and estimated their size and orbital periods (see table 6.8). Of these, the majority (40) had posterior radius distributions entirely within the "planetary" regime ($R < 1.5R_{\rm Jup}$). A further 32 exist in the "ambiguous" region, and only three are entirely ruled out as planets. The number of detections is too many to discuss on a case-by-case basis, instead we break the sample up into patterns, discussing specific cases within each. We show the candidates as a function of magnitude, period and radius in figure 6.19.

Previously detected planets

Three of the candidates have previously been detected. EPIC60021410 as K2-2b Vanderburg et al. (2015b). The orbital prediction of K2-2 b of $7.14^{+7.5}_{-2.9}$d is consistent with the true period of 9.12d.

The HIP41378 system (EPIC211311380 Vanderburg et al., 2016) has two inner planets and three long-period single transiting planets. Due in part to the V-shaped nature of the transit, and the high level of out-of-transit systematics, we were unable to fit the lightcurve of the shallowest transit of the three ($t_0 \sim 2457166$), so only the two deepest

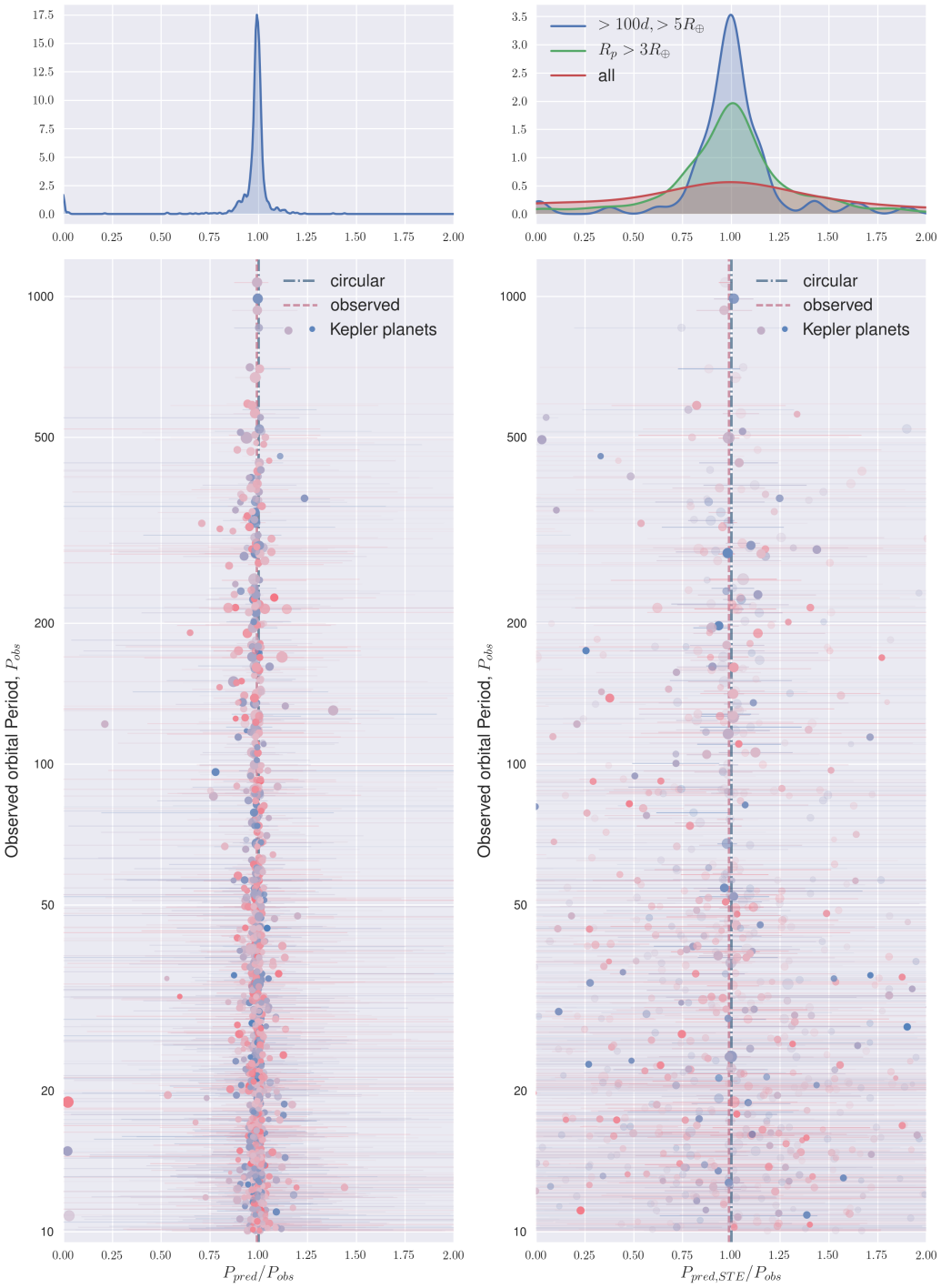

Figure 6.18: Kepler planets as a function of observed orbital period (y-axes) and the ratio of the orbital period predicted from only the lightcurve, and that observed (x-axes). Left panels show planetary information derived from multiple transits. Right panels show planetary information derived from only single transits, predicted using the formulation of Yee and Gaudi (2008). Upper figures show the kernel densities of these distributions as a function of period ratio.

single transits are explored here. We derive a period of $159.0^{+90.0}_{-49.0}$d for the initial single transit, which matches that of Vanderburg et al. (2016) very closely (156^{+163}_{-78}d), and with better constraints on the period. For the outer planet we find $P = 703^{+340}_{-480}$d which is within 1-σ but significantly longer than the estimate of 324^{+121}_{-126}d from Vanderburg et al. (2016).

Ultra-short period candidates

Some give estimated periods far shorter than the minimum period apparent using the duration of observations in K2 light curves. In the majority of such cases (e.g. EPICs 211411112.01, 211598816.01, etc.) these Ultra-short period candidates are also co-incident with low planet probabilities. This is highly suggestive that these candidates are in fact false positives such as grazing EBs. This is consistent with the fact that deep V-shaped EBs were excluded as obvious unplanetary candidates during the compilation of the transit list, leaving only shallow-depth, high impact parameter binaries to populate the candidate list.

A few candidates with high planetary probability also showed periods at least 1-sigma shorter than the minimum period as set from the lightcurve. These include EPICs 228723696.1 (1.8d), 206169660.01 (4.1d), 211351543 (8d) and 211821192 (24d). There are three plausible solutions to these systems: (i) These cases may be extremely eccentric planets, which have a far greater transit probability at perihelion and would transit with a much faster velocity that expected. (ii) The star is misclassified, for example as a giant or sub-giant, which could cause a hundred-fold difference in stellar density (and equivalently orbital period). (iii) An extremely high impact-parameter transit (or eclipse).

Ultra-long period candidates

In the opposite case, we also see transits with extremely long durations leading to extremely long-period orbit estimates, far higher than we might expect to observe given the number of stars in the sample, and the transit probability of distant objects. These include EPICs 201363650.01 (10^6d), 202089948.01 (5×10^5d), 211390677.01 (1.7×10^4d), 212459241.01 (1.8×10^5d), 212535624.01 (3.7×10^5d), 212694013.01 (9×10^4d), etc. These periods are such that, even if many planets were present at such distances around every star, the transit probability ($< 0.02\%$ for a 10^5d period) combined with the mission duration of *K2* ($< 0.1\%$ for 10^5d) should never produce any such detections. Hence, in these cases, it would appear most likely that the star is misclassified as a dwarf. The far lower density of giant stars (as low as $10^{-4}\rho_\odot$), means the orbital period is equivalently shorter, moving a 10^5d planet to only 100d - a far more likely proposition. The dominant luminosity of a giant to a dwarf star also means eclipses across giants appear much the same as exoplanetary transits. Alternative, a blended giant-dwarf binary within the Kepler aperture could provide the same

EPIC	Epoch	mag	R_p	Per	P(PL)	$K_{\rm RV}$
60023342.1	6700.3111 ± 0.0035	11.4	0.371 ± 0.045	$18._{-6.5}^{+24}$	1.0	$2.9_{-1.6}^{+5.1}$
201264724.1	7604.5897 ± 0.0037	10.1	0.278 ± 0.0048	$40{+}60_{-20}$	1.0	$1.1_{-0.4}^{+1.3}$
201346989.1	7621.5808 ± 0.0032	12.4	0.5 ± 0.5	290_{250}^{+2400}	0.8	$4.0_{-3.0}^{+54}$
201781021.1	6789.3002 ± 0.0015	12.6	0.219 ± 0.05	1250_{-930}^{+6700}	1.0	$0.3_{-0.13}^{+0.22}$
201781021.2	6873.9915 ± 0.0036	12.6	0.3 ± 0.07	1200_{-800}^{+3100}	1.0	$0.42_{-0.58}^{+0.20}$
202068800.1	6775.3045 ± 0.002	11.4	0.162 ± 0.012	65.0_{-37}^{+60}	1.0	$0.46_{-0.14}^{+0.24}$
202071690.1	6792.5897 ± 0.0014	10.7	0.63 ± 0.24	1100_{-800}^{+1700}	1.0	$2.28_{-1.63}^{+5.32}$
203311200.1	6954.01453 ± 0.0008	11.9	0.757 ± 0.029	499_{-79}^{+92}	1.0	$5.1_{-2.8}^{+29.8}$
210853606.1	7081.7202 ± 0.006	11.3	0.15 ± 0.1	490_{-480}^{+310}	1.0	$0.36_{-0.24}^{+0.33}$
211311380.1	7186.9143 ± 0.0011	9.13	0.629 ± 0.085	703_{-480}^{+340}	0.8	$3.9_{-2.5}^{+6.0}$
211311380.2	7142.0168 ± 0.0018	9.13	0315 ± 0.05	159_{-49}^{+90}	1.0	$0.84_{-0.28}^{+1.4}$
211503363.1	7197.5175 ± 0.0032	13.2	0.471 ± 0.042	9500_{-6400}^{+7800}	1.0	$0.95_{-0.69}^{+1.05}$
211633458.1	7201.76 ± 0.009	10.7	0.44 ± 0.12	60_{-40}^{+120}	1.0	$3.27_{-2.29}^{+5.31}$
211829796.1	7145.979 ± 0.004	11.7	0.28 ± 0.12	31_{-7}^{+22}	1.0	$1.39_{-0.59}^{+3.32}$
212485410.1	7226.0177 ± 0.0026	11.2	0.279 ± 0.073	250_{-130}^{+350}	1.0	$0.72_{-0.28}^{+0.74}$
212542155.1	7222.6897 ± 0.0025	12.5	0.256 ± 0.051	87_{-34}^{+81}	1.0	$0.54_{-0.17}^{+0.19}$
220152847.1	7401.8668 ± 0.0011	13.2	0.7 ± 1.1	760_{-320}^{+830}	0.6	76_{-75}^{+1100}
220562610.1	7396.6903 ± 0.0011	12.5	0.69 ± 0.3	110_{-70}^{+230}	1.0	$8.3_{-6.4}^{+53}$
220606084.1	7451.25239 ± 0.0008	13.0	0.97 ± 0.25	26_{-15}^{+43}	1.0	101_{-88}^{+346}
228817292.1	7651.63 ± 0.025	13.1	0.463 ± 0.065	160 ± 100	1.0	$3.9_{-2.9}^{+4.2}$

Table 6.9: Parameters for a subset of K2 single transit candidates with reasonable period estimates, high $P_{\rm PL}$ values, and orbiting bright stars (mag<13.2).

affect.

In both cases, spectroscopic follow-up can improve our understanding of the system.

Well-fitted Candidates

The majority of candidates appear both planetary and with reasonable period and planetary radius constraints. Some of these stick out immediately as excellent planet candidates, with bright magntidues allowing their follow-up with other techniques including RVs. This subset is listed in Table 6.9.

6.4.3 EB candidates

The increased number of degeneracies and decreased level of precision on stellar parameters mean we are unable to perform model fits for the single eclipsing binary candidates as they stand. However, we note that the eccentricity of long-period eclipsing binaries appears significant, with 16 of the 26 detected clearly having non-zero eccentricities. This is

Figure 6.19: Distribution of K2 single transit candidates as a function of estimated period (x-axis), magnitude (y-axis) and size (marker diameter).

partially a selection effect, as eccentric binaries are statistically more likely to eclipse, as briefly explored for planets in section 6.2.4.

6.4.4 Source of Uncertainty

For our best-constrained K2 candidates, the dominant source of error is stellar density. Even for a main sequence star with a well-constrained stellar temperature, density uncertainties can be on the order of 50%.

For less well-constrained probability distributions, for example from noisy lightcurves, the uncertainty in planetary velocity can be important. This is especially true for small planets for which impact parameter becomes more degenerate.

As shown in section 2.4, eccentricity also has a role in increasing period uncertainties. However, the majority of exoplanets are expected to be on circular or near-circular orbits for which the correction is minimal (Kipping, 2013). If density can be constrained by follow-up observations, however, eccentricity could become an important factor when searching for a subsequent transit.

One interesting exception may be known multiplanet systems, which improve the single transit method in three ways: The low mutual inclination in such systems increases the transit probability of exterior planets; stability constraints and formation pathways also limit long-period planets to more circular orbits; and stellar parameters such as density are significantly improved due to the information gathered by interior planets (for example densities through transit durations). As such, searches for single transits in known multiplanet systems could have valuable results.

6.4.5 Follow-up Observations

A key strategy of follow-up would first be to obtain a single high-SNR, modreate resolution spectrum to rule out giant star eclipses, and to better characterise the parent. We have so far only obtained such spectra for 23 targets, but plan to expand this to more. Lucky or AO imaging could rule out close companions that could either be the source of a false positive EB system, or diluting the transit depth.

To confirm the planet, constrain the orbital period, and determine its mass (and therefore density), radial velocity observations are required. Such a strategy is only sensible for the brightest (V<13.5) and largest ($R_p > 4R_\oplus$) targets for which the reflex motion is strong and the noise during a sensible length exposure is short. Radial Velocities can be tailored to the likely period to give best observing strategy.

Good period estimates from single transit candidates could then be used to search for repeat transits. Precise transit survey telescopes such as MEarth (Irwin et al., 2008)

EPIC	Instrument	Number	Comment	Result
201631267	Sophie	x1	SB2 - False Positive	EB/FP
203311200	Coralie	x4	Trend in measurements (230ms^{-1})	PL?
204634789	Coralie	x1	No obvious EB (<2 kms^{-1}).	?
206169660	Coralie	x1	No obvious EB (<2 kms^{-1}).	?
211503363	Sophie	x2	SB1 - kms^{-1} variation in RVs suggests EB	EB/FP
211892898	Sophie	x1	No obvious EB (<2 kms^{-1}).	?
211924561	Sophie	x1	No obvious EB (<2 kms^{-1}).	?
212011230	Sophie	x1	No obvious EB (<2 kms^{-1}).	?
212485410	Coralie	x2	No trend or variation in RVs (<15ms^{-1})	PL?
212542155	Coralie	x3	No trend or variation in RVs (<20ms^{-1})	PL?
212694013	Coralie	x1	No obvious EB (<2 kms^{-1}).	?
212820423	Coralie	x1	No obvious EB (<2 kms^{-1}).	?
218187050	Coralie	x1	No obvious EB (<2 kms^{-1}).	?
229021605	Coralie	x2	SB1 - kms^{-1} variation in RVs suggests EB	EB/FP

Table 6.10: RV follow-up information.

or NGTS (Wheatley et al., 2013), and even amateur observer programs, could be used. However, to cover a transit range of many days, such redetections would ideally utilise observers at different longitudes (e.g. LCO Brown et al., 2013), or a satellite in space (e.g. CHEOPS Broeg et al., 2013). Alternatively, future all-sky photometric missions (e.g. TESS Ricker et al. (2010), or PLATO Rauer et al. (2014)) may serendipitously re-detect some of these objects.

6.4.6 Validation

We have shown that, for favourable single transits, the orbit and size of a transiting exoplanet can be accurately determined, especially for giant planets. However, alternative sources for such transits (e.g. from background eclipsing binaries) remain. As has been shown (Morton, 2012), the source of such false positives can be probabilistically excluded with follow-up data. For example sub-arcsecond imaging can rule out stellar companions that could be producing spurious signals. Spectral fitting to high-SNR spectra can be used to rule out closer binary companions. Radial velocity measurements (even where the detection of the signal from planet is impossible) could be used to place limits on the size of any companion. In those cases without close companions, the planetary radius of the eclipsing object can be probabilistically limited to a planetary, rather than stellar, origin.

Such follow-up could, in a similar way to the validation of other single transiting systems such as Kepler-452 (Jenkins et al., 2015), constitute a probabilistic validation of the planet without observing subsequent transits. Similarly, three of the 17 single transiting exoplanets detected by Wang et al. (2015) were probabilistically validated using such

methods.

6.5 Conclusion

We have developed `Namaste`, a method of combining stellar parameters with the lightcurve of a single transit to estimate orbital parameters. We have tested this analysis on published transit parameters for a large sample of *Kepler* multiplanets, showing close agreement. A test of the full fitting method on the lightcurves of four known *Kepler* planets and two KOI candidates showed extremely good agreement, with the periods of Kepler-51 d, Kepler-117 c, Kepler-111 c and KOI1431.01 all estimated to within 10%.

We performed a search on all available campaigns of K2 data and identified 72 transit signals with small (<2.5%) eclipses likely to be planetary, and 72 eclipsing binaries. To estimate their radius and orbital period, the fitting procedure `Namaste` was utilised. Of the 72 planets found, three are ruled out by these fits, and two more by follow-up measurements. Of the remaining planets, the majority (39) appear to have planetary radii, and 25 orbit stars bright than 12th magnitude. More follow-up is required to definitely confirm these as *bona fide* planets. However, such long-period planets, especially if found around bright stars, could pave the way for a new regime of exoplanetary science. This includes the detection of planets within the astrometric sensitivity of Gaia, and cold Jupiters with atmospheres observable in transmission spectroscopy by JWST. The candidates EPIC202071690 (Kmag= 10.7,R_p = 0.63R$_J$,P = 1100d), EPIC203311200 (Kmag= 11.9,R_p = 0.76R$_J$,P = 500d), EPIC210853606 (Kmag= 11.3,R_p = 0.76R$_J$,P = 490d), EPIC211392382 (Kmag= 8.2,R_p = 0.51R$_J$,P = 5500d) and EPIC212485410 (Kmag= 11.2,R_p = 0.28R$_J$,P = 250d) could be the first exoplanets to push into this regime.

Chapter 7

Conclusion and Future Work

"Don't think I'm ever going to see intelligent life in my lifetime" - djh1975, UK.
" indeed, especially judging by these comments." - Zach Cano, Iceland, Daily Mail

7.1 Conclusion

The detection, confirmation and subsequent study of transiting exoplanets has been the key to the rapid advancement of exoplanetary science in the last decade. The rise of a K2 mission capable of detecting planets around hundreds of bright stars on the ecliptic plane has further advanced the field. In Chapter 3 of this thesis I presented the detection of around 200 transiting planet candidates on 1 to 40 day orbits around bright stars. As a result of this search, many candidates have featured in numerous follow-up confirmation and characterisation results, including the multiplanet system K2-19b & c; hot Jupiters K2-30b, K2-34b and K2-29b; and multiple other results currently under peer review.

The dense mini-Neptune K2-110b, detected in this search and subsequently confirmed by HARPS and HARPS-N RV observations, is especially interesting and much of Chapter 3 was devoted to its detection and characterisation. Its 2.6±0.1 $R_\oplus$ radius contains 16.7 ± 3.2 $M_\oplus$ of material, giving it an earth-like bulk density of 5.2±1.2 gcm^{-3}. The well-constrained density, however, is enough to rule out earth-like rocky compositions, and is instead indicative of a thin but low-mass (∼1%) shell of H/He gas. This low volatile fraction appears unusual for a planet of its size, which is above the likely gas accretion mass, and orbit, which is both too far away for significant evaporation and for dynamic (e.g. non gas-disc) orbital migration. K2-110 b may therefore be evidence for the disc migration of material close to their star (either in the form of dust, protoplanets, or a destabilised multiplanet system) followed by their assembly into super-earths and mini-Neptunes after the

dispersion of the gas disc, as suggested by some theorists (Ida and Lin, 2008; Boley et al., 2015).

Where transiting exoplanet surveys have lacked, especially compared to other methods such as RVs, Imaging and Microlensing, is their ability to detect long-period planets. This is especially true with ground-based photometric surveys, for which the median planetary period is only a few days, and the maximum period is 16d. However, the more precise ground-based surveys are capable of detecting giant planets on orbits longer than this for single transits but often require many (> 3) transits before detecting and following-up planet candidates.

Presented in Chapter 4 this thesis is a technique to search and detect long-period planets from a single orbit in ground-based data. This used a combination of an iterative dip-searching and model-fitting search combined with supervised machine learning using a random forest and injected planetary signals to detect likely planet transits. This was performed on 126,000 stars (36 fields) in NGTS and 136,000 stars in WASP (38 "Stare mode" fields). Using the recovery rate of injections and the occurrence rates of planets, the likely planet haul of long period planets in WASP and NGTS data sets was computed, and many candidate planet signals detected. This showed that, provided the false positive rate can be lowered, NGTS and the WASP "stare" mode can detect up to 4.2 and 1.2 planets with periods > 12d per year. However, due primarily to instrumental effects, this method produces a high false positives (>99% for the numbers above), and development of this search technique is required before planets can be plausibly detected in this manner.

The detection of long-duration eclipses from dust-shrouded objects (including planetary-mass objects like J1407) is much more amenable to detection by ground-based detection. A similar injection and recovery method on nightly-average WASP data showed that more than 50% such eclipses (> 15d & > 15%) can be detected, and use this to place an upper limit on the occurrence rate of such events around stars in the WASP field of 10 per million stars per year.

An interesting example of the benefit of ground-based surveys for such detections was presented in Chapter 5. This described the detection and analysis of a 30%, 3-week long eclipse of the young star PDS 110. A second eclipse 2.2 years later was detected in KELT photometry and, combined with analysis of the eclipses and the stellar environment, led to the conclusion that the same dust-encircled and potentially planetary-mass object eclipses PDS-110 once every 2.2 year orbit. Fine structure (seen as sharp gradients in the eclipsing light curves) may also be indicative of a tilted ring system. The predicted period suggests a further eclipse in September 2017, for which detailed photometric follow-up is planned.

Finally, in Chapter 6, this thesis presented the detection of 71 long-period planet

candidates and 72 long-period eclipsing binary candidates from analysis of K2 photometry. To extract as much information on the planetary orbit and size as possible, a unique transit model code `Namaste` (An MCMC Analysis of Single Transiting Exoplanets) was developed. This uses the transit light curve, smoothed using Gaussian processes, and stellar information from either follow-up spectra or previously assembled catalogue data to predict orbital periods and first-order planetary classification for these monotransit candidates. The candidate planets have sizes as small as super Earths (e.g. EPIC210853606, $\sim$1.7 $R_{\oplus}$), and orbital periods potentially many years in duration (e.g. EPIC211503363, $\sim$26 years). On-going RV measurements may confirm some of the larger candidates as bona fide planets, while for others future photometric observations (by e.g. K2 and TESS) may detect subsequent transits.

7.2 Future Work

7.2.1 Single Transit Detection - Improved Automation

Efforts to detect K2 candidates (on both short- and long-periods) have, for the most part, relied on manual eye-balling. However, a fully computational technique using the techniques touched on in Chapter 4 should be implemented. The `steve` code, developed in Chapter 4 for detecting single transits from ground-based surveys, should be directly applied to all eleven K2 campaigns in order to detect more candidates in a less time-intensive manner. If a suitable unbiased selection of K2 target stars are selected, such a method could also be used to infer occurrence rates for this long-period regime, thereby comparing with past Kepler occurrences and those of RV, Microlensing, etc. Other data sets would seem equally amenable to such an analysis, including the four years of CoRoT photometry.

This detection technique would benefit from multiple improvements. The first would be to add distinct categories for eclipsing binaries, and known false positives (e.g. from flux drops common to multiple stars). This would vastly decrease the current FP ratios, therefore reducing both the amount of human inspection of candidates and increasing the number of detectable planets. Current detectability calculations, which used equivalent binning techniques along multiple parameters, could be improved by using smoothly varying multivariate kernel density estimations, thereby allowing the recoverability of injections and detectability of transits (and the change in these numbers as a function of multiple parameters) to be studied on a sub-bin basis.

7.2.2 Single Transit Candidates - Follow-up Campaigns

The list of candidates detected in ground-based data (e.g.. WASP and NGTS) requires more thorough vetting to provide a short list of potential events. The full season of photometry can be used to search for the potential planetary period, by anchoring the phase fold at the candidate detection and phase-folding the data. In the case of WASP, although the data from past seasons is not as stable or with as rapid cadence as stare fields, it can contribute data for candidate objects that may help constrain potential periods. Such a technique will detect potential other dips that could give orbital periods, or provide a probabilistic minimum likely period from the data. For the best candidates, two or three low-resolution observations spaced at the minimum period may be able to rule out eclipsing binary scenarios. This would then pave the way for high-resolution RVs, which may enable an orbital period to be determined, and a transit reobserved.

In the case of K2, the near-continuous phase coverage means a minimum period is already known accurately. Many of the single transit candidates detected in K2 offer excellent opportunities for RV follow-up and eventually the mass measurement, confirmation, and transit re-observation of long-period planets. These could contribute to our understanding of planetary bulk compositions, planetary migration & evolution and even occurrence rates. Hence a programme of RV observations on these targets may prove extremely valuable to the field. In both cases, the precise RV strategy, given a period estimate (or at least minimum period constraint), could also be developed.

For PDS 110, the presence of two events mean the predicted eclipse is constrained to within a few weeks. Photometric observations in September will confirm or rule out the periodic nature of the eclipses. In the former case, multiband photometry over many weeks will allow the dust grain size to be constrained and allow the sub-structure of the object to be studied in more detail. High-resolution spectroscopy out-of-eclipse will enable an estimate (or upper limit) on the mass of any secondary, and multiple such observations during eclipse may even enable the dust gradients to be crudely imaged through their effect on the shape of absorption lines in the star.

For all cases, extensive long-duration photometry of known candidates would be useful, and may allow further transits without radial velocities. A full catalogue of candidate transits could also be compiled across all transit surveys (ground and space-based) which, with the upcoming all-sky TESS mission, may enable their reobservation and confirmation. Proposals for TESS short-cadence data are possible, and should be attempted for these objects.

7.2.3 Long-Period Planets from Future Missions

TESS

The Transiting Exoplanet Survey Satellite (TESS Ricker et al., 2015) will monitor 200,000 stars on 2min cadence over 26 different 28-day observing windows. Studies of TESS planet yield suggest more than 100 single transits could be detected above a noise threshold of 7.3σ (Sullivan et al., 2015).

To assess this figure, a similar study of the TESS input catalogue was performed. Using the noise profile from Ricker et al. (2015) combined with the mass-radius-temperature formulations of Boyajian et al. (2012), we reproduce a plausible TESS input catalogue for the 200,000 stars to be observed with 2 minute cadence.

To determine the likely number of planets detectable, we modify the occurrence rates from Fressin et al. (2013), extending them beyond 85d with a trend flat in log period space. A random number was assigned to each radius and period bin for each target and, in the cases where this was below the occurrence rate of that bin, a planet was generated at random inclination and phase. To smooth the distribution we produced a (linearly) random period and radius within each bin. For each inserted planet, we gave it a random field duration according to the proportions of targets in multiple fields given in Ricker et al. (2015) and calculated whether its orbit crossed the stellar disc. We then estimated the transit signal and light curve noise from the planetary characteristics and the stellar magnitude, and calculated whether the planet would transit multiple times during the observations, or just once. All planets with SNR>7.0 were assumed to be detectable.

In total, we found that ~4500 multi-transiting planets may be detectable in the two years of TESS operations, more than triple the estimate of Sullivan et al. (2015) (1700), and far more than expected from the past two years of K2. However, the number of expected single transiting planets (750) was nearly seven times that of Sullivan et al. (2015) (110). While some of the difference may be from the more complicated analysis of systematic variability and blending performed in that study, these effects should modify the detectable ratio of multi- and single- transiting systems equally. The previous study did not simulate planets with occurrence rates >1 year, which may have somewhat influenced the single transit yield. Therefore we suggest that Sullivan et al. (2015) may have significantly underestimated the number of single transiting exoplanets detectable with TESS, which could increase the planet yield by up to 17%.

Added to this, nearly the entire sky (including up to 20 million stars and galaxies brighter than I=15) will also be observed with 30 minute cadence in the full frame images. Although the fainter objects with lower SNR and the lack of pre-vetting will increase blending and therefore FP ratio, many hundreds more single transits may also be discovered in

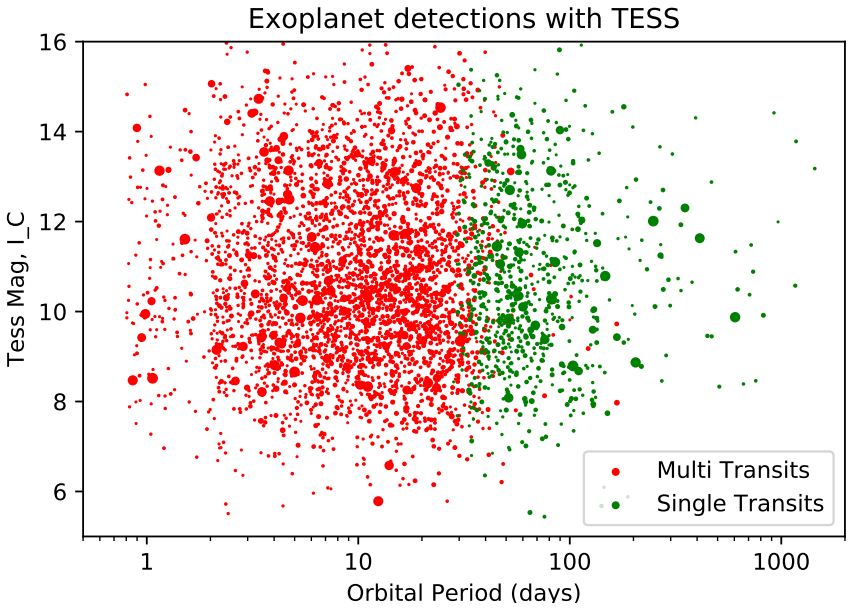

Figure 7.1: Likely number transits (detectable to $> 7\sigma$ found in TESS as a function of orbital period, magnitude and planetary radius (marker size). In red are multi-transiting planets detectable through "classical" means, and in green are single transiting candidates.

this sample. The search techniques developed here, combined with analysis with `Namaste`, will prove important tools in the detection and follow up of these planets.

PLATO

Initial observing plans for the PLAnetary Transits and Oscillation of Stars (PLATO) mission suggest 6 fields could be observed on 2-5 month campaigns, yielding 60,000 bright stars (Vmag < 12) with 30s cadence and hundreds of thousands of fainter stars ($12 <$ Vmag < 16) with 10-minute cadence (Rauer et al., 2014). The potential combination of asteroseismology-derived densities (accurate to 10%) with high-cadence, high-precision photometric data could produce dozens of validated long-period planets. As the period prediction is primarily a function of density and light curve photometric accuracy, PLATO could enable period estimates with 10% precision. This could hugely reduce the follow-up time necessary to confirm such planets.

Another combination possible with PLATO may be to detect long-period planets from a single transit during the ongoing observations. This could then allowing simultaneous radial velocities with continuous space-based photometry, which can help improve RV precision by tracking stellar variation (Haywood et al., 2014). The improved precision and brighter stars also means that PLATO may be capable of reaching the terrestrial planet

regime from a single transit. If, as expected, a 10th magnitude star produces only 20ppm/hr of photon noise, an earth-radius planet with a 6-hour transit across a G-type star would be detectable to 10-σ in a single transit.

Gaia and Direct Imaging

On their long orbits, single transiting exoplanets found in our search of K2, as well as those found in subsequent transit campaigns, could prove the first bridges between the close-in transit regime, and the far-out regime studied by radial velocities (which are already being utilised in follow-up), astrometry and direct imaging.

Gaia has the capability to detect tens of thousands of giant planets on 1 to 4 year orbits (Dzigan and Zucker, 2012). However, due to their long orbits, only ~3 in every 1000 will transit, producing on the order of 10-40 transiting planets (Perryman et al., 2014). However, the precision to confirm (or rule out) a long-period planet may be less than that required to detect the initial orbit, providing a new mechanism for follow-up, therefore transiting gas giants on these orbits found by TESS, PLATO or from the ground stand a good chance of being confirmed by Gaia astrometry. Gaia's precision photometry of 1 billion stars will also enable the detection of long-period eclipsing binaries on both foreground and background sources which are currently a source of false positives. In the coming decades, only exoplanets on long orbits, and therefore only those detected by single transits, will allow the first overlaps between the realms of transiting and astrometric exoplanet astronomy.

We also computed the likelihood of detecting single transiting planets capable of follow-up by detecting with direct imaging. Assuming average orbits from 1 to 4 years and an occurrence rate of 10% for FGK stars, we used Gaia stellar information for nearby main sequence stars (Michalik et al., 2015) to compute the likely distribution of nearby transiting giant planets. We find that approximately one in every 250 of the nearest FGK stars would contain transiting giant planets, with the closest transiting giant planets likely $\sim$ 25 parsecs away, with the brightest such case typically around a $\sim$ 6th magnitude star. The largest angular distance of the sample is typically 55mas, more than ten times the current resolution of Sphere (5mas; Beuzit et al., 2008b), although likely far below the necessary contrast level of $\sim 10^8$. This level of angular separation and contrast would be easily achievable by the next generation of telescopes, however, including E-ELT EPICS (Kasper et al., 2010), TMT-PFI (Macintosh et al., 2006) and WFIRST-AFTA (Zhao, 2014).

As such, single transiting giant exoplanets could allow the first comparison of planetary characterisation via the full suite of transit, RVs, astrometry and direct imaging. Such a fleet of resources to characterise an extrasolar world would likely also be necessary for the detailed characterisation of solar-system analogues and earth-like planets in the near future.

With future transit missions, the detection and analysis of single events as detailed in this thesis may allow transiting exoplanet science to push beyond the hot inner regions of planetary systems. This will probe new parameter spaces, including the internal structure and atmospheric compositions of cool worlds. Markers of formation such as eccentricity and spin-orbit angle may also be more pronounced in "Warm" planets, and measurements of these effects allowing insights into formation and evolution of extrasolar systems. The occurrence rates of such worlds may bridge the gulf between transit surveys and those from other methods (RVs, Astrometry and Microlensing) PLATO, for example, will provide long-period planet candidates in abundance around bright and nearby K or G dwarfs, including of solar system analogues such as cold gas giants and exo-Earths.

7.3 Closing Statements

For most of the history of our field, other solar systems were often assumed to exist, but astronomers had to make do with only dreams of their discovery and exploration. Twenty years ago that dream finally came true, and began an astronomical revolution, marked by an exponential increase in the number and diversity of planets found around distant stars since then. And with new missions and improved technology, that explosion looks set to continue well into the 21st century.

Transiting planetary systems offer the most detailed look at an exoplanet, with measurements of bulk density, orbital dynamics and even atmospheric composition possible. But, with classical detection methods and short-duration surveys such as K2 and TESS, such planets are limited to only the hot inner regions of extrasolar systems. The techniques developed in this thesis help push those current boundaries towards cooler planets and the eye-catching planet candidates detected in K2 photometry will, if confirmed, provide benchmark systems for future transit surveys. The signals of many more key long-period planets may have already been recorded by ground- and space-based transit surveys, which future analyses based on methods presented by this thesis may reveal. Eventually, such methods will unlock planets capable of being directly imaged by future giant telescopes and, with high-precision transit missions, may even offer a new way of detecting Earth-like planets around sunlike stars.

Chapter 8

Full Author Publication List

-

1 : Andrew J Rushby, Mark W Claire, Hugh Osborn, and Andrew J Watson. Habitable zone lifetimes of exoplanets around main sequence stars. *Astrobiology*, 13(9):833–849, 2013

2 : David J Armstrong, Hugh P Osborn, DJA Brown, Francesca Faedi, Y Gómez Maqueo Chew, David V Martin, Don Pollacco, and S Udry. On the abundance of circumbinary planets. *Monthly Notices of the Royal Astronomical Society*, 444(2):1873–1883, 2014a

3 : AMS Smith, DR Anderson, David J Armstrong, SCC Barros, AS Bonomo, F Bouchy, DJA Brown, A Collier Cameron, Laetitia Delrez, Francesca Faedi, et al. Wasp-104b and wasp-106b: two transiting hot jupiters in 1.75-day and 9.3-day orbits. *Astronomy & Astrophysics*, 570:A64, 2014

4 : DJ Armstrong, HP Osborn, DJA Brown, J Kirk, KWF Lam, DL Pollacco, J Spake, and SR Walker. K2 variable catalogue i: A catalogue of variable stars from k2 field 0. *arXiv preprint arXiv:1411.6830*, 2014b

5 : David J Armstrong, Alexandre Santerne, Dimitri Veras, Susana CC Barros, Olivier Demangeon, Jorge Lillo-Box, James McCormac, Hugh P Osborn, Maria Tsantaki, José-Manuel Almenara, et al. One of the closest exoplanet pairs to the 3: 2 mean motion resonance: K2-19b and c. *Astronomy & Astrophysics*, 582:A33, 2015b

6 : David J Armstrong, J Kirk, KWF Lam, J McCormac, SR Walker, DJA Brown, Hugh P Osborn, DL Pollacco, and J Spake. K2 variable catalogue: Variable stars and eclipsing binaries in k2 campaigns 1 and 0. *Astronomy & Astrophysics*, 579:A19, 2015a

7 : SCC Barros, JM Almenara, O Demangeon, M Tsantaki, A Santerne, David J Armstrong, D Barrado, D Brown, M Deleuil, J Lillo-Box, et al. Photodynamical mass determination of the multiplanetary system k2-19. *Monthly Notices of the Royal Astronomical Society*, 454(4):4267–4276, 2015

8 : F Faedi, Y Chew, D Pollacco, DJA Brown, G Hébrard, B Smalley, KWF Lam, D Veras, D Anderson, AP Doyle, et al. Wasp-86b and wasp-102b: super-dense versus bloated planets. *arXiv preprint arXiv:1608.04225*, 2016

9 : David J Armstrong, J Kirk, KWF Lam, J McCormac, HP Osborn, J Spake, S Walker, DJA Brown, MH Kristiansen, Don Pollacco, et al. K2 variable catalogue–ii. machine learning classification of variable stars and eclipsing binaries in k2 fields 0–4. *Monthly Notices of the Royal Astronomical Society*, 456(2):2260–2272, 2016a

10 : J Lillo-Box, O Demangeon, A Santerne, SCC Barros, D Barrado, G Hébrard, Hugh P Osborn, David J Armstrong, J-M Almenara, I Boisse, et al. K2-30 b and k2-34 b: Two inflated hot jupiters around solar-type stars. *Astronomy & Astrophysics*, 594:A50, 2016

11 : Jessica J Spake, David JA Brown, Amanda P Doyle, Guillaume Hébrard, James McCormac, David J Armstrong, Don Pollacco, Y Gómez Maqueo Chew, David R Anderson, Susana CC Barros, et al. Wasp-135b: a highly irradiated, inflated hot jupiter orbiting a g5v star. *Publications of the Astronomical Society of the Pacific*, 128(960):024401, 2016

12 : D Bayliss, S Hojjatpanah, A Santerne, D Dragomir, G Zhou, A Shporer, KD Colón, J Almenara, DJ Armstrong, D Barrado, et al. Epic 201702477b: A transiting brown dwarf from k2 in a 41 day orbit. *The Astronomical Journal*, 153(1):15, 2016

13 : David J Armstrong, CE Pugh, A-M Broomhall, DJA Brown, MN Lund, Hugh P Osborn, and DL Pollacco. The host stars of kepler's habitable exoplanets: superflares, rotation and activity. *Monthly Notices of the Royal Astronomical Society*, 455(3):3110–3125, 2016b

14 : A Santerne, G Hébrard, J Lillo-Box, David J Armstrong, SCC Barros, O Demangeon, D Barrado, A Debackere, M Deleuil, E Delgado Mena, et al. K2-29 b/wasp-152 b: an aligned and inflated hot jupiter in a young visual binary. *The Astrophysical Journal*, 824(1):55, 2016

15 : DJ Armstrong, E de Mooij, J Barstow, HP Osborn, J Blake, and N Fereshteh Saniee. Variability in the atmosphere of the hot giant planet hat-p-7 b. *Nature Astronomy*, 1:0004, 2016c

16 : Joseph E Rodriguez, George Zhou, Phillip A Cargile, Daniel J Stevens, Hugh P Osborn, Benjamin J Shappee, Phillip A Reed, Michael B Lund, Howard M Relles, David W Latham, et al. The mysterious dimmings of the t tauri star v1334 tau. *arXiv preprint arXiv:1701.03044*, 2017

17 : KWF Lam, F Faedi, DJA Brown, DR Anderson, Laetitia Delrez, Michaël Gillon, G Hébrard, M Lendl, L Mancini, J Southworth, et al. From dense hot jupiter to low-density neptune: The discovery of wasp-127b, wasp-136b, and wasp-138b. *Astronomy & Astrophysics*, 599:A3, 2017

18 : HP Osborn, JE Rodriguez, MA Kenworthy, GM Kennedy, EE Mamajek, CE Robinson, CC Espaillat, DJ Armstrong, BJ Shappee, A Bieryla, DW Latham, DR Anderson, TG Beatty, P Berlind, ML Calkins, GA Esquerdo, BS Gaudi, C Hellier, TW-S Holoien, D James, CS Kochanek, RB Kuhn, MB Lund, J Pepper, DL Pollacco, JL Prieto, RJ Siverd, KG Stassun, DJ Stevens, KZ Stanek, and RG West. Periodic eclipses of the young star pds 110 discovered with wasp and kelt photometry. *Monthly Notices of the Royal Astronomical Society*, page stx1249, 2017a

19 : HP Osborn, A Santerne, SCC Barros, NC Santos, X Dumusque, L Malavoltacnmsep, DJ Armstrong, S Hojjatpanah, O Demangeon, V Adibekyan, J-M Almenara, D Barrado, D Bayliss, I Boisse, F Bouchy, DJA Brown, AC Cameron, D Charbonneau, M Deleuil, E DelgadoMena, R Diaz, G H'ebrard, J Kirk, GW King, KWF Lam, D Latham, J Lillo-Box, TM Louden, C Lovis, M Marmier, J McCormac, E Molinari, F Pepe, D Pollacco, SG Sousa, S Udry, and SR Walker. K2-110 b: a massive mini-neptune exoplanet. *Astronomy & Astrophysics*, 604:A19, 2017b

Bibliography

J Aceituno, SF Sánchez, F Grupp, J Lillo, M Hernán-Obispo, D Benitez, LM Montoya, U Thiele, S Pedraz, D Barrado, et al. Cafe: Calar alto fiber-fed échelle spectrograph. *Astronomy & Astrophysics*, 552:A31, 2013.

Elisabeth R Adams, Brian Jackson, and Michael Endl. Ultra-short-period planets in k2 superpig results for campaigns 0–5. *The Astronomical Journal*, 152(2):47, 2016.

ER Adams, S Seager, and L Elkins-Tanton. Ocean planet or thick atmosphere: On the mass-radius relationship for solid exoplanets with massive atmospheres. *The Astrophysical Journal*, 673(2):1160, 2008.

V. Adibekyan, E. Delgado-Mena, P. Figueira, S. G. Sousa, N. C. Santos, J. P. Faria, J. I. Gonzalez Hernandez, G. Israelian, G. Harutyunyan, L. Suarez-Andres, and A. A. Hakobyan. ζ^2 Ret, its debris disk, and its lonely stellar companion ζ^1 Ret. Different T_c trends for different spectra. *ArXiv e-prints*, May 2016.

V. Z. Adibekyan, N. C. Santos, S. G. Sousa, G. Israelian, E. Delgado Mena, J. I. González Hernández, M. Mayor, C. Lovis, and S. Udry. Overabundance of α-elements in exoplanet-hosting stars. *Astronomy and Astrophysics*, 543:A89, July 2012. doi: 10.1051/0004-6361/201219564.

V Silva Aguirre, GR Davies, S Basu, J Christensen-Dalsgaard, O Creevey, TS Metcalfe, Timothy Russell Bedding, Luca Casagrande, R Handberg, MN Lund, et al. Ages and fundamental properties of kepler exoplanet host stars from asteroseismology. *Monthly Notices of the Royal Astronomical Society*, 452(2):2127–2148, 2015.

S. Aigrain and F. Favata. Bayesian detection of planetary transits. A modified version of the Gregory-Loredo method for Bayesian periodic signal detection. *Astronomy and Astrophysics*, 395:625–636, November 2002. doi: 10.1051/0004-6361:20021290.

S. Aigrain, S. T. Hodgkin, M. J. Irwin, J. R. Lewis, and S. J. Roberts. Precise time se-

ries photometry for the Kepler-2.0 mission. *Monthly Notices of the Royal Astronomical Society*, 447:2880–2893, March 2015. doi: 10.1093/mnras/stu2638.

S. Aigrain, H. Parviainen, and B. J. S. Pope. K2SC: flexible systematics correction and detrending of K2 light curves using Gaussian process regression. *Monthly Notices of the Royal Astronomical Society*, 459:2408–2419, July 2016. doi: 10.1093/mnras/stw706.

Suzanne Aigrain and M Irwin. Practical planet prospecting. *Monthly Notices of the Royal Astronomical Society*, 350(1):331–345, 2004.

Suzanne Aigrain, Hannu Parviainen, and Benjamin Pope. EPIC212521166: a transiting planet candidate discovered in Campaign 6 data from the K2 Mission, February 2016a. URL `http://dx.doi.org/10.5281/zenodo.45873`.

Suzanne Aigrain, Hannu Parviainen, and BJS Pope. K2sc: flexible systematics correction and detrending of k2 light curves using gaussian process regression. *Monthly Notices of the Royal Astronomical Society*, 459(3):2408–2419, 2016b.

Masataka Aizawa, Sho Uehara, Kento Masuda, Hajime Kawahara, and Yasushi Suto. Toward detection of exoplanetary rings via transit photometry: Methodology and a possible candidate. *The Astronomical Journal*, 153(4):193, 2017.

RL Akeson, X Chen, D Ciardi, M Crane, J Good, M Harbut, E Jackson, SR Kane, AC Laity, S Leifer, et al. The nasa exoplanet archive: data and tools for exoplanet research. *Publications of the Astronomical Society of the Pacific*, 125(930):989–999, 2013.

J. Alfonso-Garzon, A. Domingo, J. M. Mas-Hesse, and A. Gimenez. VizieR Online Data Catalog: INTEGRAL-OMC optically variable sources (Alfonso-Garzon+, 2012). *VizieR Online Data Catalog*, 354, October 2012.

France Allard, D Homeier, and Bernd Freytag. Models of very-low-mass stars, brown dwarfs and exoplanets. *Philosophical Transactions of the Royal Society of London A: Mathematical, Physical and Engineering Sciences*, 370(1968):2765–2777, 2012.

JM Almenara, N Astudillo-Defru, X Bonfils, T Forveille, A Santerne, S Albrecht, SCC Barros, F Bouchy, X Delfosse, O Demangeon, et al. A harps view on k2-3. *Astronomy & Astrophysics*, 581:L7, 2015.

Roi Alonso, Timothy M Brown, Guillermo Torres, David W Latham, Alessandro Sozzetti, Georgi Mandushev, Juan A Belmonte, David Charbonneau, Hans J Deeg, Edward W Dunham, et al. Tres-1: The transiting planet of a bright k0 v star. *The Astrophysical Journal Letters*, 613(2):L153, 2004.

DR Anderson, A Collier Cameron, C Hellier, M Lendl, PFL Maxted, Don Pollacco, D Queloz, B Smalley, AMS Smith, I Todd, et al. Wasp-30b: A 61 m jup brown dwarf transiting av= 12, f8 star. *The Astrophysical Journal Letters*, 726(2):L19, 2010.

Guillem Anglada-Escudé, Pedro J Amado, John Barnes, Zaira M Berdiñas, R Paul Butler, Gavin AL Coleman, Ignacio de La Cueva, Stefan Dreizler, Michael Endl, Benjamin Giesers, et al. A terrestrial planet candidate in a temperate orbit around proxima centauri. *Nature*, 536(7617):437–440, 2016.

Ruth Angus, Suzanne Aigrain, Daniel Foreman-Mackey, and Amy McQuillan. Calibrating gyrochronology using kepler asteroseismic targets. *Monthly Notices of the Royal Astronomical Society*, 450(2):1787–1798, 2015.

M Ansdell, E Gaidos, SA Rappaport, TL Jacobs, DM LaCourse, KJ Jek, AW Mann, MC Wyatt, G Kennedy, JP Williams, et al. Young âĂIJdipperâĂİ stars in upper sco and oph observed by k2. *The Astrophysical Journal*, 816(2):69, 2016.

David J Armstrong, Hugh P Osborn, DJA Brown, Francesca Faedi, Y Gómez Maqueo Chew, David V Martin, Don Pollacco, and S Udry. On the abundance of circumbinary planets. *Monthly Notices of the Royal Astronomical Society*, 444(2):1873–1883, 2014a.

David J Armstrong, J Kirk, KWF Lam, J McCormac, SR Walker, DJA Brown, Hugh P Osborn, DL Pollacco, and J Spake. K2 variable catalogue: Variable stars and eclipsing binaries in k2 campaigns 1 and 0. *Astronomy & Astrophysics*, 579:A19, 2015a.

David J Armstrong, Alexandre Santerne, Dimitri Veras, Susana CC Barros, Olivier Demangeon, Jorge Lillo-Box, James McCormac, Hugh P Osborn, Maria Tsantaki, José-Manuel Almenara, et al. One of the closest exoplanet pairs to the 3: 2 mean motion resonance: K2-19b and c. *Astronomy & Astrophysics*, 582:A33, 2015b.

David J Armstrong, J Kirk, KWF Lam, J McCormac, HP Osborn, J Spake, S Walker, DJA Brown, MH Kristiansen, Don Pollacco, et al. K2 variable catalogue–ii. machine learning classification of variable stars and eclipsing binaries in k2 fields 0–4. *Monthly Notices of the Royal Astronomical Society*, 456(2):2260–2272, 2016a.

David J Armstrong, CE Pugh, A-M Broomhall, DJA Brown, MN Lund, Hugh P Osborn, and DL Pollacco. The host stars of kepler's habitable exoplanets: superflares, rotation and activity. *Monthly Notices of the Royal Astronomical Society*, 455(3):3110–3125, 2016b.

David J Armstrong, Don Pollacco, and Alexandre Santerne. Transit shapes and self-organizing maps as a tool for ranking planetary candidates: application to kepler and k2. *Monthly Notices of the Royal Astronomical Society*, 465(3):2634–2642, 2017.

DJ Armstrong, HP Osborn, DJA Brown, J Kirk, KWF Lam, DL Pollacco, J Spake, and SR Walker. K2 variable catalogue i: A catalogue of variable stars from k2 field 0. *arXiv preprint arXiv:1411.6830*, 2014b.

DJ Armstrong, E de Mooij, J Barstow, HP Osborn, J Blake, and N Fereshteh Saniee. Variability in the atmosphere of the hot giant planet hat-p-7 b. *Nature Astronomy*, 1:0004, 2016c.

Tri L Astraatmadja and Coryn AL Bailer-Jones. Estimating distances from parallaxes. iii. distances of two million stars in the gaia dr1 catalogue. *The Astrophysical Journal*, 833 (1):119, 2016.

N Astudillo-Defru, T Forveille, X Bonfils, D Ségransan, F Bouchy, X Delfosse, C Lovis, M Mayor, F Murgas, F Pepe, et al. The harps search for southern extra-solar planets xli. a dozen planets around the m dwarfs gj 3138, gj 3323, gj 273, gj 628, and gj 3293. *arXiv preprint arXiv:1703.05386*, 2017.

A Baglin, M Auvergne, L Boisnard, T Lam-Trong, P Barge, C Catala, M Deleuil, E Michel, and W Weiss. Corot: a high precision photometer for stellar ecolution and exoplanet finding. In *36th COSPAR Scientific assembly*, volume 36, 2006.

G Bakos, C Afonso, T Henning, A Jordán, M Holman, RW Noyes, PD Sackett, D Sasselov, Gábor Kovács, Z Csubry, et al. Hat-south: a global network of southern hemisphere automated telescopes to detect transiting exoplanets. *Proceedings of the International Astronomical Union*, 4(S253):354–357, 2008.

G. Á. Bakos, J. Lázár, I. Papp, P. Sári, and E. M. Green. System Description and First Light Curves of the Hungarian Automated Telescope, an Autonomous Observatory for Variability Search. *Publications of the Astronomical Society of the Pacific*, 114:974–987, September 2002. doi: 10.1086/342382.

G. Á. Bakos, R. W. Noyes, G. Kovács, D. W. Latham, D. D. Sasselov, G. Torres, D. A. Fischer, R. P. Stefanik, B. Sato, J. A. Johnson, A. Pál, G. W. Marcy, R. P. Butler, G. A. Esquerdo, K. Z. Stanek, J. Lázár, I. Papp, P. Sári, and B. Sipőcz. HAT-P-1b: A Large-Radius, Low-Density Exoplanet Transiting One Member of a Stellar Binary. *The Astrophysical Journal*, 656:552–559, February 2007. doi: 10.1086/509874.

S. L. Baliunas, R. A. Donahue, W. H. Soon, J. H. Horne, J. Frazer, L. Woodard-Eklund, M. Bradford, L. M. Rao, O. C. Wilson, Q. Zhang, W. Bennett, J. Briggs, S. M. Carroll, D. K. Duncan, D. Figueroa, H. H. Lanning, T. Misch, J. Mueller, R. W. Noyes, D. Poppe, A. C. Porter, C. R. Robinson, J. Russell, J. C. Shelton, T. Soyumer, A. H. Vaughan, and J. H. Whitney. Chromospheric variations in main-sequence stars. *The Astrophysical Journal*, 438:269–287, January 1995. doi: 10.1086/175072.

Sarah Ballard, Daniel Fabrycky, Francois Fressin, David Charbonneau, Jean-Michel Desert, Guillermo Torres, Geoffrey Marcy, Christopher J Burke, Howard Isaacson, Christopher Henze, et al. The kepler-19 system: A transiting 2.2 râŁŢ planet and a second planet detected via transit timing variations. *The Astrophysical Journal*, 743(2):200, 2011.

I. Baraffe, G. Chabrier, F. Allard, and P. H. Hauschildt. Evolutionary models for solar metallicity low-mass stars: mass-magnitude relationships and color-magnitude diagrams. *Astronomy and Astrophysics*, 337:403–412, September 1998.

A Baranne, M Mayor, and JL Poncet. CoravelâĂŤa new tool for radial velocity measurements. *Vistas in Astronomy*, 23:279–316, 1979.

André Baranne, D Queloz, Michel Mayor, G Adrianzyk, G Knispel, D Kohler, D Lacroix, J-P Meunier, G Rimbaud, and A Vin. Elodie: A spectrograph for accurate radial velocity measurements. *Astronomy and Astrophysics Supplement Series*, 119(2):373–390, 1996.

Jason W Barnes. Effects of orbital eccentricity on extrasolar planet transit detectability and light curves. *Publications of the Astronomical Society of the Pacific*, 119(859):986–993, 2007.

Jason W Barnes and Jonathan J Fortney. Transit detectability of ring systems around extrasolar giant planets. *The Astrophysical Journal*, 616(2):1193, 2004.

SCC Barros, JM Almenara, O Demangeon, M Tsantaki, A Santerne, David J Armstrong, D Barrado, D Brown, M Deleuil, J Lillo-Box, et al. Photodynamical mass determination of the multiplanetary system k2-19. *Monthly Notices of the Royal Astronomical Society*, 454(4):4267–4276, 2015.

SCC Barros, O Demangeon, and M Deleuil. New planetary and eclipsing binary candidates from campaigns 1- 6 of the k2 mission. *Astronomy & Astrophysics*, 594:A100, 2016.

SCC Barros, H Gosselin, J Lillo-Box, D Bayliss, E DelgadoMena, A Santerne, , NC Santos, X Dumusque, L Malavoltacnmsep, DJ Armstrong, S Hojjatpanah, O Demangeon, V Adibekyan, J-M Almenara, D Barrado, I Boisse, F Bouchy, DJA Brown, AC Cameron, D Charbonneau, M Deleuil, R Diaz, G H'ebrard, J Kirk, GW King, KWF Lam,

D Latham, TM Louden, C Lovis, M Marmier, J McCormac, E Molinari, HP Osborn, F Pepe, D Pollacco, SG Sousa, S Udry, and SR Walker. Precise masses for the transiting planetary system hd 106315 with harps. *arXiv preprint arXiv:1709.00865*, 2017.

Gibor Basri, Lucianne M Walkowicz, and Ansgar Reiners. Comparison of kepler photometric variability with the sun on different timescales. *The Astrophysical Journal*, 769 (1):37, 2013.

D Bayliss, S Hojjatpanah, A Santerne, D Dragomir, G Zhou, A Shporer, KD Colón, J Almenara, DJ Armstrong, D Barrado, et al. Epic 201702477b: A transiting brown dwarf from k2 in a 41 day orbit. *The Astronomical Journal*, 153(1):15, 2016.

J-P Beaulieu, DP Bennett, P Fouqué, Andrew Williams, M Dominik, UG Jørgensen, D Kubas, A Cassan, C Coutures, J Greenhill, et al. Discovery of a cool planet of 5.5 earth masses through gravitational microlensing. *Nature*, 439(7075):437–440, 2006.

M. Benisty, T. Stolker, A. Pohl, J. de Boer, G. Lesur, C. Dominik, C. P. Dullemond, M. Langlois, M. Min, K. Wagner, T. Henning, A. Juhasz, P. Pinilla, S. Facchini, D. Apai, R. van Boekel, A. Garufi, C. Ginski, F. Ménard, C. Pinte, S. P. Quanz, A. Zurlo, A. Boccaletti, M. Bonnefoy, J. L. Beuzit, G. Chauvin, M. Cudel, S. Desidera, M. Feldt, C. Fontanive, R. Gratton, M. Kasper, A.-M. Lagrange, H. LeCoroller, D. Mouillet, D. Mesa, E. Sissa, A. Vigan, J. Antichi, T. Buey, T. Fusco, D. Gisler, M. Llored, Y. Magnard, O. Moeller-Nilsson, J. Pragt, R. Roelfsema, J.-F. Sauvage, and F. Wildi. Shadows and spirals in the protoplanetary disk HD 100453. *ArXiv e-prints*, October 2016.

David P Bennett and Sun Hong Rhie. Detecting earth-mass planets with gravitational microlensing. *The Astrophysical Journal*, 472(2):660, 1996.

Zachory K Berta-Thompson, Jonathan Irwin, David Charbonneau, Elisabeth R Newton, Jason A Dittmann, Nicola Astudillo-Defru, Xavier Bonfils, Michaël Gillon, Emmanuël Jehin, Antony A Stark, et al. A rocky planet transiting a nearby low-mass star. *Nature*, 527(7577):204–207, 2015.

C. Bertout. Occultation of young stellar objects by circumstellar disks. I. Theoretical expectations and preliminary comparison with observations. *Astronomy and Astrophysics*, 363:984–990, November 2000.

MS Bessell, F Castelli, and Bertrand Plez. Model atmospheres broad-band colors, bolometric corrections and temperature calibrations for o-m stars. *Astronomy and astrophysics*, 333:231–250, 1998.

Jean-Luc Beuzit, Markus Feldt, Kjetil Dohlen, David Mouillet, Pascal Puget, Francois Wildi, Lyu Abe, Jacopo Antichi, Andrea Baruffolo, Pierre Baudoz, et al. Sphere: a'planet finder'instrument for the vlt. In *SPIE Astronomical Telescopes+ Instrumentation*, pages 701418–701418. International Society for Optics and Photonics, 2008a.

Jean-Luc Beuzit, Markus Feldt, Kjetil Dohlen, David Mouillet, Pascal Puget, Francois Wildi, Lyu Abe, Jacopo Antichi, Andrea Baruffolo, Pierre Baudoz, et al. Sphere: a'planet finder'instrument for the vlt. In *SPIE Astronomical Telescopes+ Instrumentation*, pages 701418–701418. International Society for Optics and Photonics, 2008b.

S. Blanco-Cuaresma, C. Soubiran, U. Heiter, and P. Jofré. Determining stellar atmospheric parameters and chemical abundances of FGK stars with iSpec. *Astronomy and Astrophysics*, 569:A111, September 2014. doi: 10.1051/0004-6361/201423945.

Jürgen Blum and Gerhard Wurm. The growth mechanisms of macroscopic bodies in protoplanetary disks. *Annu. Rev. Astron. Astrophys.*, 46:21–56, 2008.

AC Boley, AP Contreras, and B Gladman. The in situ formation of giant planets at short orbital periods. *arXiv preprint arXiv:1510.04276*, 2015.

William J Borucki, DG Koch, EW Dunham, and JM Jenkins. The kepler mission: A mission to detennine the frequency of inner planets near the habitable zone for a wide range of stars. In *Planets beyond the solar system and the next generation of space missions*, volume 119, page 153, 1997.

William J Borucki, David Koch, Gibor Basri, Natalie Batalha, Timothy Brown, Douglas Caldwell, John Caldwell, Jørgen Christensen-Dalsgaard, William D Cochran, Edna DeVore, et al. Kepler planet-detection mission: introduction and first results. *Science*, 327 (5968):977–980, 2010.

WJ Borucki, JD Scargle, and HS Hudson. Detectability of extrasolar planetary transits. *The Astrophysical Journal*, 291:852–854, 1985.

Alan P Boss. Giant planet formation by gravitational instability. *Science*, 276(5320):1836–1839, 1997.

Alan P Boss. Rapid formation of gas giant planets around m dwarf stars. *The Astrophysical Journal*, 643(1):501, 2006.

F Bouchy, F Pepe, and D Queloz. Fundamental photon noise limit to radial velocity measurements. *Astronomy & Astrophysics*, 374(2):733–739, 2001.

J. Bouvier, A. Chelli, S. Allain, L. Carrasco, R. Costero, I. Cruz-Gonzalez, C. Dougados, M. Fernández, E. L. Martín, F. Ménard, C. Mennessier, R. Mujica, E. Recillas, L. Salas, G. Schmidt, and R. Wichmann. Magnetospheric accretion onto the T Tauri star AA Tauri. I. Constraints from multisite spectrophotometric monitoring. *Astronomy and Astrophysics*, 349:619–635, September 1999.

Brendan P Bowler, Michael C Liu, Trent J Dupuy, and Michael C Cushing. Near-infrared spectroscopy of the extrasolar planet hr 8799 b. *The Astrophysical Journal*, 723(1):850, 2010.

Tabetha S Boyajian, Kaspar von Braun, Gerard van Belle, Harold A McAlister, A Theo, Stephen R Kane, Philip S Muirhead, Jeremy Jones, Russel White, Gail Schaefer, et al. Stellar diameters and temperatures. ii. main-sequence k-and m-stars. *The Astrophysical Journal*, 757(2):112, 2012.

TS Boyajian, DM LaCourse, SA Rappaport, D Fabrycky, DA Fischer, D Gandolfi, GM Kennedy, H Korhonen, MC Liu, A Moor, et al. Planet hunters ix. kic 8462852–where's the flux? *Monthly Notices of the Royal Astronomical Society*, 457(4):3988–4004, 2016.

R Brahm, A Jordán, GÁ Bakos, K Penev, N Espinoza, M Rabus, JD Hartman, D Bayliss, S Ciceri, G Zhou, et al. Hats-17b: A transiting compact warm jupiter in a 16.3 day circular orbitthe hatsouth network is operated by a collaboration consisting of princeton university (pu), the max planck institute für astronomie (mpia), the australian national university (anu), and the pontificia universidad católica de chile (puc). the station at las campanas observatory (lco) of the carnegie institute is operated by pu in conjunction with puc, the station at the high energy spectroscopic survey (hess) site is operated in conjunction with mpia, and the station at siding spring observatory (sso) is operated jointly with anu. this paper includes data gathered with the mpg 2.2 m telescope at the eso observatory in la silla and with the 3.9 m aat in siding spring observatory. this paper uses observations obtained with facilities of the las cumbres observatory global telescope. based on observations taken with the harps spectrograph (eso 3.6 m telescope at la silla) under programme 097. c-0571. *The Astronomical Journal*, 151(4):89, 2016.

Leo Breiman. Random forests. *Machine learning*, 45(1):5–32, 2001.

C. Briceño, L. Hartmann, J. Hernández, N. Calvet, A. K. Vivas, G. Furesz, and A. Szentgyorgyi. 25 Orionis: A Kinematically Distinct 10 Myr Old Group in Orion OB1a. *"The Astrophysical Journal"*, 661:1119–1128, June 2007. doi: 10.1086/513087.

C Broeg, A Fortier, D Ehrenreich, Y Alibert, W Baumjohann, W Benz, M Deleuil, Michaël Gillon, A Ivanov, R Liseau, et al. Cheops: A transit photometry mission for esa's small mission programme. In *EPJ Web of Conferences*, volume 47, page 03005. EDP Sciences, 2013.

Matteo Brogi, Ignas AG Snellen, Remco J de Kok, Simon Albrecht, Jayne Birkby, and Ernst JW de Mooij. The signature of orbital motion from the dayside of the planet [tgr] bootis b. *Nature*, 486(7404):502–504, 2012.

A. G. A. Brown, E. J. de Geus, and P. T. de Zeeuw. The Orion OB1 association. 1: Stellar content. *Astronomy and Astrophysics*, 289:101–120, September 1994.

TM Brown, N Baliber, FB Bianco, M Bowman, B Burleson, P Conway, M Crellin, É Depagne, J De Vera, B Dilday, et al. Las cumbres observatory global telescope network. *Publications of the Astronomical Society of the Pacific*, 125(931):1031, 2013.

G Bruno, J-M Almenara, SCC Barros, A Santerne, RF Díaz, M Deleuil, C Damiani, AS Bonomo, I Boisse, F Bouchy, et al. Sophie velocimetry of kepler transit candidates: a joint photometric, spectroscopic and dynamical analysis of the kepler-117 system. In *EPJ Web of Conferences*, volume 101, page 06014. EDP Sciences, 2015.

Giordano Bruno. *La cena de le ceneri, ed. M.* 1584.

Lars A Buchhave, David W Latham, Anders Johansen, Martin Bizzarro, Guillermo Torres, Jason F Rowe, Natalie M Batalha, William J Borucki, Erik Brugamyer, Caroline Caldwell, et al. An abundance of small exoplanets around stars with a wide range of metallicities. *Nature*, 486(7403):375–377, 2012.

Christopher J Burke, Jessie L Christiansen, F Mullally, Shawn Seader, Daniel Huber, Jason F Rowe, Jeffrey L Coughlin, Susan E Thompson, Joseph Catanzarite, Bruce D Clarke, et al. Terrestrial planet occurrence rates for the kepler gk dwarf sample. *The Astrophysical Journal*, 809(1):8, 2015.

R Paul Butler, Steven S Vogt, Geoffrey W Marcy, Debra A Fischer, Jason T Wright, Gregory W Henry, Greg Laughlin, and Jack J Lissauer. A neptune-mass planet orbiting the nearby m dwarf gj 436. *The Astrophysical Journal*, 617(1):580, 2004.

José A Caballero. The occultation events of the herbig ae/be star v1247 orionis. *Astronomy & Astrophysics*, 511:L9, 2010.

A Collier Cameron, F Bouchy, G Hébrard, P Maxted, Don Pollacco, F Pont, I Skillen, B Smalley, RA Street, Richard G West, et al. Wasp-1b and wasp-2b: two new transiting

exoplanets detected with superwasp and sophie. *Monthly Notices of the Royal Astronomical Society*, 375(3):951–957, 2007.

BRUCE Campbell and GAH Walker. Precision radial velocities with an absorption cell. *Publications of the Astronomical Society of the Pacific*, 91(542):540, 1979.

Bruce Campbell and GAH Walker. Stellar radial velocities of high precision: Techniques and results. In *International Astronomical Union Colloquium*, volume 88, pages 5–19. Cambridge Univ Press, 1984.

Bruce Campbell, Gordon AH Walker, and Stevenson Yang. A search for substellar companions to solar-type stars. *The Astrophysical Journal*, 331:902–921, 1988.

A. J. Cannon and E. Pickering. *The Henry Draper (HD) Catalogue. Vol.112: HD extension*. 1949.

S. M. Carroll, E. F. Guinan, G. P. McCook, and R. A. Donahue. Interpreting Epsilon Aurigae. *"The Astrophysical Journal"*, 367:278–287, January 1991. doi: 10.1086/169626.

Timothy A Cassidy, Rolando Mendez, Phil Arras, Robert E Johnson, and Michael F Skrutskie. Massive satellites of close-in gas giant exoplanets. *The Astrophysical Journal*, 704 (2):1341, 2009.

Frederic H Chaffee and Daniel J Schroeder. Astronomical applications of echelle spectroscopy. *Annual Review of Astronomy and Astrophysics*, 14(1):23–42, 1976.

David Charbonneau, Timothy M Brown, David W Latham, and Michel Mayor. Detection of planetary transits across a sun-like star. *The Astrophysical Journal Letters*, 529(1): L45, 1999.

David Charbonneau, Timothy M Brown, Robert W Noyes, and Ronald L Gilliland. Detection of an extrasolar planet atmosphere. *The Astrophysical Journal*, 568(1):377, 2002.

David Charbonneau, Zachory K Berta, Jonathan Irwin, Christopher J Burke, Philip Nutzman, Lars A Buchhave, Christophe Lovis, Xavier Bonfils, David W Latham, Stéphane Udry, et al. A super-earth transiting a nearby low-mass star. *Nature*, 462(7275):891–894, 2009.

Sourav Chatterjee and Jonathan C Tan. Inside-out planet formation. *The Astrophysical Journal*, 780(1):53, 2013.

G Chauvin, A Vigan, M Bonnefoy, S Desidera, M Bonavita, D Mesa, A Boccaletti, E Buenzli, J Carson, P Delorme, et al. The vlt/naco large program to probe the occurrence of

exoplanets and brown dwarfs at wide orbits-ii. survey description, results, and performances. *Astronomy & Astrophysics*, 573:A127, 2015.

Gael Chauvin, A-M Lagrange, C Dumas, B Zuckerman, D Mouillet, I Song, J-L Beuzit, and P Lowrance. A giant planet candidate near a young brown dwarf-direct vlt/naco observations using ir wavefront sensing. *Astronomy & Astrophysics*, 425(2):L29–L32, 2004.

Jessie L Christiansen, Jon M Jenkins, Douglas A Caldwell, Christopher J Burke, Peter Tenenbaum, Shawn Seader, Susan E Thompson, Thomas S Barclay, Bruce D Clarke, Jie Li, et al. The derivation, properties, and value of keplerâĂŹs combined differential photometric precision. *Publications of the Astronomical Society of the Pacific*, 124(922): 1279, 2012.

David R Ciardi, CA Beichman, SJ Carey, C Crockett, CM Johns-Krull, SR Kane, J McLane, P Plavchan, LA Prato, JR Stauffer, et al. Observations of the pre-main sequence exoplanet candidate ptfo 8-8695. In *American Astronomical Society Meeting Abstracts# 223*, volume 223, 2014.

Christian Clanton and B Scott Gaudi. Synthesizing exoplanet demographics: A single population of long-period planetary companions to m dwarfs consistent with microlensing, radial velocity, and direct imaging surveys. *The Astrophysical Journal*, 819(2):125, 2016.

A Claret and Steven Bloemen. Gravity and limb-darkening coefficients for the kepler, corot, spitzer, uvby, ubvrijhk, and sloan photometric systems. *Astronomy & Astrophysics*, 529: A75, 2011.

A. M. Cody, J. Stauffer, A. Baglin, G. Micela, L. M. Rebull, E. Flaccomio, M. Morales-Calderón, S. Aigrain, J. Bouvier, L. A. Hillenbrand, R. Gutermuth, I. Song, N. Turner, S. H. P. Alencar, K. Zwintz, P. Plavchan, J. Carpenter, K. Findeisen, S. Carey, S. Terebey, L. Hartmann, N. Calvet, P. Teixeira, F. J. Vrba, S. Wolk, K. Covey, K. Poppenhaeger, H. M. Günther, J. Forbrich, B. Whitney, L. Affer, W. Herbst, J. Hora, D. Barrado, J. Holtzman, F. Marchis, K. Wood, M. Medeiros Guimarães, J. Lillo Box, E. Gillen, A. McQuillan, C. Espaillat, L. Allen, P. D'Alessio, and F. Favata. CSI 2264: Simultaneous Optical and Infrared Light Curves of Young Disk-bearing Stars in NGC 2264 with CoRoT and Spitzer - Evidence for Multiple Origins of Variability. *The Astronomical Journal*, 147:82, April 2014. doi: 10.1088/0004-6256/147/4/82.

A. Collier Cameron, D. Pollacco, R. A. Street, T. A. Lister, R. G. West, D. M. Wilson, F. Pont, D. J. Christian, W. I. Clarkson, B. Enoch, A. Evans, A. Fitzsimmons, C. A. Haswell, C. Hellier, S. T. Hodgkin, K. Horne, J. Irwin, S. R. Kane, F. P. Keenan, A. J.

Norton, N. R. Parley, J. Osborne, R. Ryans, I. Skillen, and P. J. Wheatley. A fast hybrid algorithm for exoplanetary transit searches. *Monthly Notices of the Royal Astronomical Society*, 373:799–810, December 2006. doi: 10.1111/j.1365-2966.2006.11074.x.

A Collier-Cameron, DM Wilson, Richard G West, L Hebb, X-B Wang, S Aigrain, F Bouchy, DJ Christian, WI Clarkson, B Enoch, et al. Efficient identification of exoplanetary transit candidates from superwasp light curves. *Monthly Notices of the Royal Astronomical Society*, 380(3):1230–1244, 2007.

Rosario Cosentino, Christophe Lovis, Francesco Pepe, Andrew Collier Cameron, David W Latham, Emilio Molinari, Stephane Udry, Naidu Bezawada, Martin Black, Andy Born, et al. Harps-n: the new planet hunter at tng. In *SPIE Astronomical Telescopes+ Instrumentation*, pages 84461V–84461V. International Society for Optics and Photonics, 2012.

Christophe Cossou, Sean N Raymond, and Arnaud Pierens. Convergence zones for type i migration: an inward shift for multiple planet systems. *Astronomy & Astrophysics*, 553: L2, 2013.

Bastien Courcol, François Bouchy, and Magali Deleuil. An upper boundary in the mass-metallicity plane of exo-neptunes. *Monthly Notices of the Royal Astronomical Society*, page stw1049, 2016.

I. J. M. Crossfield, E. Petigura, J. E. Schlieder, A. W. Howard, B. J. Fulton, K. M. Aller, D. R. Ciardi, S. Lépine, T. Barclay, I. de Pater, K. de Kleer, E. V. Quintana, J. L. Christiansen, E. Schlafly, L. Kaltenegger, J. R. Crepp, T. Henning, C. Obermeier, N. Deacon, L. M. Weiss, H. T. Isaacson, B. M. S. Hansen, M. C. Liu, T. Greene, S. B. Howell, T. Barman, and C. Mordasini. A Nearby M Star with Three Transiting Super-Earths Discovered by K2. *The Astrophysical Journal*, 804:10, May 2015. doi: 10.1088/0004-637X/804/1/10.

Ian JM Crossfield, Erik Petigura, Joshua E Schlieder, Andrew W Howard, BJ Fulton, Kimberly M Aller, David R Ciardi, Sébastien Lépine, Thomas Barclay, Imke De Pater, et al. A nearby m star with three transiting super-earths discovered by k2. *The Astrophysical Journal*, 804(1):10, 2015.

Ian JM Crossfield, David R Ciardi, Erik A Petigura, Evan Sinukoff, Joshua E Schlieder, Andrew W Howard, Charles A Beichman, Howard Isaacson, Courtney D Dressing, Jessie L Christiansen, et al. 197 candidates and 104 validated planets in k2's first five fields. *The Astrophysical Journal Supplement Series*, 226(1):7, 2016.

Sz Csizmadia, Th Pasternacki, C Dreyer, J Cabrera, A Erikson, and H Rauer. The effect of stellar limb darkening values on the accuracy of the planet radii derived from photometric transit observations. *Astronomy & Astrophysics*, 549:A9, 2013.

R. M. Cutri, M. F. Skrutskie, S. van Dyk, C. A. Beichman, J. M. Carpenter, T. Chester, L. Cambresy, T. Evans, J. Fowler, J. Gizis, E. Howard, J. Huchra, T. Jarrett, E. L. Kopan, J. D. Kirkpatrick, R. M. Light, K. A. Marsh, H. McCallon, S. Schneider, R. Stiening, M. Sykes, M. Weinberg, W. A. Wheaton, S. Wheelock, and N. Zacarias. VizieR Online Data Catalog: 2MASS All-Sky Catalog of Point Sources (Cutri+ 2003). *VizieR Online Data Catalog*, 2246:0, June 2003.

R. M. Cutri, E. L. Wright, Conrow T., and at al. VizieR Online Data Catalog: WISE All-Sky Data Release (Cutri+ 2012). *VizieR Online Data Catalog*, 2311:0, 2012.

RM Cutri, MF Skrutskie, S Van Dyk, CA Beichman, JM Carpenter, T Chester, L Cambresy, T Evans, J Fowler, J Gizis, et al. 2mass all sky catalog of point sources. 2003.

RM Cutri et al. Vizier online data catalog: Allwise data release (cutri+ 2013). *VizieR Online Data Catalog*, 2328:0, 2014.

Fei Dai, Joshua N Winn, Simon Albrecht, Pamela Arriagada, Allyson Bieryla, R Paul Butler, Jeffrey D Crane, Teriyaki Hirano, John Asher Johnson, Amanda Kiilerich, et al. Doppler monitoring of five k2 transiting planetary systems. *The Astrophysical Journal*, 823(2):115, 2016.

Paola D'Alessio, Jorge Cantó, Lee Hartmann, Nuria Calvet, and Susana Lizano. On the thermal stability of irradiation-dominated pre-main-sequence disks. *The Astrophysical Journal*, 511(2):896, 1999.

Paola D'Alessio, Nuria Calvet, Lee Hartmann, Ramiro Franco-Hernández, and Hermelinda Servín. Effects of dust growth and settling in t tauri disks. *The Astrophysical Journal*, 638(1):314, 2006.

Rebekah I Dawson and Eugene Chiang. A class of warm jupiters with mutually inclined, apsidally misaligned close friends. *science*, 346(6206):212–216, 2014.

Pierre Simon de Laplace. *Recherches sur plusieurs points de systeme du monde*. 1777.

Drake Deming, Heather Knutson, Joshua Kammer, Benjamin J Fulton, James Ingalls, Sean Carey, Adam Burrows, Jonathan J Fortney, Kamen Todorov, Eric Agol, et al. Spitzer secondary eclipses of the dense, modestly-irradiated, giant exoplanet hat-p-using pixel-level decorrelation. *The Astrophysical Journal*, 805(2):132, 2015.

A Lecavelier Des Etangs, F Pont, A Vidal-Madjar, and D Sing. Rayleigh scattering in the transit spectrum of hd 189733b. *Astronomy & Astrophysics*, 481(2):L83–L86, 2008.

Rodrigo F Díaz, José M Almenara, Alexandre Santerne, Claire Moutou, Anthony Lethuillier, and Magali Deleuil. pastis: Bayesian extrasolar planet validation–i. general framework, models, and performance. *Monthly Notices of the Royal Astronomical Society*, 441 (2):983–1004, 2014.

Jason A Dittmann, Jonathan M Irwin, David Charbonneau, Xavier Bonfils, Nicola Astudillo-Defru, Raphaëlle D Haywood, Zachory K Berta-Thompson, Elisabeth R Newton, Joseph E Rodriguez, Jennifer G Winters, et al. A temperate rocky super-earth transiting a nearby cool star. *Nature*, 544(7650):333–336, 2017.

Sarah E Dodson-Robinson, Dimitri Veras, Eric B Ford, and Charles A Beichman. The formation mechanism of gas giants on wide orbits. *The Astrophysical Journal*, 707(1): 79, 2009.

Christian Doppler. *Ueber das farbige Licht der Doppelsterne und einiger anderer Gestirne des Himmels: Versuch einer das Bradley'sche Aberrations-Theorem als integrirenden Theil in sich schliessenden allgemeineren Theorie*. In Commission bei Borrosch & André, 1842.

Aaron Dotter, Brian Chaboyer, Darko Jevremović, Veselin Kostov, E Baron, and Jason W Ferguson. The dartmouth stellar evolution database. *The Astrophysical Journal Supplement Series*, 178(1):89, 2008.

Courtney D Dressing and David Charbonneau. The occurrence of potentially habitable planets orbiting m dwarfs estimated from the full kepler dataset and an empirical measurement of the detection sensitivity. *The Astrophysical Journal*, 807(1):45, 2015.

C. P. Dullemond, M. E. van den Ancker, B. Acke, and R. van Boekel. Explaining UX Orionis Star Variability with Self-shadowed Disks. *Astrophysical Journal, Letters*, 594: L47–L50, September 2003. doi: 10.1086/378400.

CP Dullemond and C Dominik. Flaring vs. self-shadowed disks: The seds of herbig ae/be stars. *Astronomy & Astrophysics*, 417(1):159–168, 2004.

X. Dumusque, A. S. Bonomo, R. D. Haywood, L. Malavolta, D. Ségransan, L. A. Buchhave, A. Collier Cameron, D. W. Latham, E. Molinari, F. Pepe, S. Udry, D. Charbonneau, R. Cosentino, C. D. Dressing, P. Figueira, A. F. M. Fiorenzano, S. Gettel, A. Harutyunyan, K. Horne, M. Lopez-Morales, C. Lovis, M. Mayor, G. Micela, F. Motalebi, V. Nascimbeni, D. F. Phillips, G. Piotto, D. Pollacco, D. Queloz, K. Rice, D. Sasselov,

A. Sozzetti, A. Szentgyorgyi, and C. Watson. The Kepler-10 Planetary System Revisited by HARPS-N: A Hot Rocky World and a Solid Neptune-Mass Planet. *"The Astrophysical Journal"*, 789:154, July 2014. doi: 10.1088/0004-637X/789/2/154.

X. Dumusque, F. Borsa, M. Damasso, R. F. Díaz, P. C. Gregory, N. C. Hara, A. Hatzes, V. Rajpaul, M. Tuomi, S. Aigrain, G. Anglada-Escudé, A. S. Bonomo, G. Boué, F. Dauvergne, G. Frustagli, P. Giacobbe, R. D. Haywood, H. R. A. Jones, J. Laskar, M. Pinamonti, E. Poretti, M. Rainer, D. Ségransan, A. Sozzetti, and S. Udry. Radial-velocity fitting challenge. II. First results of the analysis of the data set. *Astronomy & Astrophysics*, 598:A133, February 2017. doi: 10.1051/0004-6361/201628671.

Yifat Dzigan and Shay Zucker. Detection of transiting jovian exoplanets by gaia photometryâĂŤexpected yield. *The Astrophysical Journal Letters*, 753(1):L1, 2012.

Linda T Elkins-Tanton and Sara Seager. Ranges of atmospheric mass and composition of super-earth exoplanets. *The Astrophysical Journal*, 685(2):1237, 2008.

Néstor Espinoza and Andrés Jordán. Limb darkening and exoplanets–ii. choosing the best law for optimal retrieval of transit parameters. *Monthly Notices of the Royal Astronomical Society*, 457(4):3573–3581, 2016.

Lisa J Esteves, Ernst JW De Mooij, and Ray Jayawardhana. Optical phase curves of kepler exoplanets. *The Astrophysical Journal*, 772(1):51, 2013.

Thomas M Evans, Suzanne Aigrain, Neale Gibson, Joanna K Barstow, David S Amundsen, Pascal Tremblin, and Pierre Mourier. A uniform analysis of hd 209458b spitzer/irac light curves with gaussian process models. *Monthly Notices of the Royal Astronomical Society*, 451(1):680–694, 2015.

Vincent Van Eylen and Simon Albrecht. Eccentricity from transit photometry: Small planets in kepler multi-planet systems have low eccentricities. *The Astrophysical Journal*, 808(2):126, 2015. URL `http://stacks.iop.org/0004-637X/808/i=2/a=126`.

Daniel Fabrycky and Scott Tremaine. Shrinking binary and planetary orbits by kozai cycles with tidal friction. *The Astrophysical Journal*, 669(2):1298, 2007.

Daniel C Fabrycky, Jack J Lissauer, Darin Ragozzine, Jason F Rowe, Jason H Steffen, Eric Agol, Thomas Barclay, Natalie Batalha, William Borucki, David R Ciardi, et al. Architecture of kepler's multi-transiting systems. ii. new investigations with twice as many candidates. *The Astrophysical Journal*, 790(2):146, 2014.

F Faedi, Y Chew, D Pollacco, DJA Brown, G Hébrard, B Smalley, KWF Lam, D Veras, D Anderson, AP Doyle, et al. Wasp-86b and wasp-102b: super-dense versus bloated planets. *arXiv preprint arXiv:1608.04225*, 2016.

Debra A Fischer and Jeff Valenti. The planet-metallicity correlation. *The Astrophysical Journal*, 622(2):1102, 2005.

M Fitzgerald. The intrinsic colours of stars and two-colour reddening lines. *Astronomy and Astrophysics*, 4:234, 1970.

Dora Fohring. *The Effect of Scintillation on Ground-Based Exoplanet Transit Photometry*. PhD thesis, Durham University, 2014.

Dan Foreman-Mackey. George: Gaussian process regression. *Astrophysics Source Code Library*, 2015.

Daniel Foreman-Mackey, David W Hogg, Dustin Lang, and Jonathan Goodman. emcee: The mcmc hammer. *Publications of the Astronomical Society of the Pacific*, 125(925): 306, 2013a.

Daniel Foreman-Mackey, David W Hogg, Dustin Lang, and Jonathan Goodman. emcee: The mcmc hammer. *Publications of the Astronomical Society of the Pacific*, 125(925): 306–312, 2013b.

Daniel Foreman-Mackey, Benjamin T Montet, David W Hogg, Timothy D Morton, Dun Wang, and Bernhard Schölkopf. A systematic search for transiting planets in the k2 data. *arXiv preprint arXiv:1502.04715*, 2015.

Daniel Foreman-Mackey, Timothy D Morton, David W Hogg, Eric Agol, and Bernhard Schölkopf. The population of long-period transiting exoplanets. *The Astronomical Journal*, 152(6):206, 2016.

Joseph Fraunhofer. Bestimmung des brechungs-und des farbenzerstreungs-vermögens verschiedener glasarten, in bezug auf die vervollkommnung achromatischer fernröhre. *Annalen der Physik*, 56(7):264–313, 1817.

François Fressin, Guillermo Torres, Jean-Michel Désert, David Charbonneau, Natalie M Batalha, Jonathan J Fortney, Jason F Rowe, Christopher Allen, William J Borucki, Timothy M Brown, et al. Kepler-10 c: A 2.2 earth radius transiting planet in a multiple system. *The Astrophysical Journal Supplement Series*, 197(1):5, 2011.

François Fressin, Guillermo Torres, David Charbonneau, Stephen T Bryson, Jessie Christiansen, Courtney D Dressing, Jon M Jenkins, Lucianne M Walkowicz, and Natalie M

Batalha. The false positive rate of kepler and the occurrence of planets. *The Astrophysical Journal*, 766(2):81, 2013.

M Fukugita, T Ichikawa, JE Gunn, M Doi, K Shimasaku, and DP Schneider. The sloan digital sky survey photometric system. *The Astronomical Journal*, 111:1748, 1996.

Benjamin J Fulton, Erik A Petigura, Andrew W Howard, Howard Isaacson, Geoffrey W Marcy, Phillip A Cargile, Leslie Hebb, Lauren M Weiss, John Asher Johnson, Timothy D Morton, et al. The california-kepler survey. iii. a gap in the radius distribution of small planets. *arXiv preprint arXiv:1703.10375*, 2017.

Gábor Fűrész, Andrew H. Szentgyorgyi, and Søren Meibom. *Precision of Radial Velocity Surveys using Multiobject Spectrographs — Experiences with Hectochelle*, pages 287–289. Springer Berlin Heidelberg, Berlin, Heidelberg, 2008. ISBN 978-3-540-75485-5.

Gaia Collaboration, A. G. A. Brown, A. Vallenari, T. Prusti, J. de Bruijne, F. Mignard, R. Drimmel, and 5. co-authors. Gaia Data Release 1. Summary of the astrometric, photometric, and survey properties. *ArXiv e-prints*, September 2016.

C Gałan, M Mikołajewski, T Tomov, D Graczyk, G Apostolovska, I Barzova, I Bellas-Velidis, B Bilkina, RM Blake, CT Bolton, et al. International observational campaigns of the last two eclipses in ee cephei: 2003 and 2008/9. *Astronomy & Astrophysics*, 544: A53, 2012.

BT Gänsicke, Detlev Koester, J Farihi, Jonathan Girven, SG Parsons, and E Breedt. The chemical diversity of exo-terrestrial planetary debris around white dwarfs. *Monthly Notices of the Royal Astronomical Society*, 424(1):333–347, 2012.

P. Garcia-Lario, A. Manchado, S. R. Suso, S. R. Pottasch, and R. Olling. Near infrared survey of IRAS sources with colours like planetary nebulae. II. *"The Astronomy and Astrophysics, Supplement"*, 82:497–512, March 1990.

Pierre Gassendi. Mercurius in sole visus, et venus inuisa parisiis. 1632.

NP Gibson, S Aigrain, S Roberts, TM Evans, M Osborne, and F Pont. A gaussian process framework for modelling instrumental systematics: application to transmission spectroscopy. *Monthly notices of the royal astronomical society*, 419(3):2683–2694, 2012.

Ronald L Gilliland, Timothy M Brown, Jørgen Christensen-Dalsgaard, Hans Kjeldsen, Conny Aerts, Thierry Appourchaux, Sarbani Basu, Timothy R Bedding, William J Chaplin, Margarida S Cunha, et al. Kepler asteroseismology program: introduction and first results. *Publications of the Astronomical Society of the Pacific*, 122(888):131, 2010.

Michaël Gillon, F Courbin, Pierre Magain, and Benoît Borguet. On the potential of extra-solar planet transit surveys. *Astronomy & Astrophysics*, 442(2):731–744, 2005.

Michaël Gillon, Amaury HMJ Triaud, Brice-Olivier Demory, Emmanuël Jehin, Eric Agol, Katherine M Deck, Susan M Lederer, Julien De Wit, Artem Burdanov, James G Ingalls, et al. Seven temperate terrestrial planets around the nearby ultracool dwarf star trappist-1. *Nature*, 542(7642):456–460, 2017.

Adam Ginsburg, Thomas Robitaille, Madhura Parikh, Christoph Deil, Jordan Mirocha, Julien Woillez, Brian Svoboda, Kyle Willett, James T Allen, Frederic Grollier, Magnus Vilhelm Persson, and David Shiga. Astroquery v0.1. 9 2013.

L. Girardi, M. Barbieri, M. A. T. Groenewegen, P. Marigo, A. Bressan, H. J. Rocha-Pinto, B. X. Santiago, J. I. B. Camargo, and L. N. da Costa. TRILEGAL, a TRIdimensional modeL of thE GALaxy: Status and Future. *Astrophysics and Space Science Proceedings*, 26:165, 2012.

Jonathan Goodman and Jonathan Weare. Ensemble samplers with affine invariance. *Communications in applied mathematics and computational science*, 5(1):65–80, 2010.

John Goodricke. On the periods of the changes of light in the star algol, 1784.

C. A. Grady, M. L. Sitko, R. W. Russell, D. K. Lynch, M. S. Hanner, M. R. Perez, K. S. Bjorkman, and D. de Winter. Infalling Planetesimals in Pre-Main Stellar Systems. *Protostars and Planets IV*, page 613, May 2000.

David F Gray. Empirical decoding of the shapes of spectral-line bisectors. *The Astrophysical Journal*, 710(2):1003, 2010.

J. Gregorio-Hetem and A. Hetem. Classification of a selected sample of weak T Tauri stars. *Monthly Notices of the Royal Astronomical Society*, 336:197–206, October 2002. doi: 10.1046/j.1365-8711.2002.05716.x.

Daniel Grether and Charles H Lineweaver. How dry is the brown dwarf desert? quantifying the relative number of planets, brown dwarfs, and stellar companions around nearby sun-like stars. *The Astrophysical Journal*, 640(2):1051, 2006.

R Griffin. On the possibility of determining stellar radial velocities to 0.01 km s- 1. *Monthly Notices of the Royal Astronomical Society*, 162(3):243–253, 1973.

RF Griffin. A photoelectric radial-velocity spectrometer. *The Astrophysical Journal*, 148: 465, 1967.

CJ Grillmair, D Charbonneau, A Burrows, L Armus, J Stauffer, V Meadows, J Van Cleve, and D Levine. A spitzer spectrum of the exoplanet hd 189733b. *The Astrophysical Journal Letters*, 658(2):L115, 2007.

V. P. Grinin. On the Blue Emission Visible during Deep Minima of Young Irregular Variables. *Soviet Astronomy Letters*, 14:27, February 1988.

Maximilian N Günther, Didier Queloz, Brice-Olivier Demory, and Francois Bouchy. A new yield simulator for transiting planets and false positives: application to the next generation transit survey. *Monthly Notices of the Royal Astronomical Society*, 465(3): 3379–3389, 2017.

Bengt Gustafsson, Bengt Edvardsson, Kjell Eriksson, Uffe Gråe Jørgensen, Åke Nordlund, and Bertrand Plez. A grid of marcs model atmospheres for late-type stars-i. methods and general properties. *Astronomy & Astrophysics*, 486(3):951–970, 2008.

Sam Hadden and Yoram Lithwick. Densities and eccentricities of 139 kepler planets from transit time variations. *The Astrophysical Journal*, 787(1):80, 2014.

George Depue Hadzsits. The lucretian theory of providence. *The Classical Weekly*, pages 146–148, 1916.

Edmund Halley. A new method of determining the parallax of the sun, or his distance from the earth. *Philosophical Transactions of the Royal Society of London*, (348):454, 1716.

E. Han, S. X. Wang, J. T. Wright, Y. K. Feng, M. Zhao, O. Fakhouri, J. I. Brown, and C. Hancock. Exoplanet Orbit Database. II. Updates to Exoplanets.org. *Publications of the Astronomical Society of the Pacific*, 126:827–837, September 2014. doi: 10.1086/678447.

Brad MS Hansen and Norm Murray. Migration then assembly: Formation of neptune-mass planets inside 1 au. *The Astrophysical Journal*, 751(2):158, 2012.

JD Hartman, GÁ Bakos, G Torres, DW Latham, Géza Kovács, B Béky, SN Quinn, T Mazeh, A Shporer, GW Marcy, et al. Hat-p-32b and hat-p-33b: Two highly inflated hot jupiters transiting high-jitter stars. *The Astrophysical Journal*, 742(1):59, 2011.

Carole A Haswell. *Transiting exoplanets*. Cambridge University Press, 2010.

A. P. Hatzes, M. Fridlund, G. Nachmani, T. Mazeh, D. Valencia, G. Hébrard, L. Carone, M. Pätzold, S. Udry, F. Bouchy, M. Deleuil, C. Moutou, P. Barge, P. Bordé, H. Deeg, B. Tingley, R. Dvorak, D. Gandolfi, S. Ferraz-Mello, G. Wuchterl, E. Guenther, T. Guillot, H. Rauer, A. Erikson, J. Cabrera, S. Csizmadia, A. Léger, H. Lammer, J. Weingrill,

D. Queloz, R. Alonso, D. Rouan, and J. Schneider. The Mass of CoRoT-7b. *The Astrophysical Journal*, 743:75, December 2011. doi: 10.1088/0004-637X/743/1/75.

Peter H Hauschildt, France Allard, and E Baron. The nextgen model atmosphere grid for 3000âL'd' teffâL'd' 10,000 k. *The Astrophysical Journal*, 512(1):377, 1999.

RD Haywood, A Collier Cameron, D Queloz, SCC Barros, M Deleuil, R Fares, Michaël Gillon, AF Lanza, C Lovis, C Moutou, et al. Planets and stellar activity: hide and seek in the corot-7 system. *Monthly notices of the royal astronomical society*, 443(3):2517–2531, 2014.

G. Helou and D. W. Walker, editors. *Infrared astronomical satellite (IRAS) catalogs and atlases. Volume 7: The small scale structure catalog*, volume 7, 1988.

A. A. Henden, S. Levine, D. Terrell, and D. L. Welch. APASS - The Latest Data Release. In *American Astronomical Society Meeting Abstracts*, volume 225 of *American Astronomical Society Meeting Abstracts*, page 336.16, January 2015.

George H Herbig. The properties and problems of t tauri stars and related objects. *Advances in Astronomy and Astrophysics*, 1:47–103, 1962.

W. Herbst, D. K. Herbst, E. J. Grossman, and D. Weinstein. Catalogue of UBVRI photometry of T Tauri stars and analysis of the causes of their variability. *The Astronomical Journal*, 108:1906–1923, November 1994. doi: 10.1086/117204.

William Herbst, Catrina M Hamilton, Frederick J Vrba, Mansur A Ibrahimov, Coryn AL Bailer-Jones, Reinhard Mundt, Markus Lamm, Tsevi Mazeh, Zodiac T Webster, Karl E Haisch, et al. Fine structure in the circumstellar environment of a young, solar-like star: the unique eclipses of kh 15d. *Publications of the Astronomical Society of the Pacific*, 114(801):1167, 2002.

Jesús Hernández, Nuria Calvet, Lee Hartmann, César Briceno, Aurora Sicilia-Aguilar, and Perry Berlind. Herbig ae/be stars in nearby ob associations. *The Astronomical Journal*, 129(2):856, 2005.

William Herschel. Continuation of an account of the changes that have happened in the relative situation of double stars. *Philosophical Transactions of the Royal Society of London*, 94:353–384, 1804.

Sasha Hinkley. Adaptive optics observations of exoplanets, brown dwarfs, and binary stars. *Proceedings of the International Astronomical Union*, 7(S282):181–188, 2011.

E. Høg, C. Fabricius, V. V. Makarov, S. Urban, T. Corbin, G. Wycoff, U. Bastian, P. Schwekendiek, and A. Wicenec. The Tycho-2 catalogue of the 2.5 million brightest stars. *Astronomy and Astrophysics*, 355:L27–L30, March 2000.

David W Hogg, Jo Bovy, and Dustin Lang. Data analysis recipes: Fitting a model to data. *arXiv preprint arXiv:1008.4686*, 2010.

Matthew J Holman and Norman W Murray. The use of transit timing to detect terrestrial-mass extrasolar planets. *Science*, 307(5713):1288–1291, 2005.

Felix Hormuth, Wolfgang Brandner, Stefan Hippler, and Th Henning. Astralux-the calar alto 2.2-m telescope lucky imaging camera. In *Journal of Physics: Conference Series*, volume 131, page 012051. IOP Publishing, 2008.

Jeremiah Horrocks. Venus in sole visa. *Hevelius'âĂIJMercurius in sole visusâĂİ. Gedani*, pages 111–145, 1662.

James R Houck, Thomas L Roellig, Jeff Van Cleve, William J Forrest, T Herter, Charles R Lawrence, Keith Matthews, Harold J Reitsema, BT Soifer, Dan M Watson, et al. The infrared spectrograph*(irs) on the spitzer space telescope. *The Astrophysical Journal Supplement Series*, 154(1):18, 2004.

Andrew W Howard, Geoffrey W Marcy, John Asher Johnson, Debra A Fischer, Jason T Wright, Howard Isaacson, Jeff A Valenti, Jay Anderson, Doug NC Lin, and Shigeru Ida. The occurrence and mass distribution of close-in super-earths, neptunes, and jupiters. *Science*, 330(6004):653–655, 2010.

Andrew W Howard, Geoffrey W Marcy, Stephen T Bryson, Jon M Jenkins, Jason F Rowe, Natalie M Batalha, William J Borucki, David G Koch, Edward W Dunham, Thomas N Gautier III, et al. Planet occurrence within 0.25 au of solar-type stars from kepler. *The Astrophysical Journal Supplement Series*, 201(2):15, 2012.

Steve B Howell. Introduction to differential time-series astronomical photometry using charged-coupled devices. In *Astronomical CCD Observing and reduction techniques*, volume 23, page 105, 1992.

Steve B Howell, Charlie Sobeck, Michael Haas, Martin Still, Thomas Barclay, Fergal Mullally, John Troeltzsch, Suzanne Aigrain, Stephen T Bryson, Doug Caldwell, et al. The k2 mission: characterization and early results. *Publications of the Astronomical Society of the Pacific*, 126(938):398–408, 2014.

Daniel Huber, William J Chaplin, Jørgen Christensen-Dalsgaard, Ronald L Gilliland, Hans Kjeldsen, Lars A Buchhave, Debra A Fischer, Jack J Lissauer, Jason F Rowe, Roberto Sanchis-Ojeda, et al. Fundamental properties of kepler planet-candidate host stars using asteroseismology. *The Astrophysical Journal*, 767(2):127, 2013.

Daniel Huber, Stephen T Bryson, Michael R Haas, Thomas Barclay, Geert Barentsen, Steve B Howell, Sanjib Sharma, Dennis Stello, and Susan E Thompson. The k2 ecliptic plane input catalog (epic) and stellar classifications of 138,600 targets in campaigns 1–8. *The Astrophysical Journal Supplement Series*, 224(1):2, 2016.

Shigeru Ida and DNC Lin. Toward a deterministic model of planetary formation. iv. effects of type i migration. *The Astrophysical Journal*, 673(1):487, 2008.

Niraj K Inamdar and Hilke E Schlichting. Stealing the gas: Giant impacts and the large diversity in exoplanet densities. *The Astrophysical Journal Letters*, 817(2):L13, 2016.

L. Ingleby, N. Calvet, J. Hernández, L. Hartmann, C. Briceno, J. Miller, C. Espaillat, and M. McClure. The Evolution of Accretion in Young Stellar Objects: Strong Accretors at 3-10 Myr. *"The Astrophysical Journal"*, 790:47, July 2014. doi: 10.1088/0004-637X/790/1/47.

Jonathan Irwin, David Charbonneau, Philip Nutzman, and Emilio Falco. The mearth project: searching for transiting habitable super-earths around nearby m dwarfs. *Proceedings of the International Astronomical Union*, 4(S253):37–43, 2008.

Jonathan M Irwin, Zachory K Berta-Thompson, David Charbonneau, Jason Dittmann, Emilio E Falco, Elisabeth R Newton, and Philip Nutzman. The mearth-north and mearth-south transit surveys: searching for habitable super-earth exoplanets around nearby m-dwarfs. *arXiv preprint arXiv:1409.0891*, 2014.

Alan P Jackson, Timothy A Davis, and Peter J Wheatley. The coronal x-ray–age relation and its implications for the evaporation of exoplanets. *Monthly Notices of the Royal Astronomical Society*, 422(3):2024–2043, 2012.

Brian K Jackson, Elisabeth R Adams, and Michael Endl. Superpig's ultra-short-period planets from k2 campaigns 6 through 8. In *American Astronomical Society Meeting Abstracts*, volume 229, 2017.

WS Jacob. On certain anomalies presented by the binary star 70 ophiuchi. *Monthly Notices of the Royal Astronomical Society*, 15:228, 1855.

Emmanuel Jehin, Michaël Gillon, D Queloz, Pierre Magain, Jean Manfroid, Virginie Chantry, M Lendl, Damien Hutsemekers, and S Udry. Trappist: Transiting planets and planetesimals small telescope. *The Messenger*, 145:2–6, 2011.

Jon M Jenkins, Douglas A Caldwell, Hema Chandrasekaran, Joseph D Twicken, Stephen T Bryson, Elisa V Quintana, Bruce D Clarke, Jie Li, Christopher Allen, Peter Tenenbaum, et al. Overview of the kepler science processing pipeline. *The Astrophysical Journal Letters*, 713(2):L87, 2010.

Jon M Jenkins, Joseph D Twicken, Natalie M Batalha, Douglas A Caldwell, William D Cochran, Michael Endl, David W Latham, Gilbert A Esquerdo, Shawn Seader, Allyson Bieryla, et al. Discovery and validation of kepler-452b: A 1.6 râĺĄ super earth exoplanet in the habitable zone of a g2 star. *The Astronomical Journal*, 150(2):56, 2015.

John Asher Johnson, Erik A Petigura, Benjamin J Fulton, Geoffrey W Marcy, Andrew W Howard, Howard Isaacson, Leslie Hebb, Phillip A Cargile, Timothy D Morton, Lauren M Weiss, et al. The california-kepler survey. ii. precise physical properties of 2025 kepler planets and their host stars. *arXiv preprint arXiv:1703.10402*, 2017.

Daniel Jontof-Hutter, Jack J Lissauer, Jason F Rowe, and Daniel C Fabrycky. Kepler-79's low density planets. *The Astrophysical Journal*, 785(1):15, 2014.

Markus Kasper, Jean-Luc Beuzit, Christophe Verinaud, Raffaele G Gratton, Florian Kerber, Natalia Yaitskova, Anthony Boccaletti, Niranjan Thatte, Hans Martin Schmid, Christoph Keller, et al. Epics: direct imaging of exoplanets with the e-elt. In *SPIE Astronomical Telescopes+ Instrumentation*, pages 77352E–77352E. International Society for Optics and Photonics, 2010.

James F Kasting, Daniel P Whitmire, and Ray T Reynolds. Habitable zones around main sequence stars. *Icarus*, 101(1):108–128, 1993.

Grant M Kennedy and Scott J Kenyon. Planet formation around stars of various masses: the snow line and the frequency of giant planets. *The Astrophysical Journal*, 673(1):502, 2008.

Grant M Kennedy, Matthew A Kenworthy, Joshua Pepper, Joseph E Rodriguez, Robert J Siverd, Keivan G Stassun, and Mark C Wyatt. The transiting dust clumps in the evolved disc of the sun-like uxor rz psc. *Royal Society Open Science*, 4(1):160652, 2017.

M. A. Kenworthy and E. E. Mamajek. Modeling Giant Extrasolar Ring Systems in Eclipse and the Case of J1407b: Sculpting by Exomoons? *"The Astrophysical Journal"*, 800: 126, February 2015. doi: 10.1088/0004-637X/800/2/126.

Johannes Kepler. Astronomia nova. *Johannes Kepler Gesammelte Werke*, 3:156, 1609.

David M Kipping. Transit timing effects due to an exomoon. *Monthly Notices of the Royal Astronomical Society*, 392(1):181–189, 2009.

David M Kipping. Binning is sinning: morphological light-curve distortions due to finite integration time. *Monthly Notices of the Royal Astronomical Society*, 408(3):1758–1769, 2010.

David M Kipping. Parametrizing the exoplanet eccentricity distribution with the beta distribution. *Monthly Notices of the Royal Astronomical Society: Letters*, 434(1):L51–L55, 2013.

David M Kipping, Chris Cameron, Joel D Hartman, James RA Davenport, Jaymie M Matthews, Dimitar Sasselov, Jason Rowe, Robert J Siverd, Jingjing Chen, Emily Sandford, et al. No conclusive evidence for transits of proxima b in most photometry. *The Astronomical Journal*, 153(3):93, 2017.

Wilhelm Kley and RP Nelson. Planet-disk interaction and orbital evolution. *Annual Review of Astronomy and Astrophysics*, 50:211–249, 2012.

David G Koch, William J Borucki, Gibor Basri, Natalie M Batalha, Timothy M Brown, Douglas Caldwell, Jørgen Christensen-Dalsgaard, William D Cochran, Edna DeVore, Edward W Dunham, et al. Kepler mission design, realized photometric performance, and early science. *The Astrophysical Journal Letters*, 713(2):L79, 2010.

R. K. Kopparapu. A Revised Estimate of the Occurrence Rate of Terrestrial Planets in the Habitable Zones around Kepler M-dwarfs. *The Astrophysical Journal Letters*, 767:L8, April 2013. doi: 10.1088/2041-8205/767/1/L8.

Ravi Kumar Kopparapu, Ramses Ramirez, James F Kasting, Vincent Eymet, Tyler D Robinson, Suvrath Mahadevan, Ryan C Terrien, Shawn Domagal-Goldman, Victoria Meadows, and Rohit Deshpande. Habitable zones around main-sequence stars: new estimates. *The Astrophysical Journal*, 765(2):131, 2013.

Geza Kovács, Shay Zucker, and Tsevi Mazeh. A box-fitting algorithm in the search for periodic transits. *Astronomy & Astrophysics*, 391(1):369–377, 2002.

Yoshihide Kozai. Secular perturbations of asteroids with high inclination and eccentricity. *The Astronomical Journal*, 67:591, 1962.

Laura Kreidberg. batman: Basic transit model calculation in python. *Publications of the Astronomical Society of the Pacific*, 127(957):1161, 2015.

R. B. Kuhn, J. E. Rodriguez, K. A. Collins, M. B. Lund, R. J. Siverd, K. D. Colón, J. Pepper, K. G. Stassun, P. A. Cargile, D. J. James, K. Penev, G. Zhou, D. Bayliss, T. G. Tan, I. A. Curtis, S. Udry, D. Segransan, D. Mawet, S. Dhital, J. Soutter, R. Hart, B. Carter, B. S. Gaudi, G. Myers, T. G. Beatty, J. D. Eastman, D. E. Reichart, J. B. Haislip, J. Kielkopf, A. Bieryla, D. W. Latham, E. L. N. Jensen, T. E. Oberst, and D. J. Stevens. KELT-10b: the first transiting exoplanet from the KELT-South survey - a hot sub-Jupiter transiting a V = 10.7 early G-star. *Monthly Notices of the Royal Astronomical Society*, 459:4281–4298, July 2016. doi: 10.1093/mnras/stw880.

R. Kurucz. ATLAS9 Stellar Atmosphere Programs and 2 km/s grid. *R. Kurucz CD-ROM No. 13. (Cambridge, Mass.: Smithsonian Astrophysical Observatory)*, 13, 1993.

Daryll M LaCourse, Kian J Jek, Thomas L Jacobs, Troy Winarski, Tabetha S Boyajian, Saul A Rappaport, Roberto Sanchis-Ojeda, Kyle E Conroy, Lorne Nelson, Tom Barclay, et al. Kepler eclipsing binary stars–vi. identification of eclipsing binaries in the k2 campaign 0 data set. *Monthly Notices of the Royal Astronomical Society*, 452(4):3561–3592, 2015.

J Lafler and TD Kinman. An rr lyrae star survey with ihe lick 20-inch astrograph ii. the calculation of rr lyrae periods by electronic computer. *The Astrophysical Journal Supplement Series*, 11:216, 1965.

Joseph-Louis Lagrange. Essai sur le probleme des trois corps. *Prix de lâĂŹacadémie royale des Sciences de paris*, 9:292, 1772.

KWF Lam, F Faedi, DJA Brown, DR Anderson, Laetitia Delrez, Michaël Gillon, G Hébrard, M Lendl, L Mancini, J Southworth, et al. From dense hot jupiter to low-density neptune: The discovery of wasp-127b, wasp-136b, and wasp-138b. *Astronomy & Astrophysics*, 599:A3, 2017.

J Lannier, P Delorme, AM Lagrange, S Borgniet, J Rameau, JE Schlieder, J Gagné, MA Bonavita, L Malo, G Chauvin, et al. Massive: A bayesian analysis of giant planet populations around low-mass stars. *Astronomy & Astrophysics*, 596:A83, 2016.

David W Latham, Tsevi Mazeh, Robert P Stefanik, Michel Mayor, and Gilbert Burki. The unseen companion of hd114762: a probable brown dwarf. 1989.

V Lebouteiller, DJ Barry, HWW Spoon, J Bernard-Salas, GC Sloan, JR Houck, and DW Weedman. Cassis: The cornell atlas of spitzer/infrared spectrograph sources. *The Astrophysical Journal Supplement Series*, 196(1):8, 2011.

Alain Lecavelier des Étangs. A diagram to determine the evaporation status of extrasolar planets. *Astronomy & Astrophysics*, 461(3):1185–1193, 2007.

A Léger, D Rouan, Jodi Schneider, P Barge, M Fridlund, B Samuel, M Ollivier, E Guenther, M Deleuil, HJ Deeg, et al. Transiting exoplanets from the corot space mission-viii. corot-7b: the first super-earth with measured radius. *Astronomy & Astrophysics*, 506(1): 287–302, 2009.

Gottfried Wilhelm Leibniz. De causa gravitatis, et defensio sententiae suae de veris naturae legibus contra cartesianos. *Acta Eruditorum*, 1690:228–39, 1690.

ML Lidov. The evolution of orbits of artificial satellites of planets under the action of gravitational perturbations of external bodies. *Planetary and Space Science*, 9(10):719–759, 1962.

J Lillo-Box, O Demangeon, A Santerne, SCC Barros, D Barrado, G Hébrard, Hugh P Osborn, David J Armstrong, J-M Almenara, I Boisse, et al. K2-30 b and k2-34 b: Two inflated hot jupiters around solar-type stars. *Astronomy & Astrophysics*, 594:A50, 2016.

Jack J Lissauer. Planet formation. *Annual review of astronomy and astrophysics*, 31(1): 129–172, 1993.

Jack J Lissauer, Daniel Jontof-Hutter, Jason F Rowe, Daniel C Fabrycky, Eric D Lopez, Eric Agol, Geoffrey W Marcy, Katherine M Deck, Debra A Fischer, Jonathan J Fortney, et al. All six planets known to orbit kepler-11 have low densities. *The Astrophysical Journal*, 770(2):131, 2013.

Yoram Lithwick, Jiwei Xie, and Yanqin Wu. Extracting planet mass and eccentricity from ttv data. *The Astrophysical Journal*, 761(2):122, 2012.

Shang-Fei Liu, Yasunori Hori, DNC Lin, and Erik Asphaug. Giant impact: An efficient mechanism for the devolatilization of super-earths. *The Astrophysical Journal*, 812(2): 164, 2015.

Eric D Lopez and Jonathan J Fortney. Understanding the mass-radius relation for sub-neptunes: Radius as a proxy for composition. *The Astrophysical Journal*, 792(1):1, 2014.

Eric D Lopez and Ken Rice. Predictions for the period dependence of the transition between rocky super-earths and gaseous sub-neptunes and implications for eta earth. *arXiv preprint arXiv:1610.09390*, 2016.

Rodrigo Luger, Eric Agol, Ethan Kruse, Rory Barnes, Andrew Becker, Daniel Foreman-Mackey, and Drake Deming. Everest: Pixel level decorrelation of k2 light curves. *The Astronomical Journal*, 152(4):100, 2016.

Rodrigo Luger, Ethan Kruse, Daniel Foreman-Mackey, Eric Agol, and Nicholas Saunders. An update to the everest k2 pipeline: Short cadence, saturated stars, and kepler-like photometry down to kp= 15. *arXiv preprint arXiv:1702.05488*, 2017.

D. J. MacConnell. Discoveries on southern, red-sensitive objective-prism plates. IV Extension to higher latitudes. *"The Astronomy and Astrophysics, Supplement"*, 48:355–361, June 1982.

Bruce Macintosh, Mitchell Troy, Rene Doyon, James Graham, Kevin Baker, Brian Bauman, Christian Marois, David Palmer, Donald Phillion, Lisa Poyneer, et al. Extreme adaptive optics for the thirty meter telescope. In *SPIE Astronomical Telescopes+ Instrumentation*, pages 62720N–62720N. International Society for Optics and Photonics, 2006.

David JC MacKay. Introduction to gaussian processes. *NATO ASI Series F Computer and Systems Sciences*, 168:133–166, 1998.

David JC MacKay. *Information theory, inference and learning algorithms*. Cambridge university press, 2003.

L. Malavolta, L. Borsato, V. Granata, G. Piotto, E. Lopez, A. Vanderburg, P. Figueira, A. Mortier, V. Nascimbeni, L. Affer, A. S. Bonomo, F. Bouchy, L. A. Buchhave, D. Charbonneau, A. Collier Cameron, R. Cosentino, C. D. Dressing, X. Dumusque, A. F. M. Fiorenzano, A. Harutyunyan, R. D. Haywood, J. A. Johnson, D. W. Latham, M. Lopez-Morales, C. Lovis, M. Mayor, G. Micela, E. Molinari, F. Motalebi, F. Pepe, D. F. Phillips, D. Pollacco, D. Queloz, K. Rice, D. Sasselov, D. Ségransan, A. Sozzetti, S. Udry, and C. Watson. The Kepler-19 system: a thick-envelope super-Earth with two Neptune-mass companions characterized using Radial Velocities and Transit Timing Variations. *ArXiv e-prints*, March 2017.

E. E. Mamajek, A. C. Quillen, M. J. Pecaut, F. Moolekamp, E. L. Scott, M. A. Kenworthy, A. Collier Cameron, and N. R. Parley. Planetary Construction Zones in Occultation: Discovery of an Extrasolar Ring System Transiting a Young Sun-like Star and Future Prospects for Detecting Eclipses by Circumsecondary and Circumplanetary Disks. *The Astronomical Journal*, 143:72, March 2012. doi: 10.1088/0004-6256/143/3/72.

Kaisey Mandel and Eric Agol. Analytic light curves for planetary transit searches. *The Astrophysical Journal Letters*, 580(2):L171, 2002.

Shude Mao and Bohdan Paczynski. Gravitational microlensing by double stars and planetary systems. *The Astrophysical Journal*, 374:L37–L40, 1991.

Geoffrey W Marcy, Howard Isaacson, Andrew W Howard, Jason F Rowe, Jon M Jenkins, Stephen T Bryson, David W Latham, Steve B Howell, Thomas N Gautier III, Natalie M Batalha, et al. Masses, radii, and orbits of small kepler planets: The transition from gaseous to rocky planetsbased in part on observations obtained at the wm keck observatory, which is operated by the university of california and the california institute of technology. *The Astrophysical Journal Supplement Series*, 210(2):20, 2014.

JM Mas-Hesse, A Giménez, JL Culhane, Claude Jamar, B McBreen, J Torra, R Hudec, J Fabregat, E Meurs, Jean-Pierre Swings, et al. Omc: An optical monitoring camera for integral-instrument description and performance. *Astronomy & Astrophysics*, 411(1): L261–L268, 2003.

Kento Masuda. Very low density planets around kepler-51 revealed with transit timing variations and an anomaly similar to a planet-planet eclipse event. *The Astrophysical Journal*, 783(1):53, 2014.

Rachel A Matson, Douglas R Gies, Zhao Guo, and Jerome A Orosz. Fundamental parameters of kepler eclipsing binaries. i. kic 5738698. *The Astronomical Journal*, 151(6):139, 2016.

Taro Matsuo, H Shibai, T Ootsubo, and M Tamura. Planetary formation scenarios revisited: core-accretion versus disk instability. *The Astrophysical Journal*, 662(2):1282, 2007.

Christian Mayer. De novis in coelo sidereo phaenomenis in miris stellarum fixarum comitibus, 1779.

M Mayor, F Pepe, D Queloz, F Bouchy, G Rupprecht, G Lo Curto, G Avila, W Benz, J-L Bertaux, X Bonfils, et al. Setting new standards with harps. *The Messenger*, 114:20–24, 2003.

Michel Mayor and Didier Queloz. A jupiter-mass companion to a solar-type star, 1995.

Michel Mayor, M Marmier, Ch Lovis, S Udry, D Ségransan, F Pepe, W Benz, J-L Bertaux, F Bouchy, X Dumusque, et al. The harps search for southern extra-solar planets xxxiv. occurrence, mass distribution and orbital properties of super-earths and neptune-mass planets. *arXiv preprint arXiv:1109.2497*, 2011.

Tsevi Mazeh, Dominique Naef, Guillermo Torres, David W Latham, Michel Mayor, Jean-Luc Beuzit, Timothy M Brown, Lars Buchhave, Michel Burnet, Bruce W Carney, et al.

The spectroscopic orbit of the planetary companion transiting hd 209458. *The Astrophysical Journal Letters*, 532(1):L55, 2000.

Tsevi Mazeh, Gil Nachmani, Tomer Holczer, Daniel C Fabrycky, Eric B Ford, Roberto Sanchis-Ojeda, Gil Sokol, Jason F Rowe, Shay Zucker, Eric Agol, et al. Transit timing observations from kepler. viii. catalog of transit timing measurements of the first twelve quarters. *The Astrophysical Journal Supplement Series*, 208(2):16, 2013.

P. R. McCullough, J. E. Stys, J. A. Valenti, S. W. Fleming, K. A. Janes, and J. N. Heasley. The XO Project: Searching for Transiting Extrasolar Planet Candidates. *Publications of the ASP*, 117:783–795, August 2005. doi: 10.1086/432024.

P. R. McCullough, J. E. Stys, J. A. Valenti, C. M. Johns-Krull, K. A. Janes, J. N. Heasley, B. A. Bye, C. Dodd, S. W. Fleming, A. Pinnick, R. Bissinger, B. L. Gary, P. J. Howell, and T. Vanmunster. A Transiting Planet of a Sun-like Star. *The Astrophysical Journal*, 648:1228–1238, September 2006. doi: 10.1086/505651.

DB McLaughlin. Some results of a spectrographic study of the algol system. *The Astrophysical Journal*, 60, 1924.

DS McNeil and RP Nelson. On the formation of hot neptunes and super-earths. *Monthly Notices of the Royal Astronomical Society*, 401(3):1691–1708, 2010.

Daniel Michalik, Lennart Lindegren, and David Hobbs. The tycho-gaia astrometric solution-how to get 2.5 million parallaxes with less than one year of gaia data. *Astronomy & Astrophysics*, 574:A115, 2015.

John Michell. An inquiry into the probable parallax, and magnitude of the fixed stars, from the quantity of light which they afford us, and the particular circumstances of their situation, by the rev. john michell, bdfrs. *Philosophical transactions*, 57:234–264, 1767.

A. Miroshnichenko, Ž. Ivezić , D. Vinković , and M. Elitzur. Dust Emission from Herbig AE/BE Stars: Evidence for Disks and Envelopes. *Astrophysical Journal, Letters*, 520: L115–L118, August 1999. doi: 10.1086/312159.

David G Monet, Stephen E Levine, Blaise Canzian, Harold D Ables, Alan R Bird, Conard C Dahn, Harry H Guetter, Hugh C Harris, Arne A Henden, Sandy K Leggett, et al. The usno-b catalog. *The Astronomical Journal*, 125(2):984, 2003.

Benjamin T Montet, Timothy D Morton, Daniel Foreman-Mackey, John Asher Johnson, David W Hogg, Brendan P Bowler, David W Latham, Allyson Bieryla, and Andrew W Mann. Stellar and planetary properties of k2 campaign 1 candidates and validation of

17 planets, including a planet receiving earth-like insolation. *The Astrophysical Journal*, 809(1):25, 2015.

Timothy D Morton. An efficient automated validation procedure for exoplanet transit candidates. *The Astrophysical Journal*, 761(1):6, 2012.

Timothy D Morton, Stephen T Bryson, Jeffrey L Coughlin, Jason F Rowe, Ganesh Ravichandran, Erik A Petigura, Michael R Haas, and Natalie M Batalha. False positive probabilities for all kepler objects of interest: 1284 newly validated planets and 428 likely false positives. *The Astrophysical Journal*, 822(2):86, 2016.

Claire Moutou, Magali Deleuil, Tristan Guillot, Annie Baglin, Pascal Bordé, Francois Bouchy, Juan Cabrera, Szilárd Csizmadia, Hans J Deeg, et al. Corot: Harvest of the exoplanet program. *Icarus*, 226(2):1625–1634, 2013.

U Munari, A Henden, A Frigo, T Zwitter, O Bienaymé, Joss Bland-Hawthorn, C Boeche, KC Freeman, Bradley K Gibson, G Gilmore, et al. Apass landolt-sloan bvgri photometry of rave stars. i. data, effective temperatures, and reddenings. *The Astronomical Journal*, 148(5):81, 2014.

T Muto, CA Grady, J Hashimoto, M Fukagawa, JB Hornbeck, M Sitko, R Russell, C Werren, M Curé, T Currie, et al. Discovery of small-scale spiral structures in the disk of sao 206462 (hd 135344b): Implications for the physical state of the disk from spiral density wave theory. *The Astrophysical Journal Letters*, 748(2):L22, 2012.

Radford M Neal. Monte carlo implementation of gaussian process models for bayesian regression and classification. *arXiv preprint physics/9701026*, 1997.

David Nesvornỳ, Jose LA Alvarellos, Luke Dones, and Harold F Levison. Orbital and collisional evolution of the irregular satellites. *The Astronomical Journal*, 126(1):398, 2003.

David Nesvornỳ, David Kipping, Dirk Terrell, Joel Hartman, Gáspár Á Bakos, and Lars A Buchhave. Koi-142, the king of transit variations, is a pair of planets near the 2: 1 resonance. *The Astrophysical Journal*, 777(1):3, 2013.

Isaac Newton. *Philosophiae naturalis principia mathematica*. 1687.

P. E. Nissen. High-precision abundances of elements in solar twin stars. Trends with stellar age and elemental condensation temperature. *Astronomy and Astrophysics*, 579:A52, July 2015. doi: 10.1051/0004-6361/201526269.

HP Osborn, David J Armstrong, DJA Brown, J McCormac, AP Doyle, Tom M Louden, J Kirk, Jessica J Spake, KWF Lam, SR Walker, et al. Single transit candidates from k2: detection and period estimation. *Monthly Notices of the Royal Astronomical Society*, 457 (3):2273–2286, 2016.

HP Osborn, JE Rodriguez, MA Kenworthy, GM Kennedy, EE Mamajek, CE Robinson, CC Espaillat, DJ Armstrong, BJ Shappee, A Bieryla, DW Latham, DR Anderson, TG Beatty, P Berlind, ML Calkins, GA Esquerdo, BS Gaudi, C Hellier, TW-S Holoien, D James, CS Kochanek, RB Kuhn, MB Lund, J Pepper, DL Pollacco, JL Prieto, RJ Siverd, KG Stassun, DJ Stevens, KZ Stanek, and RG West. Periodic eclipses of the young star pds 110 discovered with wasp and kelt photometry. *Monthly Notices of the Royal Astronomical Society*, page stx1249, 2017a.

HP Osborn, A Santerne, SCC Barros, NC Santos, X Dumusque, L Malavoltacnmsep, DJ Armstrong, S Hojjatpanah, O Demangeon, V Adibekyan, J-M Almenara, D Barrado, D Bayliss, I Boisse, F Bouchy, DJA Brown, AC Cameron, D Charbonneau, M Deleuil, E DelgadoMena, R Diaz, G H'ebrard, J Kirk, GW King, KWF Lam, D Latham, J Lillo-Box, TM Louden, C Lovis, M Marmier, J McCormac, E Molinari, F Pepe, D Pollacco, SG Sousa, S Udry, and SR Walker. K2-110 b: a massive mini-neptune exoplanet. *Astronomy & Astrophysics*, 604:A19, 2017b.

James E Owen and Alan P Jackson. Planetary evaporation by uv and x-ray radiation: basic hydrodynamics. *Monthly Notices of the Royal Astronomical Society*, 425(4):2931–2947, 2012.

M. J. Pecaut and E. E. Mamajek. Intrinsic Colors, Temperatures, and Bolometric Corrections of Pre-main-sequence Stars. *"Astrophysical Journal, Supplement"*, 208:9, September 2013. doi: 10.1088/0067-0049/208/1/9.

M. J. Pecaut and E. E. Mamajek. The star formation history and accretion-disc fraction among the K-type members of the Scorpius-Centaurus OB association. *Monthly Notices of the Royal Astronomical Society*, 461:794–815, September 2016. doi: 10.1093/mnras/stw1300.

Mark J Pecaut and Eric E Mamajek. Intrinsic colors, temperatures, and bolometric corrections of pre-main-sequence stars. *The Astrophysical Journal Supplement Series*, 208(1): 9, 2013.

Fabian Pedregosa, Gaël Varoquaux, Alexandre Gramfort, Vincent Michel, Bertrand Thirion, Olivier Grisel, Mathieu Blondel, Peter Prettenhofer, Ron Weiss, Vincent

Dubourg, et al. Scikit-learn: Machine learning in python. *Journal of Machine Learning Research*, 12(Oct):2825–2830, 2011.

WD Pence. Fitsio and fits file utility software. In *Astronomical Data Analysis Software and Systems I*, volume 25, page 22, 1992.

Francesco Pepe, Michel Mayor, Bernard Delabre, Dominique Kohler, Daniel Lacroix, Didier Queloz, Stephane Udry, Willy Benz, Jean-Loup Bertaux, and Jean-Pierre Sivan. Harps: a new high-resolution spectrograph for the search of extrasolar planets. In *Astronomical Telescopes and Instrumentation*, pages 582–592. International Society for Optics and Photonics, 2000.

J. Pepper, R. W. Pogge, D. L. DePoy, J. L. Marshall, K. Z. Stanek, A. M. Stutz, S. Poindexter, R. Siverd, T. P. O'Brien, M. Trueblood, and P. Trueblood. The Kilodegree Extremely Little Telescope (KELT): A Small Robotic Telescope for Large-Area Synoptic Surveys. *Publications of the Astronomical Society of the Pacific*, 119:923–935, August 2007. doi: 10.1086/521836.

J. Pepper, R. B. Kuhn, R. Siverd, D. James, and K. Stassun. The KELT-South Telescope. *Publications of the Astronomical Society of the Pacific*, 124:230–241, March 2012. doi: 10.1086/665044.

S Perruchot, D Kohler, F Bouchy, Y Richaud, P Richaud, G Moreaux, M Merzougui, R Sottile, L Hill, G Knispel, et al. The sophie spectrograph: design and technical key-points for high throughput and high stability. In *SPIE Astronomical Telescopes+ Instrumentation*, pages 70140J–70140J. International Society for Optics and Photonics, 2008.

Michael Perryman, Joel Hartman, Gáspár Á Bakos, and Lennart Lindegren. Astrometric exoplanet detection with gaia. *The Astrophysical Journal*, 797(1):14, 2014.

Erik A Petigura, Andrew W Howard, and Geoffrey W Marcy. Prevalence of earth-size planets orbiting sun-like stars. *Proceedings of the National Academy of Sciences*, 110 (48):19273–19278, 2013.

Erik A Petigura, Evan Sinukoff, Eric D Lopez, Ian JM Crossfield, Andrew W Howard, John M Brewer, Benjamin J Fulton, Howard T Isaacson, David R Ciardi, Steve B Howell, et al. Four sub-saturns with dissimilar densities: Windows into planetary cores and envelopes. *The Astronomical Journal*, 153(4):142, 2017.

Edward C Pickering. Dimensions of the fixed stars, with especial reference to binaries and variables of the algol type. In *Proceedings of the American Academy of Arts and Sciences*, volume 16, pages 1–37. JSTOR, 1880.

G. Pojmanski. The All Sky Automated Survey. *Acta Astronomica*, 47:467–481, October 1997.

G Pojmanski. The all sky automated survey. catalog of variable stars. i. 0 h-6 hquarter of the southern hemisphere. *Acta Astronomica*, 52:397–427, 2002.

D L Pollacco, I Skillen, A Collier Cameron, D J Christian, C Hellier, J Irwin, T A Lister, R A Street, R G West, D Anderson, W I Clarkson, H Deeg, B Enoch, A Evans, A Fitzsimmons, C A Haswell, S Hodgkin, K Horne, S R Kane, F P Keenan, P F L Maxted, A J Norton, J Osborne, N R Parley, R S I Ryans, B Smalley, P J Wheatley, and D M Wilson. The WASP Project and the SuperWASP Cameras. *Publications of the Astronomical Society of the Pacific*, 118(848):1407–1418, 2006.

James B Pollack, Olenka Hubickyj, Peter Bodenheimer, Jack J Lissauer, Morris Podolak, and Yuval Greenzweig. Formation of the giant planets by concurrent accretion of solids and gas. *icarus*, 124(1):62–85, 1996.

Frédéric Pont, Shay Zucker, and Didier Queloz. The effect of red noise on planetary transit detection. *Monthly Notices of the Royal Astronomical Society*, 373(1):231–242, 2006.

Benjamin JS Pope, Hannu Parviainen, and Suzanne Aigrain. Transiting exoplanet candidates from k2 campaigns 5 and 6. *Monthly Notices of the Royal Astronomical Society*, page stw1373, 2016.

W. H. Press and G. B. Rybicki. Fast algorithm for spectral analysis of unevenly sampled data. *The Astrophysical Journal*, 338:277–280, March 1989. doi: 10.1086/167197.

Ellen M Price, Leslie A Rogers, John Asher Johnson, and Rebekah I Dawson. How low can you go? the photoeccentric effect for planets of various sizes. *The Astrophysical Journal*, 799(1):17, 2015.

Dustin Putnam and Douglas Wiemer. Hybrid control architecture for the kepler spacecraft. In *Proceedings of the 2014 Gudance Navigation and Control Conference January*, pages 14–102, 2014.

D Queloz, Michel Mayor, Luc Weber, André Blécha, Michel Burnet, B Confino, D Naef, F Pepe, N Santos, and S Udry. The coralie survey for southern extra-solar planets. i. a planet orbiting the star gliese 86. *Astronomy and Astrophysics*, 354:99–102, 2000.

Didier Queloz. Echelle spectroscopy with a ccd at low signal-to-noise ratio. In *New Developments in Array Technology and Applications*, pages 221–229. Springer, 1995.

AC Quillen and DE Trilling. Do proto-jovian planets drive outflows? *The Astrophysical Journal*, 508(2):707, 1998.

Vinesh Rajpaul, Suzanne Aigrain, Michael A Osborne, Steven Reece, and S Roberts. A gaussian process framework for modelling stellar activity signals in radial velocity data. *Monthly Notices of the Royal Astronomical Society*, 452(3):2269–2291, 2015.

Carl Edward Rasmussen. *Evaluation of Gaussian processes and other methods for non-linear regression*. PhD thesis, Citeseer, 1996.

Heike Rauer, Claude Catala, Conny Aerts, Thierry Appourchaux, Willy Benz, Alexis Brandeker, Jorgen Christensen-Dalsgaard, Magali Deleuil, Laurent Gizon, M-J Goupil, et al. The plato 2.0 mission. *Experimental Astronomy*, 38(1-2):249–330, 2014.

Hanno Rein. Period ratios in multiplanetary systems discovered by kepler are consistent with planet migration. *Monthly Notices of the Royal Astronomical Society: Letters*, 427 (1):L21–L24, 2012.

George R Ricker, DW Latham, RK Vanderspek, KA Ennico, G Bakos, TM Brown, AJ Burgasser, D Charbonneau, M Clampin, LD Deming, et al. Transiting exoplanet survey satellite (tess). In *Bulletin of the American Astronomical Society*, volume 42, page 459, 2010.

George R Ricker, Joshua N Winn, Roland Vanderspek, David W Latham, Gáspár Á Bakos, Jacob L Bean, Zachory K Berta-Thompson, Timothy M Brown, Lars Buchhave, Nathaniel R Butler, et al. Transiting exoplanet survey satellite. *Journal of Astronomical Telescopes, Instruments, and Systems*, 1(1):014003–014003, 2015.

Stephen Roberts, M Osborne, M Ebden, Steven Reece, N Gibson, and S Aigrain. Gaussian processes for time-series modelling. *Phil. Trans. R. Soc. A*, 371(1984):20110550, 2013.

Thomas P Robitaille, Erik J Tollerud, Perry Greenfield, Michael Droettboom, Erik Bray, Tom Aldcroft, Matt Davis, Adam Ginsburg, Adrian M Price-Whelan, Wolfgang E Kerzendorf, et al. Astropy: A community python package for astronomy. *Astronomy and Astrophysics*, 558:A33, 2013.

J. E. Rodriguez, J. Pepper, K. G. Stassun, R. J. Siverd, P. Cargile, T. G. Beatty, and B. S. Gaudi. Occultation of the T Tauri Star RW Aurigae A by its Tidally Disrupted Disk. *The Astronomical Journal*, 146:112, November 2013. doi: 10.1088/0004-6256/146/5/112.

J. E. Rodriguez, J. Pepper, K. G. Stassun, R. J. Siverd, P. Cargile, D. A. Weintraub, T. G. Beatty, B. S. Gaudi, E. E. Mamajek, and N. N. Sanchez. V409 Tau as Another AA

Tau: Photometric Observations of Stellar Occultations by the Circumstellar Disk. *The Astronomical Journal*, 150:32, July 2015. doi: 10.1088/0004-6256/150/1/32.

J. E. Rodriguez, J. Pepper, and K. G. Stassun. First Results from the Disk Eclipse Search with KELT (DESK) Survey. In J. H. Kastner, B. Stelzer, and S. A. Metchev, editors, *Young Stars & Planets Near the Sun*, volume 314 of *IAU Symposium*, pages 167–170, January 2016a. doi: 10.1017/S1743921315005931.

J. E. Rodriguez, P. A. Reed, R. J. Siverd, J. Pepper, K. G. Stassun, B. S. Gaudi, D. A. Weintraub, T. G. Beatty, M. B. Lund, and D. J. Stevens. Recurring Occultations of RW Aurigae by Coagulated Dust in the Tidally Disrupted Circumstellar Disk. *The Astronomical Journal*, 151:29, February 2016b. doi: 10.3847/0004-6256/151/2/29.

J. E. Rodriguez, K. G. Stassun, P. Cargile, B. J. Shappee, R. J. Siverd, J. Pepper, M. B. Lund, C. S. Kochanek, D. James, R. B. Kuhn, T. G. Beatty, B. S. Gaudi, D. A. Weintraub, K. Z. Stanek, T. W.-S. Holoien, J. L. Prieto, D. M. Feldman, and C. C. Espaillat. DM Ori: A Young Star Occulted by a Disturbance in Its Protoplanetary Disk. *"The Astrophysical Journal"*, 831:74, November 2016c. doi: 10.3847/0004-637X/831/1/74.

J. E. Rodriguez, K. G. Stassun, M. B. Lund, R. J. Siverd, J. Pepper, S. Tang, S. Kafka, B. S. Gaudi, K. E. Conroy, T. G. Beatty, D. J. Stevens, B. J. Shappee, and C. S. Kochanek. An Extreme Analogue of ϵ Aurigae: An M-giant Eclipsed Every 69 Years by a Large Opaque Disk Surrounding a Small Hot Source. *The Astronomical Journal*, 151:123, May 2016d. doi: 10.3847/0004-6256/151/5/123.

Joseph E Rodriguez, George Zhou, Phillip A Cargile, Daniel J Stevens, Hugh P Osborn, Benjamin J Shappee, Phillip A Reed, Michael B Lund, Howard M Relles, David W Latham, et al. The mysterious dimmings of the t tauri star v1334 tau. *arXiv preprint arXiv:1701.03044*, 2017.

G. Rojas, J. Gregorio-Hetem, and A. Hetem. Towards the main sequence: detailed analysis of weak line and post-T Tauri stars. *Monthly Notices of the Royal Astronomical Society*, 387:1335–1343, July 2008. doi: 10.1111/j.1365-2966.2008.13355.x.

Frank Rosenblatt. A two-color photometric method for detection of extra-solar planetary systems. *Icarus*, 14(1):71–93, 1971.

RA Rossiter. On the detection of an effect of rotation during eclipse in the velocity of the brigher component of beta lyrae, and on the constancy of velocity of this system. *The Astrophysical Journal*, 60:15–21, 1924.

Jason F Rowe, Stephen T Bryson, Geoffrey W Marcy, Jack J Lissauer, Daniel Jontof-Hutter, Fergal Mullally, Ronald L Gilliland, Howard Issacson, Eric Ford, Steve B Howell, et al. Validation of kepler's multiple planet candidates. iii. light curve analysis and announcement of hundreds of new multi-planet systems. *The Astrophysical Journal*, 784(1):45, 2014.

Slavek M Rucinski, Jaymie M Matthews, Rainer Kuschnig, Grzegorz Pojmański, Jason Rowe, David B Guenther, Anthony FJ Moffat, Dimitar Sasselov, Gordon AH Walker, and Werner W Weiss. Photometric variability of the t tauri star tw hya on time-scales of hours to years. *Monthly Notices of the Royal Astronomical Society*, 391(4):1913–1924, 2008.

Andrew J Rushby, Mark W Claire, Hugh Osborn, and Andrew J Watson. Habitable zone lifetimes of exoplanets around main sequence stars. *Astrobiology*, 13(9):833–849, 2013.

A Santerne, RF Díaz, J-M Almenara, F Bouchy, M Deleuil, P Figueira, G Hébrard, C Moutou, S Rodionov, and NC Santos. pastis: Bayesian extrasolar planet validation–ii. constraining exoplanet blend scenarios using spectroscopic diagnoses. *Monthly Notices of the Royal Astronomical Society*, 451(3):2337–2351, 2015.

A Santerne, G Hébrard, J Lillo-Box, David J Armstrong, SCC Barros, O Demangeon, D Barrado, A Debackere, M Deleuil, E Delgado Mena, et al. K2-29 b/wasp-152 b: an aligned and inflated hot jupiter in a young visual binary. *The Astrophysical Journal*, 824(1):55, 2016.

N. C. Santos, S. G. Sousa, A. Mortier, V. Neves, V. Adibekyan, M. Tsantaki, E. Delgado Mena, X. Bonfils, G. Israelian, M. Mayor, and S. Udry. SWEET-Cat: A catalogue of parameters for Stars With ExoplanETs. I. New atmospheric parameters and masses for 48 stars with planets. *A&A*, 556:A150, August 2013. doi: 10.1051/0004-6361/201321286.

N. C. Santos, V. Adibekyan, C. Mordasini, W. Benz, E. Delgado-Mena, C. Dorn, L. Buchhave, P. Figueira, A. Mortier, F. Pepe, A. Santerne, S. G. Sousa, and S. Udry. Constraining planet structure from stellar chemistry: the cases of CoRoT-7, Kepler-10, and Kepler-93. *Astronomy and Astrophysics*, 580:L13, August 2015. doi: 10.1051/0004-6361/201526850.

Hilke E. Schlichting. Formation of close in super-earths and mini-neptunes: Required disk masses and their implications. *The Astrophysical Journal Letters*, 795(1):L15, 2014. URL `http://stacks.iop.org/2041-8205/795/i=1/a=L15`.

E. L. Scott, E. E. Mamajek, M. J. Pecaut, A. C. Quillen, F. Moolekamp, and C. P. M. Bell. Modeling Transiting Circumstellar Disks: Characterizing the Newly Discovered

Eclipsing Disk System OGLE LMC-ECL-11893. *"The Astrophysical Journal"*, 797:6, December 2014. doi: 10.1088/0004-637X/797/1/6.

Sara Seager and Drake Deming. Exoplanet atmospheres. *Annual Review of Astronomy and Astrophysics*, 48:631–672, 2010.

Sara Seager and Gabriela Mallen-Ornelas. A unique solution of planet and star parameters from an extrasolar planet transit light curve. *The Astrophysical Journal*, 585(2):1038, 2003.

Angelo Secchi. Schreiben des herrn prof. secchi, dir. der sternw. des collegio rom. an den herausgeber. *Astronomische Nachrichten*, 59:193, 1863.

B. J. Shappee, J. L. Prieto, D. Grupe, C. S. Kochanek, K. Z. Stanek, G. De Rosa, S. Mathur, Y. Zu, B. M. Peterson, R. W. Pogge, S. Komossa, M. Im, J. Jencson, T. W.-S. Holoien, U. Basu, J. F. Beacom, D. M. Szczygieł, J. Brimacombe, S. Adams, A. Campillay, C. Choi, C. Contreras, M. Dietrich, M. Dubberley, M. Elphick, S. Foale, M. Giustini, C. Gonzalez, E. Hawkins, D. A. Howell, E. Y. Hsiao, M. Koss, K. M. Leighly, N. Morrell, D. Mudd, D. Mullins, J. M. Nugent, J. Parrent, M. M. Phillips, G. Pojmanski, W. Rosing, R. Ross, D. Sand, D. M. Terndrup, S. Valenti, Z. Walker, and Y. Yoon. The Man behind the Curtain: X-Rays Drive the UV through NIR Variability in the 2013 Active Galactic Nucleus Outburst in NGC 2617. *"The Astrophysical Journal"*, 788:48, June 2014. doi: 10.1088/0004-637X/788/1/48.

Avi Shporer, Tim Brown, Tim Lister, Rachel Street, Yiannis Tsapras, Federica Bianco, Benjamin Fulton, and Andy Howell. The lcogt network. *Proceedings of the International Astronomical Union*, 6(S276):553–555, 2010.

L. Siess, E. Dufour, and M. Forestini. An internet server for pre-main sequence tracks of low- and intermediate-mass stars. *Astronomy and Astrophysics*, 358:593–599, June 2000.

SM Simkin. Measurements of velocity dispersions and doppler shifts from digitized optical spectra. *Astronomy and Astrophysics*, 31:129, 1974.

AE Simon, Gy M Szabó, LL Kiss, and K Szatmáry. Signals of exomoons in averaged light curves of exoplanets. *Monthly Notices of the Royal Astronomical Society*, 419(1): 164–171, 2012.

David K Sing. Stellar limb-darkening coefficients for corot and kepler. *Astronomy & Astrophysics*, 510:A21, 2010.

David K Sing, Jonathan J Fortney, Nikolay Nikolov, Hannah R Wakeford, Tiffany Kataria, Thomas M Evans, Suzanne Aigrain, Gilda E Ballester, Adam S Burrows, Drake Deming, et al. A continuum from clear to cloudy hot-jupiter exoplanets without primordial water depletion. *Nature*, 529(7584):59–62, 2016.

Evan Sinukoff, Andrew W Howard, Erik A Petigura, Joshua E Schlieder, Ian JM Crossfield, David R Ciardi, Benjamin J Fulton, Howard Isaacson, Kimberly M Aller, Christoph Baranec, et al. Ten multi-planet systems from k2 campaigns 1 & 2 and the masses of two hot super-earths. *arXiv preprint arXiv:1511.09213*, 2015.

Evan Sinukoff, Andrew W Howard, Erik A Petigura, Joshua E Schlieder, Ian JM Crossfield, David R Ciardi, Benjamin J Fulton, Howard Isaacson, Kimberly M Aller, Christoph Baranec, et al. Eleven multiplanet systems from k2 campaigns 1 and 2 and the masses of two hot super-earths. *The Astrophysical Journal*, 827(1):78, 2016.

R. J. Siverd, T. G. Beatty, J. Pepper, J. D. Eastman, K. Collins, A. Bieryla, D. W. Latham, L. A. Buchhave, E. L. N. Jensen, J. R. Crepp, R. Street, K. G. Stassun, B. S. Gaudi, P. Berlind, M. L. Calkins, D. L. DePoy, G. A. Esquerdo, B. J. Fulton, G. Fűrész, J. C. Geary, A. Gould, L. Hebb, J. F. Kielkopf, J. L. Marshall, R. Pogge, K. Z. Stanek, R. P. Stefanik, A. H. Szentgyorgyi, M. Trueblood, P. Trueblood, A. M. Stutz, and J. L. van Saders. KELT-1b: A Strongly Irradiated, Highly Inflated, Short Period, 27 Jupiter-mass Companion Transiting a Mid-F Star. *"The Astrophysical Journal"*, 761:123, December 2012. doi: 10.1088/0004-637X/761/2/123.

M. Siwak, S. M. Rucinski, J. M. Matthews, G. Pojmański, R. Kuschnig, D. B. Guenther, A. F. J. Moffat, D. Sasselov, and W. W. Weiss. Analysis of variability of TW Hya as observed by MOST and ASAS in 2009. *Monthly Notices of the Royal Astronomical Society*, 410:2725–2729, February 2011. doi: 10.1111/j.1365-2966.2010.17649.x.

MF Skrutskie, RM Cutri, R Stiening, MD Weinberg, S Schneider, JM Carpenter, Capps Beichman, R Capps, T Chester, J Elias, et al. The two micron all sky survey (2mass). *The Astronomical Journal*, 131(2):1163, 2006.

AMS Smith, DR Anderson, David J Armstrong, SCC Barros, AS Bonomo, F Bouchy, DJA Brown, A Collier Cameron, Laetitia Delrez, Francesca Faedi, et al. Wasp-104b and wasp-106b: two transiting hot jupiters in 1.75-day and 9.3-day orbits. *Astronomy & Astrophysics*, 570:A64, 2014.

C. Sneden. Phd thesis. *Ph.D. Thesis, Austin, Univ. of Texas*, 1973.

Sérgio G Sousa, Nuno C Santos, Garik Israelian, Michel Mayor, and Stéphane Udry. Spectroscopic stellar parameters for 582 fgk stars in the harps volume-limited sample-revising the metallicity-planet correlation. *Astronomy & Astrophysics*, 533:A141, 2011.

John Southworth. Homogeneous studies of transiting extrasolar planets–i. light-curve analyses. *Monthly Notices of the Royal Astronomical Society*, 386(3):1644–1666, 2008.

Jessica J Spake, David JA Brown, Amanda P Doyle, Guillaume Hébrard, James McCormac, David J Armstrong, Don Pollacco, Y Gómez Maqueo Chew, David R Anderson, Susana CC Barros, et al. Wasp-135b: a highly irradiated, inflated hot jupiter orbiting a g5v star. *Publications of the Astronomical Society of the Pacific*, 128(960):024401, 2016.

Ronald C Stone. A comparison of digital centering algorithms. *The Astronomical Journal*, 97:1227–1237, 1989.

V Straižys and G Kuriliene. Fundamental stellar parameters derived from the evolutionary tracks. *Astrophysics and Space Science*, 80(2):353–368, 1981.

O. Struve. Proposal for a project of high-precision stellar radial velocity work. *The Observatory*, 72:199–200, October 1952.

Martin C Stumpe, Jeffrey C Smith, Jeffrey E Van Cleve, Joseph D Twicken, Thomas S Barclay, Michael N Fanelli, Forrest R Girouard, Jon M Jenkins, Jeffery J Kolodziejczak, Sean D McCauliff, et al. Kepler presearch data conditioning iâĂŤarchitecture and algorithms for error correction in kepler light curves. *Publications of the Astronomical Society of the Pacific*, 124(919):985, 2012.

O. Suárez, P. García-Lario, A. Manchado, M. Manteiga, A. Ulla, and S. R. Pottasch. A spectroscopic atlas of post-AGB stars and planetary nebulae selected from the IRAS point source catalogue. *Astronomy and Astrophysics*, 458:173–180, October 2006. doi: 10.1051/0004-6361:20054108.

Peter W Sullivan, Joshua N Winn, Zachory K Berta-Thompson, David Charbonneau, Drake Deming, Courtney D Dressing, David W Latham, Alan M Levine, Peter R McCullough, Timothy Morton, et al. The transiting exoplanet survey satellite: Simulations of planet detections and astrophysical false positives. *The Astrophysical Journal*, 809(1):77, 2015.

AH Szentgyorgyi and G Furész. Precision radial velocities for the kepler era. In *The 3rd Mexico-Korea Conference on Astrophysics: Telescopes of the Future and San Pedro Mártir: México DF, México, Noviembre 8-11, 2005*, volume 28, pages 129–133. Instituto de Astronomia Universidad Nacional Autonoma de Mex, 2007.

GJJ Talens, JFP Spronck, A-L Lesage, GPPL Otten, R Stuik, D Pollacco, and IAG Snellen. The multi-site all-sky camera (mascara)-finding transiting exoplanets around bright (mv< 8) stars. *Astronomy & Astrophysics*, 601:A11, 2017.

O. Tamuz, T. Mazeh, and S. Zucker. Correcting systematic effects in a large set of photometric light curves. *Monthly Notices of the Royal Astronomical Society*, 356:1466–1470, February 2005. doi: 10.1111/j.1365-2966.2004.08585.x.

Omer Tamuz, Tsevi Mazeh, and Shay Zucker. Correcting systematic effects in a large set of photometric light curves. *Monthly Notices of the Royal Astronomical Society*, 356(4): 1466–1470, 2005.

Peter Tenenbaum, Jon M Jenkins, Shawn Seader, Christopher J Burke, Jessie L Christiansen, Jason F Rowe, Douglas A Caldwell, Bruce D Clarke, Jeffrey L Coughlin, Jie Li, et al. Detection of potential transit signals in 16 quarters of kepler mission data. *The Astrophysical Journal Supplement Series*, 211(1):6, 2014.

Giovanna Tinetti, Alfred Vidal-Madjar, Mao-Chang Liang, Jean-Philippe Beaulieu, Yuk Yung, Sean Carey, Robert J Barber, Jonathan Tennyson, Ignasi Ribas, Nicole Allard, et al. Water vapour in the atmosphere of a transiting extrasolar planet. *Nature*, 448 (7150):169–171, 2007.

C. A. O. Torres, G. Quast, R. de La Reza, J. Gregorio-Hetem, and J. R. D. Lepine. Search for T Tauri Stars Based on the IRAS Point Source Catalog. II. *The Astronomical Journal*, 109:2146, May 1995. doi: 10.1086/117440.

G Torres, Johannes Andersen, and A Giménez. Accurate masses and radii of normal stars: modern results and applications. *The Astronomy and Astrophysics Review*, 18(1-2):67–126, 2010.

Guillermo Torres, Joshua N Winn, and Matthew J Holman. Improved parameters for extrasolar transiting planets. *The Astrophysical Journal*, 677(2):1324, 2008.

M. Tsantaki, S. G. Sousa, V. Z. Adibekyan, N. C. Santos, A. Mortier, and G. Israelian. Deriving precise parameters for cool solar-type stars. Optimizing the iron line list. *ArXiv e-prints*, April 2013.

M. Tucci Maia, I. Ramírez, J. Meléndez, M. Bedell, J. L. Bean, and M. Asplund. The Solar Twin Planet Search III. The [Y/Mg] clock: estimating stellar ages of solar-type stars. *ArXiv e-prints*, April 2016.

Mikko Tuomi, Guillem Anglada-Escude, James S Jenkins, and Hugh RA Jones. Filtering out activity-related variations from radial velocities in a search for low-mass planets. *arXiv preprint arXiv:1405.2016*, 2014.

Joseph D Twicken, Hema Chandrasekaran, Jon M Jenkins, Jay P Gunter, Forrest Girouard, and Todd C Klaus. Presearch data conditioning in the kepler science operations center pipeline. In *SPIE Astronomical Telescopes+ Instrumentation*, pages 77401U–77401U. International Society for Optics and Photonics, 2010.

A Udalski. The optical gravitational lensing experiment. real time data analysis systems in the ogle-iii survey. *Acta Astronomica*, 53:291–305, 2003.

A. Udalski, O. Szewczyk, K. Zebrun, G. Pietrzynski, M. Szymanski, M. Kubiak, I. Soszynski, and L. Wyrzykowski. The Optical Gravitational Lensing Experiment. Planetary and Low-Luminosity Object Transits in the Carina Fields of the Galactic Disk. *Acta Astronomica*, 52:317–359, December 2002.

A Udalski, M Jaroszyński, B Paczyński, M Kubiak, MK Szymański, I Soszyński, G Pietrzyński, K Ulaczyk, O Szewczyk, GW Christie, et al. A jovian-mass planet in microlensing event ogle-2005-blg-071. *The Astrophysical Journal Letters*, 628(2):L109, 2005.

Sho Uehara, Hajime Kawahara, Kento Masuda, ShinâĂŹya Yamada, and Masataka Aizawa. Transiting planet candidates beyond the snow line detected by visual inspection of 7557 kepler objects of interest. *The Astrophysical Journal*, 822(1):2, 2016.

Francesca Valsecchi and Frederic A Rasio. Tidal dissipation and obliquity evolution in hot jupiter systems. *The Astrophysical Journal*, 786(2):102, 2014.

Peter Van de Kamp. Astrometric study of barnard's star from plates taken with the 24-inch sproul refractor. *The Astronomical Journal*, 68:515–521, 1963.

Julian C Van Eyken, David R Ciardi, Kaspar Von Braun, Stephen R Kane, Peter Plavchan, Chad F Bender, Timothy M Brown, Justin R Crepp, Benjamin J Fulton, Andrew W Howard, et al. The ptf orion project: A possible planet transiting a t-tauri star. *The Astrophysical Journal*, 755(1):42, 2012.

Vincent Van Eylen, Mikkel N Lund, V Silva Aguirre, Torben Arentoft, Hans Kjeldsen, Simon Albrecht, William J Chaplin, Howard Isaacson, May G Pedersen, Jens Jessen-Hansen, et al. What asteroseismology can do for exoplanets: Kepler-410a b is a small neptune around a bright star, in an eccentric orbit consistent with low obliquity. *The Astrophysical Journal*, 782(1):14, 2014.

Andrew Vanderburg and John Asher Johnson. A technique for extracting highly precise photometry for the two-wheeled kepler mission. *Publications of the Astronomical Society of the Pacific*, 126(944):948, 2014.

Andrew Vanderburg, David W Latham, Lars A Buchhave, Allyson Bieryla, Perry Berlind, Michael L Calkins, Gilbert A Esquerdo, Sophie Welsh, and John Asher Johnson. Planetary candidates from the first year of the k2 mission. *arXiv preprint arXiv:1511.07820*, 2015a.

Andrew Vanderburg, Benjamin T Montet, John Asher Johnson, Lars A Buchhave, Li Zeng, Francesco Pepe, Andrew Collier Cameron, David W Latham, Emilio Molinari, Stephane Udry, et al. Characterizing k2 planet discoveries: a super-earth transiting the bright k dwarf hip 116454. *The Astrophysical Journal*, 800(1):59, 2015b.

Andrew Vanderburg, Juliette C Becker, Martti H Kristiansen, Allyson Bieryla, Dmitry A Duev, Rebecca Jensen-Clem, Timothy D Morton, David W Latham, Fred C Adams, Christoph Baranec, et al. Five planets transiting a ninth magnitude star. *The Astrophysical Journal Letters*, 827(1):L10, 2016.

W Thomas Vestrand, Konstantin N Borozdin, Steven P Brumby, Donald E Casperson, Edward E Fenimore, Mark C Galassi, Katherine McGowan, Simon J Perkins, William C Priedhorsky, Daniel Starr, et al. The raptor experiment: a system for monitoring the optical sky in real time. In *Astronomical Telescopes and Instrumentation*, pages 126–136. International Society for Optics and Photonics, 2002.

N. V. Voshchinnikov. Dust around young stars. Model of Algol-type minima of UX Orionis stars. *Astrophysics*, 30:313–321, May 1989. doi: 10.1007/BF01003892.

Gordon AH Walker, David A Bohlender, Andrew R Walker, Alan W Irwin, Stephenson LS Yang, and Ana Larson. Gamma cephei-rotation or planetary companion? *The Astrophysical Journal*, 396:L91–L94, 1992.

Gordon AH Walker, Andrew R Walker, Alan W Irwin, Ana M Larson, Stephenson LS Yang, and Derek C Richardson. A search for jupiter-mass companions to nearby stars. *Icarus*, 116(2):359–375, 1995.

Ji Wang, Debra A Fischer, Thomas Barclay, Alyssa Picard, Bo Ma, Brendan P Bowler, Joseph R Schmitt, Tabetha S Boyajian, Kian J Jek, Daryll LaCourse, et al. Planet hunters. viii. characterization of 41 long-period exoplanet candidates from kepler archival datathis publication has been made possible by the participation of more than 200,000 volunteers in the planet hunters project. their contributions are individually acknowledged at

http://www. planethunters. org/#/acknowledgements. *The Astrophysical Journal*, 815(2): 127, 2015.

Lauren M Weiss and Geoffrey W Marcy. The mass-radius relation for 65 exoplanets smaller than 4 earth radii. *The Astrophysical Journal Letters*, 783(1):L6, 2014.

MW Werner, TL Roellig, FJ Low, GH Rieke, M Rieke, WF Hoffmann, E Young, JR Houck, B Brandl, GG Fazio, et al. The spitzer space telescope mission. *The Astrophysical Journal Supplement Series*, 154(1):1, 2004.

Peter J Wheatley, Don L Pollacco, Didier Queloz, Heike Rauer, Christopher A Watson, Richard G West, Bruno Chazelas, Tom M Louden, Simon Walker, Nigel Bannister, et al. The next generation transit survey (ngts). In *EPJ Web of Conferences*, volume 47, page 13002. EDP Sciences, 2013.

P.J. Wheatley, R.G. West, M.R Goad, J.S. Jenkins, D.L. Pollacco, D. Queloz, H. Rauer, C.A. Watson, B. Chazelas, P. Eigmüller, G. Lambert, J. McCormac, and S.R. Walker. The next generation transit survey (ngts). in prep,.

Christopher KI Williams and Carl Edward Rasmussen. Gaussian processes for regression. *Advances in neural information processing systems*, pages 514–520, 1996.

D. J. Wilson, B. T. Gänsicke, J. Farihi, and D. Koester. Carbon to oxygen ratios in extrasolar planetesimals. *Monthly Notices of the Royal Astronomical Society*, 459:3282–3286, July 2016. doi: 10.1093/mnras/stw844.

Christoph Winkler, TJ-L Courvoisier, G Di Cocco, N Gehrels, A Giménez, S Grebenev, W Hermsen, JM Mas-Hesse, F Lebrun, Niels Lund, et al. The integral mission. *Astronomy & Astrophysics*, 411(1):L1–L6, 2003.

Aleksander Wolszczan and Dail A Frail. A planetary system around the millisecond pulsar psr1257 (plus) 12. *Nature*, 355(6356):145, 1992.

Alwyn Wootten and A Richard Thompson. The atacama large millimeter/submillimeter array. *Proceedings of the IEEE*, 97(8):1463–1471, 2009.

Jason T Wright, S Upadhyay, GW Marcy, DA Fischer, Eric B Ford, and John Asher Johnson. Ten new and updated multiplanet systems and a survey of exoplanetary systems. *The Astrophysical Journal*, 693(2):1084, 2009.

Zhen-Yu Wu, Xu Zhou, Jun Ma, and Cui-Hua Du. The orbits of open clusters in the galaxy. *Monthly Notices of the Royal Astronomical Society*, 399(4):2146–2164, 2009.

Jennifer C Yee and B Scott Gaudi. Characterizing long-period transiting planets observed by kepler. *The Astrophysical Journal*, 688(1):616, 2008.

N. Zacharias, D. G. Monet, S. E. Levine, S. E. Urban, R. Gaume, and G. L. Wycoff. The Naval Observatory Merged Astrometric Dataset (NOMAD). In *American Astronomical Society Meeting Abstracts*, volume 36 of *Bulletin of the American Astronomical Society*, page 1418, December 2004.

Norbert Zacharias, Dave G Monet, Stephen E Levine, Sean E Urban, Ralph Gaume, and Gary L Wycoff. The naval observatory merged astrometric dataset (nomad). In *Americal Astronomical Society 205th Meeting*, 2005.

L. Zeng and D. Sasselov. A Detailed Model Grid for Solid Planets from 0.1 through 100 Earth Masses. *Publications of the Astronomical Society of the Pacific*, 125:227–239, March 2013. doi: 10.1086/669163.

Li Zeng and Dimitar Sasselov. The effect of temperature evolution on the interior structure of h2o-rich planets. *The Astrophysical Journal*, 784(2):96, 2014.

Feng Zhao. Wfirst-afta coronagraph instrument overview. In *SPIE Astronomical Telescopes+ Instrumentation*, pages 91430O–91430O. International Society for Optics and Photonics, 2014.